

ON THE DRIVING SOURCES AND VARIABILITY OF NORTH ATLANTIC
DEEP WATER

by

Yarisbel Garcia Quintana

A thesis submitted in partial fulfilment of the requirements for the degree of

Doctor of Philosophy

Department of Earth and Atmospheric Sciences
University of Alberta

© Yarisbel Garcia Quintana, 2019

Abstract

The rising concentration of anthropogenic heat-trapping gasses has resulted in an energy imbalance in the Earth's climate system. As a consequence of it, an enhanced hydrological cycle and the continuous decline of the ice sheets are expected to increase the freshwater input into the Arctic and Sub-Arctic basins. The input of cold and fresh waters limits vertical mixing processes in the upper ocean, and there is currently a rising concern on how these future changes might impact open ocean deep convection regions. To understand the implications of the global warming related changes on the basins and the waters formed within, it is imperative to have a better understanding of the processes involved in deep water formation. By using a numerical model with horizontal resolutions of $1/4^\circ$ and $1/12^\circ$, I investigated the sensitivity and variability of two components of the North Atlantic Deep Water under climate change-like and present-day scenarios. I found that: (I) increased Greenland melt and precipitation impact denser Labrador Sea Water (LSW) replenishment; (II) potential decreases in Labrador Sea winter heat loss due to global warming may be a bigger threat to LSW formation than freshwater increase; (III) strong light-to-dense Atlantic Water (AW) transformation driven by heat loss occurs in the boundary currents of the Nordic Seas, with densities reaching that of the overflow waters; (IV) AW entering the Nordic Seas is transformed into overflow waters in the shelf system of the basin within 6 years; (V) along the north Icelandic shelfbreak the transformation is faster with export of the transformed waters occurring in the North Icelandic Jet (NIJ) within 1 year; (VI) a new overturning loop is proposed in this thesis with the North Icelandic Irminger Current (NIIC) being the upper limb and the NIJ the lower limb. Contrary to what has been thought, I found that the transformation of the NIIC waters occurs on and along the west/northwest portion of the Icelandic shelf.

Preface

Chapter 3 has been published as:

Garcia-Quintana, Y., Courtois, P., Hu, X., Pennelly, C., Kieke, D., & Myers, P. G. (2019). *Sensitivity of Labrador Sea Water formation to changes in model resolution, atmospheric forcing, and freshwater input*. *Journal of Geophysical Research: Oceans*, 124. <https://doi.org/10.1029/2018JC014459>

I was responsible for the data analysis, running the filtered simulation and writing of the manuscript. Courtois, P. assisted with subduction calculation and manuscript edits. Hu, X. and Pennelly, C. ran the rest of the simulations, assisted with the data analysis and manuscript edits. Kieke, D. and Myers, P. G. provided advice and manuscript edits.

Chapter 4 has been submitted for publication as:

Garcia-Quintana, Y., More, C., Wiesner, P., Hu, X., Kieke, D., Sutherland B.R., & Myers P.G (2019): *Transformation of the North Icelandic Irminger Current waters in the Nordic Seas and its link to the Denmark Strait Overflow Water*. *Journal of Geophysical Research: Oceans*.

I was responsible for the data analysis of the ANHA4 experiment and writing of the manuscript. More, C. was responsible for the analysis and discussion of the older KAB001 experiment. Wiesner, P. assisted with the data analysis. Hu, X. ran the ANHA4 experiment and assisted with manuscript edits. Kieke, D., Sutherland B.R., and Myers, P. G. provided advice and manuscript edits.

Dedication

To Lucas, who came into our lives in the middle of the chaos to put everything in place, dragging me down to the Earth's surface everyday after school, forcing me to stay sane, because I had to but mostly because I wanted to, for him.

To Kaidel, who followed me North, way far from his comfort (climate) zone. For joining me in this crazy adventure that is Life. For counting, in English, in Spanish, back and forth.

"There is a driving force more powerful than steam, electricity, and atomic energy: the will."

— Albert Einstein

Acknowledgements

First of all I want to thank my supervisor, Prof. Paul G. Myers. His guidance, advise and supervision have been beyond valuable during my years as a PhD student. I am very grateful for his careful editing of my writing, always catching up any remaining Spanglish. Thanks to the rest of my committee members Dr. Gerhard W. Reuter and Dr. Andrew B.G. Bush for their insightful comments and advices during our meetings.

Thanks to Dr. Dagmar Kieke for her help on making my manuscripts stronger, always looking into every detail. Her guidance and supervision during my research stay at the University of Bremen were invaluable. Thanks to the ArcTrain program, to their students and professors: I will treasure forever our adventures into the "Arctic Realm".

Thanks to my colleagues for their friendship and constant support: Xianmin Hu, Natasha Ridenour, Nathan Grivault, Laura Gillard, Clark Pennelly, Juliana Marson, Charlene Feucher, Andrew Hamilton, Amanda Kahn, Peggy Courtois and Alain Gervais. Special thanks to Laura Castro de la Guardia (Lauri), a true friend and one of the smartest persons I know. I was lucky enough to have her guidance, advice and friendship since the very beginning of my journey as a PhD student.

Last but certainly not least, thanks to my Family, physically far and yet very much present. Thanks to my Mum, who has flew to my aid every time I have needed her, so I could get to the finishing line. The strength and resilience in me, comes entirely from her. Thanks to my Dad, surely the person which is the most proud of my journey no matter where it takes me, even if it means that he only gets to see me once every couple of years and haven't met his first grandson yet. Thanks to my sisters and to my husband's family, for caring about my work and always pending on how we were doing in our side of the world.

Contents

List of Tables	x
List of Figures	xi
1 Introduction	1
1.1 Deep Water Formation in the North Atlantic Ocean	2
1.1.1 Labrador Sea	5
1.1.1.1 Winter Convection	6
1.1.1.2 LSW Formation	8
1.1.2 Nordic Seas	9
1.1.2.1 Water Formation and Transformation	11
1.2 Thesis Objectives and Outline	13
Bibliography	16
2 Nucleus for European Modelling of the Ocean (NEMO): ocean engine	23
2.1 Introduction	23
2.2 Ocean Component	24
2.2.0.1 Primitive Equations	26
2.2.0.2 Boundary Conditions	27
2.2.0.3 Curvilinear Coordinate System and Spatial Discretization	30
2.2.0.4 Subgrid Scale Physics	32
2.2.0.4.1 Vertical Subgrid Scale Physics.	32
2.2.0.4.2 Lateral Subgrid Scale Physics.	34
2.2.0.5 Time Discretization	35
2.3 Sea Ice Component	38

2.3.1	Dynamics of Sea Ice	38
2.3.2	Thermodynamics of Sea Ice	40
2.3.3	Coupling the Ocean and Ice components	42
2.4	List of parameters	44
	Bibliography	46
3	Sensitivity of Labrador Sea Water formation to changes in model resolution, atmospheric forcing and freshwater input	48
3.1	Introduction	49
3.2	Model Description and Experiments Setup	55
3.2.1	Ocean-Sea Ice Model	55
3.2.2	Sensitivity Experiments Set-up	57
3.2.3	Model Evaluation	60
3.3	Analysis Methods	63
3.4	Results	66
3.4.1	Changing the Horizontal Resolution (SPG12 Experiment)	66
3.4.2	Impact of Removing Greenland Freshwater Discharge (GMR Experiment)	73
3.4.3	Impact of High Frequency Atmospheric Phenomena (Filtered Experiment)	77
3.4.4	Impact of Decreased Precipitation (PD Experiment)	78
3.5	Discussion and Conclusions	79
3.6	Acknowledgements	88
	Bibliography	90
4	Transformation of the North Icelandic Irminger Current waters in the Nordic Seas and its link to the Denmark Strait Overflow Water	103
4.1	Introduction	104
4.2	Analysis Methods	108
4.3	NIIC waters pathways into the Nordic Seas	111
4.3.1	KAB001 experiment	111
4.3.2	ANHA4 experiment	113
4.4	NIIC waters transformation north of Iceland	120

4.5	Discussion and Conclusions	125
4.6	Acknowledgements	128
	Bibliography	130
5	The North Icelandic Jet is fed by transformation of Atlantic Waters on the Icelandic shelf	138
5.1	Introduction	139
5.2	Methods and Data	144
5.2.1	Ocean-Sea Ice Model	144
5.2.2	Model Evaluation	146
5.3	Results	150
5.3.1	December 2007 to March 2008: a Case of Study	150
5.3.2	On the Relationship between Winter Heat Loss and NIIC Transformation	150
5.3.3	Dense Plume Evolution	155
5.3.4	Dense Water Transport	156
5.4	Discussion and Conclusions	163
	Bibliography	173
6	Conclusions	177
6.1	Principal findings	178
6.1.1	Labrador Sea Water formation sensitivity	178
6.1.2	Atlantic Water transformation in the Nordic Seas as a source to the overflow waters	179
6.1.3	A new source for the North Icelandic Jet	180
6.1.4	Thesis Summary	181
	Bibliography	183
	Bibliography	186
A	Trajectories of all the particles entering and leaving the Nordic Seas through Denmark Strait for different releases.	208

List of Tables

3.1	Set of simulations used in the present study: <i>Control</i> (reference simulation), <i>SPG12</i> (horizontal resolution increased to $1/12^\circ$), <i>Greenland Melt Removed</i> (GMR), <i>Filtered</i> (filtered winds and temperature fields) and <i>Precipitation Decreased</i> (PD). bold is used to show what is different between the simulations of an experiment. CGRF (\bullet) refers to a version of the atmospheric forcing containing a decrease in precipitation. CGRF ($\bullet\bullet$) refers to the filtered (temperature and wind fields) version of the atmospheric forcing. The period considered for all the experiment was 2004 to 2016.	58
3.2	Resolution-dependent parameters whose numerical values changed from <i>Control</i> to <i>SPG12</i>	59
3.3	Magnitude of the components in Eq.1 and maximum 2004-2016 mean subduction rate, for the five simulations used in the sensitivity experiments. As there is almost no contribution from W_b to the maximum subduction rate, it was excluded from the table.	80
4.1	Table highlighting the main differences between the KAB001 and the ANHA4 experiments.	110

List of Figures

1.1	Schematic diagram showing the North Atlantic circulation pattern following García-Ibáñez et al. (2015) and Våge et al. (2018)	4
1.2	Schematic showing the different stages of convection in the Labrador Sea	7
2.1	Spherical coordinate system in NEMO	26
2.2	Schematic of the surface and bottom boundaries in NEMO	30
2.3	Top down and 3D views of the variable arrangement in the model mesh grid.	31
2.4	Vertical model grid in traditional z-coordinate with full steps and z-coordinate with partial steps.	32
2.5	Temporal and spatial pattern of the time stepping in the Leapfrog scheme	36
3.1	Schematic showing the boundary current system around the Labrador Sea and a summary of the results from different studies investigating LSW formation rates using four methods	53
3.2	Horizontal resolution for the ANHA4 domain and for <i>SPG12</i> . Model evaluation is also presented.	62
3.3	Schematic showing the subduction and obduction process and a map of the Labrador Sea showing the study region	64
3.4	Monthly subduction and obduction rates	68
3.5	Averaged seasonal subduction and obduction rates as a function of the potential density	69
3.6	March mixed layer depths (MLD) in the Labrador Sea	71
3.7	Climatology of Irminger Water and Arctic Water spawned out of the West Greenland Current into the study region	73

3.8	Mean total subduction rate as a function of the potential density	74
3.9	Time averaged subduction components as a function of the potential density . .	75
3.10	Averaged January heat flux	78
3.11	Climatological differences between <i>Control</i> and the perturbation experiments .	82
3.12	Mean total subduction rate as a function of the potential density for the <i>Control</i> simulation with different adjustment periods	85
4.1	Schematic of the Nordic Seas, showing the main basins, inflows, outflows and geographical features	105
4.2	For the experiment KAB001: depth and density distributions in terms of relative percentages, and particle tracks for floats that enter through Denmark Strait and then leave through Denmark Strait at different depths	112
4.3	Total number of particles entering the Nordic Seas through Denmark Strait in every release	114
4.4	For the experiment ANHA4: Trajectories and main routes of all the particles released on January 1 st , 2005 and integrated up to December 31 st 2014, entering and leaving the Nordic Seas through Denmark Strait	115
4.5	Depth and density distributions, in terms of relative percentages, for floats that enter through Denmark Strait and then leave through Denmark Strait at depths greater than 200 m	116
4.6	Properties of the floats that enter the Nordic Seas within the NIIC and are transformed to DSOW with densities higher than 27.93 kg/m^3 (ANHA4): (a) density, (b) depth, (c) salinity, (d) temperature and (e) transformation time. . .	119
4.7	Properties of the floats that enter the Nordic Seas within the NIIC and are transformed to densities higher than 27.93 kg/m^3 in less than 1 year (ANHA4): (a) density, (b) depth, (c) salinity, (d) temperature and (e) transformation time.	122
4.8	Seasonal flow velocity normal to a cross section of the north Icelandic shelfbreak	123
4.9	Monthly climatology (2005-2014) of total heat loss diagnosed from the exper- iment ANHA4, for the months: a) October, b) November, c) December, d) January, e) February, and f) March	124

5.1	Schematic, following Våge et al. (2013), showing the main currents northwest of Iceland	141
5.2	ANHA12 horisontal resolution (in km) over its entire domain.	145
5.3	Mean February density (a,b), salinity (c,d) and temperature (e,f), averaged over the period 2004 to 2012 along the Latrabjarg section (shown in Figure 5.1). Panels on the left show model data while those on the right represent data from observations.	147
5.4	Mean November density (a,b), salinity (c,d) and temperature (e,f), averaged over the period 2004 to 2012 along the Latrabjarg section (shown in Figure 5.1). Panels on the left show model data while those on the right represent data from observations.	148
5.5	Mean vertical profiles (model and observations) of density, salinity and temperature along the Kogur section	149
5.6	Model monthly heat loss around Iceland for the months of December 2007 (a) and from January to March of 2008 (b to d).	151
5.7	TS diagrams over the study region	152
5.8	Model time series over the study region (shown in deep blue in the map attached to the upper left corner in panel a) of maximum density (a-b), resistance energy (b-c) and heat loss (a and c), from 2002 to 2018.	153
5.9	Model time series over the study region (shown in deep blue in the map attached to the upper left corner in panel a) of maximum density (a-b), salinity (a) and temperature (b), from 2002 to 2018. Note that for temperature (left y-axis in a) the scale have been inverted.	154
5.10	Model position of the maximum density (represented in Figures 5.8 and 5.9) for every model output over the study region (shown in deep blue in the map attached to the upper left corner in Figure 5.8.a). This means one unique value for each model output. No density threshold was considered.	155
5.11	Model bottom density for different model outputs from January 2008 to the end of March 2008. The exact date of each output is labeled on the bottom of each panel (slightly towards the right).	156

5.12	Model time series (from 2002 to 2018) of transport for waters denser than 27.8 kg/m^3 , across 7 different sections located from west to east around the Icelandic shelf, from the coast to 250 m depth.	160
5.13	Model time series (from 2002 to 2018) of transport for waters denser than 27.8 kg/m^3 across the 250, 500 and 750 m isobaths around Icelandic shelf, from the Faxaflói (west of Iceland) to the Krossanes (east of Iceland) sections	161
5.14	Model time series (from 2002 to 2018) of transport for waters denser than 27.8 kg/m^3 , across 7 different sections located from west to east around the Icelandic shelfbreak, from 250 to 750 m depth.	162
5.15	Model time series of mean SSH and maximum density, from 2002 to 2018 over the study region (area represented in deep blue in the map attached to the upper left corner of the figure). Note that the scale for the left y-axis have been inverted.	166
5.16	Model sea surface height (SSH) and ocean current speed at 5 m depth, for a) January 5 th and b) and March 11 th , 2008. The date of each output is labeled in the upper left corner of every panel.	167
5.17	Model along-section velocity at the Húnaflói section for different model outputs from January 2008 to the end of March 2008	168
5.18	Temperature and salinity profiles, from 1929 to present, between -28° to -17° W and 64° to 67° N	169
5.19	Temperature and salinity diagram of the profiles represented in Figures 5.18.b and 5.18.d (profiles on the Icelandic shelf, in waters shallower than 250 m and points denser than 27.8 kg/m^3).	170
5.20	Schematic circulation in the area northwest/north of Iceland discussed in the chapter	171
A.1	Trajectories of all the particles (released each January from 2005 to 2014) entering and leaving the Nordic Seas through Denmark Strait	209
A.2	Four main pathways follow by the particles (released each January from 2005 to 2014) entering and leaving the Nordic Seas through Denmark Strait	210

A.3	Four main pathways follow by the particles (released each April from 2005 to 2014) entering and leaving the Nordic Seas through Denmark Strait	211
A.4	Four main pathways follow by the particles (released each July from 2005 to 2014) entering and leaving the Nordic Seas through Denmark Strait	212
A.5	Four main pathways follow by the particles (released each October from 2005 to 2014) entering and leaving the Nordic Seas through Denmark Strait	213
B.1	TS diagram of the water masses in Denmark Strait	215

Chapter 1

Introduction

The rising concentration of heat-trapping gases, caused mainly by human activity, has resulted in an energy imbalance in the Earth's climate system. Around 93% of the imbalance has accumulated in the oceans, increasing the ocean heat content (Rhein et al., 2013). Recent studies based on observations (Cheng et al., 2019) have shown a rapid increase in the ocean heat content since 1990. Such increases have contributed to the destruction of coral reefs (Rhein et al., 2013), the declining of the ocean oxygen levels (Ciais et al., 2013), the increase in the precipitation intensity (Trenberth et al., 2003), rising sea levels and the declining of the ice sheets (e.g., Greenland Ice Sheet - GrIS) (Rhein et al., 2013). An enhanced hydrological cycle and the continuous decline of the ice sheets is expected to increase the freshwater input into the Arctic and Sub-Arctic basins (Wentz et al., 2007).

The input of cold and fresh waters limit vertical mixing processes in the upper ocean, which drive meridional ocean heat transport cells such as the Atlantic Meridional Overturning Circulation (AMOC). The AMOC (explained in detail in the next section), which feeds from deep water formation regions (Kuhlbrodt et al., 2007), is known to strongly moderate the climate in densely populated mid-latitude regions such as western Europe. There is currently a rising concern on how those future changes might affect open ocean deep convection regions and in turn the AMOC. A significant factor is that the GrIS lies in between two of the most important of those regions found in the North Atlantic: the Labrador Sea and the Nordic Seas.

1.1 Deep Water Formation in the North Atlantic Ocean

Formed by a complex system of currents, the AMOC transports warm surface waters towards the subpolar and polar regions, where they are transformed through cooling processes, get denser and sink to greater depths. Figure 1.1 shows an illustrative sketch of the circulation within the North Atlantic Ocean, which plays a vital role in the AMOC variability and strength. Flowing northward carrying surface saline and warm waters, the North Atlantic Current (NAC) is the uppermost component of the AMOC (Figure 1.1). The NAC transforms as it travels around the different basins within the North Atlantic (Figure 1.1). The type of transformation and where it occurs results in particular (and new) water masses that will sink to a greater depth. Within the subpolar gyre the NAC branches into the Norwegian Atlantic Current (NrAC) and the Irminger Current (IC) (Figure 1.1). The NrAC and a branch of the IC (North Icelandic Irminger Current - NIIC) bring Atlantic Water into the Nordic Seas (Figure 1.1).

These waters will go through a transformation process, losing heat into the atmosphere as they travel around the Nordic Seas, while gaining in density and sinking to a greater depth (Figure 1.1). The waters transformed will contribute to the pool that feeds the overflow waters (Aagaard et al., 1985). The overflow waters eventually find their way out of the Nordic Seas and into the North Atlantic basin through different passages located east and west of Iceland (Dickson et al., 2008). Depending on this, they will later be known as Denmark Strait Overflow Water (DSOW - spills through Denmark Strait, located between Greenland and Iceland) and Iceland-Scotland Overflow Water (ISOW - spills through gaps between the Iceland and Scotland ridge). In the particular case of the DSOW, the waters that contribute to it are carried towards the Denmark Strait by the North Icelandic Jet (NIJ), the separated East Greenland Current (EGC) and the shelfbreak EGC (Våge et al., 2013).

Warm and salty waters from the Irminger Current (IC) are also advected into the Labrador Sea by the West Greenland Current (WGC) (McCartney and Talley, 1982). The Irminger Water is a component of the boundary current system found in the Labrador Sea. It can be identified around the rim of the basin (Figure 1.1) and its core can be found at a depth range of 200 to 1000 m over the slope (Myers et al., 2007). In the upper layer of the Labrador

Sea, the Labrador and WGC pass around the Labrador Sea margins (Figure 1.1). These two currents form a counter-clockwise boundary current, carrying sea-ice, icebergs and low-salinity water from the Arctic as well as runoff from North America and the Greenland ice cap (e.g., Dickson et al., 2007, 2008; Yashayaev and Dickson, 2008; Yang et al., 2016). Once formed, LSW spreads out from its formation region loaded with high concentrations of dissolved oxygen and anthropogenic tracers like chlorofluorocarbons (CFCs), and can be tracked throughout the entire North Atlantic and beyond (e.g., Rhein et al., 2002; Dickson et al., 2007; Rhein et al., 2015; Kieke and Yashayaev, 2015). Part of the LSW recirculates around the subpolar gyre while another part joins the DSOW and ISOW, feeding the AMOC. These newly formed water masses find latter their way towards the southern oceans, ventilating the deeper layers along their journey.

The strength of the AMOC has been observed continuously at $26.5^{\circ}N$ since April 2004 (Figure 1.1). The array is part of the RAPID-MOCHA-WBTS (**R**apid Climate Change - **M**eridional **O**verturning **C**irculation **H**eat-transport **A**rray - **W**estern **B**oundary **T**ime **S**eries) program. It was implemented by combining a transatlantic array of moored instruments with submarine-cable-based measurements of the Gulf Stream and satellite-derived Ekman transport. Using these observations McCarthy et al. (2015) determined the strength of the AMOC and meridional heat transport as $17.2Sv$ and $1.25PW$ respectively, from April 2004 to October 2012.

Considering the same data-set, Smeed et al. (2014) observed a downward trend in the AMOC strength since 2004. They also showed that, from April 2008 to March 2012, the AMOC was an average of $2.7Sv$ weaker than in the first four years of observation. More recently, Smeed et al. (2018) concluded that the AMOC has been in a state of reduced overturning since 2008. The reasons and consequences behind this weakening are still topic of study. It has long been assumed that, an increase in deep water formation would lead to a strengthening of the AMOC, or on the contrary, a weakening in deep water formation, to a decrease. Model based studies have already suggested this link (Getzlaff et al., 2005; Böning et al., 2006; Biastoch et al., 2008; Feucher et al., 2019).

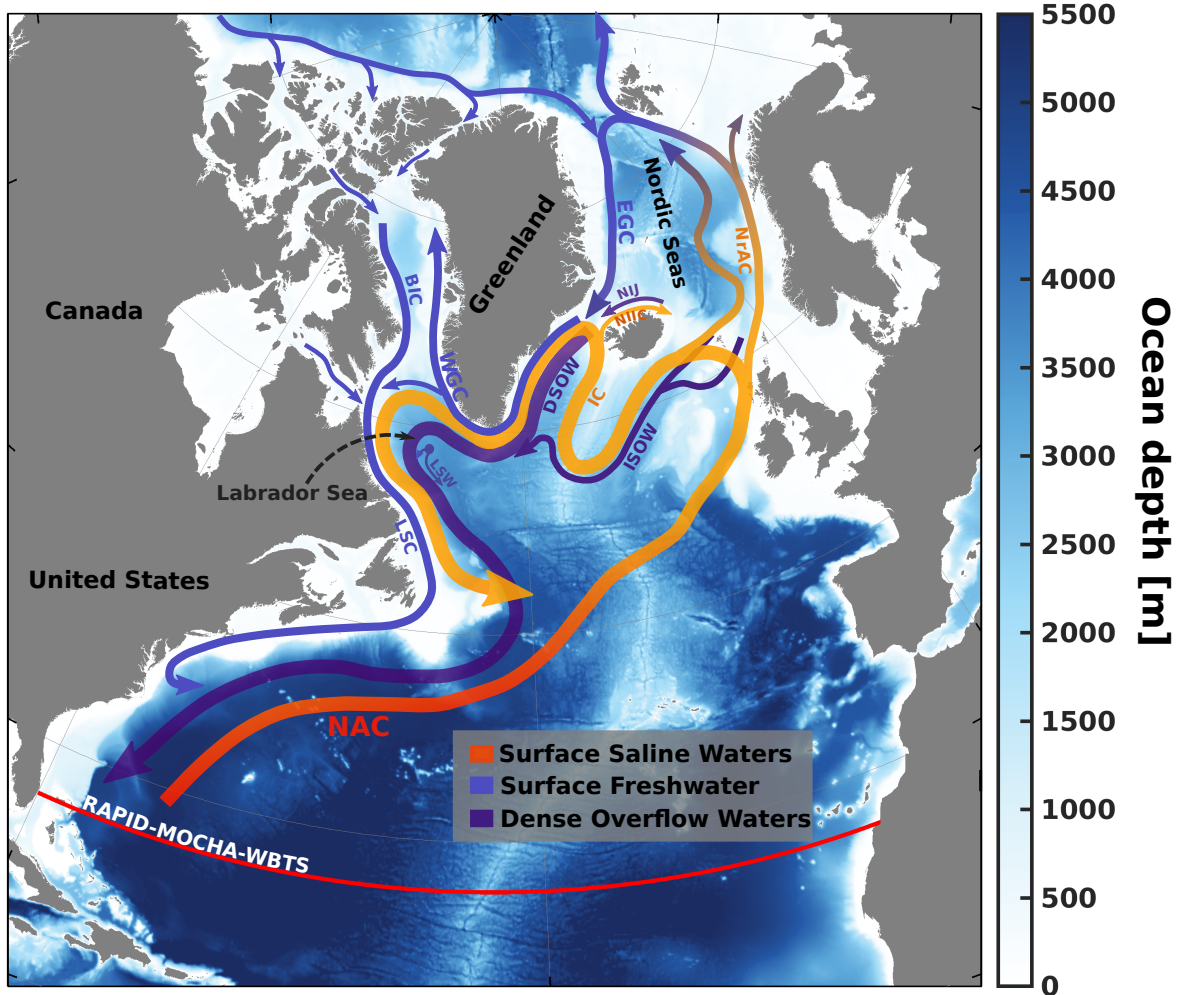


Figure 1.1: Schematic diagram showing the North Atlantic circulation pattern following García-Ibáñez et al. (2015) and Våge et al. (2018). The geographical locations for the Labrador Sea and the Nordic Seas are also indicated. Main topographic features and circulation for each basin are represented in details in Chapters 3 and 4, respectively. The main currents are represented in different colors in order to highlight their basic properties and origin. Orange to yellow colors represent the surface/sub-surface saline waters flowing northward within the North Atlantic Current (NAC) and its branches: Irminger Current (IC), North Icelandic Irminger Current (NIIC) and the Norwegian Atlantic Current (NrAC). The blue color represent the southward flowing Arctic-origin fresh and surface currents: East Greenland Current (EGC), West Greenland Currents (WGC), Baffin Island Current (BIC) and the Labrador Sea Current (LSC). The purple colors identify the denser waters which feed the lower limb of the AMOC: Labrador Sea Water (LSW), Iceland Scotland Overflow Water (ISOW) and the Denmark Strait Overflow Water (DSOW). Within the Labrador Sea a light purple dot represents roughly the formation site for LSW which spreads southward within the Western Boundary Current and around the subpolar Gyre (more on this in Chapter 3). The North Icelandic Jet (NIJ) is the densest component of the DSOW (more on this in Chapters 4 and 5).

However there is still some controversy when it comes to observational studies (Smed et al.,

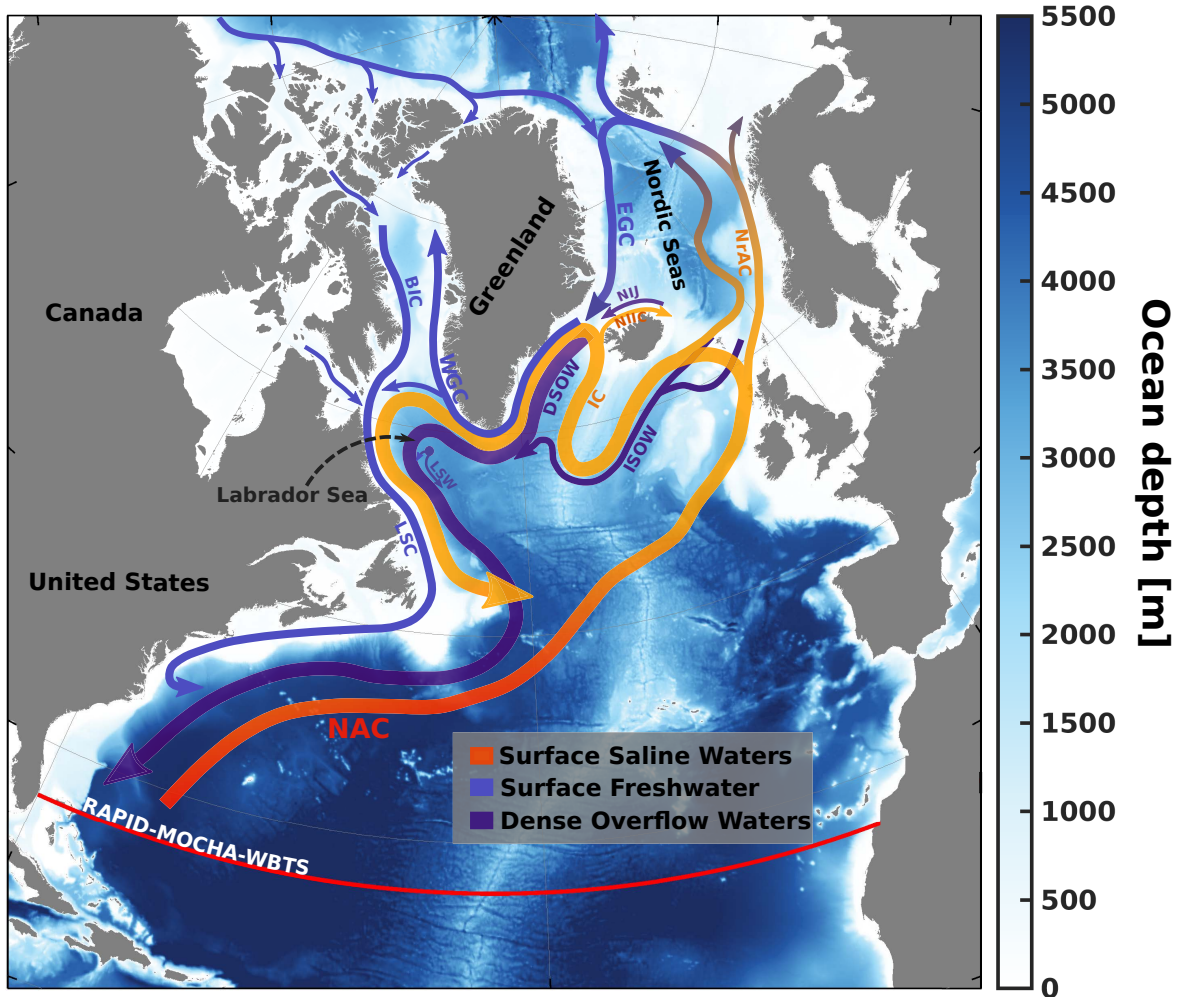


Figure 1.1: Schematic diagram showing the North Atlantic circulation pattern following García-Ibáñez et al. (2015) and Våge et al. (2018). The geographical locations for the Labrador Sea and the Nordic Seas are also indicated. Main topographic features and circulation for each basin are represented in details in Chapters 3 and 4, respectively. The main currents are represented in different colors in order to highlight their basic properties and origin. Orange to yellow colors represent the surface/sub-surface saline waters flowing northward within the North Atlantic Current (NAC) and its branches: Irminger Current (IC), North Icelandic Irminger Current (NIIC) and the Norwegian Atlantic Current (NrAC). The blue color represent the southward flowing Arctic-origin fresh and surface currents: East Greenland Current (EGC), West Greenland Currents (WGC), Baffin Island Current (BIC) and the Labrador Sea Current (LSC). The purple colors identify the denser waters which feed the lower limb of the AMOC: Labrador Sea Water (LSW), Iceland Scotland Overflow Water (ISOW) and the Denmark Strait Overflow Water (DSOW). Within the Labrador Sea a light purple dot represents roughly the formation site for LSW which spreads southward within the Western Boundary Current and around the subpolar Gyre (more on this in Chapter 3). The North Icelandic Jet (NIJ) is the densest component of the DSOW (more on this in Chapters 4 and 5).

However there is still some controversy when it comes to observational studies (Smed et al.,

2018; Lozier et al., 2019), which is mostly due to the fact that most of the observational time series are no longer than 15 years. In their review paper, Kuhlbrodt et al. (2007) state that the strength of the AMOC is set by deep water formation processes. Through such processes surface and sub-surface (recently ventilated) waters gain in density and sink to greater depths. In the North Atlantic ocean some of the processes linked to deep water formation (Kuhlbrodt et al., 2007) are: open ocean convection where turbulent vertical mixing goes along with ocean heat loss; salt input or brine rejection which occurs when sea ice freezes; and sill overflow, entrainment and sinking of dense water in the boundary currents which are linked to the actual downward motion. Within the North Atlantic there are two basins where surface waters are transformed to intermediate and deep waters through a complex chain of physical processes: the Labrador Sea and the Nordic Seas. These basins are the sources of both the lightest (Labrador Sea) and densest (Nordic Seas) contribution to the North Atlantic Deep Water (NADW) (Kieke and Yashayaev, 2015; Haine et al., 2008).

NADW is a water mass of major importance to the dynamics and hydrography of the deep Atlantic Ocean, the global and Atlantic MOC and thus for the climate of the Earth (Haine et al., 2008). NADW consists mainly of DSOW, ISOW, both originating from mid-depths in the Nordic Seas, and LSW formed by intense winter-time air-sea interaction in the Labrador Sea. Two of the components of the NADW, the LSW and the DSOW, are the main topic of this thesis. They are introduced in the sections below and will be described in more details in Chapters 3, 4 and 5.

1.1.1 Labrador Sea

The subpolar North Atlantic (Figure 1.1) is a vital area for heat and freshwater exchange between low and high latitude regions, and where the major intermediate and deep waters of the North Atlantic develop, gaining their characteristic properties and signatures (Dickson et al., 2008). Within the subpolar North Atlantic, the Labrador Sea is the coldest and freshest basin (Yashayaev et al., 2008). It is commonly recognized as a crucial location for the development of regional and large-scale anomalies in ocean properties, and consequently, as a region exerting a significant influence on the climate system (Dickson et al., 2008). It has been argued to be a receiver, transformer and a water masses producer basin (Yashayaev

et al., 2008; Yashayaev, 2007; Yashayaev et al., 2007).

In the upper layer of the basin, cold low salinity waters arrive from the Arctic Ocean by way of the Canadian Arctic Archipelago and the East Greenland shelf. The Labrador and West Greenland Currents pass around the Labrador Sea margins (Figure 1.1). These two fresh and cold inflows form cyclonic boundary currents in the Labrador Sea carrying sea-ice and low salinity water from the Arctic as well as runoff from North America and the Greenland ice cap (Rykova et al., 2015; Dickson et al., 2008; Yashayaev et al., 2008; Dickson et al., 2007; Yashayaev, 2007; Yashayaev et al., 2007). Their fresh and cold cores can be easily identified over the upper continental slopes.

The Labrador Sea is also the final destination for the warm and salty Irminger waters (McCartney and Talley, 1982) which are carried into the Labrador Sea by the Irminger Current (Figure 1.1). These waters can be identified around the Labrador Sea rim as a counter-clockwise flow of warm and salty water (Jochumsen et al., 2012; Macrander, 2004; Käse et al., 2003). As a result of the cooling and freshening of this water along their passage around the sub-polar gyre the stratification of the Atlantic water reduces. Yet substantial temperature and salinity contrasts in the upper layer of the Labrador Sea remain leading to an intense vertical and horizontal mixing (Straneo, 2006). The derived eddies contribute to the overall heat, salt and freshwater budget of the basin and influence the development of winter convection by setting the flux of heat and salt toward the center of the basin (Yashayaev et al., 2007). Labrador Sea Water is formed as a result of the strong mixing reached by the water column during deep convection events.

1.1.1.1 Winter Convection

There are certain recurrent features and conditions that have to be involved for a region to have deep convection:

- I Strong atmospheric forcing which can be either due to thermal and/or haline surface fluxes. Basins adjacent to land are favoured as it is common for cold and dry winds to blow from land or ice over the ocean inducing strong sea-to-atmosphere latent and sensible heat and moisture fluxes.

II Weak ocean stratification beneath the surface (Figure 1.2.c). This can be induced for example due to convection in the previous year .

III Weakly stratified underlying waters must be brought up so they can be exposed to the strong surface atmosphere forcing. The presence of a cyclonic boundary currents in the Labrador Sea enables a doming of the isopycnals up to the surface (Figure 1.2.b).

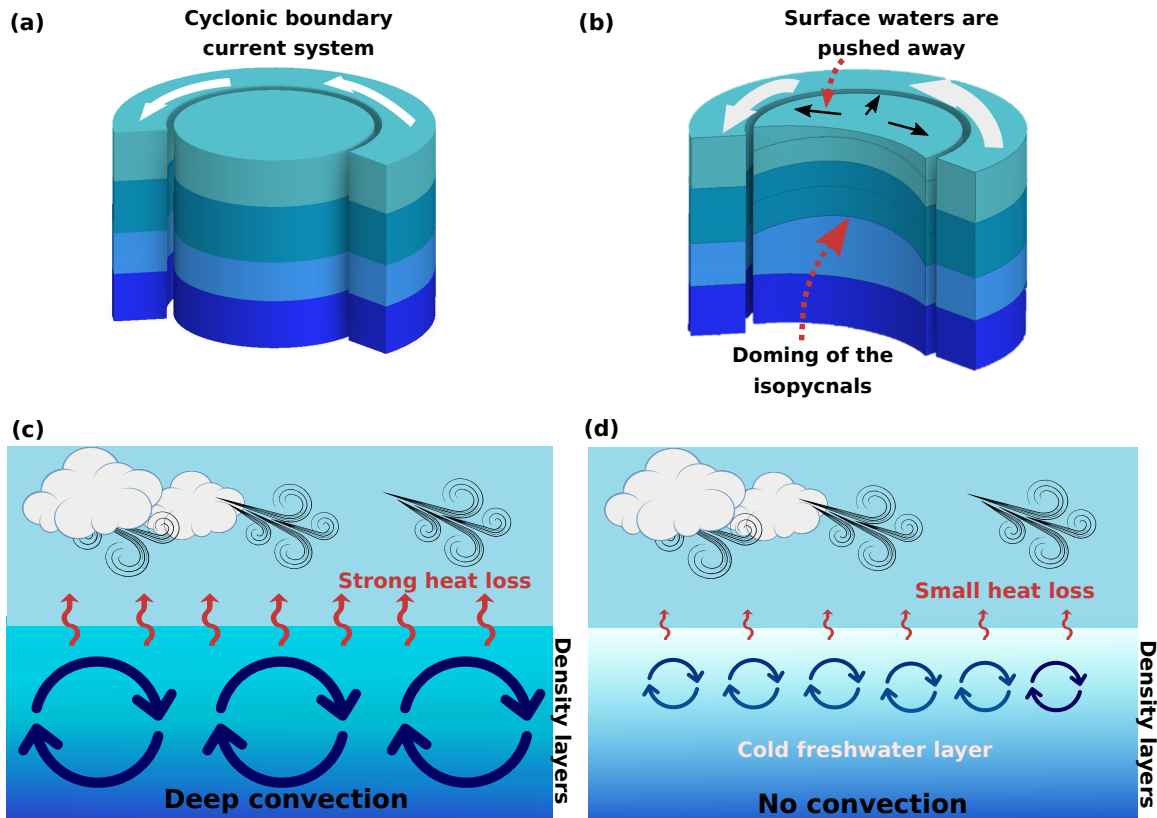


Figure 1.2: Schematic showing the different stages of convection in the Labrador Sea: pre-conditioning (a and b) and convection (c) or its absence (d) given the existence of a cold and fresh layer of water at the surface of the ocean. Cyclonic boundary circulation in the Labrador Seas is indicated with white arrows (a and b), while the black arrows in (b) indicate the surface waters being pushed away due to the cyclonic circulation. The strength of the convection is represented by circular dark blue arrows while the magnitude of the ocean heat loss is represented by the wavy red arrows (c and d).

The last two conditions (II and III) are satisfied in the Labrador Sea and they are commonly referred to as "preconditioning" (The Lab Sea Group, 1998). Figure 1.2 illustrates these different processes leading to deep convection. There are, however, processes that could potentially affect the depth of the convection in the Labrador Sea. Some of them are, for example, a

sufficient freshwater input (Figure 1.2.d) in higher latitudes (increased precipitation, river runoff or melting of the Greenland Ice Sheet) and a lack of storms to drive the oceanic heat loss which triggers convection (mild winters or a northward shift of subpolar storms track).

A likely consequence of the ongoing global warming is the increment of run-off discharge due to glacial and ice-sheets melting (Rhein et al., 2013) or precipitation increase (Wentz et al., 2007). Such an increase would imply the occurrence of substantial changes in the water column, water masses and hence the ocean circulation. A sufficient amount of freshwater input in basins where convection occurs would reduce the surface salinity, contributing to the stability of the water column, and potentially reducing the deep water formation. When surface salinity decreases below the critical value of 34.7, the surface layers will not reach a sufficiently high density (even at a freezing point) to mix with the underlying warmer and more saline water, but instead ice will tend to form (Dickson et al., 1988).

High frequency atmospheric phenomena (mesoscale cyclones, cold air outbreaks, fronts and topographic jets) known to play an important role in the convection depth (Holdsworth and Myers, 2015), are expected to show certain changes with future climate warming (Kolstad and Bracegirdle, 2008; Zahn and von Storch, 2010a) and questions about how the ocean will respond to those changes are arising. Studies have shown already a potential shift of the subpolar storm track towards higher latitudes (Våge et al., 2008a). Zahn and von Storch (2010a) have predicted a decrease in the annual number of the polar lows if the atmospheric temperatures would continue to rise. At the same time, a decrease in the ice covered land surface would imply a decrease in cold air outbreaks, which are also responsible for strong wintertime oceanic heat loss episodes over the Labrador Sea.

1.1.1.2 LSW Formation

In the Labrador Sea, open ocean deep convection, which during severe winters can reach water depths of 2 km (e.g., Dickson et al., 2008; Yashayaev and Loder, 2009, 2017), results in the formation of LSW. LSW is the lightest component of the NADW, hence it feeds the deep and abyssal limb of the AMOC (e.g., Haine et al., 2008; Rhein et al., 2015). The formation rate of the LSW has been investigated using numerous methods increasingly since 1990: chlorofluorocarbons (CFCs) inventories, numerical models, hydrographic changes, mass budget, heat

budget, etc. Unsurprisingly differences might arise when comparing different studies due to inconsistencies in the definition of LSW. Tight criteria on LSW will naturally lead to smaller formation rates than more broad definitions. Moreover, there exist about ten distinct methods to infer LSW formation rate, and each of them has random and systematic errors which are essentially unknown (Haine et al., 2008).

However, beyond the method used to calculate LSW formation rate and the definition used, changes in the LSW production, properties and thickness have direct consequences for the ventilation of the deep ocean (Kieke and Yashayaev, 2015; Stendaro and Gruber, 2012; Körtzinger et al., 2004), the ocean’s potential to store anthropogenic carbon (Steinfeldt et al., 2009; Sabine et al., 2004), and the strength of the AMOC and the associated heat transport (Srokosz et al., 2012).

Variability of LSW formation has been widely analyzed (García-Ibáñez et al., 2015; Kieke and Yashayaev, 2015; Houssais and Herbaut, 2011; Azetsu-Scott et al., 2010; Yashayaev et al., 2007; Kieke et al., 2006). Changes might be induced for instance, by changes in the atmospheric forcing (Holdsworth and Myers, 2015) like the phases and persistence of the North Atlantic Oscillation (NAO) (Dickson et al., 1996, 2008; Kieke and Yashayaev, 2015), advection of freshwater from the Arctic (for example the great salinity anomaly observed in the Labrador Sea in the early 1970s which progressively inhibited deep convection in the Labrador Sea (Gelderoos et al., 2012; Dickson et al., 1988; McCartney and Talley, 1982) and also due to reinforcement of local freshening, either by an increase in Greenland Ice Sheet (GrIS) melt, in river discharge and in precipitation (Brunnabend et al., 2015; Bamber et al., 2012; van den Broeke et al., 2009; Myers, 2005). Chapter 3 of this Thesis explores into LSW formation, and describes in detail the characteristics mentioned in this section.

1.1.2 Nordic Seas

The Nordic Seas are defined here as the region north of the Greenland-Scotland Ridge (GSR) and south of the Fram Strait-Spitsbergen-northern Norway transect. They cover about 2.5×10^6 km^2 and comprise the Greenland, Iceland and Norwegian Seas (Figure 1.1). Despite their small extent (0.75% of the world’s ocean) the region is very dynamic and diverse (Hawker, 2005). The Nordic Seas is one of the few regions of the world’s oceans that takes up substantial amounts

of atmospheric carbon dioxide (CO_2) throughout the year, ranging from 20-85 $gCm^{-2}y^{-1}$, which is among the highest of such fluxes in the world's oceans (Hollingworth, 2005; Takahashi et al., 2002; Anderson et al., 2000).

The region is the main oceanic connection between the Arctic and the deep global oceans via dense overflows between Greenland and Scotland, and provides a substantial part of the headwaters of the Atlantic thermohaline circulation (Isachsen et al., 2007; Hawker, 2005). The water mass transformation that occurs within them provide a direct link between the atmosphere and the ocean, which is vital for the stability of the global thermohaline circulation (Drange et al., 2005).

The topography of the sea floor is complex with shallow shelves, deep basins, mid oceanic ridge systems, and steep slopes where the geomorphology directs and limits its circulation (Drange et al., 2005; Blindheim and Østerhus, 2005; Hopkins, 1991). Although the generic features of the Nordic Seas (inflows, overflows, boundary currents, basin-scale gyre circulations) are relatively well understood, the specific details of the interior circulation, in particular, are not yet well determined.

The general oceanic circulation of the Nordic Seas is characterized by a surface inflow of Atlantic Water towards the Arctic (via Barents Sea and Fram Strait), an overflow of dense waters and a surface outflow of cold, fresh water from the Arctic to the North Atlantic, separated by cyclonic gyres in the Greenland, Iceland and Norwegian Seas (Hopkins, 1991).

Here water masses originating from low and high latitudes meet and interact by means of frontal mixing, deep convective mixing, subduction, and entrainment. Sea ice is formed in the northern and western parts of the Nordic Seas in winter, whereas the region is essentially ice-free during summer. The inflow of warm and salty Atlantic waters and the outflow of fresh and cold Arctic waters, form two major components of the Nordic Sea circulation, which influence the long-term variability of the dense overflows into the North Atlantic (Hawker, 2005). The dense waters overflowed from the Nordic Seas are known to be denser than anything formed in the Subpolar Gyre and, as such, are the largest contributors to the AMOC (Eldevik et al., 2009).

The annual and winter mean temperatures of the central and eastern Nordic Seas are respectively 10° C and 20° C higher than the zonal means. The anomalously high temperatures

are caused by three mechanisms: (1) Prevailing westerly and southwesterly vapor-laden winds; (2) poleward transport of heat by the Gulf Stream and the North Atlantic Current system; and (3) heat released from the seasonally warmed North Atlantic mixed layer (Rhines and Häkkinen, 2003; Seager et al., 2002). Changes in any of these three mechanisms have the potential to significantly alter the climate in the region.

1.1.2.1 Water Formation and Transformation

Heat is mainly removed in the Nordic Seas, leading to dense water formation. The atmosphere-ocean transfers of momentum, heat, fresh-water and gases are strong, notably during the cold winter months, from November to April (Drange et al., 2005). Over the Greenland Sea for example large heat and freshwater fluxes are induced by cold and dry winds blowing over the water from land or ice surfaces. Within the Greenland Sea, the weakly stratified waters of the interior are close to the surface where they are subject to intense surface forcing during winter. In the interior of the Greenland Sea gyre a thin layer of Arctic surface water originating from the East Greenland Current overlies a layer of intermediate water. Weakly stratified Greenland Sea Deep Water (GSDW), formed during previous convection events, lies below these water masses. In early winter, as ice is formed eastward across the Greenland Sea, brine rejection increases the density of the surface layer, while the mixed layer under the ice cools and deepens to about 150 m (Dickson and Brown, 1994a).

The eventual occurrence of deep convection depends on the seasonal development of the surface buoyancy flux with respect to the initial stratification at the beginning of the winter period. If the near surface stratification is eroded by the winter buoyancy loss and meteorological conditions are favourable, then deep convection may occur.

However, Moore et al. (2015) found that due to the wintertime retreat of sea ice in the region, together with different rates of warming for the atmosphere and sea surface of the Greenland and Iceland seas, has resulted in approximately 20% reduction of the winter air-sea heat fluxes since 1979. They argued that, if these conditions were to continued, the convection in both basins would be depth-limited. More recently Brakstad et al. (2019), by using hydrographic measurements from ships, autonomous profiling floats, and instrumented seals over the period 1986-2016, did not find indications of shallower convection in the Greenland

Sea after 1993. They did find, however, that since 1994 the main product of deep convection in the Greenland Sea has become less dense. This is particularly important considering that the Nordic Seas is the producer of the densest component of the AMOC.

In addition to open ocean deep convection, dense waters are also formed by downward mixing mechanisms due to the formation of ice. During periods of ice growth the salinity of the underlying water is increased as brine is rejected. The high density of this cold and saline surface water, causes it to sink entraining the ambient water. When this occurs on the shelf, these waters accumulate and spread from the interior shelves towards the shelf edge. As they sink to depth in the central ocean basins they modify and contribute to the deep waters which later overflow into the Atlantic Ocean.

Mauritzen (1996) proposed that inflowing Atlantic Water (AW) is gradually densified via heat loss as it circulates in the Norwegian Atlantic Current. The dense water is then transported to the outflows by the boundary currents surrounding the Iceland and Greenland Seas at both shallow and intermediate depths. Eldevik et al. (2009) supported this idea, arguing that the AW circulation and transformation within the boundary currents of the Nordic Seas was the main source for the overflows.

The Nordic Seas dense water outflow occurs in three locations along the Greenland-Faroe ridge: through Denmark Strait (between Greenland and Iceland), across the Iceland-Faroe ridge (between Iceland and the Faroe Islands), and through the Faroe-Shetland channel (between the Faroe and Shetland Islands) (Figure 1.1). All three locations have relatively shallow sills. The dense water flowing southward over the sills plunges downward in plumes, entraining and mixing with surrounding waters in the process.

The combination of the large heat import from south and the polar location of the basin, implies that the Nordic Seas is prone to climate variations and particularly vulnerable to external forcings. Changes in the forcings induced by the ongoing global warming (freshwater increase or atmospheric forcing changes) will definitely be reflected in the overflows production and variability, and hence the AMOC strength.

1.2 Thesis Objectives and Outline

Future changes, like the already mentioned freshwater increase, will not come just as a direct response from river discharge or precipitation increase. The fresh water content within the Arctic Ocean has been increasing during the last decade and is not clear yet when or under which circumstances it would be released out of the basin, either through the Canadian Arctic Archipelago or Fram Strait. We expect that by investigating the modelled temporal and spatial variability of the deep water formation in the Labrador and Nordic Seas, we would contribute to a better understanding of their governing physical processes. This way, we would be able to understand how such processes will be impacted by the ongoing and projected changes.

Thus, to have a better understanding of the processes involved in deep water formation in the Labrador and Greenland Seas, this thesis will focus on:

- I. To study the hydrodynamic response of water formation in the Labrador Sea due to an increase in precipitation and GrIS melt, a decrease in the number of storms crossing the basin, and changes in model resolution.
 - LSW is the lightest contribution to the NADW and it has been claimed to be a key component of the AMOC. Given its (LSW) significance we explore the impact of enhanced freshwater discharge (either by glacial melting or precipitation increase), high frequency atmospheric forcing (e.g., storms) and model resolution on LSW formation. These different scenarios were selected in order to investigate how the LSW formation might respond under changes predicted to occur due to the ongoing global warming (except in the case of model resolution): increase in Greenland Ice sheet melt, decrease of precipitation over the mid latitudes and the decrease of high frequency atmospheric phenomena over the Labrador Sea linked to the poleward shift of the extra-tropical storm track. By exploring the LSW formation under different horizontal resolutions, we are looking to tackle how the model resolution might impact the understanding. Numerical ocean models play an important role in increasing our ability to comprehend oceanic processes, monitor the current state of the oceans, and to a limited extent (for now), even predict their future state. We use a kinematic subduction approach to quantify the LSW formation rate in the period 2004 to 2016. To our knowledge

this study is the first to use this method to investigate the variability of the LSW formation rate under different sensitivity experiments, while using hourly atmospheric forcing data that allows the representation of a wide range of atmospheric phenomena. Chapter 3 of this Thesis investigates the subject in more detail.

II. To investigate the transformation of AW as it enters the Nordic Seas and its role on driving the densest component of the DSOW;

- Most of the studies investigating deep water formation in the Nordic Seas look mainly into deep convection in the Greenland and the Iceland Seas as the main source for the overflow waters. However it has also been argued that the Atlantic inflow gets transformed as it travels around the Nordic Seas and it eventually leaves the basin as a denser water mass (Mauritzen, 1996). In the Chapter 4 of this Thesis we look into these transformation processes in more detail. This is particularly relevant given that, even when freshwater outflow from the Arctic Ocean or from the GrIS may impact the deep convection in the Nordic Seas, dense water would form as long as the Atlantic Water is transformed in the boundary currents.

III. To explore the possible existence of a not-yet-accounted-for source for DSOW.

- Currently the NIJ (densest component of the DSOW and hence part of the lower limb of the AMOC) is thought to be formed in the interior of the Iceland Sea and then exported out of the basin through eddies (Våge et al., 2011). Our theory, on the other hand, is that the NIJ is sourced by the transformation (from light to dense) of the Atlantic Water that occurs west/north-west of Iceland. Linked to the previous point, this would imply that, even a significant input of freshwater into the Iceland Sea (leading to a prolonged cessation of convection), will not impact the formation of the NIJ nor the strength of the AMOC. The Chapter 5 of this Thesis explores the subject in more detail.

This thesis is divided into six chapters, where the Introduction is considered as Chapter 1. Chapter 2 describes the main features and aspects of the modelling framework of NEMO. The following Chapters (Chapter 3, Chapter 4 and Chapter 5) are written as independent

papers. There, the goals enumerated above (I, II and III) are addressed. Finally, in Chapter 6, a concluding statement summarizing the Thesis main findings, scientific contributions and future work, is provided.

Bibliography

- Anderson, L. G., Drange, H., Chierici, M., Fransson, A., Johannessen, T., Skjelvan, I., and Rey, F. (2000). Annual carbon fluxes in the upper Greenland Sea based on measurements and a box-model approach. *Tellus B*, 52(3):1013–1024.
- Azetsu-Scott, K., Clarke, A., Falkner, K., Hamilton, J., Jones, E. P., Lee, C., Petrie, B., Prinsenber, S., Starr, M., and Yeats, P. (2010). Calcium carbonate saturation states in the waters of the Canadian Arctic Archipelago and the Labrador Sea. *Journal of Geophysical Research: Oceans*, 115(C11).
- Bamber, J., den Broeke, M., Ettema, J., Lenaerts, J., and Rignot, E. (2012). Recent large increases in freshwater fluxes from Greenland into the North Atlantic. *Geophysical Research Letters*, 39(19).
- Biastoch, A., Böning, C. W., Getzlaff, J., Molines, J.-M., and Madec, G. (2008). Causes of Interannual–Decadal Variability in the Meridional Overturning Circulation of the Midlatitude North Atlantic Ocean. *Journal of Climate*, 21(24):6599–6615.
- Blindheim, J. and Østerhus, S. (2005). The Nordic Seas, main oceanographic features. *The Nordic seas: An integrated perspective*, pages 11–37.
- Böning, C. W., Scheinert, M., Dengg, J., Biastoch, A., and Funk, A. (2006). Decadal variability of subpolar gyre transport and its reverberation in the North Atlantic overturning. *Geophysical Research Letters*, 33(21):n/a–n/a. L21S01.
- Brakstad, A., Våge, K., Håvik, L., and Moore, G. W. K. (2019). Water mass transformation in the greenland sea during the period 1986–2016. *Journal of Physical Oceanography*, 49(1):121–140.
- Brunnabend, S.-E., Schröter, J., Rietbroek, R., and Kusche, J. (2015). Regional sea level change in response to ice mass loss in Greenland, the West Antarctic and Alaska. *Journal of Geophysical Research: Oceans*.
- Cheng, L., Abraham, J., Hausfather, Z., and Trenberth, K. E. (2019). How fast are the oceans warming? *Science*, 363(6423):128–129.

- Ciais, P., Sabine, C., Bala, G., Bopp, L., Brovkin, V., Canadell, J., Chhabra, A., DeFries, R., Galloway, J., Heimann, M., Jones, C., Quéré, C. L., Myneni, R., Piao, S., and Thornton, P. (2013). Carbon and Other Biogeochemical Cycles. In: *Climate Change 2013: The Physical Science Basis. Contribution of Working Group I to the Fifth Assessment Report of the Intergovernmental Panel on Climate Change* [Stocker, T.F., D. Qin, G.-K. Plattner, M. Tignor, S.K. Allen, J. Boschung, A. Nauels, Y. Xia, V. Bex and P.M. Midgley (eds.)], publisher = Cambridge University Press, Cambridge, United Kingdom and New York, NY, USA.
- Dickson, B., Meincke, J., and Rhines, P. (2008). *Arctic–Subarctic Ocean Fluxes: Defining the Role of the Northern Seas in Climate*. Springer.
- Dickson, R., Lazier, J., Meincke, J., and Rhines, P. (1996). Long-term coordinated changes in the convective activity of the North Atlantic. In *Decadal Climate Variability*, pages 211–261. Springer.
- Dickson, R., Rudels, B., Dye, S., Karcher, M., Meincke, J., and Yashayaev, I. (2007). Current estimates of freshwater flux through arctic and subarctic seas. *Progress in Oceanography*, 73:210–230.
- Dickson, R. R. and Brown, J. (1994). The production of north atlantic deep water: Sources, rates, and pathways. *Journal of Geophysical Research: Oceans*, 99(C6):12319–12341.
- Dickson, R. R., Meincke, J., Malmberg, S.-A., and Lee, A. J. (1988). The “great salinity anomaly” in the northern North Atlantic 1968–1982. *Progress in Oceanography*, 20(2):103–151.
- Drange, H., Dokken, T., Furevik, T., Gerdes, R., Berger, W., Nesje, A., Arild Orvik, K., Skagseth, Ø., Skjelvan, I., and Østerhus, S. (2005). *The Nordic Seas: an overview*. Wiley Online Library.
- Eldevik, T., Nilsen, J. E. Ø., Iovino, D., Olsson, K. A., Sandø, A. B., and Drange, H. (2009). Observed sources and variability of Nordic seas overflow. *Nature Geoscience*, 2(6):406–410.

- Feucher, C., Garcia-Quintana, Y., Yashayaev, I., Hu, X., and Myers, P. (2019). Labrador sea water formation rate and its impact on the meridional overturning circulation. *Geophysical Research Oceans*.
- García-Ibáñez, M. I., Pardo, P. C., Carracedo, L. I., Mercier, H., Lherminier, P., Ríos, A. F., and Pérez, F. F. (2015). Structure, transports and transformations of the water masses in the Atlantic Subpolar Gyre. *Progress in Oceanography*, 135:18–36.
- Gelderoos, R., Straneo, F., and Katsman, C. (2012). Mechanisms behind the temporary shutdown of deep convection in the Labrador Sea: Lessons from the Great Salinity Anomaly Years 1968-71. *Journal of Climate*, 25:6743–6755.
- Getzlaff, J., Böning, C. W., Eden, C., and Biastoch, A. (2005). Signal propagation related to the North Atlantic overturning. *Geophysical Research Letters*, 32(9):n/a–n/a. L09602.
- Haine, T., Böning, C., Brandt, P., Fischer, J., Funk, A., Kieke, D., Kvaleberg, E., Rhein, M., and Visbeck, M. (2008). North Atlantic deep water formation in the Labrador Sea, recirculation through the subpolar gyre, and discharge to the subtropics. In *Arctic–Subarctic Ocean Fluxes*, pages 653–701. Springer.
- Hawker, E. J. (2005). *The Nordic Seas circulation and exchanges*. PhD thesis, University of Southampton.
- Holdsworth, A. M. and Myers, P. G. (2015). The Influence of high-frequency atmospheric forcing on the circulation and deep convection of the Labrador Sea. *Journal of Climate*, 28(12):4980–4996.
- Hollingworth, C. (2005). The Norwegian Sea Ecosystem. *Fish and Fisheries*, 6(1):90–91.
- Hopkins, T. S. (1991). The GIN Sea—A synthesis of its physical oceanography and literature review 1972–1985. *Earth-Science Reviews*, 30(3):175–318.
- Houssais, M.-N. and Herbaut, C. (2011). Atmospheric forcing on the Canadian Arctic Archipelago freshwater outflow and implications for the Labrador Sea variability. *Journal of Geophysical Research: Oceans*, 116(C8).

- Isachsen, P. E., Mauritzen, C., and Svendsen, H. (2007). Dense water formation in the Nordic Seas diagnosed from sea surface buoyancy fluxes. *Deep Sea Research Part I: Oceanographic Research Papers*, 54(1):22–41.
- Jochumsen, K., Quadfasel, D., Valdimarsson, H., and Jónsson, S. (2012). Variability of the Denmark Strait overflow: Moored time series from 1996–2011. *Journal of Geophysical Research: Oceans*, 117(C12).
- Käse, R. H., Girton, J., and Sanford, T. (2003). Structure and variability of the Denmark Strait Overflow: Model and observations. *Journal of Geophysical Research: Oceans*, 108(C6).
- Kieke, D., Rhein, M., Stramma, L., Smethie, W. M., LeBel, D. A., and Zenk, W. (2006). Changes in the CFC inventories and formation rates of Upper Labrador Sea Water, 1997–2001. *Journal of Physical Oceanography*, 36(1):64–86.
- Kieke, D. and Yashayaev, I. (2015). Studies of Labrador Sea Water formation and variability in the subpolar North Atlantic in the light of international partnership and collaboration. *Progress in Oceanography*, 132:220–232.
- Kolstad, E. W. and Bracegirdle, T. J. (2008). Marine cold-air outbreaks in the future: an assessment of IPCC AR4 model results for the Northern Hemisphere. *Climate Dynamics*, 30(7-8):871–885.
- Körtzinger, A., Schimanski, J., Send, U., and Wallace, D. (2004). The ocean takes a deep breath. *Science*, 306(5700):1337–1337.
- Kuhlbrodt, T., Griesel, A., Montoya, M., Levermann, A., Hofmann, M., and Rahmstorf, S. (2007). On the driving processes of the Atlantic meridional overturning circulation. *Reviews of Geophysics*, 45(2).
- Lozier, M. S., Li, F., Bacon, S., Bahr, F., Bower, A. S., Cunningham, S. A., de Jong, M. F., de Steur, L., deYoung, B., Fischer, J., Gary, S. F., Greenan, B. J. W., Holliday, N. P., Houk, A., Houpert, L., Inall, M. E., Johns, W. E., Johnson, H. L., Johnson, C., Karstensen, J., Koman, G., Le Bras, I. A., Lin, X., Mackay, N., Marshall, D. P., Mercier, H., Oltmanns, M., Pickart, R. S., Ramsey, A. L., Rayner, D., Straneo, F., Thierry, V., Torres, D. J., Williams,

- R. G., Wilson, C., Yang, J., Yashayaev, I., and Zhao, J. (2019). A sea change in our view of overturning in the subpolar north atlantic. *Science*, 363(6426):516–521.
- Macrander, A. (2004). *Variability and processes of the Denmark Strait overflow*. PhD thesis, Uni Kiel.
- Mauritzen, C. (1996). Production of dense overflow waters feeding the North Atlantic across the Greenland-Scotland Ridge. Part 1: Evidence for a revised circulation scheme. *Deep Sea Research Part I: Oceanographic Research Papers*, 43(6):769 – 806.
- McCarthy, G., Smeed, D., Johns, W., Frajka-Williams, E., Moat, B., Rayner, D., Baringer, M., Meinen, C., Collins, J., and Bryden, H. (2015). Measuring the Atlantic Meridional Overturning Circulation at 26° N. *Progress in Oceanography*, 130:91–111.
- McCartney, M. S. and Talley, L. D. (1982). The subpolar mode water of the North Atlantic Ocean. *Journal of Physical Oceanography*, 12(11):1169–1188.
- Moore, G. W. K., Våge, K., Pickart, R. S., and Renfrew, I. A. (2015). Decreasing intensity of open-ocean convection in the greenland and iceland seas. *Nature Climate Change*, 5.
- Myers, P. G. (2005). Impact of freshwater from the Canadian Arctic archipelago on Labrador Sea water formation. *Geophysical Research Letters*, 32(6).
- Rhein, M., Rintoul, S., Aoki, S., Campos, E., Chambers, D., Feely, R., Gulev, S., Johnson, G., Josey, S., Kostianoy, A., Mauritzen, C., Roemmich, D., Talley, L., and Wang, F. (2013). Observations: Ocean. In: *Climate Change 2013: The Physical Science Basis. Contribution of Working Group I to the Fifth Assessment Report of the Intergovernmental Panel on Climate Change* [Stocker, T.F., D. Qin, G.-K. Plattner, M. Tignor, S.K. Allen, J. Boschung, A. Nauels, Y. Xia, V. Bex and P.M. Midgley (eds.)].
- Rhines, P. B. and Häkkinen, S. (2003). Is the oceanic heat transport in the North Atlantic irrelevant to the climate in Europe. *ASOF Newsletter*, 2:13–17.
- Rykova, T., Straneo, F., and Bower, A. S. (2015). Seasonal and interannual variability of the West Greenland Current System in the Labrador Sea in 1993–2008. *Journal of Geophysical Research: Oceans*, 120(2):1318–1332.

- Sabine, C. L., Feely, R. A., Gruber, N., Key, R. M., Lee, K., Bullister, J. L., Wanninkhof, R., Wong, C., Wallace, D. W., Tilbrook, B., et al. (2004). The oceanic sink for anthropogenic CO₂. *science*, 305(5682):367–371.
- Seager, R., Battisti, D. S., Yin, J., Gordon, N., Naik, N., Clement, A. C., and Cane, M. A. (2002). Is the Gulf Stream responsible for Europe’s mild winters? *Quarterly Journal of the Royal Meteorological Society*, 128(586):2563–2586.
- Smeed, D., McCarthy, G., Cunningham, S., Frajka-Williams, E., Rayner, D., Johns, W., Meinen, C., Baringer, M., Moat, B., Duchez, A., et al. (2014). Observed decline of the Atlantic meridional overturning circulation 2004–2012. *Ocean Science*, 10(1):29–38.
- Smeed, D. A., Josey, S. A., Beaulieu, C., Johns, W. E., Moat, B. I., Frajka-Williams, E., Rayner, D., Meinen, C. S., Baringer, M. O., Bryden, H. L., and McCarthy, G. D. (2018). The north atlantic ocean is in a state of reduced overturning. *Geophysical Research Letters*, 45(3):1527–1533.
- Srokosz, M., Baringer, M., Bryden, H., Cunningham, S., Delworth, T., Lozier, S., Marotzke, J., and Sutton, R. (2012). Past, present, and future changes in the Atlantic meridional overturning circulation. *Bulletin of the American Meteorological Society*, 93(11):1663–1676.
- Steinfeldt, R., Rhein, M., Bullister, J. L., and Tanhua, T. (2009). Inventory changes in anthropogenic carbon from 1997–2003 in the Atlantic Ocean between 20 S and 65 N. *Global Biogeochemical Cycles*, 23(3).
- Stendardo, I. and Gruber, N. (2012). Oxygen trends over five decades in the North Atlantic. *Journal of Geophysical Research: Oceans*, 117(C11).
- Straneo, F. (2006). Heat and freshwater transport through the central Labrador Sea*. *Journal of Physical Oceanography*, 36(4):606–628.
- Takahashi, T., Sutherland, S. C., Sweeney, C., Poisson, A., Metzl, N., Tilbrook, B., Bates, N., Wanninkhof, R., Feely, R. A., Sabine, C., et al. (2002). Global sea–air CO₂ flux based on climatological surface ocean pCO₂, and seasonal biological and temperature effects. *Deep Sea Research Part II: Topical Studies in Oceanography*, 49(9):1601–1622.

- The Lab Sea Group (1998). The Labrador Sea Deep Convection Experiment. *Bulletin of the American Meteorological Society*, 79(10):2033–2058.
- Trenberth, K. E., Dai, A., Rasmussen, R. M., and Parsons, D. B. (2003). The changing character of precipitation. *Bulletin of the American Meteorological Society*, 84(9):1205–1218.
- van den Broeke, M., Bamber, J., Ettema, J., Rignot, E., Schrama, E., van de Berg, W. J., van Meijgaard, E., Velicogna, I., and Wouters, B. (2009). Partitioning recent Greenland mass loss. *science*, 326(5955):984–986.
- Våge, K., Papritz, L., Håvik, L., Spall, M. A., and Moore, G. W. K. (2018). Ocean convection linked to the recent ice edge retreat along east greenland. *Nature Communications*, 9.
- Våge, K., Pickart, R. S., Spall, M. A., Valdimarsson, H., Jonsson, S., Torres, D. J., Østerhus, S., and Eldevik, T. (2011). Significant role of the North Icelandic Jet in the formation of Denmark Strait overflow water. *Nature Geoscience*, 4:723 – 727.
- Våge, K., Pickart, R. S., Thierry, V., Reverdin, G., Lee, C. M., Petrie, B., Agnew, T. A., Wong, A., and Ribergaard, M. H. (2008). Surprising return of deep convection to the subpolar north atlantic ocean in winter 2007-2008. *Nature Geoscience*, 2:67–72.
- Wentz, F. J., Ricciardulli, L., Hilburn, K., and Mears, C. (2007). How much more rain will global warming bring? *Science*, 317(5835):233–235.
- Yashayaev, I. (2007). Hydrographic changes in the Labrador Sea, 1960–2005. *Progress in Oceanography*, 73(3):242–276.
- Yashayaev, I., Bersch, M., and van Aken, H. M. (2007). Spreading of the Labrador Sea Water to the Irminger and Iceland basins. *Geophysical Research Letters*, 34(10).
- Yashayaev, I., Holliday, N. P., Bersch, M., and Aken, H. M. (2008). *The History of the Labrador Sea Water: Production, Spreading, Transformation and Loss*. Springer.
- Zahn, M. and von Storch, H. (2010). Decreased frequency of North Atlantic polar lows associated with future climate warming. *Nature*, 467(7313):309–312.

Chapter 2

Nucleus for European Modelling of the Ocean (NEMO): ocean engine

2.1 Introduction

Oceans are an essential part of the climate system. Numerical ocean models are a key element towards understanding the climate system and its variability. They provide estimates of ocean currents, water masses properties and an idea of the state of the ocean in general.

Thirty years ago it would have been rare for an observational oceanographer to consult numerical model output in planning a field campaign. Today the reverse is true. Numerical modelling of the ocean, for a variety of applications, has made great advances both through increase in computational resource and the advances in our ability to effectively use the resource.

The model Nucleus for European Modelling of the Ocean (NEMO) numerical framework (version 3.4) is a state-of-art modelling framework that is used for seasonal forecasting, climate studies, oceanographic research as well as operational oceanography (Madec, 2008). NEMO is composed of five major components: ocean dynamics, sea ice, biogeochemistry, an adaptative mesh refinement software and the assimilation component. The assimilation tool allows for re-forecasts and model constraining. NEMO also has two additional numerical tools, a two-way nesting tool which allows for higher resolution regions within a coarser grid. This chapter aims to provide information about the physics represented by the ocean component of NEMO

and the rationale for the choice of numerical schemes, emphasising those aspects that are fundamental for this thesis.

2.2 Ocean Component

The ocean component of NEMO has been developed from a primitive equation model for both global and regional ocean circulation simulations: Océan PARallélisé (OPA). The reference manual for NEMO 3.4 has been published by Madec (2008). The set of primitive equations used in OPA to describe the ocean follows a group of assumptions for scale considerations:

1. Spherical Earth approximation

The actual topographic surface of the Earth is most apparent with its variety of land forms and water areas. This is, in fact, the surface on which actual Earth measurements are made. However, it is not feasible for exact mathematical analysis, because the formulas which would be required to take the irregularities into account would need a prohibitive amount of computation. This approximation maps the original shape of the Earth on to spherical equipotential surface where gravity g is assumed constant, with the vertical gravity vector always directed towards the centre of the Earth.

2. Thin-shell approximation

The depth of the ocean (z), with an average of < 4 km and maximum $\simeq 11$ km, is much smaller than the earth radius ($r \simeq 6000$ km). In this case, the ocean depth is neglected compared to the radius of the Earth and it is assumed that the distance from the center of the Earth to any location within the ocean is equal to the radius of the Earth ($r + z$, is replaced by r).

3. Turbulent closure hypothesis

An instantaneous flow can be decomposed into its mean motion (time mean flow) and relative motion (turbulent flow) (Reynolds, 1895). Applying the Reynolds averaging on the Navier-Stokes (NS) equations always involves extra unknown turbulent fluxes terms. To close the whole system, eliminating the unknown turbulent fluxes terms, a common

solution is to parameterize the turbulent fluxes in terms of the mean flow. The turbulent closure scheme is used in OPA to parameterize the small-scale processes (e.g., subgrid scale processes) and their effect on the mean flow.

4. Boussinesq hypothesis

This approximation states that the variations in the ocean density compared to a reference density, which can be assumed constant throughout the water column, are very small. This way the density in the momentum equation is replaced by a constant value ρ_0 , with the exception of when the density is multiplying the gravity acceleration g . Thus, density variations are neglected except in their contribution to the buoyancy force.

5. Hydrostatic hypothesis

The vertical momentum equation is reduced to the hydrostatic balance (or equilibrium), where the vertical pressure gradient is balanced by the buoyancy (gravitational) force. This assumption removes convective processes from the initial Navier-Stokes equations and so convective processes must be parameterized instead.

6. Incompressibility hypothesis

It assumes that the density (ρ) of the fluid will not change and that its volume will remain unaltered even when a stress is applied on it. Thus,

$$\frac{D\rho}{Dt} = 0 \tag{2.1}$$

combined with the continuity equation,

$$\frac{\partial \rho}{\partial t} + \nabla \cdot (\rho \mathbf{U}) = 0 \tag{2.2}$$

results in a zero divergence velocity field,

$$\rho \nabla \cdot \mathbf{U} = 0 \tag{2.3}$$

or

$$\nabla \cdot \mathbf{U} = 0 \tag{2.4}$$

Hence, the three dimensional divergence of the velocity vector (\mathbf{U}) is assumed to be zero.

2.2.0.1 Primitive Equations

The ocean as a fluid can be described by the primitive equations, the Navier-Stokes equations along with a non-linear equation of state which couples the two active tracers (temperature and salinity) to the fluid velocity. Because the gravitational force is so dominant in the equations of large-scale, it is useful to choose an orthogonal set of unit vectors ($\mathbf{i}, \mathbf{j}, \mathbf{k}$) linked to the Earth such that \mathbf{k} is the local upward vector and (\mathbf{i}, \mathbf{j}) are two vector orthogonal to \mathbf{k} , and tangent to the geopotential surfaces (Figure 2.1).

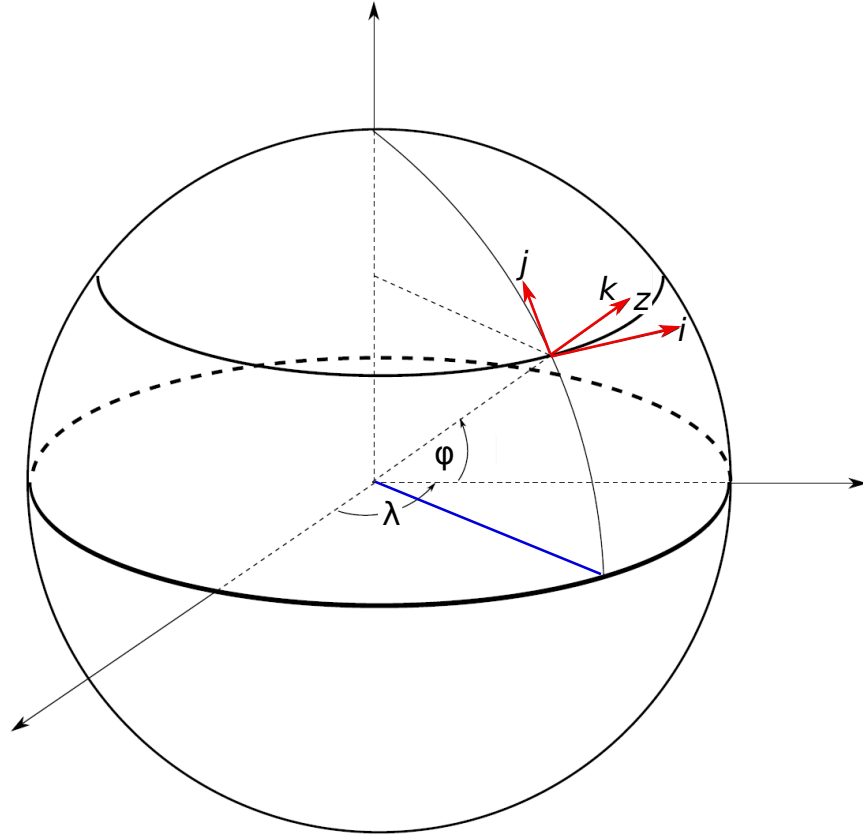


Figure 2.1: Spherical coordinate system in NEMO. The horizontal vectors i and j are described by λ and φ respectively, and are aligned with the Earth's meridians and parallels. The vertical vector k is perpendicular to both i and j , and is described by z .

The vector invariant form of the primitive equations in the $(\mathbf{i}, \mathbf{j}, \mathbf{k})$ vector system provides the following six equations: the momentum balance (E.q. 2.5), the hydrostatic equilibrium (E.q. 2.6), the incompressibility equation (E.q. 2.7), the heat and salt conservation equations

(E.q. 2.8 and 2.9, respectively) and an equation of state (E.q. 2.10).

$$\frac{\partial \mathbf{U}_h}{\partial t} = - \left[(\nabla \times \mathbf{U}) \times \mathbf{U} + \frac{1}{2} \nabla (\mathbf{U}^2) \right]_h - f \mathbf{k} \times \mathbf{U}_h - \frac{1}{\rho_0} \nabla_h p + \mathbf{D}^{\mathbf{U}} + \mathbf{F}^{\mathbf{U}} \quad (2.5)$$

$$\frac{\partial p}{\partial z} = -\rho g \quad (2.6)$$

$$\nabla \cdot \mathbf{U} = 0 \quad (2.7)$$

$$\frac{\partial T}{\partial t} = -\nabla \cdot (T\mathbf{U}) + D^T + F^T \quad (2.8)$$

$$\frac{\partial S}{\partial t} = -\nabla \cdot (S\mathbf{U}) + D^S + F^S \quad (2.9)$$

$$\rho = \rho(T, S, p) \quad (2.10)$$

where ∇ is the generalised derivative vector operator in $(\mathbf{i}, \mathbf{j}, \mathbf{k})$ directions, t is the time, z vertical coordinate, ρ is the *in situ* density given by the equation of state (2.10), ρ_0 is the reference density, p is the pressure, $f=2 \boldsymbol{\Omega} \cdot \mathbf{k}$ is the Coriolis acceleration (where $\boldsymbol{\Omega}$ is the Earth's angular velocity vector), \mathbf{U} is the vector velocity ($\mathbf{U} = \mathbf{U}_h + w\mathbf{k}$ being \mathbf{U}_h the horizontal velocity along the horizontal plane \mathbf{i} and \mathbf{j} indicated by the subscript h , and the vertical (w) velocity along the \mathbf{k} plane), T is the potential temperature, S is the salinity and g is the gravitational acceleration. $\mathbf{D}^{\mathbf{U}}$, D^T and D^S are the parametrizations of small-scale physics for momentum, temperature and salinity, respectively. The surface forcing terms are represented by $\mathbf{F}^{\mathbf{U}}$, F^T and F^S .

2.2.0.2 Boundary Conditions

In the model, the ocean is bounded by coastlines, sea floor and its topography and air-sea or ice-sea interface at its top. These boundaries can be defined by two surfaces, $z = -H(i, j)$ and $z = \eta(i, j, k, t)$, where H is the depth of the ocean bottom and η is the height of the sea surface (Figure 2.2). Through these boundaries the ocean exchanges fluxes of heat, fresh

water, salt and momentum with the solid Earth, the continental margins, the sea ice and the atmosphere. Nevertheless, some of the fluxes are so small that even on a climatic time scale can be neglected.

- **Solid Earth - ocean interface:** Heat and salt fluxes through the sea floor are very small, such is the case that in the model they are set to be zero. The boundary condition is thus set to no flux of heat and salt across solid boundaries. In the case of momentum, the velocity normal to the ocean bottom and coastlines is zero, as the bottom velocity is parallel to solid boundaries. This kinematic boundary condition can be expressed as:

$$\omega = -\mathbf{U}_h \cdot \nabla_h(H) \quad (2.11)$$

In addition the ocean exchanges momentum with the Earth through frictional processes. This momentum transfer occurs at small scales in a boundary layer. It must be parametrized in terms of turbulent fluxes using a bottom and/or lateral boundary conditions.

- **Land - ocean interface:** The major flux exchange between continental margins and the ocean is a mass exchange of freshwater through river runoff. This exchange modifies the sea surface salinity especially in the vicinity of major river mouth. In this thesis the runoff used is a volume-conserved runoff remapped from a 1° by 1° global monthly climatology dataset based on a Global River Flow and Continental Discharge Dataset (Dai and Trenberth, 2002; Dai et al., 2009). The river dataset goes up to 2007, after that the runoff from 2007 is repeated. Freshwater fluxes from Greenland (liquid component only) are also included and are based on Bamber et al. (2012). The liquid freshwater fluxes from Greenland goes up to 2010, and afterwards the runoff from 2010 is repeated. The flux is added as an idealized salt flux at the air-sea interface in the area surrounding the river or fjord (in the case of Greenland melt) mouth. An enhanced mixing over the top 10 m layer is applied in order to mimic the behaviour of the inflowing current.
- **Atmosphere - ocean interface:** Exchanges of heat, salt, freshwater and momentum occur at this interface. This boundary is assumed to be a linear free-surface, where

although the sea surface height (η) changes with time the thickness of the first vertical level ($\mathbf{k}=1$) remains unaltered (surface tension is neglected). Exchanges of momentum, heat and salt are solved using:

$$w|_{z=\eta} = \frac{\partial \eta}{\partial t} + \mathbf{U}_h \cdot \nabla \eta|_{z=\eta} - (\mathbf{P} - E + R + I) \quad (2.12)$$

where P is total precipitation, E is evaporation, R is runoff and I is ice melt flux. The prognostic equation of η can be obtained from vertical integration of the continuity equation (Eq. 2.2), applying the above bottom (Eq. 2.11) and surface kinematic (Eq. 2.12) conditions:

$$\frac{\partial \eta}{\partial t} = (\mathbf{P} - E + R + I) - \nabla \cdot [(H + \eta) \bar{\mathbf{U}}_h] \quad (2.13)$$

where the vertical averaged horizontal velocity $\bar{\mathbf{U}}_h = \frac{1}{H+\eta} \int_{-H}^{\eta} \mathbf{U}_h dz$

- **Sea ice - ocean interface:** The ocean and the sea ice exchange heat, salt, freshwater and momentum. The sea surface temperature is constrained to be at the freezing point at the interface. Sea ice salinity is equal to 4 and is assumed to be constant. The seasonal cycles related with freezing and melting are linked to freshwater and salt fluxes. During the freezing season there is a positive salt flux as the salinity at the sea surface increases. During the melting season there is a negative salt flux, as the sea surface salinity decreases. Momentum fluxes are dominated by friction when the sea ice is land-fast (e.g., drag coefficient) and by stress when the ice is moving over the sea surface.

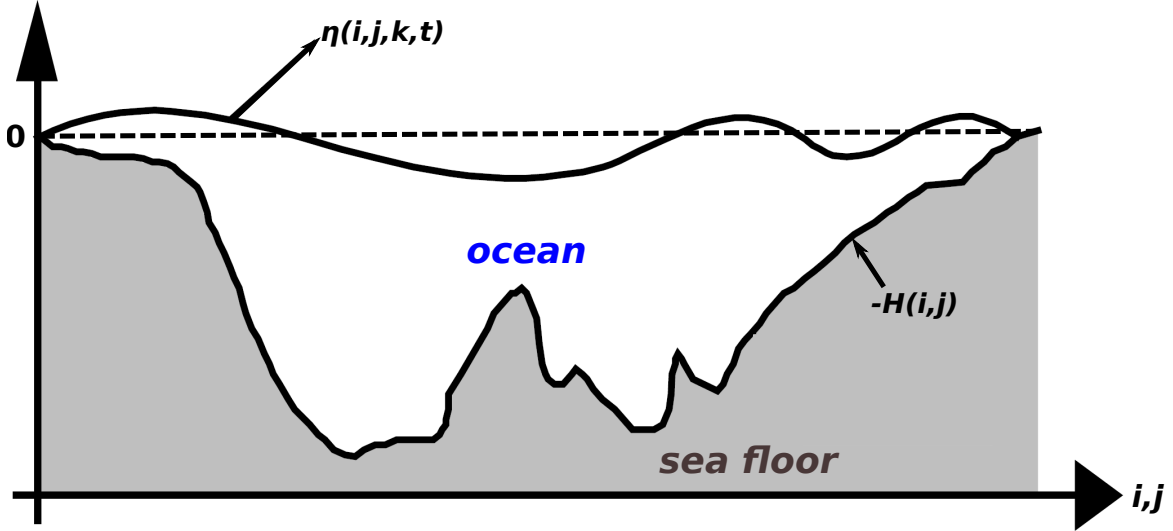


Figure 2.2: Schematic of the surface and bottom boundaries in NEMO: the ocean is bounded by two surfaces, $z = -H(i; j)$ and $z = \eta(i; j; k; t)$, where H is the depth of the sea floor and η the sea surface height. Both H and η are referenced to $z = 0$.

2.2.0.3 Curvilinear Coordinate System and Spatial Discretization

For the purposes of spatial discretization in ocean numerical models a set of orthogonal curvilinear coordinates is used. Following the sphere and thin layer assumptions, a local upward vector \mathbf{k} is chosen as the z -axis and (\mathbf{i}, \mathbf{j}) are two vectors orthogonal to \mathbf{k} and chosen as the horizontal plane (x, y) . The horizontal axis (x, y) can be arbitrary as long as they are orthogonal to each other (Figure 2.1). In spite of the convenience of having the x -axis and y -axis aligned with meridians and parallels, respectively, the convergence of the latter in the standard geographical latitude-longitude grid induces a spherical coordinate singularity close to the North Pole. Such singularity cannot be easily treated in a global model without filtering (Eby and Holloway, 1994; Murray, 1996; Roberts et al., 2006). A solution consists of introducing an appropriated coordinate transformation that shifts the singular point onto land (Dease Strait, Nunavut, Canada in our case). In this thesis a re-projected horizontal mesh is used following the tri-pole transformation proposed by Murray (1996).

As Figures 2.3.a and 2.3.b show, in the model the variables that are resolved are placed on a staggered horizontal Arakawa C grid (Mesinger and Arakawa, 1976). The scalar points T , S , p and ρ are located in the center of the cell (T -point) and vector points (U , V , W) at the

centre of cell faces (U , V and W points, respectively). Relative (ξ) and planetary (f) vorticity are defined in the F -point, located at the centre of each vertical edge. The overall cell size is defined by two horizontal grid scale factors (e_1 and e_2) and a vertical scale factor (e_3).

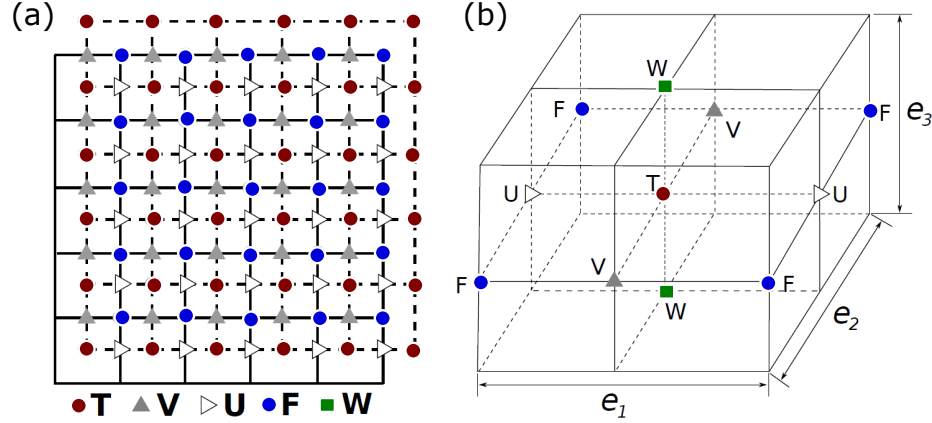


Figure 2.3: Top down (a) and 3D (b) views of the variable arrangement in the model mesh grid. The variables are resolved at different points located around a grid cell: scalar variables are located on the T point (red circle), vorticity at the F point (blue circle), meridional and zonal velocities at the V (grey filled triangle) and the U (grey contoured triangle) points, respectively. Vertical velocities are represented at the W point (green square), located half a grid cell above and below of the T point, on the top and bottom faces of the grid cell (b). e_1 , e_2 and e_3 , the three local scale factors which define the size of the grid cell are shown in (b).

In the case of the vertical grid, the z -coordinate with partial steps (Bernard et al., 2006) is used (Figure 2.4.b). This allows a better representation of the topography than the traditional z -coordinate (Figure 2.4.a). The former approach is straightforward and accurate when it comes to the pressure gradient calculation. However, the same does not apply when it comes to topography. The partial steps approach, on the other hand, has a variable thickness for the bottom-most cells (Figure 2.4.b) allowing a better representation of the sea floor, while keeping the advantages of traditional z -coordinate. Input bathymetry data determines the thickness of the bottom-most cells.

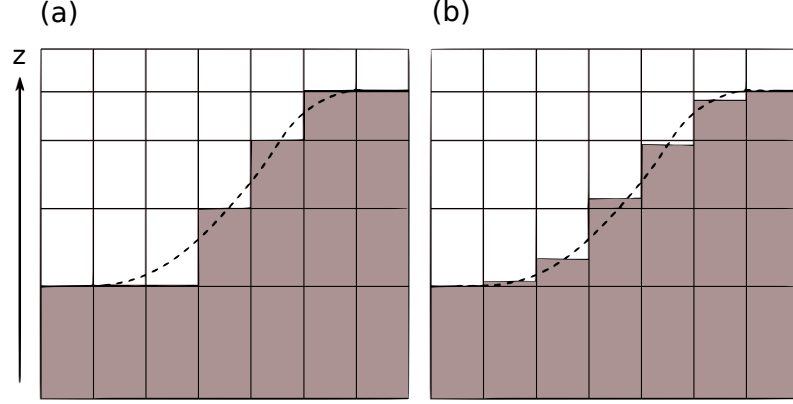


Figure 2.4: Vertical model grid in traditional z-coordinate with full steps (left) and z-coordinate with partial steps (right). Dash lines represent the real sea floor. Shaded cells show the actual sea floor in the model.

2.2.0.4 Subgrid Scale Physics

Ocean numerical models resolve numerous processes by using certain time and space resolution. Unfortunately most of the time such resolution is insufficient to resolve small-scale turbulent motions (shear instability, internal wave breaking...), coming from the advective terms in the Navier-Stokes (NS) equations. This means that small-scale turbulent motions, important on the large scale, are thus never (not even partially) explicitly solved, but always parameterized. In the primitive equations (Eq. 2.5 to Eq. 2.10) both lateral and vertical subgrid-scale physics are represented by $\mathbf{D}^{\mathbf{U}}$, D^T and D^S .

2.2.0.4.1 Vertical Subgrid Scale Physics. The vertical component of the turbulent fluxes for momentum, heat, and salinity are:

$$\mathbf{D}_v^{\mathbf{U}} = \frac{\partial}{\partial z} \left(A_v^m \frac{\partial \mathbf{U}_h}{\partial z} \right) \quad (2.14)$$

$$D_v^T = \frac{\partial}{\partial z} \left(A_v^T \frac{\partial T}{\partial z} \right) \quad (2.15)$$

$$D_v^S = \frac{\partial}{\partial z} \left(A_v^S \frac{\partial S}{\partial z} \right) \quad (2.16)$$

where A_v^m and A_v^T (A_v^S for salinity) are the vertical eddy viscosity and diffusivity coefficients, respectively.

When non-turbulent conditions are present A_v^m and A_v^T are assumed constants with values $1 \times 10^{-4} \text{ m}^2 \text{ s}^{-1}$ and $1 \times 10^{-5} \text{ m}^2 \text{ s}^{-1}$, respectively. These background values are also used as the minimum values for A_v^m and A_v^T in order to avoid numerical instabilities due to weak vertical diffusion. Under turbulent conditions the terms are calculated using the turbulent eddy kinetic (TKE) scheme. The TKE scheme is based on a prognostic equation of turbulent eddy kinetic energy (\bar{e}) defined as:

$$\bar{e} = 0.5(\overline{u'^2} + \overline{v'^2} + \overline{w'^2}) \quad (2.17)$$

$$\frac{\partial \bar{e}}{\partial t} = \frac{A_v^m}{e_3} \left(\left(\frac{\partial u}{\partial k} \right)^2 + \left(\frac{\partial v}{\partial k} \right)^2 \right) - A_v^T N^2 + \frac{1}{e_3} \frac{\partial}{\partial k} \left(\frac{A_v^m}{e_3} \frac{\partial \bar{e}}{\partial k} \right) - c_\epsilon \frac{e^{-3/2}}{l_\epsilon} \quad (2.18)$$

$$A_v^m = c_k l_k \sqrt{\bar{e}} \quad (2.19)$$

$$A_v^T = \frac{A_v^m}{P_{rt}} \quad (2.20)$$

where u' , v' and w' are the velocity turbulent components, N is the local Brunt-Vaisälä frequency, $c_\epsilon = \sqrt{2}/2$ and $c_k = 0.1$ are constants, P_{rt} is the Prandtl number (a function of local Richardson number, R_i), and l_ϵ and l_k are the dissipation and mixing length scales, respectively, which are estimated as:

$$l_k = l_\epsilon = \sqrt{2\bar{e}}/N \quad (2.21)$$

$$\frac{1}{e_3} \left| \frac{\partial l}{\partial k} \right| \leq 1 \text{ with } l = l_k = l_\epsilon$$

Open Ocean Convection. Static instabilities (denser water over lighter water) may occur in the model at particular ocean grid points. In nature, convective processes quickly re-establish the static stability of the water column. These processes have been removed from the model via the hydrostatic assumption (which ignores vertical acceleration) so they must be parameterized. On the other hand, open ocean convection occurs rapidly within plumes

with a diameter not bigger than 1 km. So for models where the hydrostatic assumption is not considered, the horizontal resolution would have to be fine enough for convection to be resolved.

In this thesis in order to parameterized the convective processes a convective scheme is used. The scheme combines an enhanced vertical diffusion scheme and the TKE scheme. The convective scheme triggers when (and where) an instability is present. In the model the instabilities are defined based on the buoyancy frequency, N^2 , such that for a particular grid cell to be considered unstable $N^2 < 10^{-12}$.

Once the instability occurs, it activates the enhanced vertical diffusion scheme for momentum and tracers. This is done by increasing the magnitude of the vertical eddy viscosity and eddy diffusivity (A_v^m and A_v^T , respectively) to $10 \text{ m}^2/\text{s}$. The magnitude of these parameters is increased at the *T-point* of the grid cell where the instability was detected and at the *T-point* of its four closest neighbouring grid cells. This way, it smooths out unstable density profiles during convection, re-establishing the water column stability.

2.2.0.4.2 Lateral Subgrid Scale Physics. Lateral turbulence can be roughly divided into mesoscale turbulence associated with eddies and submesoscale (e.g., diffusion) turbulence which is never resolved even partially, but always parameterized. The formulation of lateral eddy fluxes depends on whether the mesoscale is below or above the grid-spacing. In configurations where the lateral grid spacing is not enough to resolve mesoscale processes (not eddy-resolving), they need to be parameterized. In OPA the parameterization is done by using a scheme similar to the closure scheme used in the vertical subgrid scale physics.

In eddy-permitting configurations, a second order operator can be used. In this particular case a lateral second order tracer diffusive operator is used:

$$D_l^T = \nabla \cdot \left(A_l^T \mathfrak{R} \nabla T \right) \text{ with } \mathfrak{R} = \begin{pmatrix} 1 & 0 & -r_1 \\ 0 & 1 & -r_2 \\ -r_1 & -r_2 & r_1^2 + r_2^2 \end{pmatrix} \quad (2.22)$$

where T refers to the tracer (i.e., temperature and salinity), A_l^T is the horizontal eddy viscosity,

and r_1 and r_2 represent the slopes between the surface along which the diffusive operator acts and the model vertical level. In z -coordinates $r_1 = r_2 = 0$, given that the surface where the diffusive operator acts on is the same as the vertical model level. As a result, a much simpler horizontal diffusion equation is obtained:

$$D_l^T = \frac{1}{e_1 e_2} \left[\frac{\partial}{\partial i} \left(\frac{e_2}{e_1} A_l^T \frac{\partial T}{\partial i} \Big|_z \right) \Big|_z + \frac{\partial}{\partial j} \left(\frac{e_1}{e_2} A_l^T \frac{\partial T}{\partial j} \Big|_z \right) \Big|_z \right] \quad (2.23)$$

When using the Laplacian operator the flow can be separated into the rotational and its divergent components. The rotational part due to relative vorticity is defined as:

$$\zeta = \nabla \times \mathbf{U} \cdot \mathbf{k} = \frac{1}{e_1 e_2} \left[\frac{\partial(e_2 v)}{\partial i} - \frac{\partial(e_1 u)}{\partial j} \right] \quad (2.24)$$

and the horizontal divergence is given by:

$$\chi = \nabla \cdot \mathbf{U}_h = \frac{1}{e_1 e_2} \left[\frac{\partial(e_2 u)}{\partial i} + \frac{\partial(e_1 v)}{\partial j} \right] \quad (2.25)$$

The second order diffusion operator is given as follows:

$$\begin{aligned} D_l^{\mathbf{U}} &= \Delta_h(A_l^m \mathbf{U}) \\ &= \nabla_h(A_l^m \chi) + \nabla_h \times (A_l^m \zeta \mathbf{k}) \\ &= \left(\frac{1}{e_1} \frac{\partial(A_l^m \chi)}{\partial i} - \frac{1}{e_2 e_3} \frac{\partial(A_l^m e_3 \zeta)}{\partial j} \right) \\ &\quad \left(\frac{1}{e_2} \frac{\partial(A_l^m \chi)}{\partial j} + \frac{1}{e_1 e_3} \frac{\partial(A_l^m e_3 \zeta)}{\partial i} \right) \end{aligned} \quad (2.26)$$

For the momentum diffusion the configuration used in this thesis uses a fourth order (bi-laplacian) operator. This is basically done by applying the second order operator (Eq. 2.26), twice.

2.2.0.5 Time Discretization

The time stepping used in NEMO is a three level scheme that can be represented as follows:

$$x^{t+\Delta t} = x^{t-\Delta t} + 2\Delta t \mathbf{RHS}_x^{t-\Delta t, t, t+\Delta t} \quad (2.27)$$

where x is the prognostic variable (u, v, T or S), **RHS** stands for the Right-Hand-Side of the corresponding time evolution equation, Δt is time step, and the superscripts indicate the time at which the variable is evaluated. Each term of the **RHS** is evaluated at a specific time step depending on the physics with which it is associated.

For the **non-diffusive processes** the time stepping used is the well-known Leapfrog (Figure 2.5) scheme (Mesinger and Arakawa, 1976). The scheme may be used for momentum and tracer advection, pressure gradient and Coriolis term. It is an efficient method that achieves a second-order accuracy with just one right hand side evaluation per time step.

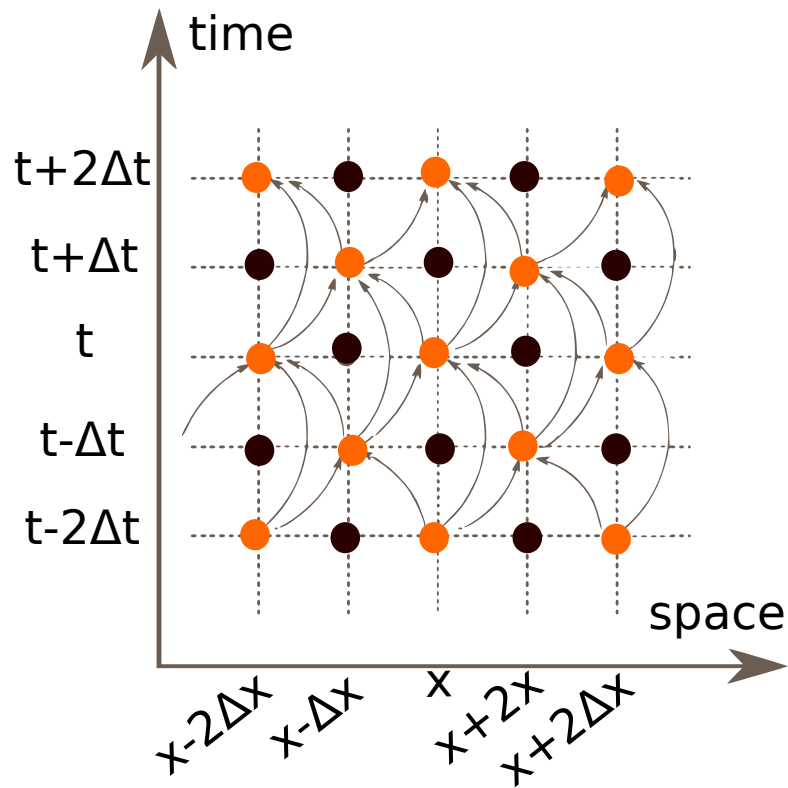


Figure 2.5: Temporal and spatial pattern of the time stepping in the Leapfrog scheme

The method does not artificially damp linear oscillatory motion nor does it produce instability by amplifying the oscillations. One disadvantage of the Leapfrog scheme is that it can introduce a computational mode. This means that the differencing decouples odd and even grid points at any given time step (e.g., orange dots in Figure 2.5). To avoid it, a Robert-Asselin time filter (Robert, 1966; Asselin, 1972) is used with the Leapfrog scheme. The filter is

a kind of laplacian diffusion in time that mixes the odd and even time steps, as the separation of the time steps can be seen in Figure 2.5, with the black dots not contributing to the time evolution of the variable. The Robert-Asselin time filter is represented as:

$$x_F^t = x^t + \gamma \left[x_F^{t-\Delta t} - 2x^t + x^{t+\Delta t} \right] \quad (2.28)$$

where γ is the Asselin filter coefficient. In the particular case of the experiments used in this thesis, $\gamma = 0.1$.

The Leapfrog differencing scheme is unsuitable for the representation of the **diffusive and damping processes** given that all the coefficients of even derivative terms are zero. In this case a forward time differencing scheme is used for the horizontal diffusion terms and tracer restoring terms:

$$x^{t+\Delta t} = x^{t-\Delta t} + 2\Delta t D_x^{t-\Delta t} \quad (2.29)$$

where D_x represents a diffusion term or a restoring term. The scheme is diffusive in time and conditionally stable. The conditions for stability of second and fourth order horizontal diffusion schemes (Griffies et al., 2009) are:

$$A^h < \begin{cases} \frac{e^2}{8\Delta t} & \text{Laplacian diffusion} \\ \frac{e^4}{64\Delta t} & \text{Bilaplacian diffusion} \end{cases} \quad (2.30)$$

where e is the smallest grid size in the two horizontal directions and A^h is the mixing coefficient. For this study, the laplacian and bilaplacian schemes are used for horizontal tracer and momentum diffusion, respectively. Thus, considering a time step $\Delta t = 1080$ s (as is the case for the $1/4^\circ$ horizontal resolution configuration) with the largest grid cell equal to 16027 m, it is required a maximum of $A^h < 2.97 \times 10^4 \text{ m}^2/\text{s}$ for the laplacian diffusion and $A^h < 9.55 \times 10^{11} \text{ m}^4/\text{s}$ for bilaplacian diffusion.

For vertical diffusion a backward (implicit) time differencing scheme (which is unconditionally stable) is used:

$$x^{t+\Delta t} = x^{t-\Delta t} + 2\Delta t RHS_x^{t+\Delta t} \quad (2.31)$$

2.3 Sea Ice Component

The sea ice model coupled with the ocean component of NEMO is the Luvain-la-Neuve sea Ice Model (LIM2) (Fichefet and Maqueda, 1997). LIM2 includes both, dynamic and thermodynamics processes. The model is basically based on a three-layer (one snow layer and two ice layers of equal thickness) model proposed by Semtner (1976), with two ice thickness categories (mean thickness and open water). Ice internal stress is calculated based on an elastic-viscous-plastic rheology assumption (EVP; for details refer to Hunke and Dukowicz, 1997).

2.3.1 Dynamics of Sea Ice

In LIM2 the ice is assumed to move in a two-dimensional plane. The momentum balance is given by:

$$m \frac{\partial \mathbf{u}}{\partial t} = A(\tau_a + \tau_w) - m f \mathbf{k} \times \mathbf{u} - m g \nabla \eta + \nabla \cdot \sigma \quad (2.32)$$

where m is the mass of snow and ice per unit area, A is the ice concentration, τ_a and τ_w are the atmosphere-ice and water-ice interfacial stresses, respectively. As well, f , g , η , \mathbf{k} and $\nabla \cdot \sigma$ are the Coriolis parameter, the acceleration of gravity, sea surface elevation, vertical upwards unit vector and the internal stress term, respectively.

The terms for the atmosphere-ice and water-ice interfacial stresses (τ_a and τ_w) are computed by using the wind data provided by the atmospheric forcing dataset (more on this in Chapter 3) used and simulated ocean currents. The computations of τ_a and τ_w are as follows:

$$\tau_a = \rho_a C_a |\mathbf{u}_a| \mathbf{u}_a \quad (2.33)$$

$$\tau_w = \rho_w C_w |\mathbf{u}_o - \mathbf{u}_i| (\mathbf{u}_o - \mathbf{u}_i) \quad (2.34)$$

where ρ_a is the density of the air, C_a is the air drag coefficient, C_w is the ocean drag coefficient ($C_w = 0.0055$), \mathbf{u}_a is the surface wind velocity at 10 m , \mathbf{u}_o is the surface layer ocean velocity, \mathbf{u}_i is the ice velocity and ρ_w is the sea water density. The air drag coefficient (C_a) is computed

in the model by using the CORE bulk formula (Large and Yeager, 2004).

For the internal ice stress (last term in Equation 2.32: $\nabla \cdot \sigma$), the EPV approach is used. The approach considers that for short time scales sea ice behaves more elastically while on longer times scales (on the order of days) the sea ice behaviour is simplified to viscous-plastic rheology (Hunke and Dukowicz, 1997; Hunke, 2001). The horizontal ice stress is computed as follows:

$$\nabla_h \cdot \sigma = \left(\frac{\partial \sigma_1}{\partial x}, \frac{\partial \sigma_2}{\partial y} \right) \quad (2.35)$$

$$\sigma_1 = \sigma_{11} + \sigma_{22} \quad (2.36)$$

$$\sigma_2 = \sigma_{11} - \sigma_{22} \quad (2.37)$$

On the other hand, sea ice divergence (D_D) and horizontal tension (D_T) and shearing (D_S) strain rates, are given by:

$$D_D = \frac{1}{e_1 e_2} \left(\frac{\partial(e_2 u)}{\partial i} + \frac{\partial(e_1 v)}{\partial j} \right) \quad (2.38)$$

$$D_T = \frac{1}{e_1 e_2} \left(e_2^2 \frac{\partial(u/e_2)}{\partial i} - e_1^2 \frac{\partial(v/e_1)}{\partial j} \right) \quad (2.39)$$

$$D_S = \frac{1}{e_1 e_2} \left(e_1^2 \frac{\partial(u/e_1)}{\partial j} - e_2^2 \frac{\partial(v/e_2)}{\partial i} \right) \quad (2.40)$$

At shorter time scales when sea ice has an elastic response, the internal stress tensor (σ) relates to the strain through the following:

$$2T_e \frac{\partial \sigma_1}{\partial t} + \sigma_1 = \left(\frac{D_D}{\Delta} - 1 \right) P \quad (2.41)$$

$$\frac{2T_e}{e^2} \frac{\partial \sigma_2}{\partial t} + \sigma_2 = \frac{D_T}{e^2 \Delta} P \quad (2.42)$$

$$\frac{2T_e}{e^2} \frac{\partial \sigma_{12}}{\partial t} + \sigma_{12} = \frac{D_T}{2e^2 \Delta} P \quad (2.43)$$

$$\Delta = \sqrt{D_D^2 + \frac{1}{e^2} (D_T^2 + D_S^2)} \quad (2.44)$$

where T_e is an elastic time scale which needs to be small enough to damp the elastic waves, e

is the eccentricity of the ice elliptical curve (which describes the relation of the two principal components of a two dimensional stress tensor and Δ is the deformation rate. P is the ice compressive strength given by a function of mean ice thickness (h) and concentration (A):

$$P = P^* h e^{-C_{reh}(1-A)} \quad (2.45)$$

here $P^* = 5000 \text{ N m}^{-2}$ and $C_{reh} = 20$ are two empirical constants.

2.3.2 Thermodynamics of Sea Ice

Ice thermodynamics comprises the processes involved in the way heat is transfer through or stored within the ice layer. These processes are associated with the vertical and lateral growth and decay of sea ice.

The conductive heat flux (Q_c) in the vertical (z) is computed by using a one dimensional heat diffusion equation, which describes the heat conduction and storage in a snow-ice system (Fichefet and Maqueda, 1997):

$$\rho c_p \frac{\partial T}{\partial t} = Gk \frac{\partial^2 T}{\partial z^2} \quad (2.46)$$

where ρ , c_p and k are the snow/ice density, specific heat and thermal conductivity, respectively. T is temperature, t is time and G is a correction factor used to convert the heat conduction change to the corresponding thickness variations (for more details refer to Fichefet and Maqueda, 1997).

The snow-ice surface heat flux balance (B_{si}), which is a function of the surface temperature, comprises five components: shortwave solar radiation (Q_{sw}), longwave radiation (Q_{lw}), sensible heat (Q_h), latent heat (Q_{le}) and the below the surface conductive heat (Q_c). The mathematical expression for B_{si} is as follows:

$$B_{si} = Q_{sw} + Q_{lw} + Q_h + Q_{le} + Q_c \quad (2.47)$$

In order to compute the first four terms in Eq. 2.47 the bulk formula provided in Large and Yeager (2004) is used:

$$Q_{sw} = (1 - i_0)(1 - \alpha)Q_{ds} \quad (2.48a)$$

$$Q_{lw} = \epsilon(Q_{dl} - \sigma SST^4) \quad (2.48b)$$

$$Q_h = \rho_a c_p C_h (T_a - SST) |\mathbf{u}_a - \mathbf{u}_o| \quad (2.48c)$$

$$Q_{le} = \sigma_a L_e C_e (q - q_s) |\mathbf{u}_a - \mathbf{u}_o| \quad (2.48d)$$

where Q_{ds} and Q_{dl} are the downward shortwave and longwave flux from the atmosphere, T_a and q are the near surface (10 m) atmosphere temperature and specific humidity, SST is the sea surface temperature, q_s is the saturated specific humidity at the ocean surface (which is a function of SST), i_0 is the fraction of net shortwave radiation that penetrates the snow/ice, α is the ocean albedo, ϵ is the emissivity, σ is the Stefan-Boltzmann constant, L_e is latent heat of vaporization of water, and C_h and C_e are the transfer coefficients of sensible and latent heat, respectively.

In the case that the surface temperature T_{sf} is greater than the melting point the excess of energy will be redirected towards snow or ice melting:

$$\left(\frac{\partial h_*}{\partial t} \right)_{surface} = \frac{B_{si}}{L_*} \quad (2.49)$$

where L is the volumetric latent heat and h is the ice or snow thickness. For both parameters (L and h) the subscript $*$ will indicate the presence of either snow (s) or ice (i).

At the interface where the ice and the ocean enter in contact, any existent imbalance in energy between the heat flux from the ocean (Q_{oi}) and the conductive heat flux at the ice bottom (Q_{cb}) will result in ice formation or melting:

$$\frac{\partial h_i}{\partial t}_{oi} = \frac{Q_{cb} - Q_{oi}}{L_i} \quad (2.50)$$

That being said, when Q_{cb} is larger than Q_{oi} , ice growth will tend to happen. If the contrary occurs ice melting predominates.

In the case of lateral growth and decay of the ice, they are both associated to the ice concentration (A), which is the percentage of a grid cell covered by ice. The way the ice concentration changes in time depends on the open water heat budget, B_l . Mathematically, such relation would be expressed as:

$$\frac{\partial A}{\partial t} = (i - A^2)^{1/2} \frac{(1 - A)B_l}{L_i h_0} \quad (2.51)$$

where h_0 is the thickness of ice formed in a lead. When $B_l > 0$, there is ice melting. On the other hand, when $B_l < 0$, ice forms.

2.3.3 Coupling the Ocean and Ice components

The ice and ocean models must be coupled together. The sea ice and the ocean, when in contact, interact between each other in a way that the presence of ice affects the heat, salt and momentum fluxes into the upper ocean, while the ocean model impacts the sea ice through heat and momentum exchange.

The short-wave radiation flux (Q_{swoc}) at the ocean surface with sea ice cover is:

$$Q_{swoc} = A Q_{str} + (1 - A)(1 - \alpha_w) Q_{ds} \quad (2.52)$$

$$Q_{str} = i_o (1 - \alpha) Q_{ds} e^{-1.5(h_i - 0.1)} \quad (2.53)$$

where Q_{str} is the amount of shortwave radiation that reaches the bottom of the ice slab as well as the ocean surface, while α is the open water albedo.

The presence of ice affects the temperature of the upper layer of the ocean. This layer is known to be well mixed (hence the name mixed layer, ML) where vertical homogeneous temperature (T_m) and salinity (S_m) are assumed. If ice exists, the temperature of the ML is set to freezing point (T_{fw} , which depends on salinity) so the thermodynamic equilibrium will be maintain. In other words, the net heat gain of the ML must be balanced by the sensible heat flux from the ocean to the ice (Q_{oi}), which is defined as:

$$Q_{oi} = (1 - i_w|_{z=-h_m})Q_{str} + \Gamma \left[\frac{(1-A)B_l}{A} \right] + Q_{ent} + Q_{dif} + Q_{ovT}|_{-h_m} + Q_{fus} \quad (2.54)$$

where h_m is the depth of the ML, i_w is the fraction of shortwave radiation that reaches the ocean and is a function of depth, Γ represents the Heaviside unit function. The last four terms on the right side are the heat fluxes due to entrainment, diffusion, overturning and salinity changes. All four of them are handled by the ocean ML model.

The heat flux budget of open water regions (e.g., polynyas) is:

$$\begin{aligned} B_l &= (1 - i_w|_{-h_m})(1 - \alpha_w)Q_{sw} \\ &+ \epsilon_w(Q_{lw} - \sigma T_m^4) \\ &+ Q_h + Q_{le} + Q_{lsi} - Q_{lpr} \\ &+ Q_{ent} + Q_{dif} + Q_{ovT}|_{-h_m} + Q_{fus} \end{aligned} \quad (2.55)$$

where Q_{lsi} is the latent heat released during snow/ice formation, and Q_{lpr} is the latent heat released associated with snow falling on the ocean.

Additionally to heat, the presence of ice and/or snow also contributes to the surface salt flux into the ML:

$$\begin{aligned} Q_{salt} &= \underbrace{S_m \frac{\partial m_s}{\partial t}}_{\text{snow melt}} + \underbrace{(S_m - S_i) \left(\frac{\partial m_i}{\partial t} \right)}_{\text{ice melt}} \\ &+ \underbrace{(S_m - S_i) \left(\frac{\partial m_s}{\partial t} + \frac{\partial m_i}{\partial t} \right)}_{\text{salt rejection}} \\ &+ \underbrace{S_i \frac{\partial m_s}{\partial t}}_{\text{artificial meteoric ice}} + \underbrace{S_m (AE - P_w)}_{\text{evaporation \& precipitation}} \end{aligned} \quad (2.56)$$

where E is evaporation over polynyas and leads, P_w is the freshwater change due to precipitation, m represents mass of ice (subscript i) or snow (subscript s), and S_i is the salinity of the sea ice. The salt rejection term also includes the impact of snow or/and ice formation.

2.4 List of parameters

Physical Constants		
Symbol	Value	Description
r	$6.731 \times 10^6 \text{ m}$	Earth radius
g	9.8 m/s^2	gravity acceleration
Ω	7.2921151 s^{-1}	Earth rotation parameter
ρ	1024 kg/m^3	sea water density
ρ_{w0}	1000 kg/m^3	pure water density
ρ_a	1.22 kg/m^3	dry air density
c_p	$1000.5 \text{ J kg}^{-1} \text{ K}^{-1}$	specific heat of air
c_{pw}	$4000.5 \text{ J kg}^{-1} \text{ K}^{-1}$	specific heat of ocean water
σ	$5.67 \times 10^{-8} \text{ kg s}^{-3} \text{ K}^{-4}$	Stefan-Boltzmann constant
L_e	$2.5 \times 10^6 \text{ J kg}^{-1}$	latent heat of the vaporization of water
L_s	$2.839 \times 10^6 \text{ J kg}^{-1}$	latent heat of sublimation of water
C_w	5×10^{-3}	sea water drag coefficient
Ocean Model		
γ	0.1	Asselin time filter
A_h^T	$300 \text{ m}^2 \text{ s}^{-1}$	horizontal tracer eddy viscosity
A_h^m	$-1.5 \times 10^{11} \text{ m}^4 \text{ s}^{-1}$	horizontal momentum eddy diffusivity
A_v^m	$1 \times 10^{-4} \text{ m}^2 \text{ s}^{-1}$	initial vertical eddy viscosity
$\frac{T}{v}$	$1 \times 10^{-5} \text{ m}^2 \text{ s}^{-1}$	initial vertical eddy diffusivity

Sea Ice Model

ρ_s	300 kg m^{-3}	snow density
ρ_i	900 kg m^{-3}	ice density
e	2	yield curve eccentricity
T_e	600 s	elastic wave time scale
P^*	$2.3 \times 10^4 \text{ N m}^{-2}$	ice strength
C_{reh}	20	2st bulk-rheology parameter
C_{ice}	1.63×10^{-3}	transfer coefficient in ice
α	0.95	surface albedo
α_w	0.066	open water albedo
ϵ	0.97	emissivity of snow or ice
S_i	6.0	salinity of sea ice
k_i	$2.034396 \text{ J s}^{-1} \text{ m}^{-1} \text{ K}^{-1}$	conductivity of sea ice
k_s	$0.22 \text{ J s}^{-1} \text{ m}^{-1} \text{ K}^{-1}$	conductivity of snow

Bibliography

- Asselin, R. (1972). Frequency filter for time integrations. *Monthly Weather Review*, 100(6):487–490.
- Bamber, J., den Broeke, M., Ettema, J., Lenaerts, J., and Rignot, E. (2012). Recent large increases in freshwater fluxes from Greenland into the North Atlantic. *Geophysical Research Letters*, 39(19).
- Bernard, B., Madec, G., Penduff, T., Molines, J.-M., Treguier, A.-M., Sommer, J. L., Beckmann, A., Biastoch, A., Böning, C., Dengg, J., Derval, C., Durand, E., Gulev, S., Remy, E., Talandier, C., Theetten, S., Maltrud, M., McClean, J., and Cuevas, B. D. (2006). Impact of partial steps and momentum advection schemes in a global ocean circulation model at eddy-permitting resolution. *Ocean Dynamics*, 56(5-6):543–567.
- Dai, A., Qian, T., Trenberth, K. E., and Milliman, J. D. (2009). Changes in continental freshwater discharge from 1948 to 2004. *Journal of Climate*, 22(10):2773–2792.
- Dai, A. and Trenberth, K. E. (2002). Estimates of Freshwater Discharge from Continents: Latitudinal and Seasonal Variations. *Journal of Hydrometeorology*, 3(6):660–687.
- Eby, M. and Holloway, G. (1994). Grid transformation for incorporating the arctic in a global ocean model. *Climate Dynamics*, 10(4):241–247.
- Fichefet, T. and Maqueda, M. (1997). Sensitivity of a global sea ice model to the treatment of ice thermodynamics and dynamics. *Journal of Geophysical Research: Oceans (1978–2012)*, 102(C6):12609–12646.
- Griffies, S. M., Biastoch, A., Böning, C., Bryan, F., Danabasoglu, G., Chassignet, E. P., England, M. H., Gerdes, R., Haak, H., Hallberg, R. W., et al. (2009). Coordinated ocean-ice reference experiments (COREs). *Ocean Modelling*, 26(1):1–46.
- Hunke, E. and Dukowicz, J. (1997). An elastic-viscous-plastic model for sea ice dynamics. *Journal of Physical Oceanography*, 27(9):1849–1867.

- Hunke, E. C. (2001). Viscous–plastic sea ice dynamics with the evp model: Linearization issues. *Journal of Computational Physics*, 170(1):18 – 38.
- Large, W. G. and Yeager, S. G. (2004). Diurnal to Decadal Global Forcing for Ocean and Sea-Ice Models: The Data Sets and Flux Climatologies. *NCAR Technical Note*.
- Madec, G. and the NEMO team (2008). *NEMO ocean engine*. Note du Pôle de modélisation, Institut Pierre-Simon Laplace (IPSL), France, No 27, ISSN No 1288-1619.
- Mesinger, F. and Arakawa, A. (1976). Numerical methods used in atmospheric models. *GARP Publication Series*, 1(17).
- Murray, R. J. (1996). Explicit generation of orthogonal grids for ocean models. *Journal of Computational Physics*, 126(2):251–273.
- Reynolds, O. (1895). IV. On the dynamical theory of incompressible viscous fluids and the determination of the criterion. *Philosophical Transactions of the Royal Society of London A: Mathematical, Physical and Engineering Sciences*, 186:123–164.
- Robert, A. J. (1966). The integration of a low order spectral form of the primitive meteorological equations. *Journal of the Meteorological Society of Japan. Ser. II*, 44(5):237–245.
- Roberts, J. L., Heil, P., Murray, R. J., Holloway, D. S., and Bindoff, N. L. (2006). Pole relocation for an orthogonal grid: An analytic method. *Ocean Modelling*, 12(1):16 – 31.
- Semtner, A. J. (1976). A model for the thermodynamic growth of sea ice in numerical investigations of climate. *Journal of Physical Oceanography*, 6(3):379–389.

Chapter 3

Sensitivity of Labrador Sea Water formation to changes in model resolution, atmospheric forcing and freshwater input

Published in Journal of Geophysical Research: Oceans (February 2019).

doi.org/10.1029/2018JC014459. **Garcia-Quintana, Y.**, Courtois, P., Hu, X., Pennelly, C., Kieke, D., & Myers, P. G.

ABSTRACT

Labrador Sea Water (LSW) is one of the main contributors to the lower limb of the Atlantic Meridional Overturning Circulation. In this study, we explore the sensitivity of LSW formation to model resolution, Greenland melt, absence of high frequency atmospheric phenomena and changes in precipitation. We use five numerical model simulations at both $1/4^\circ$ and $1/12^\circ$ resolution. A kinematic subduction approach is used to obtain the LSW formation rate over the period 2004 to 2016. The control simulation, with $1/4^\circ$ resolution, showed a mean annual production rate of 1.9 Sv ($1\text{Sv} = 10^6\text{m}^3/\text{s}$) in the density range of 27.68-27.80 kg/m^3 for the period 2004-2016. Deep convection events that occurred during 2008, 2012 and 2014-2016,

were captured. We found that with $1/4^\circ$ resolution the LSW formation rate is 19% larger compared with its counterpart at $1/12^\circ$ resolution. The presence of Greenland melt and an increase in the precipitation impact the denser LSW layer replenishment but do not decrease the overall LSW formation rate nor the maximum convection depth. A dramatic response was found when filtering the atmospheric forcing which induced a decrease of 44% in heat loss over the Labrador Sea, strong enough to halt the deep convection and decrease the LSW formation rate by 89%. Even if our experiment was extreme, a decrease in the storms crossing the Labrador Sea with a consequent reduction in the winter heat loss, might be a bigger threat to deep convection and LSW formation in the future than the expected increases in the freshwater input.

3.1 Introduction

The subpolar North Atlantic is a vital area for heat and freshwater exchange between the low and high latitudes. Within the subpolar North Atlantic, the Labrador Sea, located between the Labrador coast of Canada and Greenland, exerts a significant influence on the climate system. In the basin strong oceanic heat loss during winter (Jung et al., 2014; Holdsworth and Myers, 2015; Schulze et al., 2016) together with a strong cyclonic circulation (e.g., The Lab Sea Group, 1998), induces deep convection, which during severe winters can reach water depths of 2 km (e.g., Dickson et al., 2008; Yashayaev and Loder, 2009, 2017). The resulting product of the deep convection is Labrador Sea Water (LSW). LSW is the lightest component of the North Atlantic Deep Water (NADW), which feeds the deep and abyssal limb of the Atlantic Meridional Overturning Circulation (AMOC) (e.g., Haine et al., 2008; Rhein et al., 2015). Once formed, LSW spreads out from its formation region loaded with high concentrations of dissolved oxygen and anthropogenic tracers like chlorofluorocarbons (CFCs), and can be tracked throughout the entire North Atlantic and beyond (e.g., Rhein et al., 2002; Dickson et al., 2007; Rhein et al., 2015; Kieke and Yashayaev, 2015).

In the upper layer of the Labrador Sea, the Labrador and West Greenland Currents (LC and WGC respectively) pass around the Labrador Sea margins (Figure 3.1.a). These two currents form a counter-clockwise boundary current, carrying sea-ice, icebergs and low-salinity water

from the Arctic as well as runoff from North America and the Greenland ice cap (e.g., Dickson et al., 2007, 2008; Yashayaev and Dickson, 2008; Yang et al., 2016). Warm and salty waters from the Irminger Current (IC) are also advected into the Labrador Sea (McCartney and Talley, 1982). The Irminger Water (IW) is a component of the boundary current system found in the Labrador Sea. It can be identified around the rim of the basin (Figure 3.1.a) and its core can be found at a depth range of 200 to 1000 m over the slope (Myers et al., 2007).

Along the Greenland side, boundary current instabilities result in the formation of Irminger Rings (see, e.g., de Jong et al., 2014; Lilly et al., 2003) (Figure 3.1.a). These warm-core eddies have a diameter of 30-60 km and are known to contribute to the overall heat and salt budget of the basin (Yashayaev, 2007; Lilly et al., 2003), playing an important role during the re-stratification phase after the winter convection in the Labrador Sea (*Hátún et al.*, 2007; Gelderloos et al., 2011; de Jong et al., 2014).

Convective eddies (CE) are also known to play an important role during the re-stratification phase (Marshall and Schott, 1999). After convection, baroclinic instability generated by the strong density differences between the mixed patch and the ambient fluid breaks up into cold CE with a diameter between 10-36 km (Lilly et al., 2003). The CE mix the upper water column while the denser and mixed water core spreads along isopycnals at depth (Marshall and Schott, 1999; Gelderloos et al., 2011).

The boundary current system encircling the Labrador Sea is also associated with the doming of the isopycnals towards the center of the basin. This brings water weakly-stratified from the interior of the basin closer to the surface, reducing the stratification and setting favourable conditions for deep convection to occur (The Lab Sea Group, 1998).

The critical role played by the boundary currents and the eddies which result from them makes model resolution an important feature to investigate the LSW formation. Chanut et al. (2008) compared different model experiments with a horizontal resolution of $1/3^\circ$ and $1/15^\circ$ to investigate the role of mesoscale eddies in the variability of deep convection in the Labrador Sea. By using the $1/15^\circ$ horizontal resolution experiment they were able to have a better representation of IR, CE and Boundary Current Eddies (BCE), the interior heat budget of the Labrador Sea and therefore the variability of deep convection. Also, Marzocchi et al. (2015) found that when the resolution of the model is increased the boundary currents are better

represented, and thus the advection processes within.

The variability of LSW formation has been widely analysed (see e.g., García-Ibáñez et al., 2015; Kieke and Yashayaev, 2015; Rhein et al., 2011; Houssais and Herbaut, 2011; Yashayaev et al., 2007; Azetsu-Scott et al., 2003). Such variability is known to be closely linked to changes in the atmospheric forcing (see e.g., Schulze et al., 2016; Holdsworth and Myers, 2015) particularly to the phases and persistence of the North Atlantic Oscillation (NAO) (e.g., Kieke and Yashayaev, 2015; Dickson et al., 2008, 1996). During the positive phase of the NAO there is a stronger mean cyclonic flow over the North Atlantic Ocean and an increased circulation of cold air out of the Canadian Arctic. This generally leads to stronger heat loss over the Labrador Sea and hence deep convection (Hurrell and van Loon, 1997). During the negative phase of the NAO the situation reverses, resulting in mild winters which leads to a decrease in the heat loss over the Labrador Sea and reduced convective renewal of LSW (Hurrell and van Loon, 1997). However this is not a one-to-one relation as even during negative NAO years deep convection can occur due to the "memory" of the previous winter preconditioning of the water column (*Lazier et al.*, 2002). The years with negative NAO are also linked to the advection of freshwater into the Labrador Sea exported from the Arctic Ocean through Fram Strait, events which are known to have a negative impact on the winter deep convection (e.g., Gelderloos et al., 2012; Dickson et al., 1988; McCartney and Talley, 1982).

Besides the freshwater exported from the Arctic Ocean, there are local sources known to have an influence on the freshening of the basin: an increase in the melting of Greenland Ice Sheet (GrIS) (e.g., Brunnabend et al., 2015; Bamber et al., 2012) and in precipitation (e.g., Myers, 2005). In fact, a likely consequence of global warming is the increment of freshwater discharge due to ice melting or precipitation increase, adding freshwater into the ocean with the subsequent risk of substantial changes in ocean circulation. If transported into the interior of the Labrador Sea, such freshwater discharges would reduce the surface salinity (Josey and Marsh, 2005), contributing to the stability of the water column, and potentially reducing deep water formation.

High frequency atmospheric phenomena such as cold-air outbreaks, polar lows, mesoscale cyclones, fronts, topographic jets and extreme winter events in general, known to impact the convection depth (Holdsworth and Myers, 2015), are also expected to change with future cli-

mate warming (e.g., see details in Kolstad and Bracegirdle, 2008; Zahn and von Storch, 2010b) and questions about how the ocean will respond to those changes are arising (Holdsworth and Myers, 2015).

The formation and downstream spreading of LSW and its contribution to the NADW, make the North Atlantic Ocean the only basin amongst the world's ocean where large concentrations of anthropogenic CO_2 penetrate mid and abyssal depths (Sabine et al., 2004). At the same time strong oxygen intake occurs during deep convection events. As the mixed layer deepens it progressively exposes large volumes of under-saturated water to the atmosphere allowing the ventilation of the deep ocean (e.g., Kieke and Yashayaev, 2015; Stendardo and Gruber, 2012). So changes in LSW production, its properties and thickness would have a direct impact on the potential of the ocean to store anthropogenic carbon (see, e.g., Steinfeldt et al., 2009) and on the ventilation of the deep ocean. Given its relevance various efforts have been made to investigate the LSW formation rate using numerous methods (chlorofluorocarbons (CFC) inventories, numerical models, hydrographic changes, mass budget, heat budget, etc.). Haine et al. (2008) summarized various methods to infer the LSW formation rate and its variability, based on studies published between 1990 to 2008. The formation rates from some of those studies (in Haine et al., 2008), among others, are illustrated in Figure 3.1.b. Therein, our main goal is to illustrate some of the different methods used to study the formation of LSW together with the associated rates and to use them to place our subduction estimates in context. For more details on the specifics of the methods and LSW definition used in the different studies, please refer to the manuscripts cited in Figure 3.1.b.

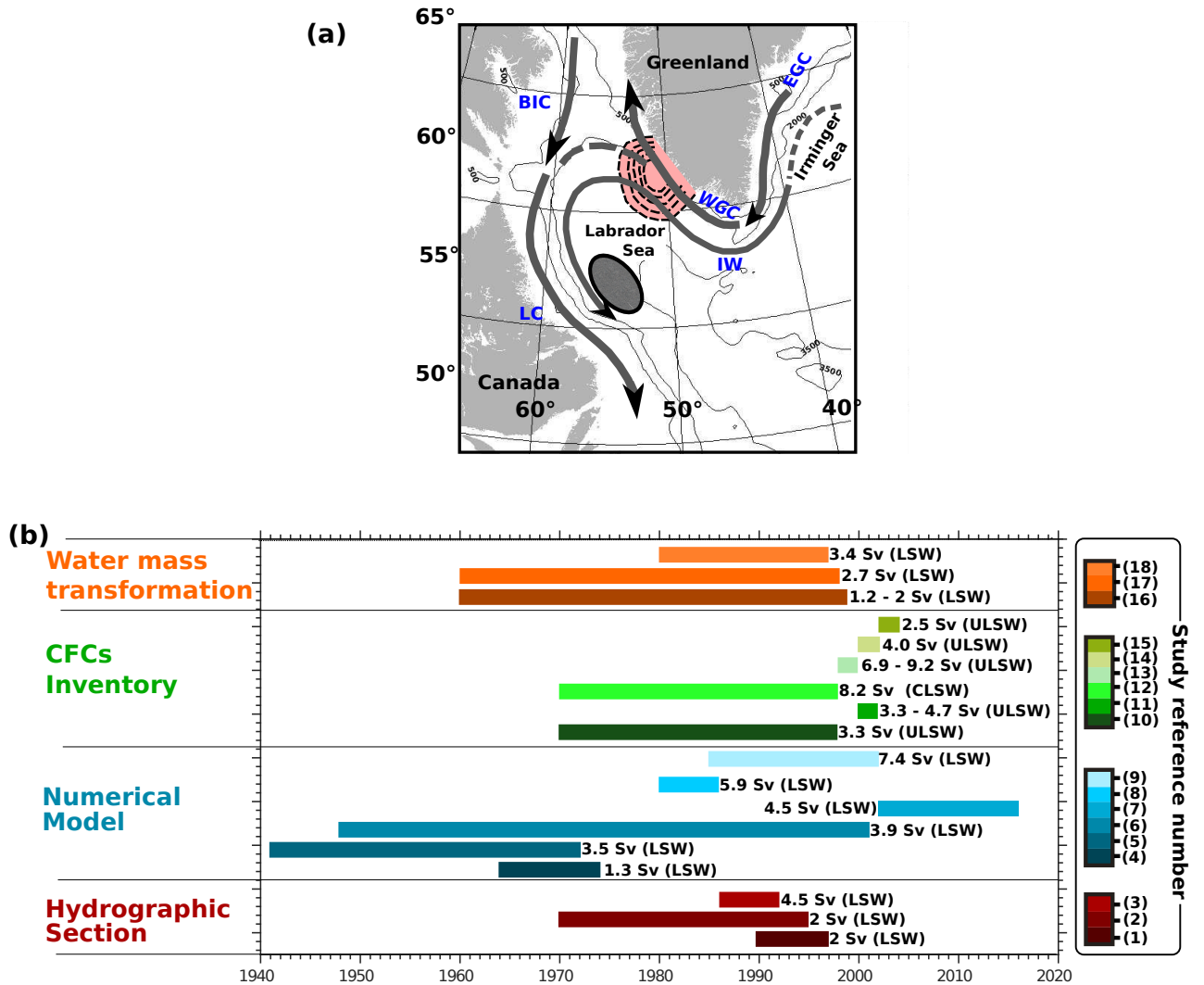


Figure 3.1: (a) Schematic showing the boundary current system around the Labrador Sea: East Greenland Current (EGC), West Greenland Current (WGC), Irminger Water (IW), Baffin Island Current (BIC), Labrador Current (LC). Also displayed in this sketch is the deep convection region (shaded ellipse) after The Lab Sea Group (1998), the region with the higher incidence of eddies shed out of the WGC (pink region contoured by black dashed lines) after Chanut et al. (2008), and the isobaths 500, 2000 and 3500 m. Panel (b) summarises the results from different studies investigating LSW formation rates using four methods: Hydrographic observations, numerical model output, CFCs inventories and water mass transformation approach. Each horizontal bar indicates the study period of the responding study (labelled with color). The resultant rate is notated adjacent to the bar. The color scales on the right refer to the studies listed as follows: (1) Pickart and Spall (2007), (2) Yashayaev et al. (2004), (3) Yashayaev and Clarke (2006), (4) Khatiwala and Visbeck (2000), (5) Boning et al. (1997), (6) Gerdes et al. (2005), (7) *Courtois et al.* (2018), (8) Mauritzen and Häkkinen (1999), (9) Marsh et al. (2005), (10), (11) and (13) Kieke et al. (2006), (12) LeBel et al. (2008), (14) and (15) Kieke et al. (2007), (16) Myers and Donnelly (2008), (17) Khatiwala et al. (2002), and (18) Marsh (2000).

The kinematic subduction approach has been used as a tool to investigate the ventilation of the ocean as well as water-mass formation (e.g., Da Costa et al., 2005; Trossman et al., 2009; Liu and Wang, 2014; *Courtois et al.*, 2018). The approach integrates the local subduction rate over outcrop areas and over density classes. In principle, it is similar to the transformation approach (Marsh, 2000) but with consideration of advection. It quantifies the transfer of water below the mixed layer into the deeper layers, effectively connecting the atmosphere to the ocean interior. One of the main advantages of the method is that it considers transfer into the ocean interior over a specific density range (Da Costa et al., 2005).

In this study we explore the impact of enhanced freshwater discharge (either by glacial melting or precipitation increase), high frequency atmospheric forcing and model resolution on LSW formation by using numerical model output. We use the kinematic subduction approach to quantify the LSW formation rate in the period 2004 to 2016. To our knowledge this study is the first to use this method to investigate the variability of the LSW formation rate under different sensitivity experiments, while using hourly atmospheric forcing data that allows the representation of a wide range of atmospheric phenomena. The study is preceded by *Courtois et al.* (2018) who, by using a high-resolution numerical simulation, investigated the subduction rate in the Labrador Sea from 2002 to 2014.

These different scenarios covered in the present manuscript were selected to investigate how the LSW formation might respond under changes predicted to occur due to the ongoing global warming (except in the case of model resolution): increase in Greenland Ice sheet melt, decrease of precipitation over the mid latitudes and the decrease of high frequency atmospheric phenomena over the Labrador Sea together with a poleward shift of the extra-tropical storm track. In the case of *SPG12* we were looking to tackle how the model resolution might impact the results. Numerical ocean models play an important role in increasing our ability to comprehend oceanic processes, monitor the current state of the oceans, and to a limited extent (for now), even predict their future state.

Holdsworth and Myers (2015) also investigated the influence of high frequency atmospheric forcing on the deep convection of the Labrador Sea using model output from 2002 to 2010 (for details see Holdsworth and Myers, 2015). One of the main differences between their and the present study is that they explored the impact on the convective energy in the Labrador Sea

while we investigate the influence on the LSW formation rate.

In order to explore the sensitivity of the LSW formation rate on changing conditions, a control simulation and four perturbation experiments were carried out using a state-of-the-art coupled ocean-sea ice model, run from 2002 to 2016. Each of the perturbation experiments have a specific alteration compared to the *Control* simulation. The model as well as a description of the experiment setup are introduced in Section 2. Section 3 gives a detailed description of the kinematic subduction approach used to estimate the LSW formation rates. Section 4 describes the results obtained with the different experiments. Section 5 covers the discussion and conclusions.

3.2 Model Description and Experiments Setup

This section describes the details of the model and the configuration used. The different simulations used within each of the sensitivity experiments are also introduced.

3.2.1 Ocean-Sea Ice Model

The model used is the Nucleus for European Modelling of the Ocean (NEMO) numerical framework version 3.4 (Madec, 2008). The sea ice module is the Louvain-la-Neuve LIM2 (Fichefet and Maqueda, 1997). The configuration used to run all the simulations in this paper is called *Arctic and Northern Hemisphere Atlantic* (ANHA) with a $1/4^\circ$ resolution (ANHA4) (Figure 3.2.a). The configuration covers the whole Arctic Ocean, North Atlantic and a part of the South Atlantic with two open boundaries, one close to Bering Strait and the other one at 20°S . Its mesh grid is extracted from the $1/4^\circ$ global tripolar grid, ORCA025 (Barnier et al., 2007). The highest horizontal resolution (~ 6 km) is in Dease Strait, an east-west waterway between the mainland of Kent Peninsula and Victoria Island in Nunavut, Canada. The lowest resolution (~ 28 km) is at the Equator. Over the Labrador Sea the horizontal resolution is around 16 km. The configuration has 50 vertical levels, with the layer thickness smoothly increasing from 1.05 m at the surface, to 453.13 m in the last level. No temperature or salinity restoring is applied, leaving the model to evolve freely without constraining the drift.

ANHA4 initial temperature, salinity, horizontal velocities (zonal and meridional) and sea

surface height fields are obtained from *Global Ocean Reanalysis and Simulations* (GLORYS2v3) from MERCATOR (Masina et al., 2017). The initial ice field is a combination of GLORYS2v3 simulation and satellite observations. Lateral open boundary conditions (salinity, temperature and horizontal velocities) are also from GLORYS2v3. This approach helps to reduce the model spin-up time by starting from a spun-up realistic state. GLORYS2v3 is a global ocean reanalysis produced by the MyOcean Global Monitoring and Forecasting Centre. The reanalysis is built to be as close as possible to the observations (i.e. realistic) and in agreement with the model physics. Using NEMO 3.1 and LIM2 EVP sea ice model, GLORYS2v3 runs from January 1993 to December 2013. The mesh grid is extracted from ORCA025. It has 75 vertical levels and an eddy-permitting horizontal resolution of $1/4^\circ$. It uses 3-hourly ERA-Interim as atmospheric forcing as well as bulk Coordinated Ocean-ice Reference Experiments (CORE) formulation with radiative flux correction and diurnal cycle. The data assimilated in GLORYS2v3 includes: Sea Surface Temperature (Reynolds AVHRR-AMSR $1/4^\circ$), reprocessed Sea Surface Height (Jason1, Jason2, Envisat, T/P, GFO, ERS1-2), reprocessed InSitu temperature and salinity vertical profiles from the Coriolis Data Center, CNES-CLS MSSH (Rio 2009) and sea ice concentration (Cersat). For more details on GLORYS2v3 please refer to https://www.mercator-ocean.fr/wp-content/uploads/2015/08/FS-GLORYS2V3_EN.pdf

The atmospheric forcing data used in ANHA4 comes from the *Canadian Meteorological Centre's Global Deterministic Prediction System* (CGRF) (Smith et al., 2014). CGRF provides 10 m surface wind, 2 m air temperature and specific humidity, downward long-wave and short-wave radiation fluxes and total precipitation. This dataset has a temporal resolution of one hour and a spatial resolution of 0.45° in longitude and 0.3° in latitude (which is still relatively coarse compared to the ANHA4 spatial resolution). The CORE bulk formulae were applied to compute fluxes of heat, water and momentum (Large and Yeager, 2009).

Monthly interannual river discharge from the 1° by 1° Global River Flow and Continental Discharge Dataset (Dai and Trenberth, 2002; Dai et al., 2009) is volume-conserved remapped onto the model grid. The original dataset goes up to 2007, after that the runoff from 2007 is repeated. The river discharge from the adjacent areas of the Labrador Sea was found to be $117.9 \text{ km}^3/\text{year}$ in this dataset. Freshwater fluxes from Greenland (liquid component only) are based on Bamber et al. (2012). The liquid freshwater fluxes from Greenland goes up to

2010, and afterwards the runoff from 2010 is repeated.

The regional configuration ANHA4 has been used in the past by Holdsworth and Myers (2015) to explore the influence of high frequency atmospheric forcing on the circulation and deep convection in the Labrador Sea. Dukhovskoy et al. (2016) used the same configuration to look at the spreading of Greenland freshwater in the sub-Arctic Seas, while Guillard et al. (prep) explored the pathways of the melt-water from marine terminating glaciers of the Greenland ice sheet. Müller et al. (2017) used the ANHA4 configuration to explore the temperature flux carried by individual eddies across 47°N in the Atlantic Ocean. They ran two different simulations using the ANHA4 configuration: one simulation with a horizontal resolution of 1/4° over the entire domain and a second simulation with a two-way nest over the subpolar gyre to increase the horizontal resolution to 1/12°. Both simulations, called ANHA4 and ANHA4-SPG12 (in Müller et al. (2017)), are used in the present study. Here nevertheless they will be found under the names *Control* and *SPG12* respectively.

3.2.2 Sensitivity Experiments Set-up

Four perturbation experiments from a *Control* simulation were carried out using ANHA4 (Table 3.1): *Subpolar Gyre 1/12° (SPG12)*, *Greenland Melt Removed (GMR)*, *Filtered and Precipitation Decreased (PD)*. All the simulations, including the control run, were ran from January 1st, 2002 to December 31st, 2016, with a temporal output resolution of 5 days. No leap years were consider as it is traditionally done for ocean models.

The perturbation experiment *SPG12* was designed to evaluate the impact of the spatial resolution when calculating the LSW formation rate. To increase the resolution from 1/4° to 1/12°, two-way nesting was implemented using the *Adaptive Grid Refinement in Fortran90* (AGRIF) (Debreu et al., 2008; Laurent et al., 2005; Blayo and Debreu, 1999). The nest was centered over the region of the subpolar gyre, approximately between 36° - 68°N and 60°W and 10°E, with the ANHA4 configuration as the parent domain (Figure 3.2.b). *SPG12* was forced using the same collection of datasets used to force *Control*. The river runoff dataset was interpolated to 1/12°, though additional care was taken to ensure that all river runoff enters ocean grid cells. While the resulting spatial area where runoff is applied to the ocean may differ slightly between the 1/4° and 1/12° datasets, the runoff volume is identical. To

Table 3.1: Set of simulations used in the present study: *Control* (reference simulation), *SPG12* (horizontal resolution increased to $1/12^\circ$), *Greenland Melt Removed* (GMR), *Filtered* (filtered winds and temperature fields) and *Precipitation Decreased* (PD). **bold** is used to show what is different between the simulations of an experiment. CGRF (\bullet) refers to a version of the atmospheric forcing containing a decrease in precipitation. CGRF ($\bullet\bullet$) refers to the filtered (temperature and wind fields) version of the atmospheric forcing. The period considered for all the experiment was 2004 to 2016.

Simulation name	Horizontal resolution	Atmospheric forcing	Greenland and River Runoff
Control	$1/4^\circ$	CGRF	Interannual-Monthly with Greenland melt
SPG12	$1/12^\circ$	CGRF	Interannual-Monthly with Greenland melt
GMR	$1/4^\circ$	CGRF	Interannual-Monthly with Greenland melt removed
Filtered	$1/4^\circ$	CGRF ($\bullet\bullet$)	Interannual-Monthly with Greenland melt
PD	$1/4^\circ$	CGRF (\bullet)	Interannual-Monthly with Greenland melt

preserve in *SPG12* the same atmospheric conditions present in *Control*, the CGRF dataset is interpolated to $1/12^\circ$, as opposed to using a higher resolution dataset. It should be noted that this does not imply true $1/12^\circ$ resolution of atmospheric forcing, as CGRF has a native resolution of around 33 km in the Labrador Sea. CGRF has however sufficient temporal and spatial resolution to capture the intense mid-latitude cyclones which heavily influence the Labrador Sea (Holdsworth and Myers, 2015). While a higher resolution atmospheric dataset might present some smaller scale features, the large scale interaction between the atmosphere and the Labrador Sea will not change if the mean state is not significantly affected. The *SPG12* simulation examines if additional eddy-resolving skill results with changes to the Labrador Sea subduction rather than the connection with the atmosphere (or Greenland melt), which the other simulations cover.

By implementing the nest, the horizontal resolution over the Labrador Sea increased from

16 km in *Control* to 5 km in *SPG12*. Due to the increased resolution, the following resolution-dependent parameters are consequently different between *Control* and *SPG12*: time-step, horizontal eddy diffusion, horizontal bilaplacian eddy viscosity, and elastic wave time-scale for sea-ice (Table 3.2). The rest of the parameters for each simulation were kept identical.

Table 3.2: Resolution-dependent parameters whose numerical values changed from *Control* to *SPG12*.

Parameter	<i>Control</i>	<i>SPG12</i>
Time-step	1080 s	180 s
Horizontal eddy diffusivity	300 m^2/s	50 m^2/s
Background horizontal bi-Laplacian eddy viscosity	$-1.5 \times 10^{11} m^4/s$	$-1 \times 10^{10} m^4/s$
Time-scale for elastic waves in sea-ice model	320 s	120 s

The second perturbation experiment, termed Greenland Melt Reduced (*GMR*), aims to determine the impact of freshwater fluxes from the GrIS on LSW formation. Compared to the *Control* run, the simulation *GMR* does not include the GrIS freshwater around Greenland from Bamber et al. (2012). The difference in LSW formation between the two *Control* and *GMR* simulations is presented in the section 4.2.

To investigate the influence of high-frequency atmospheric forcing a third perturbation experiment called *Filtered* was carried out. As high frequency atmospheric phenomena appear as short time-scale changes in temperature and wind stress, the temperature and wind speed fields only were filtered. To do so a Kolmogorov-Zurbenko filtering (Zurbenko et al., 1996; Rao and Zurbenko, 1994) was applied to the hourly atmospheric forcing data (referred to as **CGRF** (●●) in Table 3.1). The filter is based on an iterative moving average of length m , and obtained after p iterations, that removes high frequency (with respect to the window size m) variations from the original data. We used a window length width of ten days ($m = 10$) and one iteration ($p = 1$). Thus all the forcing acting over a time period of 10 days or less (e.g., storms, barrier and topographic winds and frontal jets) were removed from the original

atmospheric forcing dataset.

To analyse just the impact of the freshwater input as a consequence of changes in precipitation, a fourth perturbation experiment called Precipitation Decreased (*PD*) is considered. The precipitation used in the *PD* simulation is 1/3 of that used in *Control* (referred to as **CGRF (•)** in Table 3.1). The *Control* simulation is thus considered to be a case of increased precipitation here.

To account for the model adjustment from GLORYS2V3, we use only the output corresponding to the period January 1st, 2004 to December 31st, 2016. By analysing some of the ocean fields from the model output we found that, although short, this 2 years adjustment period is sufficient for the model to develop realistic inter-annual variability in the Labrador Sea, given the simulations start from the reanalysis solution.

3.2.3 Model Evaluation

We compared the mixed layer depth (MLD) obtained from Argo observations (for details about the Argo dataset, see: Holte et al., 2017) with the *Control* simulation (based on the analysis of Courtois et al., tted). The comparison was made over a region in the Labrador Sea selected following Yashayaev and Loder (2016) (Figure 3.2.c). The MLD from *Control* shows a good agreement with that derived from the Argo floats, especially during years when deep convection developed such as 2008, 2012, 2014 and 2015. Seasonal variability captured in the *Control* simulation corresponds well with that observed. The observed and simulated MLD time series are correlated at 81% for both periods 2002-2016 and 2004-2016. Thus there is no impact whether if we consider or not the short spin up time. At the same time there is some disagreement as *Control* shows a deeper (more than 300 m) MLD in years like 2009, 2010 and 2016. However due to the nature of the Argo floats they do not happen to be always in the convection site when deep convection is occurring, as they mainly drift within the mean flow. Based on observational data (annual conductivity-temperature-depth (CTD) survey of the AR7W section from Fisheries and Oceans Canada), Yashayaev and Loder (2017) found that the MLD during 2016 was deeper than 2000m, however the Argo data does not reach that depth. Thus, the differences found in the MLD comparison in the years 2009, 2010 and 2016 might as well come from the absence of observations from the convection region and not

necessarily due to an overestimation of the model MLD.

We also compared over-the-MLD averaged salinity and temperature time series from *Control* and from Argo floats (for details about the Argo dataset see: Holte et al., 2017) (Figures 3.2.d and 3.2.e respectively), both within the same region used for the MLD comparison. We found that (although not perfect) the model does a decent job representing the inter-annual variability and magnitudes of both fields, especially for temperature. This is reflected in the agreement between model and observations during the convection (winter) season. The mean model-observations temperature difference is 0.2° C and 0.3° C for the periods 2002-2016 and 2004-2016 respectively. In the case of salinity the mean model-observations difference is 0.1 and 0.2 for the periods 2002-2016 and 2004-2016 respectively. We found that the modelled and observed salinity time series are 69% and 74% correlated for the periods 2002-2016 and 2004-2016 respectively. At the same time in the case of the temperature field, the model and observation time series are 95% correlated for both periods 2002-2016 and 2004-2016.

The overturning transport at 26.5° N between *Control* and the observations from the RAPID-MOCHA-WBTS (RAPID-Meridional Overturning Circulation and Heat flux Array-Western Boundary Time Series) array (C.S., 2017), was also compared (Figure 3.2.f). In this particular case the comparison is done from 2004 which is when the observations at the RAPID-MOCHA-WBTS array started. Both time series are correlated at 50% with the model properly representing the inter-annual variability. However, the model overestimates the overturning transport by 2Sv with the difference increasing with time. The increase in the modelled AMOC at 26.5° N after 2009 seems to be related to numerical issues at the southern boundary (-20° S) beginning in December 2007. The signal however does not spread beyond 45° N during our integration and thus does not affect the Labrador Sea fields discussed in this manuscript.

Müller et al. (2017) compared the mean circulation patterns from *Control* and *SPG12* with that from satellite altimetry, with a focus on the region located between 60° - 5° W and 40° - 55° N within the subpolar gyre, finding a good correspondence between them. However they did point out, as one of the differences, a more pronounced coastal branch of the Labrador Current represented in the simulations compared to that from altimetry data.

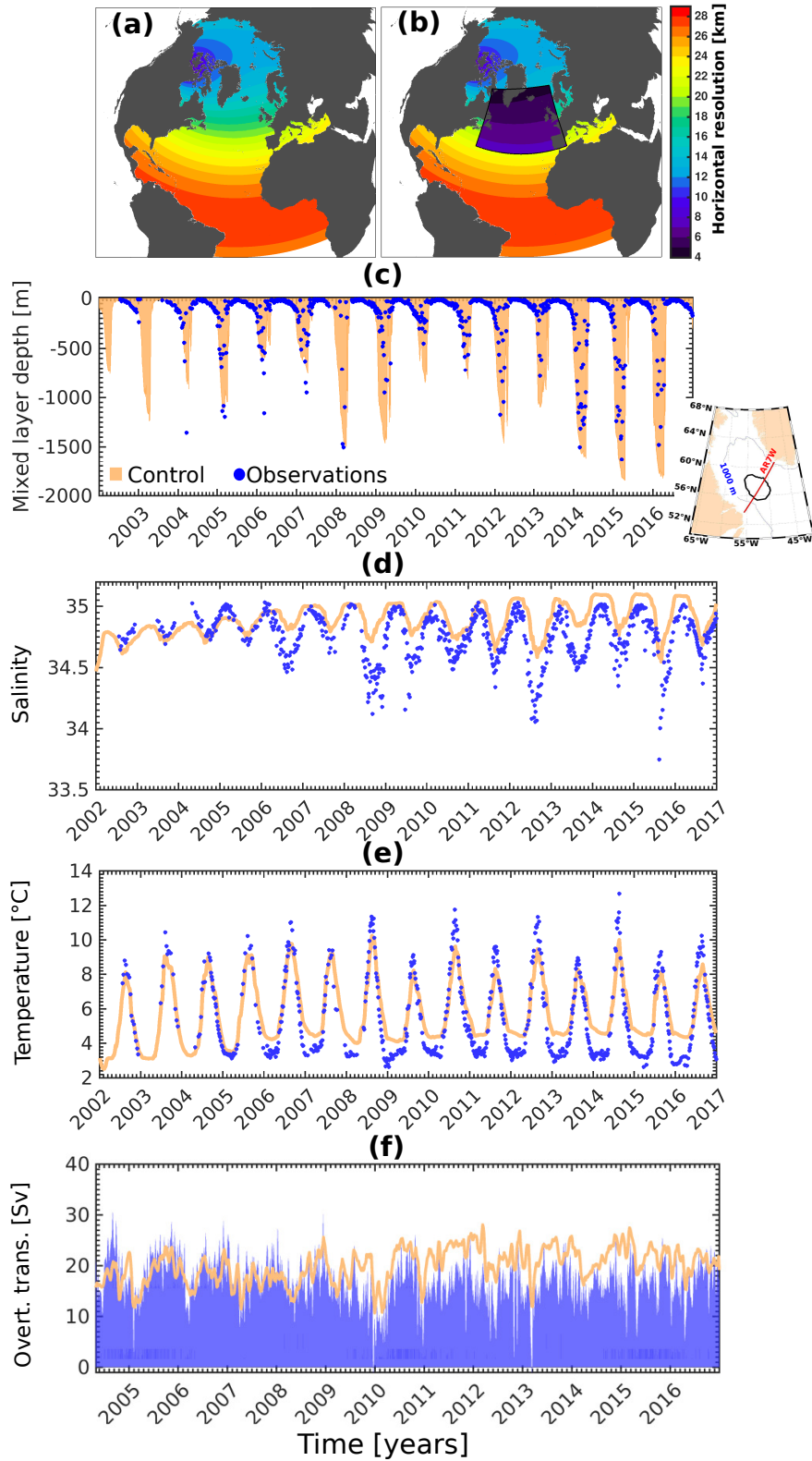


Figure 3.2: Horizontal resolution for (a) the ANHA4 domain and for (b) *SPG12*. The next panels show a comparison of the *Control* simulation and observations regarding: (c) mixed layer depth and over-the-MLD averaged (d) salinity and (e) temperature, all over the black-contoured region in the map inset in (c) (*Control* vs. Argo floats), and (f) overturning transport (Overt. trans.) at 26.5°N (*Control* vs. RAPID array).

3.3 Analysis Methods

Ocean subduction involves water mass exchange through the moving mixed layer base. When water masses are transferred beneath the base of mixed layer, they are shielded from the atmosphere and only subsequently modify their properties by mixing in the ocean interior. The process describing the temporary movement of water out of (into) the mixed layer is known as detrainment (entrainment) (see, e.g., Da Costa et al., 2005). On the other hand, when the water leaves the mixed layer, passing through the seasonal pycnocline to the permanent pycnocline (Figure 3.3.a) irreversibly in one year, it is known as subduction (e.g., Qiu and Huang, 1995). Similarly, the annual mean obduction rate is defined as the total amount of water going from the permanent pycnocline, passing through the seasonal pycnocline, into the mixed layer (Figure 3.3.a) irreversibly in one year (e.g., Qiu and Huang, 1995). We will use only the term subduction as it is the process linked to water formation, while obduction is mainly related to water erosion (e.g., Qiu and Huang, 1995; Huang, 2010).

Two main approaches can be used for calculating subduction rates. One approach is based on the analysis of ocean-atmosphere heat and mass fluxes and on the calculation of the density fluxes through the sea-air interface (Speer and Tziperman, 1992). The second approach is the so called kinematic method which is based on the analysis of the upper ocean circulation, and it can be carried out in a Lagrangian or Eulerian reference frame (e.g., Qiu and Huang, 1995). In the present work the kinematic subduction approach in Eulerian coordinates, following Da Costa et al. (2005) and *Courtois et al.* (2018), is used to calculate the subduction rate in the Labrador Sea (Figure 3.3.b). According to Da Costa et al. (2005), the approach addresses the subduction (obduction) rate as the exchange through the moving mixed layer caused by a deepening (shallowing) of the MLD, convergence of horizontal transport out of (into) the mixed layer and vertical transport out of (into) the mixed layer (Figure 3.3.a). So all the processes contributing to the transfer of water into the ocean interior are considered.

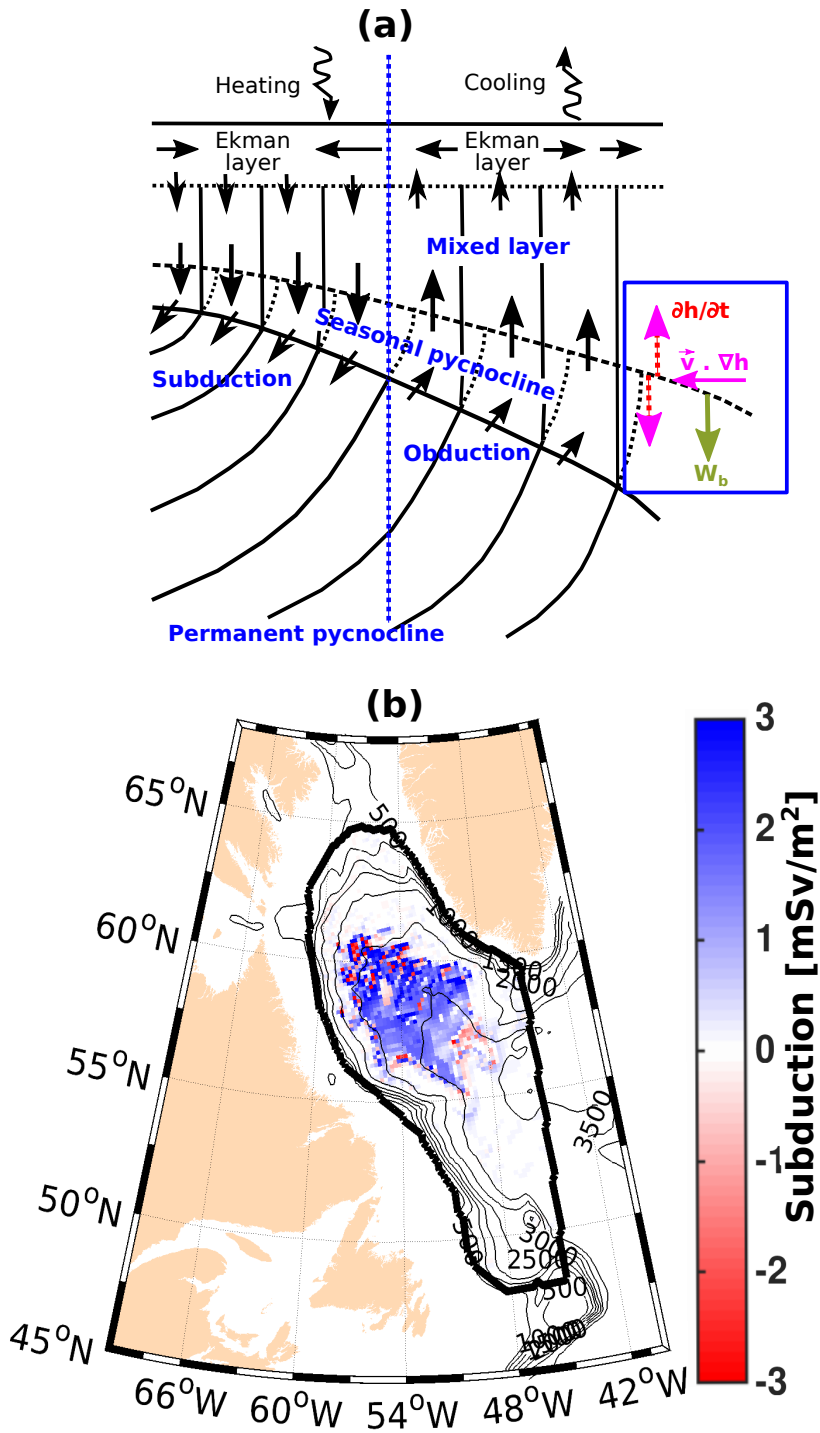


Figure 3.3: (a) Schematic showing the subduction and obduction process following Qiu and Huang (1995). The blue box represents the processes involved in subduction. The red arrows represent the change in time of the MLD, with the arrows pointing out the shallowing (up) and deepening (down) of the MLD ($\frac{\partial h}{\partial t}$). In magenta is illustrated the term that represents the convergence of horizontal transport into the MLD ($\vec{v} \cdot \nabla h$). In green appears the vertical transport of fluid (W_b) into the MLD. (b) The Labrador Sea with the region within the basin over which the net subduction was calculated. Figure (b) shows a sample field of the subduction averaged over April 26 (included) to 30 in 2012. It is chosen to illustrate a strong subduction period.

Following the discussion in Da Costa et al. (2005) and *Courtois et al.* (2018) the subduction rate S is defined as:

$$S(\sigma) = \frac{-1}{\tau} \int_0^\tau \int_{A_\sigma} [W_b + \frac{\partial h}{\partial t} + \vec{v} \cdot \nabla h] dA_\sigma dt \quad (3.1)$$

where $S(\sigma)$ is the net subduction, τ is 1 year and dA_σ is the element surface outcrop area associated with $A_\sigma = [x : \sigma \leq \sigma_h(x, t) < \sigma + \delta\sigma]$ with σ_h the instantaneous mixed layer density, $\mathbf{x} \equiv (x, y)$ are the horizontal coordinates, t is time, h is the MLD, v is the velocity and σ and $(\sigma + \delta\sigma)$ represents the density of neighbouring isopycnals. A major advantage of this method is that it considers the three main ways in which a parcel of water can leave or enter the mixed layer (ML): W_b represents the vertical velocity at the base of the ML, $\frac{\partial h}{\partial t}$ represents the changes in time of the ML thickness and $(\vec{v} \cdot \nabla h)$ the horizontal advection across the sloping base of the ML.

W_b is not extracted directly from the model output but instead is computed according to Huang (2010) where:

$$W_b = W_e - \frac{\beta}{f} \int_{-h}^0 v dz \quad (3.2)$$

Following Huang (2010), W_b is the contribution to the net subduction due to vertical pumping at the base of the mixed layer, which is slightly smaller than the Ekman pumping rate (W_e) due to the geostrophic flow ($\frac{\beta}{f} \int_{-h}^0 v dz$) in the mixed layer. Accordingly, W_e is computed as the divergence between the meridional (τ^y) and zonal (τ^x) wind stress, both given by the atmospheric forcing. The second term in Eq. (2), $\frac{\beta}{f} \int_{-h}^0 v dz$, is computed by integrating v over the mixed layer. $\beta = \frac{\partial f}{\partial y}$ and f is the Coriolis parameter.

Two density classes were considered for computing the subduction rate. Following Stramma et al. (2004), Kieke et al. (2006) defined Upper Labrador Sea Water (ULSW) and deeper Labrador Sea Water (LSW) to fall into the density range $\sigma_\theta = 27.68 - 27.74 \text{ kg/m}^3$ and $\sigma_\theta = 27.74 - 27.80 \text{ kg/m}^3$, respectively. In this paper, following both studies we define ULSW in the same density range. In the case of deeper LSW we define it as a water mass in the density range $\sigma_\theta = 27.74 - 27.82 \text{ kg/m}^3$ as *Courtois et al.* (2018) (see their manuscript for more details). Numerical simulation salinity drift in this region is a known problem (e.g.,

Rattan et al., 2010). Thus, simulated density tends to increase as the time evolves. For this reason an additional water mass is considered: a water mass with a fixed density range from $\sigma_\theta = 27.82 - 27.92 \text{ kg/m}^3$, which will be referenced as Modelled Labrador Sea Water (MLSW). However, not all the simulations show subduction occurring within such density range. In fact the *Control* simulation shows no subduction occurring at the MLSW density range.

By default in NEMO, the MLD is calculated using a density difference criterion of 0.01 kg/m^3 . As explained in Courtois et al. (tted), the MLD computed this way is over-estimated during strong deep convection events due to temperature-salinity compensation. Given the dependence of the kinematic approach on the MLD, we defined and computed MLD as explained in Courtois et al. (tted) (Figure 3.2.c for *Control* - MLD). Therein, the MLD is estimated based on the intersection of two linear fittings, one defined by the mixed layer and the other one by the slope of the underneath layer, for both potential temperature and salinity.

3.4 Results

In this section we will describe the results from the different perturbation experiments. The order of presentation will be as follows: *SPG12*, *GMR*, *Filtered* and finally *PD*. For each of the experiments the monthly mean subduction, seasonal mean subduction, averaged March MLD, mean total subduction and the averaged subduction components will be described for the period 2004-2016.

3.4.1 Changing the Horizontal Resolution (SPG12 Experiment)

Monthly average subduction time series together with the maximum model MLD were plotted to investigate the evolution of the subduction during the study period and its relation with the MLD (Figure 3.4). It is worth noting that the time series in Figure 3.4 appear to be interrupted, most of the time at the beginning of each year. This occurs when entrainment and detrainment cancel each other resulting in no net subduction. In any case, the seasonality of the subduction is well represented. As the MLD deepens the water that once was beneath the mixed layer enters it and gets mixed with the ambient waters and thus ventilated. This process is followed by the subduction (positive values), in late winter or early spring (late

March to the end of April), as the MLD starts to shallow from its late winter maximum (Holte and Straneo, 2017). Under these circumstances the water within the mixed layer leaves it and gets again trapped underneath its base.

In *Control* (Figure 3.4.a) the subduction values are between 0.2 and 6.5 Sv. Three maxima occur: the first one (~ 2.5 Sv) in 2008 in the density class of deeper LSW (1 Sv at the ULSW density class); the second one in 2012, in this case in both density classes, ULSW and deeper LSW, with values of ~ 2.6 Sv and ~ 2.5 Sv respectively and the third one in 2016, with the subduction rate reaching 6.5 Sv in the density class of deeper LSW (and 0.5 Sv at ULSW). These years (2008, 2012 and 2016) coincide with observations of strong convection in the Labrador Sea (Yashayaev and Loder, 2017). During the years 2014 and 2015 the subduction was not as pronounced as during 2012 even though they were years of strong convection. However, strong convection does not mean that subduction will occur. Convection can broadly be described as a strong mixing of the water column involving downward and upward movement of fluid within the MLD, while subduction refers only to the net downward movement of fluid beneath the MLD. Nevertheless during these years LSW was most likely building up, resulting in 6.5 Sv of deeper LSW being subducted in 2016.

In *SPG12* (Figure 3.4.b) the values of subduction are in general smaller than those in *Control*. The annual evolution of subduction in *SPG12* also shows three noticeable maxima. As in *Control*, the first one occurs in 2008 at the density class of deeper LSW, with a value of 1.52 Sv, and 1 Sv at ULSW. The second one in 2012, with 2.5 Sv at deeper LSW, and 1 Sv at ULSW. The third one occurs in 2016 with a subduction rate of 1.75 Sv at the deeper LSW and 0.25 Sv at ULSW.

In *SPG12* from 2014 onward some subduction occurs at the density range of MLSW. Comparing the values of subduction for the deeper LSW class in *SPG12* with those from *Control* we find that, for *SPG12* in 2008 the subduction rate decreases by 39%, no differences are shown in 2012, while in 2016 it decreases by 73%. As for the ULSW in *SPG12*: no differences are found in 2008, and it decreases by 62% and 50% in 2012 and 2016 respectively.

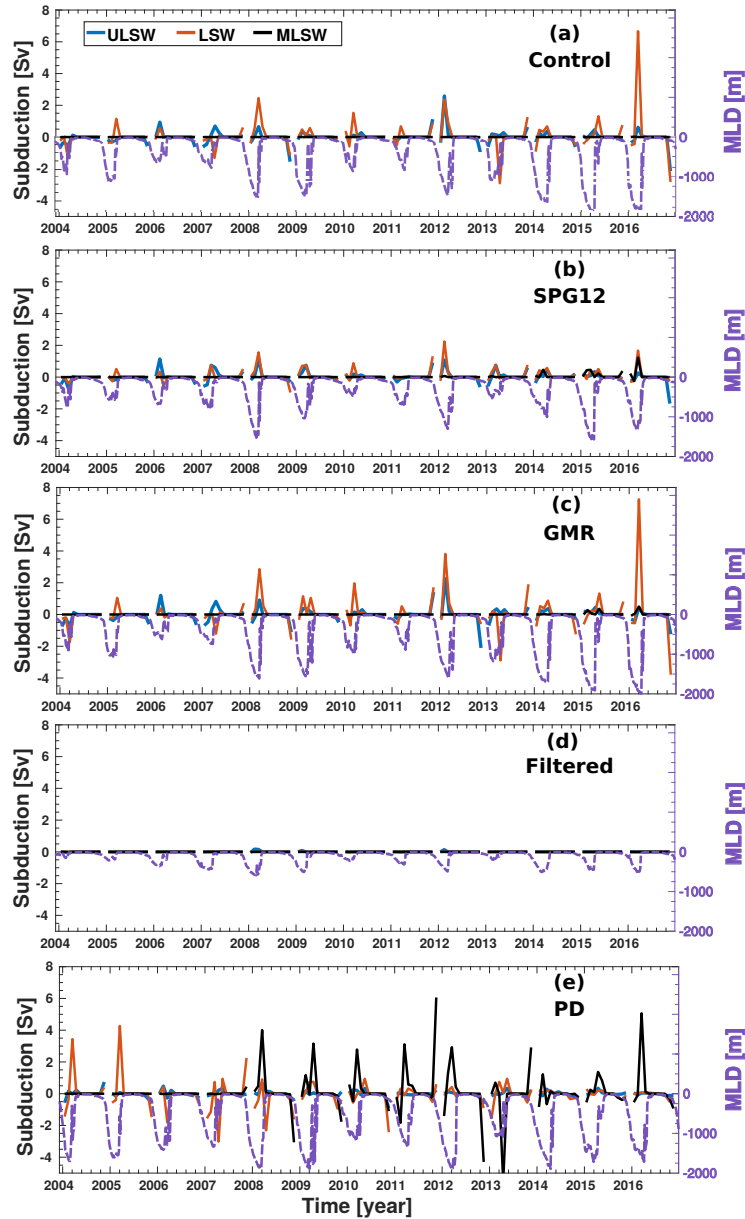


Figure 3.4: Monthly subduction and obduction rates (in Sverdrup), from January 2004 to December 2016, considering the density ranges of ULSW (Class1: blue), deeper LSW (Class 2: orange) and model LSW (Class 3: black). Shown are the simulations: (a) *Control*, (b) *SPG12*, (c) *GMR*, (d) *Filtered*, and (e) *PD*. Maximum model MLD (dashed purple lines) for each simulation appears overlaid on the subduction time series.

A seasonal decomposition of subduction for the *SPG12* and *Control* allows a closer inspection of the process by density ranges (Figure 3.5.a and 3.5.c). The subduction rates (positive) were averaged over two different periods: the re-stratification period (summer), from the beginning of April to the end of September, and the period when the mixed layer is deepening

from the beginning of October to the end of following-year March, from 2004 to 2016. Both simulations show subduction occurring in the summer period (Figure 3.5.a) which is when the MLD shallows and water gets transferred below the MLD base. In *Control* (Figure 3.5.a, blue line) the subduction goes up to a maximum of ~ 2.3 Sv, while for *SPG12* the maximum is around ~ 1.2 Sv. Both the summer and winter subduction decrease with increased resolution. Both maxima occur at the density range corresponding to deeper LSW. On average, when the resolution is increased over the subpolar gyre, the seasonal subduction rate in the Labrador Sea decreases by around 48%.

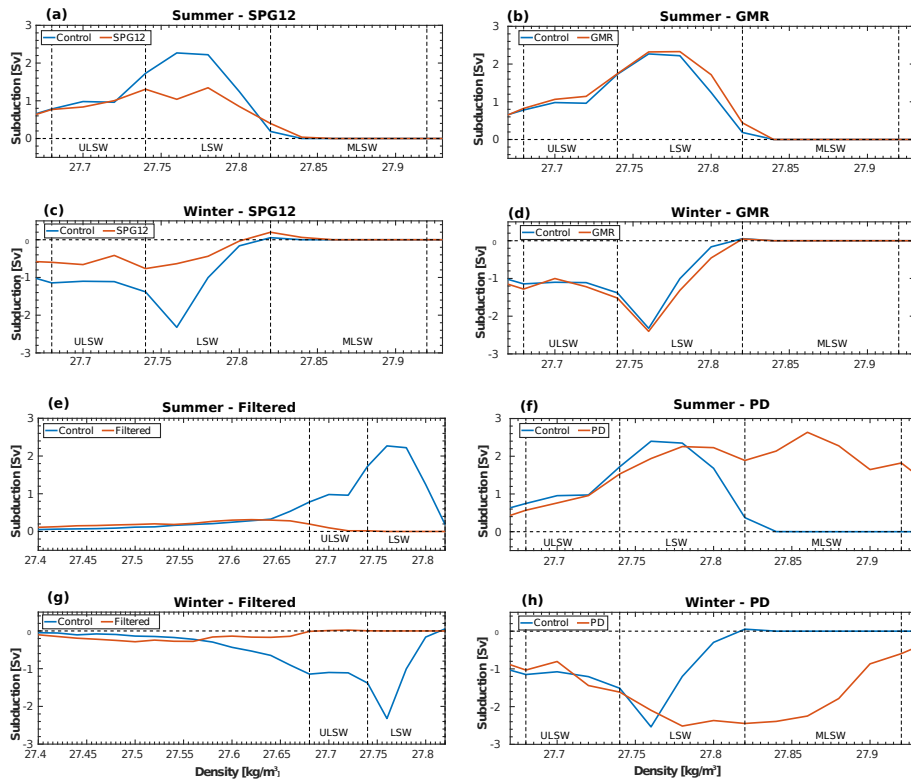


Figure 3.5: Averaged seasonal subduction and obduction rates as a function of the potential density, for each of the perturbation experiments compared to *Control*: (a, c) *SPG12*, (b, d) *GMR*, (e, g) *Filtered* and (f, h) *PD*. In all the cases the *Control* simulation appears in blue, while the perturbation (depending on the experiment) appears in orange. The **Summer** season is defined as the period from April to September, while the **Winter** season goes from October to March.

Even when the subduction is more prominent during the summer period, there is some subduction occurring in the winter period (Figure 3.5.c). This is more pronounced in the *SPG12* simulation where the subduction reaches 0.2 Sv at the interface between ULSW and deeper

LSW density classes. In the case of the *Control* simulation (Figure 3.5.c), the subduction does not even reach 0.1 Sv. The difference in the subduction magnitude found between *Control* and *SPG12* can be explained by considering how the MLD varies from one simulation to the other. Figures 3.6.a and 3.6.b show the March averaged MLD over the Labrador Sea, from 2004 to 2016, for *Control* and *SPG12* respectively. By increasing the spatial resolution not just the maximum depth of the ML decreases by around 17%, but also the area where the ML is deeper than 1000 m is reduced.

This could indicate an increase, due to increasing the resolution, in IR and BCE which would transport Irminger Water into the Labrador Sea interior. IR have warm and saline Irminger Water cores between 200 and 1000 m and low-salinity cores above 200 m. Indeed, Figure 3.7 shows higher transport of Irminger water (Figure 3.7.a) and freshwater (Figure 3.7.b) from the WGC directly into our study region, in *SPG12* compared to *Control*. A larger thermal forcing component (heat loss only in this case) of the buoyancy fluxes (Figure 3.7.c) in *SPG12* especially in fall and winter appears to follow the larger advection of Irminger Water in this simulation compared to *Control*.

Given their cold and fresh caps, mostly observed during spring (and also captured in *SPG12*: Figure 3.7.b), IR are known to be an important source of freshwater to the Labrador Sea contributing significantly to the rapid restratification of basin interior following wintertime deep convection (*Hátún et al.*, 2007; Gelderloos et al., 2011; de Jong et al., 2014). *Hátún et al.* (2007) observed and described IR spawned from the WGC as they entered the Labrador Sea interior by using high-resolution autonomous Seaglider hydrography and satellite altimetry. They suggested that the trajectory followed by these eddies keep the observed region of deep convection to be small and not spatially the same as where the atmospheric wintertime cooling is most intense. This would explain the smaller convection region found in *SPG12* compared to *Control*. BCE and CE are also known to play an important role in extracting heat from the boundary current system and transport it to the interior of the basin (Chanut et al., 2008). During deep convection all three types of eddies would strengthen the stratification throughout the water column, shallowing the MLD and limiting the LSW production. As the subduction calculations are highly dependent on the MLD, seasonal changes in the MLD are also reflected in the seasonality of the subduction.

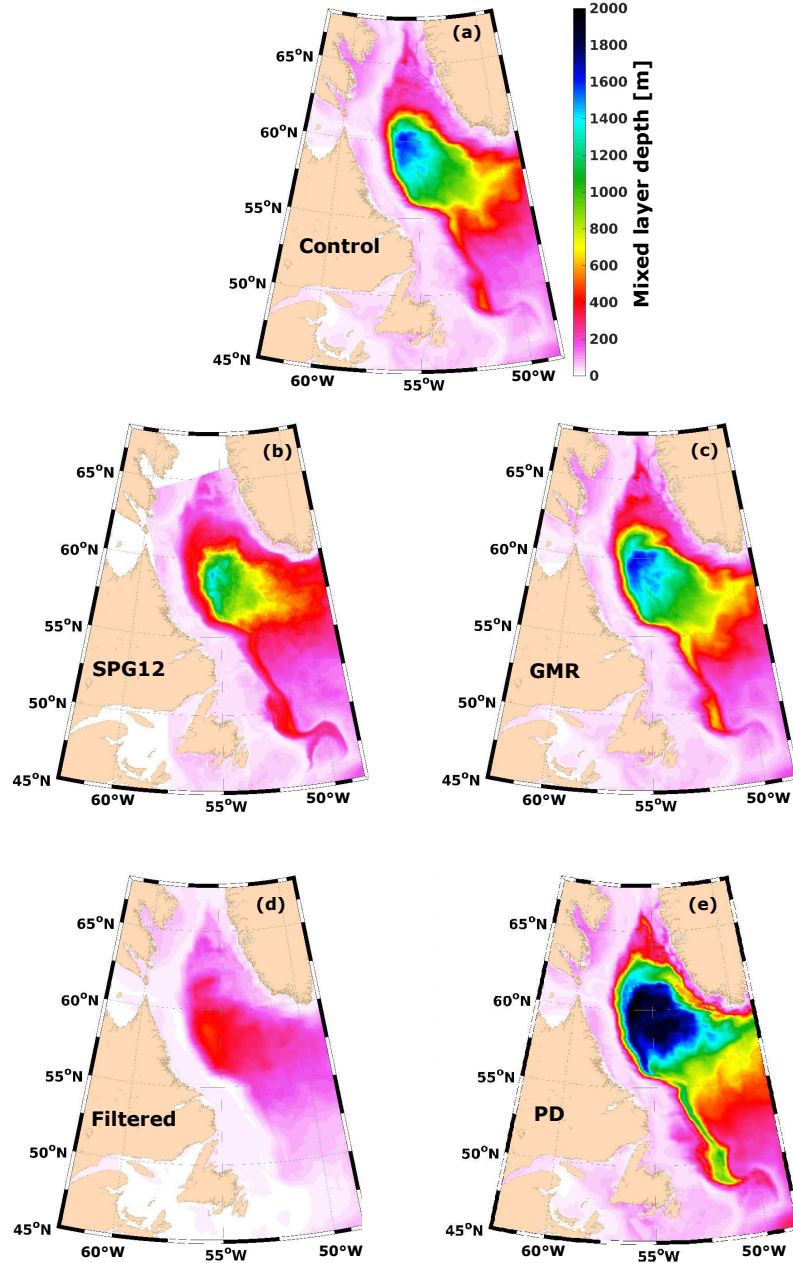


Figure 3.6: March mixed layer depths (MLD) in the Labrador Sea, averaged over the years 2004 to 2016, for (a) *Control*, (b) *SPG12*, (c) *GMR*, (d) *Filtered* and (e) *PD*. For *SPG12* (b) no MLD values are shown outside the high resolution nest (region in white).

Figure 3.8.a compares the mean total subduction rate as a function of the potential density for *SPG12* with respect to *Control*, from 2004 to 2016. Different from Figure 3.4, Figure 3.8 comprises both seasons which allows us to determine an annual formation rate. For both simulations the maximum subduction rate, with values of 1.85 and 1.1 Sv for *Control* and *SPG12* respectively, occurs at the density class corresponding to the deeper LSW. This represents a

19% decrease in the net mean subduction rate when the resolution increases. This decrease is explained by analysing all the components that impact on the net subduction rate (Eq. 3.1).

Figure 3.9.a and Figure 3.9.b show the components of the net subduction rate (3.1) as a function of the potential density, averaged from 2004 to 2016, for *Control* and *SPG12* respectively. The vertical component W_b (teal), has almost no contribution to the net subduction in both simulations. A significant term in both simulations is $\frac{\partial h}{\partial t}$ (green), which represents the change in time of the MLD. For *Control* and *SPG12* the term reaches a maximum value of 1.4 Sv and 0.6 Sv respectively, being 57% higher in *Control*. This is consistent with the average March MLD, which is deeper in *Control*. For both simulations $\frac{\partial h}{\partial t}$ is maximum at the density range of the deeper LSW.

The advective term $\vec{v} \cdot \nabla h$ (red) is larger (by 33%) at the density range of deeper LSW in *Control* relative to *SPG12*. In *Control* it reaches 0.6 Sv while in *SPG12* it reaches 0.4 Sv. However, the advective term in *SPG12* is larger at the density ranges of ULSW and MLSW, resulting in subduction values of $\simeq 0.25$ Sv and $\simeq 0.75$ Sv, respectively (Figure 3.8.a). Meanwhile in *Control* subduction at those density ranges is much smaller or non-existent. Also in *SPG12* this term is positive for all three water masses defined, contributing to the subduction rate in every LSW layer, while it is not entirely positive in the *Control* simulation.

In *Control*, the sub-components of $\vec{v} \cdot \nabla h$ do not reach their maximum values in the same density range. $u \frac{\partial h}{\partial x}$ (blue) reaches a maximum value of 1.6 Sv at the interface between ULSW and deeper LSW density classes, while $v \frac{\partial h}{\partial y}$ (gray) is maximum in the density range of ULSW, reaching -2 Sv. This explains why $\vec{v} \cdot \nabla h$ in *Control* is negative in the density range of ULSW while it is predominantly positive in the density range of deeper LSW. In *SPG12*, $u \frac{\partial h}{\partial x}$ and $v \frac{\partial h}{\partial y}$ reach a maximum of 3.5 and -3.4 Sv, respectively.

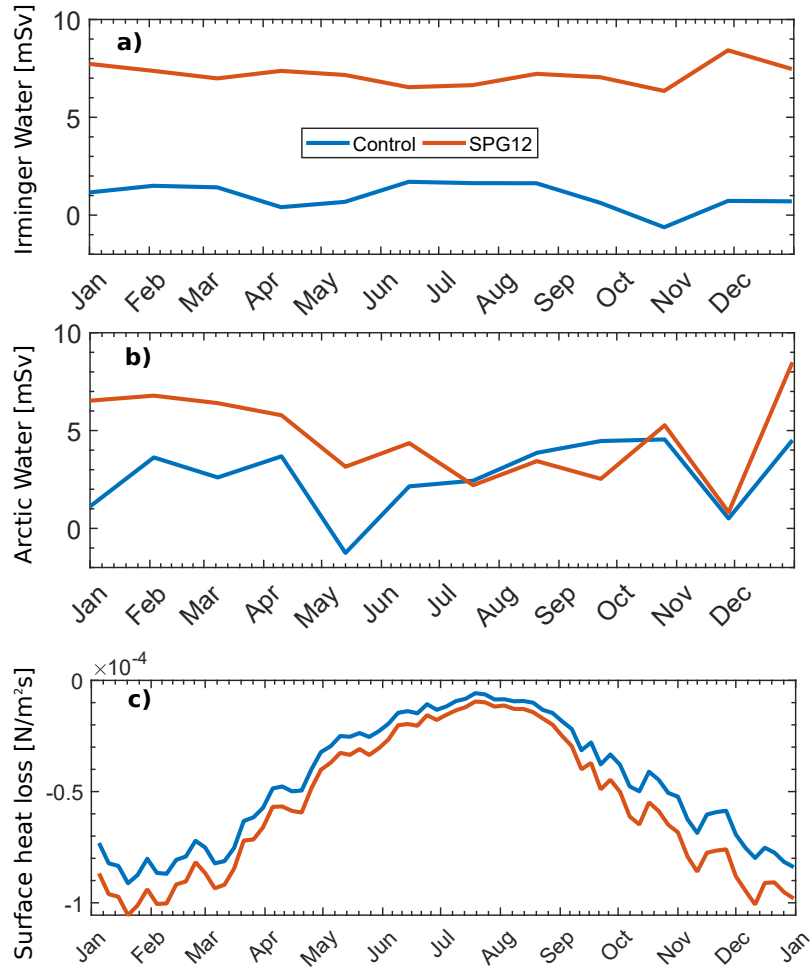


Figure 3.7: Climatology of (a) Irminger Water and (b) Arctic Water spawned out of the West Greenland Current into the study region in the Labrador Sea (Figure 3.3.b), for *Control* and *SPG12*. Arctic Water is defined as water fresher than 34.8 and lighter than $\sigma_{\theta}=27.68 \text{ kg/m}^3$. Irminger Water is defined as a watermass saltier than 34.8 and and lighter than $\sigma_{\theta}=27.68 \text{ kg/m}^3$ (our potential density minimum for ULSW). Panel c) shows the climatology for the thermal forcing component of the buoyancy fluxes for *Control* and *SPG12* (heat loss only in this case), in the same region as in (a) and (b).

3.4.2 Impact of Removing Greenland Freshwater Discharge (GMR Experiment)

The perturbation experiment *GMR* serves to analyse the impact of runoff from GrIS. As the simulation *Control* was described in the previous section, we will proceed here to describe *GMR* and address the differences or similarities between them. Monthly subduction for this experiment is shown in Figures 3.4.a and 3.4.c, for *Control* and *GMR* respectively. In *GMR* the subduction values are in general larger in magnitude compared with the same events in

Control. As in *Control*, maximum subduction occurs for *GMR* during 2008, 2012 and 2016. The subduction rate in 2008 reaches a magnitude of 3 Sv at the density class of deeper LSW and 1 Sv at the range corresponding to ULSW. This represents an increase in the subduction rate of 20% at the density class of deeper LSW, with no changes occurring for the subduction at ULSW.

For 2012 the subduction rate in *GMR* reaches values of 4.5 and 2.5 Sv in the density range of deeper LSW and ULSW, respectively. This means that in 2012 the subduction increases by 80% for deeper LSW and it decreases by 4% for ULSW, with respect to *Control*. In 2016, the subduction rate reaches 7.5 Sv at the density class of deeper LSW, and 0.5 Sv at ULSW. This represents an increase (with respect to *Control*) in the subduction rate by 15% for deeper LSW, while no changes are found for ULSW. Without the presence of Greenland melt the LSW gets denser, with an increase in the formation of deeper LSW from 2008 to 2016. As in *SPG12* there is some subduction occurring in *GMR* at the density range of MLSW after 2015.

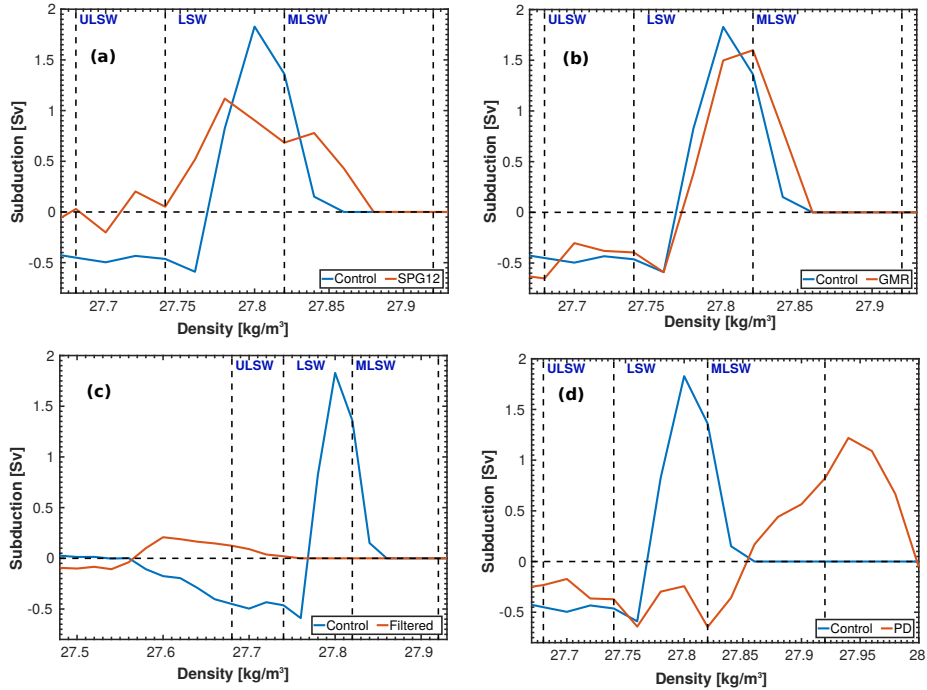


Figure 3.8: Mean total subduction rate as a function of the potential density. The average was done over the period 2004-2016 and for all the experiments. Each panel compares the *Control* simulations with its perturbations: (a) *SPG12*, (b) *GMR*, (c) *Filtered* and (d) *PD*. For each case *Control* appears in blue while the rest of the simulations, depending on the experiment, appears in orange. Notice that the x-axis in (c) and (d) are different in order to better represent the maximum subduction rate in *Filtered* and *PD*, respectively.

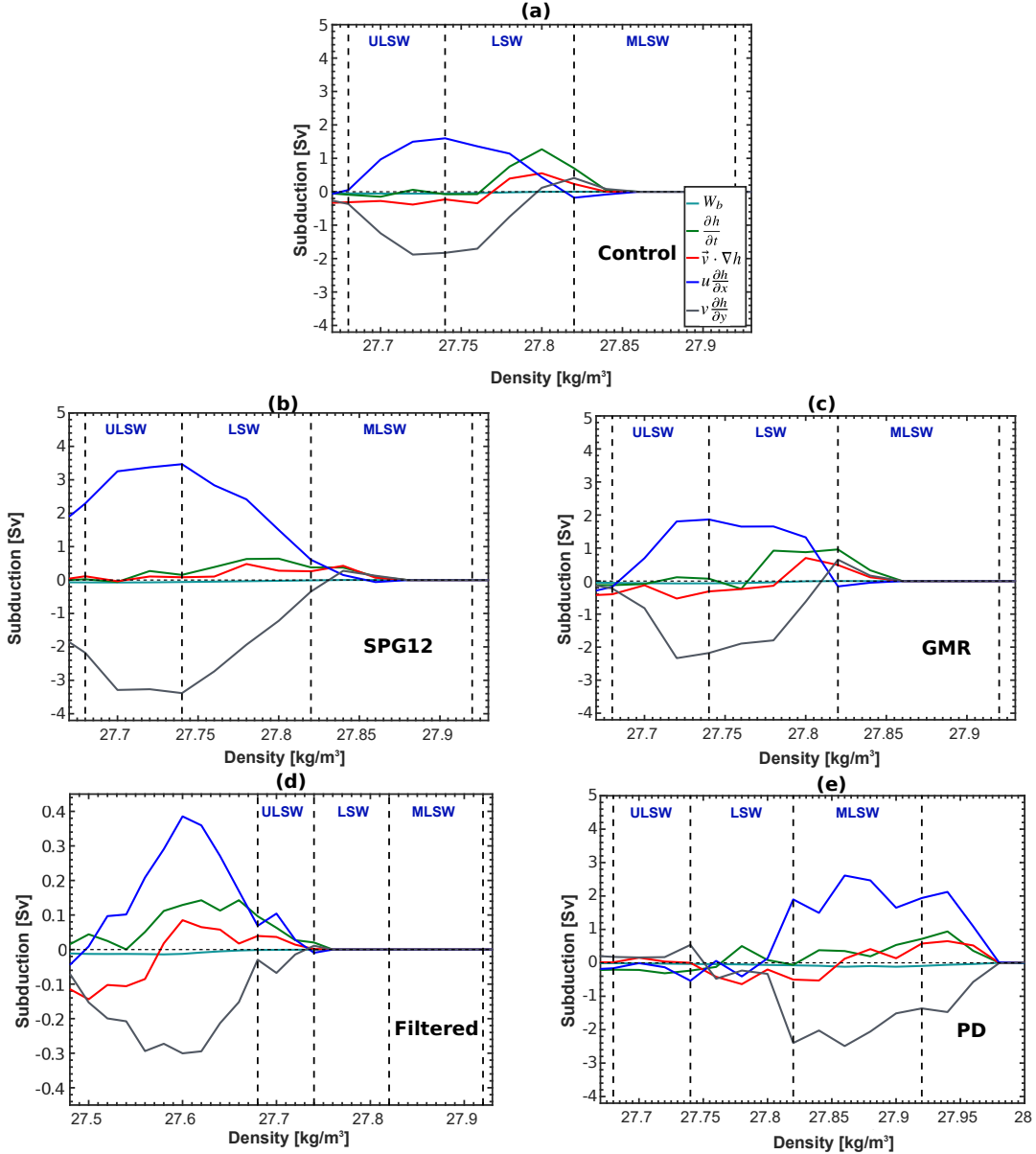


Figure 3.9: Time averaged subduction components (Eq. 3.1) as a function of the potential density. The average was done over the period 2004-2016 and for all the simulations: (a) *Control*, (b) *SPG12*, (c) *GMR*, (d) *Filtered* and (e) *PD*. Vertical velocity (W_b) is represented in teal, the change in time of the MLD ($\frac{\partial h}{\partial t}$) appears in green, components of the horizontal advection, $u \frac{\partial h}{\partial x}$ and $v \frac{\partial h}{\partial y}$, appear in blue and grey respectively, and the resultant horizontal advective term $\vec{v} \cdot \nabla h$ is represented in red. Please notice that for the cases of (d) and (e), *Filtered* and *PD* respectively, the x and y-axes are different compared to the other panels. This was done in order to better show the details of the components in each of the simulations.

The seasonality of the subduction for the *GMR* experiment is shown in Figure 3.5.b and 3.5.d. In the case of the summer subduction (Figure 3.5.b), the maximum rate occurs in both

simulations (*GMR* and *Control*) at the density of deeper LSW. The maximum rate for *GMR* is ~ 2.4 Sv, which is 4.3% larger than the 2.3 Sv reached in *Control*. During the winter season (Figure 3.5.d) both simulations show very little subduction occurring at the interface between deeper LSW and MLSW. The magnitude of the subduction in both cases is less than 0.1 Sv.

The averaged March MLD also responds to the presence, or in the case of the *GMR* experiment, the absence of Greenland melt. Comparing this simulation with *Control* we find that the maximum MLD (in *GMR*) is $\sim 5\%$ deeper than in *Control* (Figure 3.6.c). In *GMR* the area where the MLD is deepest also increases compared with *Control*. This difference in the MLD is clearly reflected in the summer subduction (mainly over the deeper LSW density class) which increases by 4.3% when the freshwater fluxes from the GrIS are not considered.

The mean net subduction rate for *GMR*, averaged from 2004 to 2016, is represented in Figure 3.8.b. While the maximum subduction in *Control* occurs in the deeper LSW density class, for *GMR* it occurs at the interface between deeper LSW and MLSW. This implies a density shift in the formation rate of LSW, being lighter in *Control* due to the influence of Greenland melt. Concerning the magnitude, there is a decrease in the subduction rate by 14% in *GMR* with respect to *Control* as the maximum subduction rate in *GMR* is ~ 1.6 Sv.

The components of the net subduction rate for *GMR* are shown in Figure 3.9.c. As in *Control*, the vertical component W_b (teal) in *GMR* has almost no contribution to the net subduction rate. The term $\frac{\partial h}{\partial t}$ (green) reaches 1 Sv (only 0.4 Sv smaller than *Control*) in the interface between deeper LSW and MLSW, denoting a shift in the density compared to *Control*. At the density of ULSW, $\frac{\partial h}{\partial t}$ is no larger than 0.2 Sv while it is around 0.9 Sv at the density of deeper LSW.

The advective term $\vec{v} \cdot \nabla h$ (red) in *GMR*, just like in *Control*, reaches its maximum of 0.6 Sv at the density of deeper LSW. By decomposing $\vec{v} \cdot \nabla h$ into $u \frac{\partial h}{\partial x}$ (blue) and $v \frac{\partial h}{\partial y}$ (grey), we notice that although their maximum values are higher than those in *Control*, their resultant component, $\vec{v} \cdot \nabla h$, is effectively lower than in *Control*. This results from the fact that $v \frac{\partial h}{\partial y}$ is larger in magnitude (-2.4 Sv) than $u \frac{\partial h}{\partial x}$ (1.8 Sv), reaching both their maxima at the density of ULSW. This is also why we notice that $\vec{v} \cdot \nabla h$ is negative at the density of ULSW, becoming positive at the density of 27.785 kg/m^3 .

3.4.3 Impact of High Frequency Atmospheric Phenomena (Filtered Experiment)

The *Filtered* experiment shows the important role of high frequency atmospheric phenomena in driving deep convection (e.g., Holdsworth and Myers, 2015). Monthly subduction for *Filtered* is shown in Figure 3.4.d, where the lack of subduction in *Filtered* shows the importance of the high frequency atmospheric phenomena. The maximum subduction in *Filtered* is ~ 0.18 Sv and occurs in 2008 at the density class corresponding to ULSW. This is 82% lower than that in *Control*. Besides 2008, there are only two other years where the subduction is different from zero: 2009 with a rate ~ 0.08 Sv and 2012 with a rate ~ 0.15 Sv, both at the density class of ULSW. Considering the same density class, the subduction in *Filtered* during the years 2009 and 2012, is 89% and 85% smaller than that in *Control*, respectively. No subduction events occur at the classes corresponding to deeper LSW and MLSW. So, even when in some years the ML reached 500 - 700 m depth there is little or no LSW formation at all.

The summer subduction for *Filtered* (Figure 3.5.e) reaches a maximum of ~ 0.4 Sv at 27.63 kg/m^3 , this is even lighter than ULSW. Compared with *Control*, this is 83% smaller in magnitude. There is no contribution at the ranges of deeper LSW and MLSW. Furthermore, in the case of the winter season (Figure 3.5.g), we find that no subduction occurs during this period. The maximum depth reached by the averaged March MLD for *Filtered* (Figure 3.6.d) is no deeper than 500 m. This is, on average, 1300 m (72%) shallower compared to *Control*. The mean total subduction rate (Figure 3.8.c) also decreases with filtered atmospheric forcing. The maximum subduction rate for *Filtered* occurs at a density class lighter than ULSW ($\sim 27.6 \text{ kg/m}^3$), and is no greater than 0.2 Sv.

Figure 3.9.d shows the components of the net subduction for *Filtered*, averaged from 2004 to 2016. In order to have a better representation of the components in *Filtered*, the y-axis as well as the x-axis do not have the same magnitude range compared to *Control*. In *Filtered* the maximum values for all the components are concentrated in the density range between $27.5 - 27.68 \text{ kg/m}^3$, lighter than ULSW. Just as in *Control*, almost no contribution comes from W_b (teal). The leading component is $\frac{\partial h}{\partial t}$ (green) and reaches 0.14 Sv. The advective term $\vec{v} \cdot \nabla h$ (red) is 0.08 Sv, 87% lower than in *Control*. By decomposing $\vec{v} \cdot \nabla h$ we see that both

sub-components reach their maximum values at $\sim 27.6 \text{ kg/m}^3$. $u \frac{\partial h}{\partial x}$ (blue) is 0.38 Sv while $v \frac{\partial h}{\partial y}$ reaches -0.3 Sv.

The shallow MLD and the low LSW formation rates appear to be a consequence of the 44% decrease in the oceanic heat loss in *Filtered* (Figure 3.10.b) with respect to *Control* (Figure 3.10.a). We present the month of January only as it is the one that shows the strongest heat loss in the Labrador Sea, thus a higher incidence of high frequency atmospheric phenomena. However, the overall statement of a decrease in the heat loss in *Filtered* is also valid for the other months.

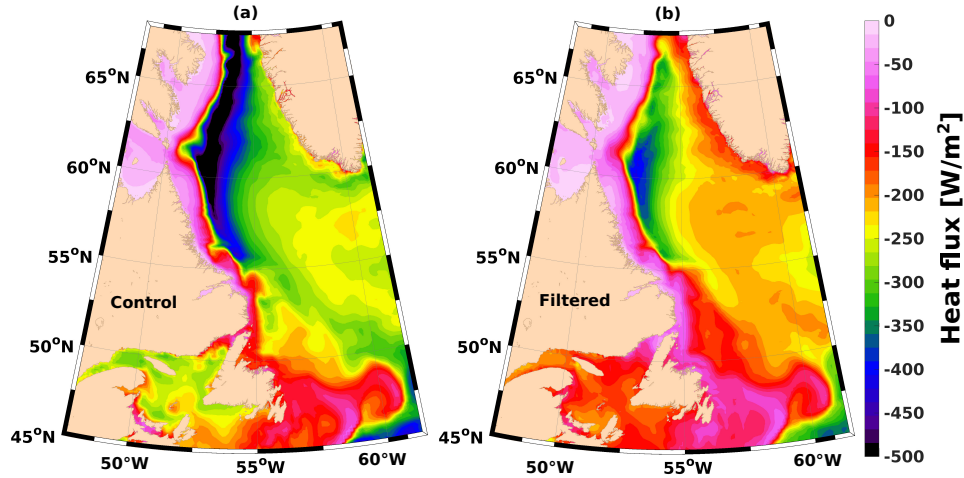


Figure 3.10: Averaged January heat flux (W/m^2) from 2004 to 2016 over the Labrador Sea, for (a) the *Control* and (b) the *Filtered* simulations.

3.4.4 Impact of Decreased Precipitation (PD Experiment)

Here we compare the simulations *Control* and *PD* to explore the sensitivity of the LSW formation rate to precipitation changes. Monthly subduction rates for *PD* are shown in Figure 3.4.e. Two noticeable maxima occur, one in 2012 with 6 Sv, and another in 2016 ~ 5 Sv. In both cases the subduction occurs at the density class of MLSW. In *Control* there is no subduction occurring at this density class. In *PD* after 2008 there is no more than 1 Sv of deeper LSW being subducted, while in the case of the ULSW this behaviour is not seen since the beginning of the time series. This indicates a transformation of the LSW into the denser water mass MLSW.

The averaged summer subduction rate for *PD* (Figure 3.5.f) reaches a maximum of 2.6 Sv

in the density range of MLSW. In the density range of ULSW both simulations, *Control* and *PD*, show the same tendency as well as similar magnitudes. In the density range of deeper LSW *PD* reaches 2.2 Sv, 8% smaller than *Control*. There is no subduction occurring during the winter period (Figure 3.5.h) for any of the water masses under study.

The average March MLD for the simulation *PD* (Figure 3.6.e) also shows the impact of a decrease in the precipitation. The maximum MLD for *PD* increases by 20%. The spatial distribution of the deepest MLD (2000 m) also increases in *PD*. Surprisingly, the net subduction does not show an increase (Figure 3.8.d). Instead the maximum subduction rate occurs at higher densities. Here, as in the *GMR*, the subduction rate decreases by 17% and shifts from 27.8 kg/m^3 (in *Control*) to 27.94 kg/m^3 (in *PD*). Nevertheless in *PD* the effect is more dramatic, as in *GMR* the freshwater anomaly occurs only around Greenland while in *PD* it is over the entire ANHA domain.

The subduction components for *PD* are shown in Figure 3.9.e. Compared to *Control*, the largest amplitudes of each of the terms are found at larger densities. The term $\frac{\partial h}{\partial t}$ has its maximum of 1 Sv at 27.85 kg/m^3 . This is actually denser than MLSW and 29% decrease with respect to *Control*.

$\vec{v} \cdot \nabla h$ on the other hand is maximum in the density of MLSW and it reaches 0.6 Sv, similar (in magnitude only) to *Control*. When decomposing $\vec{v} \cdot \nabla h$ we find that both components are maximum in the density of MLSW. $u \frac{\partial h}{\partial x}$ goes up to 2.6 Sv, while $v \frac{\partial h}{\partial y}$ reaches -2.8 Sv. Comparing them with the same terms in *Control* we found that in *PD* the advective terms gain in magnitude but their resultant ($\vec{v} \cdot \nabla h$) is actually smaller than in *Control*. The increase in the advective terms in *PD* is given by the increase in the horizontal density gradients.

3.5 Discussion and Conclusions

We have explored the sensitivity of subduction in the Labrador Sea to changes in spatial model resolution, Greenland freshwater discharge, high frequency atmospheric forcing and precipitation. A control and four perturbations experiments were implemented by using a coupled ocean-sea ice model, with an eddy permitting regional configuration and an hourly atmospheric forcing. LSW formation rates were determined using a kinematic subduction

approach. The study considered the period from January 1st, 2004 to December 31st, 2016.

Table 3.3: Magnitude of the components in Eq.1 and maximum 2004-2016 mean subduction rate, for the five simulations used in the sensitivity experiments. As there is almost no contribution from W_b to the maximum subduction rate, it was excluded from the table.

Simulation Name	$\frac{\partial h}{\partial t}$	$\vec{v} \cdot \nabla h$	Maximum subduction rate	Density of maximum subduction
<i>Control</i>	1.4 Sv	0.6 Sv	1.85 Sv	deeper LSW
<i>SPG12</i>	0.6 Sv	0.4 Sv	1.1 Sv	deeper LSW
<i>GMR</i>	1 Sv	0.6 Sv	1.6 Sv	27.82 kg/m ³
<i>Filtered</i>	0.14 Sv	0.1 Sv	0.2 Sv	27.6 kg/m ³
<i>PD</i>	1 Sv	0.6 Sv	1.25 Sv	27.94 kg/m ³

Our *Control* simulation showed a maximum subduction rate of 1.85 Sv (Table 3.3) in the density class of deeper LSW (Figure 3.8.a). Deep convection events that occurred during 2008, 2012 and 2016 (Yashayaev and Loder, 2017) were captured by *Control* (Figure 3.4.a). During 2008, 1 Sv and 2.5 Sv of ULSW and deeper LSW respectively, were formed (Figure 3.4.a). In the year 2012, 2.6 Sv and 2.5 Sv of ULSW and deeper LSW respectively, were formed (Figure 3.4.a). The model convection event in 2016 resulted in formation rates of 0.5 Sv and 6.5 Sv of ULSW and deeper LSW respectively (Figure 3.4.a). These numbers are within the range of previous studies, some of them summarized in Figure 3.1.b.

As part of a study on recurrent replacement of Labrador Sea Water, Yashayaev and Loder (2016) roughly estimated potential export rates of LSW. They did this by looking at winter to fall LSW disappearance rates, based on computing the area within the 550 m thickness contour of LSW. They indicated that their approach made a number of assumptions and likely overestimated the LSW export - which may or may not be directly tied to LSW production. Still, their analysis concluded that annual LSW export was 8.9 ± 1 Sv in strong convection year, and 3.2 ± 1 Sv in weak convection years. Given more years of weak convection than strong convection over our study period (Yashayaev and Loder, 2016), our long term mean estimate of 1.85 Sv in the density range of deeper LSW is not unreasonable. Furthermore,

our largest formation rate, of 7 Sv (0.5 Sv ULSW and 6.5 Sv deeper LSW), in 2016, is not inconsistent with Yashayaev and Loder (2016)'s estimate for strong convection years. We also note that Yashayaev and Loder (2017) point out that LSW newly formed in 2017 is the deepest, densest and most voluminous since the mid-1990s.

We found that by increasing the resolution over the subpolar gyre, even when the advective terms produce more LSW, the LSW formation rate decreased in magnitude (Figure 3.8.a). This was mostly due to shallower MLD and a decrease in the area of the deep convection in *SPG12* compared to *Control* (Figures 3.6.a and 3.6.b).

During deep convection events, strong density differences between the convective region and the ambient stratified waters induce baroclinic instability which breaks up into convective eddies (\sim diameter of 20-30 km). The convective eddies mix the upper part of the water column while the main part of the dense water sinks to its density level spreading later along isopycnals (see, e.g., Lilly et al., 2003; Chanut et al., 2008). These eddies together with boundary current eddies are thought to reduce the depth of the convective events (Jones and Marshall, 1993, 1997) as they are very effective at transporting heat and freshwater into the convective patch playing a major role in the early stages of re-stratification throughout the patch. Recently Kawasaki and Hasumi (2014) explored in a modelling study the importance of eddy-induced near surface freshwater transport for inhibiting deep convection. They concluded that lateral buoyancy transport caused by heat is actually significantly larger than that from freshwater, with the later contributing mainly to the near the surface buoyancy transport only in the northern Labrador Sea. Their results, however, might be impacted by the absence of Greenland melt in their model. The freshwater advected into the Labrador Sea interior from the WGC mainly originated from the Arctic Ocean and runoff from the south-east GrIS (Guillard et al., prep) and was transported south by the East Greenland Current. Failing to include Greenland melt in their model might explain why the upper 100 m freshwater thickness in their model is half of the observational estimates (Khatiwala et al., 2002).

Nevertheless, such processes potentially explain the averaged March MLD being shallower in *SPG12* than in *Control*. There is actually more freshwater being advected into the study region in *SPG12* (Figure 3.11.b) possibly due to an increase in IR and BCE. This is not the case, however, for heat advection (Figure 3.11.a) which is three orders of magnitude larger in

Control. This leads to the buoyancy fluxes being larger, especially in winter and fall (Figure 3.11.c), when $1/4^\circ$ is used.

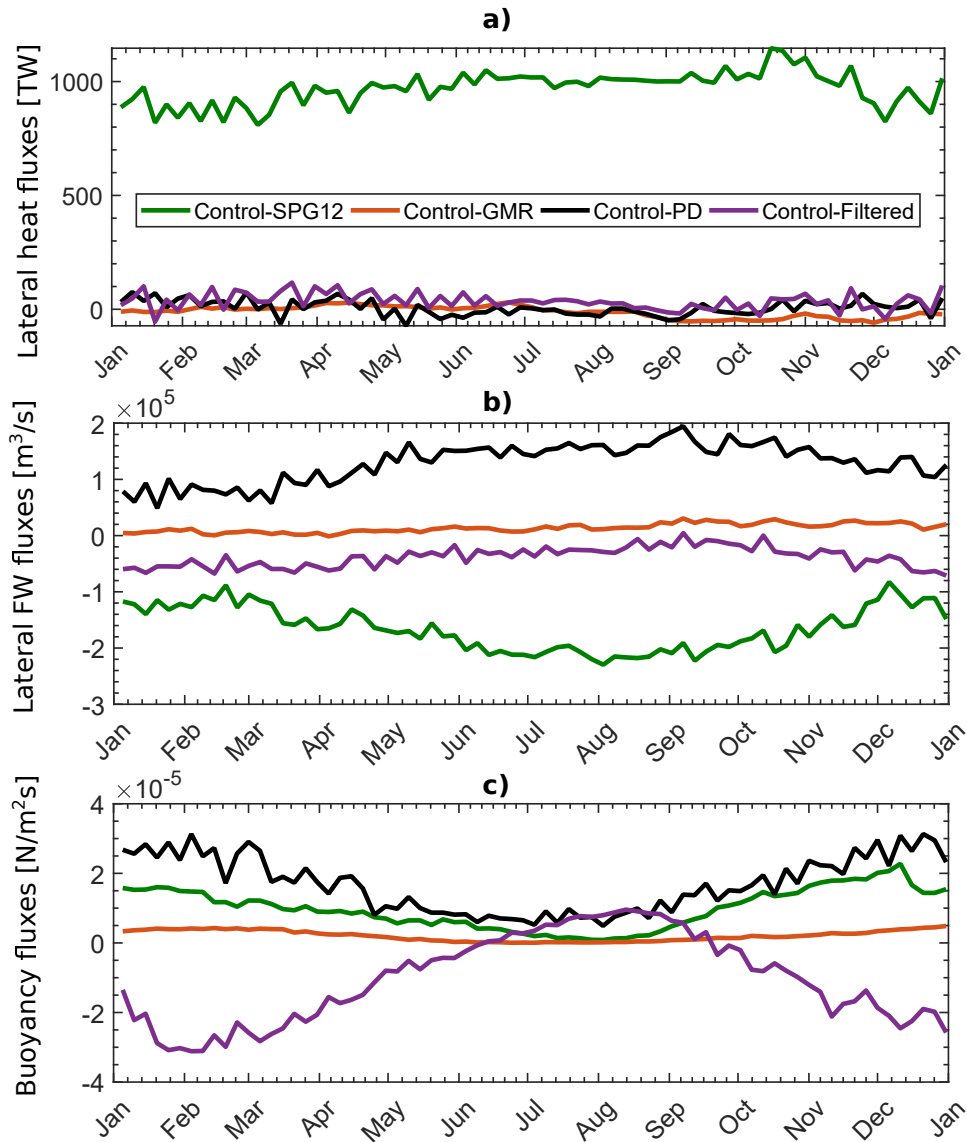


Figure 3.11: Climatological differences between *Control* and the perturbation experiments in the study region (black contour in Figure 3.3.b), for lateral (a) heat and (b) freshwater fluxes and (c) buoyancy fluxes. Positive values indicate that the magnitude of the field is larger in *Control* and vice versa.

The typical horizontal resolution of the numerical models used in the assessment reports of the Intergovernmental Panel on Climate Change (IPCC) is roughly 1° to 2° for the atmospheric component and around 1° for the ocean (Flato et al., 2013). Our results suggest that the use of ocean numerical models with coarse horizontal resolution results in LSW formation larger

compared with estimates from numerical models with higher horizontal resolution. Thankfully, the upcoming CMIP6 (Overview of the Coupled Model Intercomparison Project Phase 6) will have $1/4^\circ$ degree for the ocean as the norm (Eyring et al., 2016). Nevertheless, the implications for coupled models is unproven, and highly depends on atmosphere-ocean feedbacks, which are neglected in this study. At the same time different outcomes may result when high resolution forcing fields (rather than interpolated low resolution fields) were considered.

We found that the presence of Greenland melt affects mainly the formation of denser LSW. The formation of LSW at a density of 27.82 kg/m^3 (in *GMR*), decreased by 14% when no Greenland melt is present, while there is more LSW been formed at a density of 27.8 kg/m^3 (*Control*) when freshwater fluxes from GrIS are considered (Figure 3.8.b). However, our results indicate that the current trend in freshwater discharge from GrIS (Bamber et al., 2012) has not been followed by a decrease in the overall LSW formation rate. Also the maximum MLD was not found to be greatly impacted by the presence of Greenland melt (Figure 3.4.a and 3.4.c). At the same time *Control* and *GMR* hold very little differences concerning lateral heat and freshwater and buoyancy fluxes (Figures 3.11.a - 3.11.c)

In order to test if the integration time of the Greenland melt was actually an issue when looking at its influence on the LSW formation rate, the *Control* simulation was re-run from 2017 to 2030 using the same forcing that was used to run the period 2002 to 2016. Basically, the extended run (2017 to 2030) can be treated as a simulation over the period 2002 to 2016 but with a much longer adjustment. Figure 3.12 shows the formation rate for the two different periods: 2004 to 2016 and 2019 to 2030 (2004 to 2016 with a longer adjustment period) for the *Control* simulation. By increasing the adjustment period the formation rate does not decrease, as might be expected as the Greenland melt water increases within the Labrador Sea. Instead the LSW formation rate increases without changes in the density of the maximum subduction rate.

The use of a $1/4^\circ$ configuration might also be seen as a limitation for the *GMR* experiment given the poor representation of the eddy fluxes. By using the Parallel Ocean Program (POP) in two configurations, with horizontal resolutions of 1° and 0.1° , respectively, Weijer et al. (2012) explored the AMOC sensitivity to enhanced freshwater input from GrIS. They found that a reduction in wintertime convection (and the AMOC decline) is markedly more gradual

and persistent in the 0.1° configuration. *den Toom et al. (2014)* used the same two configurations as in *Weijer et al. (2012)* to investigate the impact of the AMOC reduction on the freshwater advection in the North Atlantic. They also found a shallowing of the MLD in the Labrador Sea as a result of a 0.5 Sv freshwater perturbation from GrIS in the strongly eddying configuration. However, the freshwater fluxes from GrIS implemented in their experiments is "a worst case scenario" compared to a "catastrophic collapse" of the GrIS (0.1 Sv and 0.5 Sv). These simulations should not be considered as a realistic scenario for present-day climate change which is the case of our study, where more realistic freshwater fluxes from the GrIS are considered. *Böning et al. (2016)* explored the impact of Greenland melt on deepwater formation in the North Atlantic Ocean by implementing a two-way nest over the polar/sub-polar regions, increasing the resolution from $1/4^\circ$ to $1/20^\circ$ (VIKING20). As in our study, they used *Bamber et al. (2012)* to represent the freshwater fluxes from the GrIS. They found that the accumulation of freshwater from GrIS so far has not been (yet) significant enough to impact the freshwater budget of the subpolar North Atlantic. In agreement with our results, they argued that the influence of meltwaters affects mainly the formation of the denser LSW. They pointed out that the dynamical implications given the decrease in the replenishment of the denser LSW might not be noticeable in less than a decade, in which case they might not emerge within the time frame of our study. The agreement between their findings and ours might make one think that a correct representation of freshwater fluxes from the GrIS is as important as the model horizontal resolution.

The experiment *PD* showed a similar behaviour as the one from the *GMR* experiment. When a decrease in the precipitation was not considered (in *Control*) the LSW formed was effectively lighter, reaching a subduction maximum at 27.8 kg/m^3 , while when the precipitation was reduced the subduction was maximum at 27.94 kg/m^3 . This transformation was as a result of a decrease in freshwater advection and hence buoyancy fluxes in *GMR* over the study region (Figure 3.11.b and 3.11.c).

Our results suggest that an increased in the precipitation would impact mainly the replenishment of the denser LSW (Figure 3.8.d). As in the *GMR* experiment, the increase in freshwater fluxes from precipitation did not impact greatly the maximum MLD in the Labrador Sea (Figure 3.4.e)

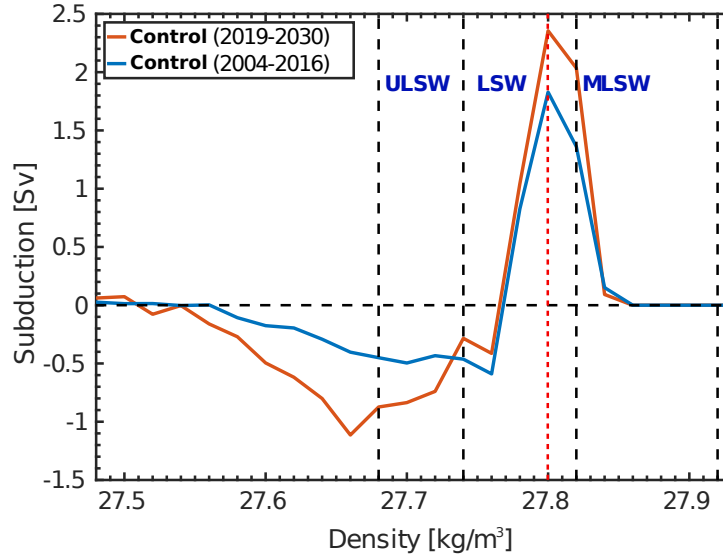


Figure 3.12: Mean total subduction rate as a function of the potential density for the *Control* simulation with different adjustment periods: 2004-2016 with 2 years of adjustment (blue) and 2019-2030 with 18 years of adjustment (orange). Red dashed line marks the density of the maximum subduction rate for both cases.

Myers and Donnelly (2008) found an increase of $P - E$ (Precipitation minus Evaporation) in the mid-1970s. Similar to the freshening investigated here for the experiments *GMR* and *PD*, they suggest that the increase must have played some role in causing freshening in the Labrador Sea. Freshwater accumulation at the ocean surface is known to increase the water column stratification making it more difficult for deep convection to occur (Dickson et al., 1988). During the last five decades GrIS has undergone significant mass loss (Bamber et al., 2012; van Angelen et al., 2013; Velicogna et al., 2014; Forsberg et al., 2017) with the consequent enhanced contribution of freshwater to the ocean. Future precipitation increases as a result of an intensification of the global water cycle (Wang et al., 2017; Huntington, 2006), are one of the warming-induced hydrological changes. As temperature and water holding capacity of the atmosphere increases, so will the precipitation. This means that warmer climates will irreparably lead to more intense precipitation events (Wang et al., 2017), potentially impacting the winter deep convection in the Labrador Sea.

However, regardless of the warming-induced changes seen so far (e.g., Greenland melt increase), there has been a progressive deepening in the observed convection in the Labrador Sea since 2012, and $LSW_{2012-2016}$ is one of the deepest ever observed back to 1983 (Yashayaev

and Loder, 2017). Our results show that, within the 12 years that our study spans, an increase in either precipitation or Greenland melt in the Labrador Sea, are not likely to decrease the overall LSW formation rate or the maximum convection depth. It would however decrease the formation of denser LSW which, by affecting the large scale density gradients, would have longer-term dynamic implications. In fact, we could speculate that, an increase in freshwater fluxes from GrIS or due to an increase in the precipitation over the mid-latitudes, would most likely impact the AMOC due to a decrease in the replenishment of denser LSW, rather than due to a decrease in the depth of the convection. These implications however, cannot be further seen in our analysis as they are not likely to emerge within the 12 years of our study (Böning et al., 2016).

High frequency atmospheric phenomena, like polar lows and cold-air outbreaks, are projected to decrease in the twenty-first century (Zahn and von Storch, 2010b; Kolstad and Bracegirdle, 2008) also as consequence of global warming. These phenomena regulate the formation of deep water in the Labrador Sea by inducing a strong oceanic heat loss (Schulze et al., 2016; Condrón and Renfrew, 2013), as they are accompanied by strong winds and a decrease in the air temperature (Zahn and von Storch, 2010b; Kolstad and Bracegirdle, 2008). Yashayaev and Loder (2009) in their study argued that enhanced atmospheric cooling associated with below-normal air temperatures in the Labrador Sea, was the predominant factor contributing to the enhanced production of LSW_{2008} . Våge et al. (2008b) found this strong cooling to be related with (amongst other factors) a shift of the storms track more to the south compared to the previous winter, with the cyclones following a better well-defined trajectory from the east coast of North America towards the Irminger Sea. We found that by filtering out such events the heat loss over the Labrador Sea decreases by 44%. This reduction was enough to shut down the deep convection in the basin, with the March MLD not going deeper than 400 m. It took less than a year of filtered atmospheric forcing for the *Filtered* simulation to show a considerably decrease the LSW formation rate. It is important to note here that high frequency atmospheric phenomena are projected to decrease based on relatively coarse resolution coupled models. How this result would change if high resolution projections were available is still uncertain.

We understand that our *Filtered* simulation is an extreme scenario as basically all the storms

are removed. In fact, if we translate the freshwater and heat fluxes of *GMR* and *PD* compared to those in *Filtered* into buoyancy fluxes it becomes clear that the increase in *Filtered* is much larger (Figure 3.11.a to 3.11.c). In terms of heat and buoyancy fluxes the *Filtered* experiment could be compared with those in Weijer et al. (2012) where a worst-case-scenario freshwater perturbation is applied, either around the perimeter of Greenland or over a broad swath (50°N - 70°N) of the northern North Atlantic, using two model configurations at different resolutions. They found a reduction in ventilation in the Labrador Sea associated with a decrease in the ocean surface heat loss, all within the first few years. In both of their configurations, the decrease in the convective activity was reflected by a weakening of the AMOC within 10 years. Thus, our results point out that, global warming in the future by reducing the occurrence of storm events over the Labrador Sea and hence a decrease in the heat loss, is potentially as bigger threat for the LSW formation as an increase in the freshwater input. However, caution is required when drawing implications for a coupled system, where heat fluxes and sea surface temperature are not prescribed in the same way as in a forced numerical model simulation.

Holdsworth and Myers (2015) explored the impact of high frequency atmospheric forcing in the convective energy on the Labrador Sea from 2002 to 2010 using model output. While convection represents vertical mixing (upward and downward), subduction focus only in the net downward transport of a specific water mass. A strong convection event (i.e., MLD deeper than 1500 m) does not necessarily translate into an increase in the formation rate (Figure 3.4.a). We found that deep convection events like those in 2014 and 2015 (Figure 3.4.a) where the MLD was deeper than 1500 m, were not followed by an increase in the formation rate. We consider that, based on our results, care needs to be taken when directly linking convective energy to LSW formation. Different from Holdsworth and Myers (2015) we offer an estimate of the LSW formation rate when storms are not present. Our results not only support their findings but also extend their analysis and objectives. At the same time, the different diagnostic used in our study adds to our understanding of the link between LSW formation and convection.

We are aware that the presence of the artificial MLSW in the simulations *SPG12*, *GMR* and *PD* (Figures 3.8.b, 3.8.c and 3.8.e) might be interpreted as if there is a significant influence from the model drift in our results. Böning et al. (2016) defined upper LSW between 27.74 -

27.82 kg/m^3 which is the density range we use here to define deeper LSW. At the same time they defined lower LSW between 27.82 - 27.92 kg/m^3 which is the density range that we use to define the MLSW. Attention needs to be paid when comparing LSW rates from different studies and their respective definitions in density ranges, and not just the names they were given. This does not mean that we are ignoring the presence of a small drift in our simulations. However, the *Control* simulation does not show the presence of subduction occurring in the density of MLSW, and it shows formation rates occurring at a density range comparable to observations (see for example studies within Table 3.1). In the case of *GMR* and *PD* the transformation of ULSW and deeper LSW into MLSW is clearly due to the lack of Greenland melt and precipitation compared to *Control*, which induces an increase in the density, reflected in the deepening of the seasonal MLD.

The annual evolution of the subduction components in the case of *SPG12* (not shown) links the transformation of ULSW and deeper LSW into the MLSW with an increase in the magnitude of the advective terms from 2014. When analysing the velocity field from the model output in *SPG12* (not shown), we found that there is an increase in the zonal velocities towards the east over the study region. The meridional velocities have a similar behaviour, with an increase mainly towards the south. When using *SPG12* to explore the temperature flux carried by individual eddies across 47°N in the Atlantic Ocean, Müller et al. (2017) compared its (*SPG12*) mean circulation patterns with satellite altimetry data, finding that the Labrador Current appeared to be more pronounced in *SPG12*. This might be a reason for the increase eastward and southward velocities found in our study region. Boundary issues between the parent domain and the nest might as well, eventually, lead to spurious solutions within the nest or child domain (Nash and Hartnett, 2014). Nevertheless, all the five simulations used were able to correctly capture the physical processes leading to LSW formation. As well the kinematic subduction approach has shown to be a useful tool when estimating LSW formation.

3.6 Acknowledgements

We gratefully acknowledge the financial and logistic support of grants from the Natural Sciences and Engineering Research Council (NSERC) of Canada. These include a Discovery

Grant (rgpin227438-09) awarded to Dr. P.G. Myers, Climate Change and Atmospheric Research Grant (VITALS - RGPCC 433898), and an International Create (ArcTrain - 432295). We are grateful to the NEMO development team and the Drakkar project for providing the model and continuous guidance, and to Westgrid and Compute Canada for computational resources. We would also like to thank G. Smith for the CGRF forcing fields, made available by Environment and Climate Change Canada. We thank Dr. Laura Castro de la Guardia for her aid in producing Figures 3.2.c-3.2.e. The Argo data used to create the climatological MLD and its properties was collected and made freely available by the International Argo Program and the national programs that contribute to it. (<http://www.argo.ucsd.edu>, <http://argo.jcommops.org>). The Argo Program is part of the Global Ocean Observing System. (<http://doi.org/10.17882/42182>). Data from the RAPID-WATCH MOC monitoring project are funded by the Natural Environment Research Council and are freely available from <http://www.rapid.ac.uk/rapidmoc>. If interested in gain access to our model data, please contact Dr. P.G. Myers. D. Kieke acknowledges funding from the BMBF-RACE program. We also thank four anonymous reviewers for suggesting substantial improvements to the manuscript.

Bibliography

- Azetsu-Scott, K., E. P. Jones, I. Yashayaev, and R. M. Gershey (2003), Time series study of CFC concentrations in the Labrador Sea during deep and shallow convection regimes (1991–2000), *Journal of Geophysical Research: Oceans*, *108*(C11), doi:10.1029/2002JC001317, 3354.
- Bamber, J., M. van den Broeke, J. Ettema, J. Lenaerts, and E. Rignot (2012), Recent large increases in freshwater fluxes from Greenland into the North Atlantic, *Geophysical Research Letters*, *39*(19), doi:10.1029/2012GL052552, L19501.
- Barnier, B., J. LeSommer, J. M. Molines, T. Penduff, S. Theetten, A. M. Treguier, G. Madec, A. Biastoch, C. Böning, J. Dengg, S. Gulev, B. R. Bourdallé, J. Chanut, G. Garric, A. Coward, B. de Cuevas, A. New, K. Haines, G. C. Smith, S. Drijfhout, W. Hazeleger, C. Severijns, and P. Myers (2007), Eddy-permitting ocean circulation hindcasts of the past decades, *CLIVAR-Exchanges*, *12*(3), 8–10.
- Blayo, E., and L. Debreu (1999), Adaptive mesh refinement for finite-difference ocean models: first experiments, *Journal of Physical Oceanography*, *29*(6), 1239–1250, doi:10.1175/1520-0485(1999)029<1239:AMRFFD>2.0.CO;2.
- Böning, C., F. Bryan, W. Holland, and R. Döscher (1996), Deep-water formation and meridional overturning in a high-resolution model of the North Atlantic, *Journal of Physical Oceanography*, *26*(7), 1142–1164, doi:10.1175/1520-0485(1996)026<1142:DWFAMO>2.0.CO;2.
- Böning, C. W., E. Behrens, A. Biastoch, K. Getzlaff, and J. L. Bamber (2016), Emerging impact of greenland meltwater on deepwater formation in the north atlantic ocean, *Nature Geoscience*, *9*(11), 523–527, doi:10.1038/ngeo2740.
- Brunnabend, S.-E., J. Schröter, R. Rietbroek, and J. Kusche (2015), Regional sea level change in response to ice mass loss in Greenland, the West Antarctic and Alaska, *Journal of Geophysical Research: Oceans*, *120*(11), 7316–7328, doi:10.1002/2015JC011244.

- Chanut, J., B. Barnier, W. Large, L. Debreu, T. Penduff, J.-M. Molines, and P. Mathiot (2008), Mesoscale Eddies in the Labrador Sea and Their Contribution to Convection and Restratification, *Journal of Physical Oceanography*, *38*(8), 1617–1643, doi:10.1175/2008JPO3485.1.
- Condron, A., and I. A. Renfrew (2013), The impact of polar mesoscale storms on northeast Atlantic Ocean circulation, *Nature Geoscience*, *6*(1), 34–37, doi:10.1038/ngeo1661.
- Courtois, P., Y. Garcia-Quintana, X. Hu, and P. Myers (2018), Kinematic subduction rate of Labrador Sea Water, *Journal of Geophysical Research - Oceans*, submitted.
- Courtois, P., X. Hu, C. Pennelly, P. Spence, and P. G. Myers (2017), Mixed layer depth calculation in deep convection regions in ocean numerical models, *Ocean Modelling*, *120*, 60 – 78, doi:https://doi.org/10.1016/j.ocemod.2017.10.007.
- Cuny, J., P. B. Rhines, P. P. Niiler, and S. Bacon (2002), Labrador sea boundary currents and the fate of the irvinger sea water, *Journal of Physical Oceanography*, *32*(2), 627–647, doi:10.1175/1520-0485(2002)032<0627:LSBCAT>2.0.CO;2.
- Da Costa, M. V., H. Mercier, and A. M. Treguier (2005), Effects of the mixed layer time variability on kinematic subduction rate diagnostics, *Journal of physical oceanography*, *35*(4), 427–443, doi:10.1175/JPO2693.1.
- Dai, A., and K. E. Trenberth (2002), Estimates of Freshwater Discharge from Continents: Latitudinal and Seasonal Variations, *Journal of Hydrometeorology*, *3*(6), 660–687, doi:10.1175/1525-7541(2002)003<0660:EOFDFC>2.0.CO;2.
- Dai, A., T. Qian, K. E. Trenberth, and J. D. Milliman (2009), Changes in continental freshwater discharge from 1948 to 2004, *Journal of Climate*, *22*(10), 2773–2792, doi:10.1175/2008JCLI2592.1.
- de Jong, M. F., A. S. Bower, and H. H. Furey (2014), Two years of observations of warm-core anticyclones in the Labrador Sea and their seasonal cycle in heat and salt stratification, *Journal of Physical Oceanography*, *44*(2), 427–444, doi:10.1175/JPO-D-13-070.1.
- Debreu, L., C. Vouland, and E. Blayo (2008), AGRIF: Adaptive grid refinement in Fortran, *Computers & Geosciences*, *34*(1), 8–13, doi:https://doi.org/10.1016/j.cageo.2007.01.009.

- den Toom, M., H. A. Dijkstra, W. Weijer, M. W. Hecht, M. E. Maltrud, and E. van Sebille (2014), Response of a strongly eddying global ocean to north atlantic freshwater perturbations, *Journal of Physical Oceanography*, *44*(2), 464–481, doi:10.1175/JPO-D-12-0155.1.
- Dickson, R., J. Lazier, J. Meincke, P. Rhines, and J. Swift (1996), Long-term coordinated changes in the convective activity of the North Atlantic, *Progress in Oceanography*, *38*(3), 241 – 295, doi:https://doi.org/10.1016/S0079-6611(97)00002-5.
- Dickson, R., B. Rudels, S. Dye, M. Karcher, J. Meincke, and I. Yashayaev (2007), Current estimates of freshwater flux through Arctic and subarctic seas, *Progress in Oceanography*, *73*(3), 210–230, doi:https://doi.org/10.1016/j.pocean.2006.12.003.
- Dickson, R. R., J. Meincke, S.-A. Malmberg, and A. J. Lee (1988), The “great salinity anomaly” in the northern North Atlantic 1968–1982, *Progress in Oceanography*, *20*(2), 103–151, doi: https://doi.org/10.1016/0079-6611(88)90049-3.
- Dukhovskoy, D. S., P. G. Myers, G. Platov, M. L. Timmermans, B. Curry, A. Proshutinsky, J. L. Bamber, E. Chassignet, X. Hu, C. M. Lee, and R. Somavilla (2016), Greenland freshwater pathways in the sub-Arctic Seas from model experiments with passive tracers, *Journal of Geophysical Research: Oceans*, *121*(1), 877–907, doi:10.1002/2015JC011290.
- Eyring, V., S. Bony, G.A. Meehl, C. A. Senior, B. Stevens, R.J. Stouffer, and K. E. Taylor (2016), Overview of the Coupled Model Intercomparison Project Phase 6 (CMIP6) experimental design and organization, *Geoscientific Model Development*, *9*(5), 1937–1958, doi: 10.5194/gmd-9-1937-2016.
- Fichefet, T., and M. A. M. Maqueda (1997), Sensitivity of a global sea ice model to the treatment of ice thermodynamics and dynamics, *Journal of Geophysical Research: Oceans (1978–2012)*, *102*(C6), 12,609–12,646, doi:10.1029/97JC00480.
- Flato, G., J. Marotzke, B. Abiodun, P. Braconnot, S. Chou, W. Collins, P. Cox, F. Driouech, S. Emori, V. Eyring, C. Forest, P. Gleckler, E. Guilyardi, C. Jakob, V. Kattsov, C. Reason, and M. Rummukainen (2013), *Evaluation of Climate Models. In: Climate Change 2013: The Physical Science Basis. Contribution of Working Group I to the Fifth Assessment Report of*

the Intergovernmental Panel on Climate Change [Solomon, S. and Qin, D. and Manning, M. and Chen, Z. and Marquis, M. and Averyt, -K.B. and Tignor, M. and Miller, H.L. (eds.)], Cambridge University Press, Cambridge, United Kingdom and New York, NY, USA.

Forsberg, R., L. Sørensen, and S. Simonsen (2017), Greenland and Antarctica ice sheet mass changes and effects on global sea level, *Surveys in Geophysics*, *38*(1), 89–104, doi:10.1007/s10712-016-9398-7.

García-Ibáñez, M. I., P. C. Pardo, L. I. Carracedo, H. Mercier, P. Lherminier, A. F. Ríos, and F. F. Pérez (2015), Structure, transports and transformations of the water masses in the Atlantic Subpolar Gyre, *Progress in Oceanography*, *135*, 18–36, doi:https://doi.org/10.1016/j.pocean.2015.03.009.

Gelderloos, R., C. A. Katsman, and S. S. Drijfhout (2011), Assessing the roles of three eddy types in restratifying the labrador sea after deep convection, *Journal of Physical Oceanography*, *41* (11), 2102–2119, doi:10.1175/JPO-D-11-054.1.

Gelderloos, R., F. Straneo, and C. A. Katsman (2012), Mechanisms behind the Temporary Shutdown of Deep Convection in the Labrador Sea: Lessons from the Great Salinity Anomaly Years 1968–71, *Journal of Climate*, *25*(19), 6743–6755, doi:10.1175/JCLI-D-11-00549.1.

Gerdes, R., J. Hurka, M. Karcher, F. Kauker, and C. Köberle (2005), *Simulated History of Convection in the Greenland and Labrador Seas, 1948-2001*, in *The Nordic Seas: An Integrated Perspective*, pp. 221–238, American Geophysical Union, doi:10.1029/158GM15.

Gillard, L. C., X. Hu, P. G. Myers, and J. L. Bamber (2016), Meltwater pathways from marine terminating glaciers of the Greenland ice sheet, *Geophysical Research Letters*, *43*(20), 10,873–10,882, doi:10.1002/2016GL070969.

Haine, T., C. Böning, P. Brandt, J. Fischer, A. Funk, D. Kieke, E. Kvaleberg, M. Rhein, and M. Visbeck (2008), *North Atlantic deep water formation in the Labrador Sea, recirculation through the subpolar gyre, and discharge to the subtropics*, in *Arctic-Subarctic Ocean Fluxes*, pp. 653–701, Springer Netherlands, Dordrecht, doi:10.1007/978-1-4020-6774-7_28.

- Hátún, H., C.C. Eriksen and P.B. Rhines (2007), *Buoyant Eddies Entering the Labrador Sea Observed with Gliders and Altimetry*, *Journal of Physical Oceanography*, *37*(12), 2838–2854, doi:10.1175/2007JPO3567.1.
- Holdsworth, A. M., and P. G. Myers (2015), The Influence of high-frequency atmospheric forcing on the circulation and deep convection of the Labrador Sea, *Journal of Climate*, *28*(12), 4980–4996, doi:10.1175/JCLI-D-14-00564.1.
- Holte, J., and F. Straneo (2017), Seasonal overturning of the Labrador Sea as observed by Argo floats, *Journal of Physical Oceanography*, *47*(10), 2531–2543, doi:10.1175/JPO-D-17-0051.1.
- Holte, J., and L. Talley (2009), A New Algorithm for Finding Mixed Layer Depths with Applications to Argo Data and Subantarctic Mode Water Formation, *Journal of Atmospheric and Oceanic Technology*, *26*(9), 1920–1939, doi:10.1175/2009JTECHO543.1.
- Holte, J., L. D. Talley, J. Gilson, and D. Roemmich (2017), An Argo mixed layer climatology and database, *Geophysical Research Letters*, *44*(11), 5618–5626, doi:10.1002/2017GL073426, 2017GL073426.
- Houssais, M.-N., and C. Herbaut (2011), Atmospheric forcing on the Canadian Arctic Archipelago freshwater outflow and implications for the Labrador Sea variability, *Journal of Geophysical Research: Oceans*, *116*(C8), doi:10.1029/2010JC006323.
- Huang, R. X. (2010), *Part II: Wind-driven and thermohaline circulation*, in *Ocean Circulation: Wind-Driven and Thermohaline Processes*, pp. 261–791, Cambridge University Press.
- Huntington, T. G. (2006), Evidence for intensification of the global water cycle: Review and synthesis, *Journal of Hydrology*, *319*(1), 83–95, doi:https://doi.org/10.1016/j.jhydrol.2005.07.003.
- Hurrell, J. W., and H. van Loon (1997), Decadal variations in climate associated with the North Atlantic Oscillation, *Climatic Change*, *36*(3), 301–326, doi:10.1023/A:1005314315270.
- Jones, H., and J. Marshall (1993), Convection with rotation in a neutral ocean: A study of open-ocean deep convection, *Journal of Physical Oceanography*, *23*(6), 1009–1039, doi:10.1175/1520-0485(1993)023<1009:CWRIAN>2.0.CO;2.

- Jones, H., and J. Marshall (1997), Restratification after Deep Convection, *Journal of Physical Oceanography*, *27*(10), 2276–2286, doi:10.1175/1520-0485(1997)027<2276:RADC>2.0.CO;2.
- Josey, S. A., and R. Marsh (2005), Surface freshwater flux variability and recent freshening of the North Atlantic in the eastern subpolar gyre, *Journal of Geophysical Research: Oceans*, *110*(C5), 2276–2287, doi:10.1029/2004JC002521.
- Jung, T., S. Serran, and Q. Wang (2014), The oceanic response to mesoscale atmospheric forcing, *Geophysical Research Letters*, *41*(4), 1255–1260, doi:10.1002/2013GL059040.
- Kawasaki, T., and H. Hasumi (2014), Effect of freshwater from the west greenland current on the winter deep convection in the labrador sea, *Ocean Modelling*, *75*, 51 – 64, doi: <https://doi.org/10.1016/j.ocemod.2014.01.003>.
- Khatiwala, S., and M. Visbeck (2000), An estimate of the eddy-induced circulation in the Labrador Sea, *Geophysical Research Letters*, *27*(15), 2277–2280, doi:10.1029/1999GL011073.
- Khatiwala, S., P. Schlosser, and M. Visbeck (2002), Rates and Mechanisms of Water Mass Transformation in the Labrador Sea as Inferred from Tracer Observations, *Journal of Physical Oceanography*, *32*(2), 666–686, doi:10.1175/1520-0485(2002)032<0666:RAMOWM>2.0.CO;2.
- Kieke, D., and I. Yashayaev (2015), Studies of Labrador Sea Water formation and variability in the subpolar North Atlantic in the light of international partnership and collaboration, *Progress in Oceanography*, *132*, 220–232, doi:<https://doi.org/10.1016/j.pocean.2014.12.010>.
- Kieke, D., M. Rhein, L. Stramma, W. M. Smethie, J. L. Bullister and D. A. LeBel (2006), Changes in the pool of Labrador Sea Water in the subpolar North Atlantic, *Geophysical Research Letters*, *34*(6), doi:10.1029/2006GL028959.
- Kieke, D., M. Rhein, L. Stramma, W. M. Smethie, D. A. LeBel, and W. Zenk (2006), Changes in the CFC inventories and formation rates of Upper Labrador Sea Water, 1997-2001, *Journal of Physical Oceanography*, *36*(1), 64–86, doi:10.1175/JPO2814.1.

- Kolstad, E. W., and T. J. Bracegirdle (2008), Marine cold-air outbreaks in the future: an assessment of IPCC AR4 model results for the Northern Hemisphere, *Climate Dynamics*, *30*(7), 871–885, doi:10.1007/s00382-007-0331-0.
- Large, W. G., and S. G. Yeager (2009), The global climatology of an interannually varying air-sea flux data set, *Climate Dynamics*, *33*(2), 341–364, doi:10.1007/s00382-008-0441-3.
- Laurent, D., B. Eric, and B. Bernard (2005), A general adaptive multi-resolution approach to ocean modelling: Experiments in a primitive equation model of the North Atlantic, in *Adaptive Mesh Refinement-Theory and Applications*, pp. 303–313, Springer.
- Lazier, J., R. Hendry, A. Clarke, I. Yashayaev and P. Rhines (2002), Convection and restratification in the Labrador Sea, 1990-2000, *Deep Sea Research Part I: Oceanographic Research Papers*, *49*(10), 1819–1835, doi:10.1016/S0967-0637(02)00064-X.
- LeBel, D. A., W. M. Smethie, M. Rhein, D. Kieke, R. A. Fine, J. L. Bullister, D.-H. Min, W. Roether, R. F. Weiss, C. Andrié, D. Smythe-Wright, and E. P. Jones (2008), The formation rate of North Atlantic Deep Water and Eighteen Degree Water calculated from CFC-11 inventories observed during WOCE, *Deep Sea Research Part I: Oceanographic Research Papers*, *55*(8), 891 – 910, doi:https://doi.org/10.1016/j.dsr.2008.03.009.
- Lilly, J. M., P. B. Rhines, F. Schott, K. Lavender, J. Lazier, U. Send, and E. D’Asaro (2003), Observations of the Labrador Sea eddy field, *Progress in Oceanography*, *59*(1), 75–176, doi:https://doi.org/10.1016/j.pocean.2003.08.013.
- Liu, C., and Z. Wang (2014), On the response of the global subduction rate to global warming in coupled climate models, *Advances in Atmospheric Sciences*, *31*(1), 211–218, doi:10.1007/s00376-013-2323-9.
- Madec, G. and the NEMO team (2008), *NEMO ocean engine*, Note du Pôle de modélisation, Institut Pierre-Simon Laplace (IPSL), France, No 27, ISSN No 1288-1619.
- Marsh, R. (2000), Recent variability of the North Atlantic thermohaline circulation inferred from surface heat and freshwater fluxes, *Journal of Climate*, *13*(18), 3239–3260, doi:10.1175/1520-0442(2000)013<3239:RVOTNA>2.0.CO;2.

- Marsh, R., S. Josey, A. De Nurser, B. Cuevas, and A. Coward (2005), Water mass transformation in the North Atlantic over 1985-2002 simulated in an eddy-permitting model, *Ocean Science*, 1 (2), 127–144, doi:10.5194/os-1-127-2005.
- Marshall, J., and F. Schott (1999), Open-ocean convection: Observations, theory, and models, *Reviews of Geophysics*, 37(1), 1–64, doi:10.1029/98RG02739.
- Marzocchi, A., J. J.-M. Hirschi, N. P. Holliday, S. A. Cunningham, A. T. Blaker, and A. C. Coward (2015), The North Atlantic subpolar circulation in an eddy-resolving global ocean model, *Journal of Marine Systems*, 142, 126 –143, doi:https://doi.org/10.1016/j.jmarsys.2014.10.007.
- Masina, S., A. Storto, N. Ferry, M. Valdivieso, K. Haines, M. Balmaseda, H. Zuo, M. Drevillon, and L. Parent (2017), An ensemble of eddy-permitting global ocean reanalyses from the MyOcean project, *Climate Dynamics*, 49(3), 813–841, doi:10.1007/s00382-015-2728-5.
- Mauritzen, C., and S. Häkkinen (1999), On the relationship between dense water formation and the “Meridional Overturning Cell” in the North Atlantic Ocean, *Deep Sea Research Part I: Oceanographic Research Papers*, 46(5), 877–894, doi:https://doi.org/10.1016/S0967-0637(98)00094-6.
- McCartney, M. S., and L. D. Talley (1982), The subpolar mode water of the North Atlantic Ocean, *Journal of Physical Oceanography*, 12(11), 1169–1188, doi:10.1175/1520-0485(1982)012<1169:TSMWOT>2.0.CO;2.
- Milanchus, M. L., S. T. Rao, and I. G. Zurbenko (1998), Evaluating the effectiveness of ozone management efforts in the presence of meteorological variability, *Journal of the Air & Waste Management Association*, 48(3), 201–215, doi:10.1080/10473289.1998.10463673.
- Müller, V., D. Kieke, P. G. Myers, C. Pennelly, and C. Mertens (2017), Temperature flux carried by individual eddies across 47°N in the Atlantic Ocean, *Journal of Geophysical Research: Oceans*, 122(3), 2441–2464, doi:10.1002/2016JC012175.
- Myers, P. G. (2005), Impact of freshwater from the Canadian Arctic archipelago on Labrador Sea water formation, *Geophysical Research Letters*, 32(6), doi:10.1029/2004GL022082.

- Myers, P. G., and C. Donnelly (2008), Water mass transformation and formation in the Labrador Sea, *Journal of Climate*, *21*(7), 1622–1638, doi:10.1175/2007JCLI1722.1.
- Myers, P. G., N. Kulan, and M. H. Ribergaard (2007), Irminger water variability in the west Greenland current, *Geophysical Research Letters*, *34*(17), doi:10.1029/2007GL030419.
- Nash, S., and M. Hartnett (2014), Development of a nested coastal circulation model: Boundary error reduction, *Environmental Modelling & Software*, *53*(Supplement C), 65 – 80, doi: <https://doi.org/10.1016/j.envsoft.2013.11.007>.
- Pickart, R. S., and M. A. Spall (2007), Impact of Labrador Sea convection on the North Atlantic meridional overturning circulation, *Journal of Physical Oceanography*, *37*(9), 2207–2227, doi:10.1175/JPO3178.1.
- Qiu, B., and R. X. Huang (1995), Ventilation of the North Atlantic and North Pacific: Subduction Versus Obduction, *Journal of Physical Oceanography*, *25*(10), 2374–2390, doi: 10.1175/1520-0485(1995)025<2374:VOTNAA>2.0.CO;2.
- Rao, S. T., E. Zalewsky, and I. G. Zurbenko (1994), Detecting and tracking changes in ozone air quality, *Journal of the Air & Waste Management Association*, *44*(9), 1089–1092, doi: 10.1080/10473289.1994.10467303.
- Rao, S. T., E. Zalewsky, and I. G. Zurbenko (1995), Determining temporal and spatial variations in ozone air quality, *Journal of the Air & Waste Management Association*, *45*(1), 57–61, doi:10.1080/10473289.1995.10467342.
- Rattan, S., P. G. Myers, A.-M. Tréguier, S. Theetten, A. Biastoch, and C. Böning (2010), Towards an understanding of Labrador Sea salinity drift in eddy-permitting simulations, *Ocean Modelling*, *35*(1), 77–88, doi:<https://doi.org/10.1016/j.ocemod.2010.06.007>.
- Rhein, M., J. Fischer, W. M. Smethie, D. Smythe-Wright, R. F. Weiss, C. Mertens, D.-H. Min, U. Fleischmann, and A. Putzka (2002), Labrador Sea Water: Pathways, CFC Inventory, and Formation Rates, *Journal of Physical Oceanography*, *32*(2), 648–665, doi: 10.1175/1520-0485(2002)032<0648:LSWPCI>2.0.CO;2.

- Rhein, M., D. Kieke, S. Hüttl-Kabus, A. Roessler, C. Mertens, R. Meissner, B. Klein, C. W. Böning, and I. Yashayaev (2011), Deep water formation, the subpolar gyre, and the Meridional Overturning Circulation in the subpolar North Atlantic, *Deep Sea Research Part II: Topical Studies in Oceanography*, *58*(17–18), 1819–1832, doi:<https://doi.org/10.1016/j.dsr2.2010.10.061>.
- Rhein, M., D. Kieke, and R. Steinfeldt (2015), Advection of North Atlantic Deep Water from the Labrador Sea to the southern hemisphere, *Journal of Geophysical Research: Oceans*, *120*(4), 2471–2487, doi:[10.1002/2014JC010605](https://doi.org/10.1002/2014JC010605).
- Sabine, C. L., R. A. Feely, N. Gruber, R. M. Key, K. Lee, J. L. Bullister, R. Wanninkhof, C. S. Wong, D. W. R. Wallace, B. Tilbrook, F. J. Millero, T.-H. Peng, A. Kozyr, T. Ono, and A. F. Rios (2004), The oceanic sink for anthropogenic CO₂, *Science*, *305*(5682), 367–371, doi:[10.1126/science.1097403](https://doi.org/10.1126/science.1097403).
- Schulze, L. M., R. S. Pickart, and G. W. K. Moore (2016), Atmospheric forcing during active convection in the Labrador Sea and its impact on mixed-layer depth, *Journal of Geophysical Research: Oceans*, *121*(9), 6978–6992, doi:[10.1002/2015JC011607](https://doi.org/10.1002/2015JC011607).
- Smith, G. C., F. Roy, P. Mann, F. Dupont, B. Brasnett, J.-F. Lemieux, S. Laroche, and S. Bélair (2014), A new atmospheric dataset for forcing ice–ocean models: Evaluation of reforecasts using the Canadian global deterministic prediction system, *Quarterly Journal of the Royal Meteorological Society*, *140*(680), 881–894, doi:[10.1002/qj.2194](https://doi.org/10.1002/qj.2194).
- Smeed, D., G. McCarthy, D. Rayner, B. I. Moat, W. E. Johns, M. O. Baringer, C.S. . Meinen (2017), Atlantic meridional overturning circulation observed by the RAPID-MOCHA-WBTS (RAPID-Meridional Overturning Circulation and Heatflux Array-Western Boundary Time Series) array at 26°N from 2004 to 2017, *British Oceanographic Data Centre - Natural Environment Research Council, UK.*, doi:[10.5285/5acfd143-1104-7b58-e053-6c86abc0d94b](https://doi.org/10.5285/5acfd143-1104-7b58-e053-6c86abc0d94b).
- Speer, K., and E. Tziperman (1992), Rates of water mass formation in the North Atlantic Ocean, *Journal of Physical Oceanography*, *22*(1), 93–104, doi:[10.1175/1520-0485\(1992\)022<0093:ROWMFI>2.0.CO;2](https://doi.org/10.1175/1520-0485(1992)022<0093:ROWMFI>2.0.CO;2).

- Steinfeldt, R., M. Rhein, J. L. Bullister, and T. Tanhua (2009), Inventory changes in anthropogenic carbon from 1997–2003 in the Atlantic Ocean between 20°S and 65°N, *Global Biogeochemical Cycles*, *23*(3), doi:10.1029/2008GB003311.
- Stendardo, I., and N. Gruber (2012), Oxygen trends over five decades in the North Atlantic, *Journal of Geophysical Research: Oceans*, *117*(C11), doi:10.1029/2012JC007909.
- Stramma, L., D. Kieke, M. Rhein, F. Schott, I. Yashayaev, and K. P. Koltermann (2004), Deep water changes at the western boundary of the subpolar North Atlantic during 1996 to 2001, *Deep Sea Research Part I: Oceanographic Research Papers*, *51*(8), 1033–1056, doi: <https://doi.org/10.1016/j.dsr.2004.04.001>.
- The Lab Sea Group (1998), The Labrador Sea Deep Convection Experiment, *Bulletin of the American Meteorological Society*, *79*(10), 2033–2058, doi:10.1175/1520-0477(1998)079<2033:TLSDCE>2.0.CO;2.
- Trossman, D. S., L. A. Thompson, K. A. Kelly, and Y.-O. Kwon (2009), Estimates of North Atlantic Ventilation and Mode Water Formation for Winters 2002–06, *Journal of Physical Oceanography*, *39*(10), 2600–2617, doi:10.1175/2009JPO3930.1.
- van Angelen, J. H., J. T. M. Lenaerts, M. R. van den Broeke, X. Fettweis, and E. van Meijgaard (2013), Rapid loss of firn pore space accelerates 21st century Greenland mass loss, *Geophysical Research Letters*, *40*(10), 2109–2113, doi:10.1002/grl.50490.
- Velicogna, I., T. C. Sutterley, and M. R. van den Broeke (2014), Regional acceleration in ice mass loss from Greenland and Antarctica using GRACE time-variable gravity data, *Geophysical Research Letters*, *41*(22), 8130–8137, doi:10.1002/2014GL061052.
- Våge, K., R. S. Pickart, V. Thierry, G. Reverdin, C. M. Lee, B. Petrie, T. A. Agnew, A. Wong, and M. H. Ribergaard (2008), Surprising return of deep convection to the subpolar North Atlantic ocean in winter 2007–2008, *Nature Geoscience*, *2*, 67–72, doi:10.1038/NGEO382.
- Wang, G., D. Wang, K. E. Trenberth, A. Erfanian, M. Yu, M. G. Bosilovich, and D. T. Parr (2017), The peak structure and future changes of the relationships between extreme precipitation and temperature, *Nature Clim. Change*, *7*, 268–274, doi:10.1038/nclimate3239.

- Weijer, W., M. E. Maltrud, M. W. Hecht, H. A. Dijkstra, and M. A. Kliphuis (2012), Response of the atlantic ocean circulation to greenland ice sheet melting in a strongly-eddy ocean model, *Geophysical Research Letters*, *39*(9), doi:10.1029/2012GL051611.
- Yang, Q., H. D. Timothy, G. M. Paul, J. Bonin, D. Chambers, R. B. van den M., H. R. Mads, and J. Mortensen (2016), Recent increases in Arctic freshwater flux affects Labrador Sea convection and Atlantic overturning circulation, *Nature Communications*, *7*, doi:10.1038/ncomms10525.
- Yashayaev, I. (2007), Hydrographic changes in the Labrador Sea, 1960–2005, *Progress in Oceanography*, *73*(3), 242–276, doi:https://doi.org/10.1016/j.pocean.2007.04.015.
- Yashayaev, I., and A. Clarke (2006), Recent warming of the Labrador Sea, *AZMP Bulletin PMZA*, *5*, 12–20.
- Yashayaev, I., and B. Dickson (2008), *Transformation and Fate of Overflows in the Northern North Atlantic, in Arctic–Subarctic Ocean Fluxes*, pp. 505–526, Springer Netherlands, Dordrecht, doi:10.1007/978-1-4020-6774-7_22.
- Yashayaev, I., and J. W. Loder (2009), Enhanced production of Labrador Sea water in 2008, *Geophysical Research Letters*, *36*(1), doi:10.1029/2008GL036162.
- Yashayaev, I., and J. W. Loder (2016), Recurrent replenishment of Labrador Sea Water and associated decadal-scale variability, *Journal of Geophysical Research: Oceans*, *121*(11), 8095–8114, doi:10.1002/2016JC012046.
- Yashayaev, I., and J. W. Loder (2017), Further intensification of deep convection in the Labrador Sea in 2016, *Geophysical Research Letters*, *44*(3), 1429–1438, doi:10.1002/2016GL071668, 2016GL071668.
- Yashayaev, I., M. Bersch, H. van Aken, and A. Clarke (2004), A new study of the production, spreading and fate of the Labrador Sea Water in the subpolar North Atlantic, *ASOF Newsletter*, (2), 20–23.
- Yashayaev, I., M. Bersch, and H. M. van Aken (2007), Spreading of the Labrador Sea

Water to the Irminger and Iceland basins, *Geophysical Research Letters*, 34(10), doi:10.1029/2006GL028999.

Yashayaev, I., N. P. Holliday, M. Bersch, and H. M. van Aken (2008), *The History of the Labrador Sea Water: Production, Spreading, Transformation and Loss, in Arctic-Subarctic Ocean Fluxes: Defining the Role of the Northern Seas in Climate*, pp. 569–612, Springer, doi:10.1007/978-1-4020-6774-7_25.

Zahn, M., and H. von Storch (2010), Decreased frequency of North Atlantic polar lows associated with future climate warming, *Nature*, 467(7313), 309–312, doi:10.1038/nature09388.

Zurbenko, I., P. Porter, R. Gui, S. Rao, J. Ku, and R. Eskridge (1996), Detecting discontinuities in time series of upper-air data: development and demonstration of an adaptive filter technique, *Journal of climate*, 9(12), 3548–3560, doi:10.1175/1520-0442(1996)009<3548:DDITSO>2.0.CO;2.

Chapter 4

Transformation of the North Icelandic Irminger Current waters in the Nordic Seas and its link to the Denmark Strait Overflow Water

Submitted for publication to Journal of Geophysical Research: Oceans (August 2018). **Garcia-Quintana, Y.**, More, C., Wiesner, P., Hu, X., Kieke, D., Sutherland B.R., & Myers P.G

ABSTRACT

Classically, the Nordic Seas are often considered the headwaters for the Meridional Overturning Circulation (MOC), for it is there where the densest component of the Deep Western Boundary Current is formed. In spite of at least two decades of observations measuring the transport of the overflows across the Greenland-Scotland Ridge into the North Atlantic Ocean, questions exist about the reservoir that drives them. We address this subject using two eddy permitting configurations of an ocean general circulation model and the Lagrangian tracking tool Ariane to explore the Atlantic Water transformation in the Nordic Seas and its influence on feeding the North Icelandic Jet. Transformation to greater densities is found to occur in the boundary currents of the Nordic Seas. These waters leave at depth through Denmark Strait

within six years. A faster transformation occurs in a loop along the shelfbreak north of Iceland with export occurring in the North Icelandic Jet within one year. Despite the transformation to denser water occurring in the boundary currents, the maximum densities reached by the particles are consistent with the maximum densities observed in the Denmark Strait Overflow Water. Thus it is possible that even the most dense parts of the Denmark Strait Overflow Water could come from boundary current transformations, rather than deep convection in the interior of the Nordic Seas.

4.1 Introduction

The Nordic Seas are a grouping of three small basins: the Iceland, Norwegian and Greenland Seas. These three seas are separated from the Atlantic Ocean by the Denmark Strait, Iceland-Faroe Ridge, and the Faroe-Shetland Channel, and from the Arctic Ocean by the Fram Strait and Barents Sea Opening (Figure 4.1). As well as having important local climatic and ecological consequences (Drinkwater et al., 2013), the region plays an important role in the global oceanographic system (e.g, Yashayaev and Seidov (2015)). The Nordic Seas allow for the exchange of warm salty waters from the Atlantic to the Arctic Ocean. They receive cold low-salinity waters and sea ice from the Arctic Ocean (Eldevik et al., 2009), which are later exported to the southern oceans through the different straits located along the Greenland-Scotland Ridge (Figure 4.1).

Additionally, the Nordic Seas have historically been known as a deep water formation site (Aagaard et al., 1985). This production forms a dense water reservoir within the basin, which has been argued to overflow the sills at Denmark Strait and the Faroe-Shetland Channel. Subsequent sinking and entrainment of surrounding waters lead to the production of North Atlantic Deep Water, which flows south in the Deep Western Boundary Current (DWBC) to become a key component in the lower limb of the Meridional Overturning Circulation (Mauritzen, 1996). The Denmark Strait Overflow Water (DSOW) is the largest and densest of these contributions (Dickson and Brown, 1994b; Send et al., 2011; Mertens et al., 2014; Fischer et al., 2015). Measurements of DSOW transport have been carried out continuously since 1996 (Macrandar et al., 2005; Jochumsen et al., 2012, 2017), but a detailed description

of where and how the DSOW is formed, is still missing.

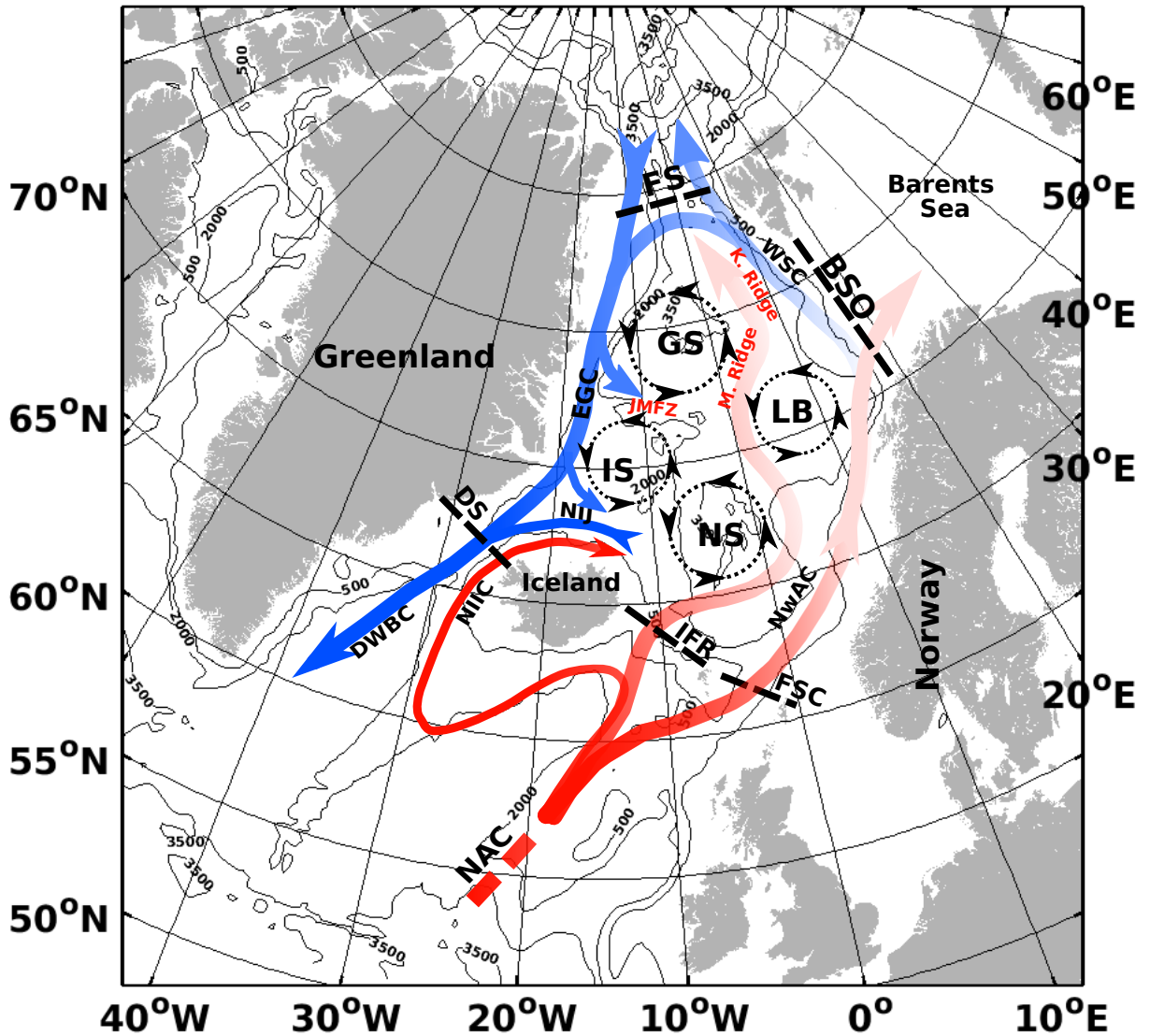


Figure 4.1: Schematic of the Nordic Seas, showing the main basins, inflows, outflows and geographical features, following Orvik and Niiler (2002) and Våge et al. (2013). For the currents, red colors represent light surface waters which are transformed into cold, dense overflow waters represented in blue colors. Main current acronyms: NAC - North Atlantic Current; NIIC - North Icelandic Irminger Current; NwAC - Norwegian Atlantic Current; WSC - West Spitsbergen Current; EGC - East Greenland Current; DWBC - Deep Western Boundary Current; NIJ - North Icelandic Jet. Black dashed lines represent the main straits that separate the Nordic Seas from the Atlantic and Arctic Oceans: Denmark Strait (DS), Iceland Faroe Ridge (IFR), Faro Shetland Channel (FSC), Barents Sea Opening (BSO) and Fram Strait (FS). Main basins: Norwegian Sea (NS), Iceland Sea (IS), Lofoten Basin (LB) and the Greenland Sea (GS). For each of the basins its circulation is illustrated by black dashed circles with the arrow heads pointing the direction of the circulation. In red appear the Knipovich Ridge (K. Ridge), Mohn Ridge and the Jan Mayen Fracture Zone (JMFZ). Black contour lines represent the isobaths, spaced every 1500 m.

Many numerical modelling studies have linked changes in freshwater, such as from the Greenland Ice Sheet, to changes in deep water formation and the MOC (e.g Gerdes et al. (2006); Stouffer et al. (2006); Swingedouw et al. (2007); Hu et al. (2011); Weijer et al. (2012)). These studies can be considered in the context of a reduction of deep convection in the Nordic Seas since 1982 (Rhein, 1991; Schlosser et al., 1991; Somavilla et al., 2013), leading to an increase of salinity and temperature in the deep Greenland Sea due to the advection of deep Arctic Ocean waters (Somavilla et al., 2013). Given that the deep overflows are driven by pressure gradients set up by transformation of Atlantic Water (AW) to increased densities in the Nordic Seas (Hansen and Østerhus, 2000), these changes led Hansen et al. (2001) to suggest that, based on an upward-looking Acoustic Doppler Current Profiler (ADCP) moored at the Faroe Bank Channel sill (from November 1995 to June 2000), the overflow through the Faroe Bank Channel was decreasing, with potential impacts on the MOC. However, with a longer dataset (1995 to 2005) from three ADCPs moored also at the Faroe Bank Channel sill, Hansen and Østerhus (2007) suggested that the overflow transport was steady. Furthermore Jochumsen et al. (2012) suggested there was no significant trend in the overflow transport at Denmark Strait, although the temperature did decrease. A number of studies [e.g. Mauritzen (1996); Eldevik et al. (2009)] have suggested that the transformation of inflowing AW in the Nordic Seas is a gradual process that occurs within the boundary currents. In fact, Eldevik et al. (2009) clearly state that the overflows are not linked to convective mixing.

Based on data from 11 oceanographic cruises covering a period of 10 years, Mauritzen (1996) argued against this widely-held paradigm of deep convection feeding the dense overflows from the Nordic Seas. Instead, she proposed that inflowing AW is gradually densified via heat loss as it circulates in the Norwegian Atlantic Current. The dense water is then transported to the outflows by the boundary currents surrounding the Iceland and Greenland Seas at both shallow and intermediate depths. Eldevik et al. (2009) supported this idea, arguing that the AW circulation and transformation within the boundary currents of the Nordic Seas was the main source for the overflows. Their circulation scheme suggested that anomalies passing through Denmark Strait had travelled along the rim of the Nordic Seas, while the Faroe-Shetland Channel overflows reflected variability within an overturning loop within the Norwegian Sea as well as a shorter pathway through the Jan Mayen Channel. Using a theoretical model,

Yang and Pratt (2013) showed that the dense water reservoir in the Nordic Seas available to drive the overflows is limited to the boundary currents, with the dense water in the interior basins kept isolated within closed geostrophic contours.

Våge et al. (2011) pointed out that although traditionally the East Greenland Current (EGC) was considered the primary pathway for supplying the Denmark Strait overflow, there is now evidence for a significant role of the North Icelandic Jet (NIJ), which supplies around a third of the overflow water transport at the sill (Våge et al., 2011; Harden et al., 2016). Våge et al. (2011) used a simplified numerical model to suggest a dynamical link between the inflowing North Icelandic Irminger Current (NIIC) and the outflowing NIJ, with the majority of transformation and sinking of the inflowing AW occurring in the boundary current north of Iceland. According to their model, the NIIC sheds eddies into the Iceland Sea interior where, due to heat loss during winter, the water carried within the eddies is made dense, returning later to the boundary, where it sinks and forms the NIJ.

Våge et al. (2013) extended the understanding of the region, showing that the circulation upstream of Denmark Strait is complex, with the source waters for the overflow mainly approaching the strait on the Icelandic side. They also confirmed that the NIJ is a distinct current from the EGC. The latter one bifurcates 450 km upstream of Denmark Strait at the northern end of the Blossville Basin, and the diverted branch is known as the separated EGC which flows south parallel to the NIJ (Våge et al., 2013).

Recently Behrens et al. (2017) supported the existence of the hypothesized overturning loop (Våge et al., 2011) along the shelfbreak north of Iceland. By using the Lagrangian tracking tool Ariane in a high-resolution model hindcast, they investigated the upstream sources of the DSOW and argued that the water carried by the NIIC transforms to feed the NIJ. What is more, while Behrens et al. (2017) claim the overturning cell to be located on the shelfbreak north of Iceland, Våge et al. (2011) and Våge et al. (2013) hypothesized the cell to occur in the Iceland Sea interior.

Our study aims to shed further light on the understanding of the NIIC transformation and its role on supplying the NIJ. For that purpose we use the fields from two different eddy permitting ocean general circulation model experiments to drive the integration of Lagrangian virtual floats. The transformation pathways for the AW as it enters the Nordic Seas via Den-

mark Strait within the NIIC and its potential contribution to DSOW are examined. Emphasis is made on the transformation occurring north of Iceland as a potential driver of the NIJ. The manuscript is structured as follows. The model description, experiment setup and details of the Lagrangian tool Ariane are topics in Section 2. Then the possible pathways of the NIIC as it enters the Nordic Seas and its transformation into overflow-like waters are examined in Section 3. Section 4 focuses on the transformation that occurs north of Iceland and its contribution to the NIJ. Discussion and conclusions are presented in Section 5.

4.2 Analysis Methods

The model used is the Nucleus for European Modelling of the Ocean (NEMO) numerical framework (Madec, 2008). NEMO is composed of five major components: ocean dynamics, sea ice, biogeochemistry, adaptative mesh refinement software, and an assimilation component. We use two configurations (Table 4.1) in order to analyse the transformation pathways of the AW once it enters the Nordic Seas via Denmark Strait:

1. ORCA025: The global hindcast experiment (ORCA025-KAB001, hereafter referred to as KAB001, carried out in Kiel) ran from 1958 to 2004 with a temporal resolution of 5 days, and is based on the eddy permitting ORCA025, a global ocean/sea-ice configuration of NEMO 3.1 (Bernard et al., 2006) implemented by the European DRAKKAR collaboration (DRAKKAR Group, 2007). The model is coupled with the Louvain-la-Neuve (LIM2) sea ice thermodynamic and dynamic numerical model (Fichefet and Maqueda, 1997). The ORCA grid becomes finer with increasing latitudes, so the effective $1/4^\circ$ resolution is 27.75 km at the equator and 13.8 km at 60°S or 60°N . There are 46 unevenly spaced vertical levels, increasing in thickness from 6 m near the surface to 250 m at depth, with partial steps in the lowest level.

Atmospheric forcing was set up in the Co-ordinated Ocean-ice Reference Experiments (CORE) framework (Griffies et al., 2009), using the forcing fields developed by *Large and Yeager* (2009). Surface forcing for KAB001 uses the standard CORE forcing data. Depending on the field, the resolution is 6-hourly, daily or monthly. Surface damping of sea surface salinity is weak (300 days for 10 m depth). In addition, a full three-

dimensional restoring is performed for both T and S in the polar regions with a timescale of 181 days (Bjastoch et al., 2008). This configuration has been used in numerous studies, including one by Behrens et al. (2013) that examined the role of subarctic freshwater forcing on trends in the meridional overturning circulation, linking it to the density of the Denmark Strait overflow.

2. ANHA4: The regional configuration Arctic and Northern Hemisphere Atlantic (ANHA) with a $1/4^\circ$ resolution, hereafter referred to as ANHA4, is also used. NEMO 3.4 is used as a framework in ANHA4. The model is coupled with the Louvain-la-Neuve (LIM2) sea ice thermodynamic and dynamic numerical model (Fichefet and Maqueda, 1997). ANHA4 covers the whole Arctic Ocean, North Atlantic and a part of the South Atlantic with two open boundaries, one close to Bering Strait and the other one at 20°S . The mesh grid is extracted from the $1/4^\circ$ global tripolar grid, ORCA025. The highest horizontal resolution ($\sim 6\text{km}$) is in Dease Strait, an east-west waterway between the mainland of Kent Peninsula and Victoria Island in Nunavut, Canada. The lowest resolution ($\sim 28\text{km}$) is at the Equator. It has 50 vertical levels, with the layer thickness smoothly increasing from 1.05 m at the surface, to 453.13 m in the last level.

Initial and monthly open boundary conditions are provided by Global Ocean Reanalyses and Simulations 2 version 3 (GLORYS2v3) (Ferry et al., 2016). The atmospheric forcing data, provided by Canadian Meteorological Centre’s global deterministic prediction system reforecasts (CGRF) data set (Smith et al., 2014), has hourly 33 km resolution for: 10 m surface wind, 2 m air temperature and humidity, downward shortwave and longwave radiation, and total precipitation. Interannual monthly river runoff is from Dai et al. (2009), while melt-water discharge from Greenland Ice Sheet is provided by Bamber et al. (2012). The simulation ran with ANHA4 covers the period from the beginning of 2002 to the end of 2016 and has a temporal resolution of 5 days. No temperature or salinity restoring is applied leaving the model to evolve freely.

The regional configuration ANHA4 has been used in the past by Holdsworth and Myers (2015) to explore the influence of high frequency atmospheric forcing on the circulation and deep convection in the Labrador Sea. Dukhovskoy et al. (2016) used the same

configuration to look at the spreading of Greenland freshwater in the sub-Arctic Seas. Guillard et al. (prep) explored the pathways of the melt-water from marine terminating glaciers of the Greenland ice sheet, also by making use of ANHA4. Müller et al. (2017) made use of the ANHA4 configuration to explore the temperature flux carried by eddies across 47°N in the Atlantic Ocean.

Table 4.1: Table highlighting the main differences between the KAB001 and the ANHA4 experiments.

	KAB001	ANHA4
Domain	Global	20° S to Bering Strait
Integration period	1958-2004	2002-2016
Radiation fluxes	CORE	CGRF
Precipitation	CORE	CGRF
3-D restoring in polar regions	181 days	None
# of particles released	2500	10000

To analyse the pathways of inflowing AW and its export, we used a well-tested (Lique et al., 2010; Hu and Myers, 2013; Guillard et al., prep; Behrens et al., 2017) off-line Lagrangian tool, Ariane (Blanke and Raynaud, 1997; Blanke et al., 1999). To compute three-dimensional (3-D) trajectories, Ariane is provided with ocean velocity fields. For the study carried out with KAB001, approximately 2500 virtual particles were initialized at the entrance of Denmark Strait each season (January, April, July, and October) every four years from 1960 to 2000 inclusive. In the case of the study carried out with ANHA4, approximately 10000 virtual particles were initialized at the entrance of Denmark Strait each season (January, April, July, and October) every year from 2005 to 2014 inclusive. The virtual particles were released along the section representing Denmark Strait in Figure 4.1.

The actual number of particles inflowing within the AW is determined by:

1. Particles are inserted based on:

$$n_i = N \left(\frac{V_i}{\sum_{j=1}^k V_j} \right) \left(\frac{v_i}{\bar{v}} \right), i \in 1..k, \quad (4.1)$$

where n_i is the number of particles to initialize around the i -th grid cell, k is the number of grid points which meet the criteria, v_i is the velocity of each identified (as AW) grid cell, \bar{v} is the mean velocity of each identified grid cell, V_i is the volume of each identified grid cell, V_j is the total volume of each identified grid cell, a given grid cell and N is the total number of particles to be initialized.

2. We define AW as: a water mass with a temperature higher than 3°C, salinity higher than 34.9 and within the density range from 26.8 kg/m^3 to 27.5 kg/m^3 . However there are very few months where densities as high as 27.5 kg/m^3 are seen. If no grid points meet this criteria at a given initialization time, no particles are seeded that month.

We use two different models, covering two time periods and with different air sea forcing to show that our results are robust and independent of the setup of a given model configuration.

4.3 NIIC waters pathways into the Nordic Seas

In this section we describe the pathways of the virtual floats entering the Nordic Seas within the NIIC and also leaving the Nordic Seas through Denmark Strait. First, we will describe the results obtained by using KAB001, followed by a description of the results obtained by using ANHA4.

4.3.1 KAB001 experiment

Overall, 72% of the particles inflowing with the AW through Denmark Strait are estimated to leave the Nordic Seas within 5 years of their entry. After 10 years, this increases to 92%. There is no dependence on the month of particle release. Most of the exported particles (61%) exit to the north, either into the Arctic Ocean via Fram Strait (45% of the northern export), or into the Barents Sea between Svalbard and Norway (55% of the northern export). The two pathways are correlated with $r=0.57$, but significant only at the 90% level. This weak correlation is stronger earlier in the analysis and breaks down in the 1990s. The mean transit time from Denmark Strait to the Barents Sea Opening is 2.3 years, and 3.4 years for Fram Strait. The majority of the particles, 78%, remain within the top 300 m and thus in the

warm Atlantic layer. Significantly fewer particles exit the Nordic Seas by the southern straits. About 10% of the total inflow leaves through Denmark Strait (17% after 10 years).

Although there is some inter-annual variability in these percentages, there are no significant correlations between the number of particles exported and the Arctic or North Atlantic Oscillations. Thus, most of the inflowing AW transits the Nordic Seas to the Barents Sea and Arctic before being transformed and returning to the Atlantic. Some water could conceivably enter the Barents Sea or Fram Strait and then recirculate into the Nordic Seas before being transformed.

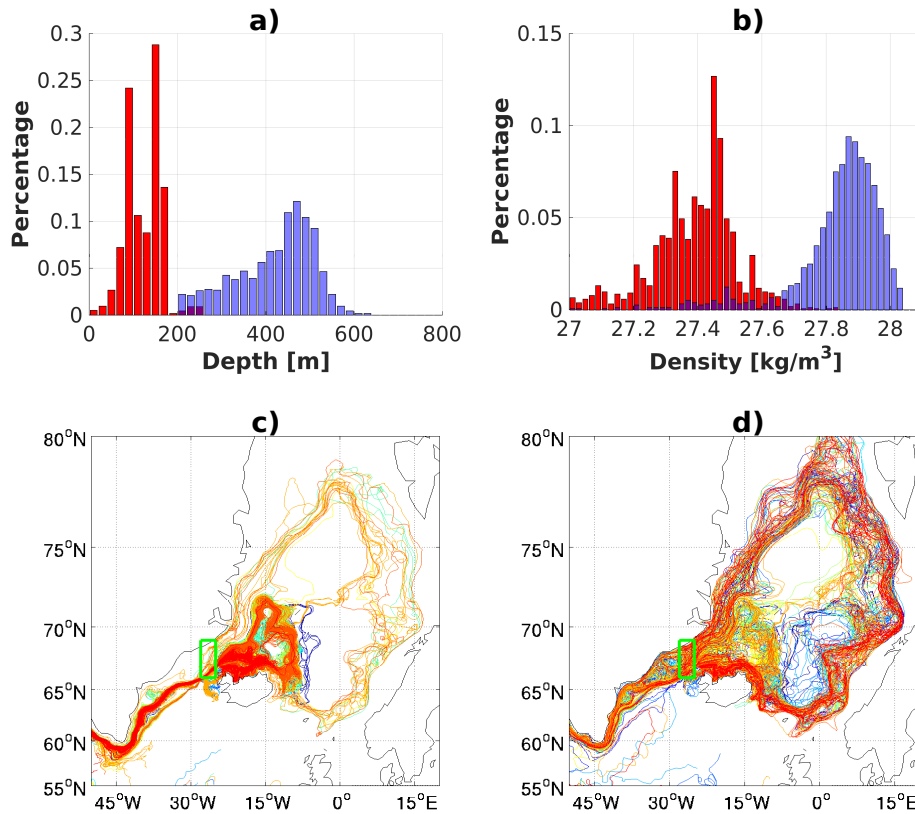


Figure 4.2: For the experiment KAB001: a) Depth distributions, in terms of relative percentages, for floats that enter through Denmark Strait (red) and then leave through Denmark Strait (blue) at depths greater than 200 m. Purple shading is used to indicate the percentage for whichever of the inflow/outflow has a smaller percentage in a given bin. b) As for a), but for density. c) Particle tracks for particles entering through Denmark Strait and then also leaving through Denmark Strait at depths greater than 200 m. d) As for c) but for particles leaving at all depths. Track colour (in c) and d)) indicates the decade in which the particle was released (Dark Blue - 1960s; Light Blue - 1970s; Green - 1980s; Orange - 1990s and Red - 2000s). The green boxes show the actual regions that were used to define the strait exits when a particle was determined to have entered the given box. For these two panels only, 1 in every 50 trajectories is plotted to reduce clutter.

Water that is transformed in the Nordic Seas tends to be saltier than water transformed within the Arctic Ocean, but also warmer. For example, Hansen and Østerhus (2000) found that the main water mass (which they call Modified East Icelandic Water, or MEIW) formed during winters in the Iceland Sea from the NIIC has a density range of $27.65 \leq \sigma_\theta \leq 27.97 \text{ kg/m}^3$. Therefore, to track how the water masses in this experiment were transformed in the Nordic Seas, we search for particles with the density of MEIW and which are exported to the south below 200m. According to our criteria, approximately 82% of the AW water imported through Denmark Strait is transformed into MEIW within the Nordic Seas. An additional 10% is transformed into even denser water. Overall, water transformed within the Nordic Seas before being exported through the Denmark Strait experiences a mean increase in density of 0.4 kg/m^3 , from $27.39 \pm 0.03 \text{ kg/m}^3$ to $27.82 \pm 0.05 \text{ kg/m}^3$. The associated increase in depth (measured at the sill) is 293m, from $109 \pm 10 \text{ m}$ to $402 \pm 26 \text{ m}$. Figures 4.2.a and 4.2.b show the relevant distributions for these properties, illustrating that outflowing particles are clearly part of a different water mass than the one they entered with and dense enough to feed the overflow waters. The particles fill all the deeper levels of the overflow down to near the sill.

To examine the pathways of the transformed particles and see where the transformation of inflowing AW to denser water is occurring, we plot a subset of particles, by decade, that exit at depths greater than 200 m (Figure 4.2.c). Although some particles do circulate around the Nordic Seas, the majority are transformed north of Iceland. We note many particles take a very short route, recirculating north of Iceland and entering the NIJ to flow back into Denmark Strait (as first suggested by Våge et al. (2011)). Other particles follow Jan Mayen Ridge to circulate around the Iceland Sea. Of those particles not transformed which remain at shallow depths, significantly more circulate the Nordic Seas before leaving in the EGC (Figure 4.2.d). Very few particles enter the interiors of the gyres in the Iceland, Norwegian and Greenland Seas, but that might be a consequence of the model resolution and underestimation of eddy exchange.

4.3.2 ANHA4 experiment

Figure 4.3 shows the number of particles that after entering the Nordic Seas through Denmark Strait in a given month and year, also leaves the Nordic Seas through Denmark Strait at some

point between their time of release and December 31st, 2014. On average, out of the 10000 floats released every January (Figure 4.3) 5223 (52%), entered and left the Nordic Seas through Denmark Strait. In the case of the particles released every April, 5133 (51%) particles leave later through Denmark Strait (Figure 4.3). For those released in July, 5184 (52%), while 5677 (57%) of those released in October leave through Denmark Strait (Figure 4.3). The average number of particles seeded in October is larger compared to the releases in other months. The reason behind this behaviour will be addressed shortly. Given that the details of different release times are qualitatively similar, we shall use the particles released on January 1st 2005 for a case study. We consider this case as it is the one that offers the longest time series in order to capture properly the floats evolution from their release date up to December 2014.

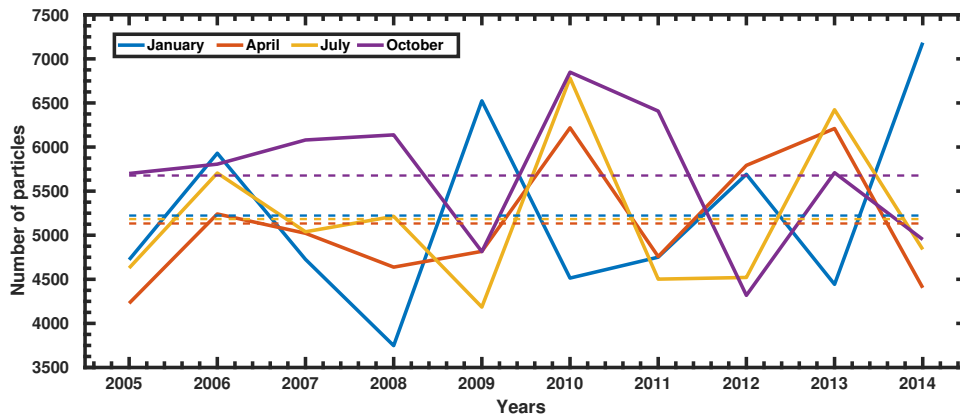


Figure 4.3: Total number of particles entering the Nordic Seas through Denmark Strait every January (solid blue line), April (solid orange line), July (solid yellow line) and October (solid purple line), from 2005 to 2014 and which leave the Nordic Seas through Denmark Strait (not necessarily within the DSOW). Their respective averages are represented with a dashed line of the same color.

Figure 4.4.a shows the trajectories of all the floats released on January 1st, 2005, that enter the Nordic Seas through Denmark Strait, and leave also through Denmark Strait. Out of the 10000 floats released, 4722 floats enter and leave the Nordic Seas through Denmark Strait. In this study we will focus on these floats to study the AW that gets transformed in the Nordic Seas and then leaves through Denmark Strait, potentially contributing to the DSOW. Different possible pathways (20 in total) were identified by using the seven boxes displayed in Figure 4.4.a. The boxes and their positions were chosen to capture all possible different routes through and around the Nordic Seas. The color scale shows how many particles would take a

certain path by considering the boxes they pass through after entering at Denmark Strait.

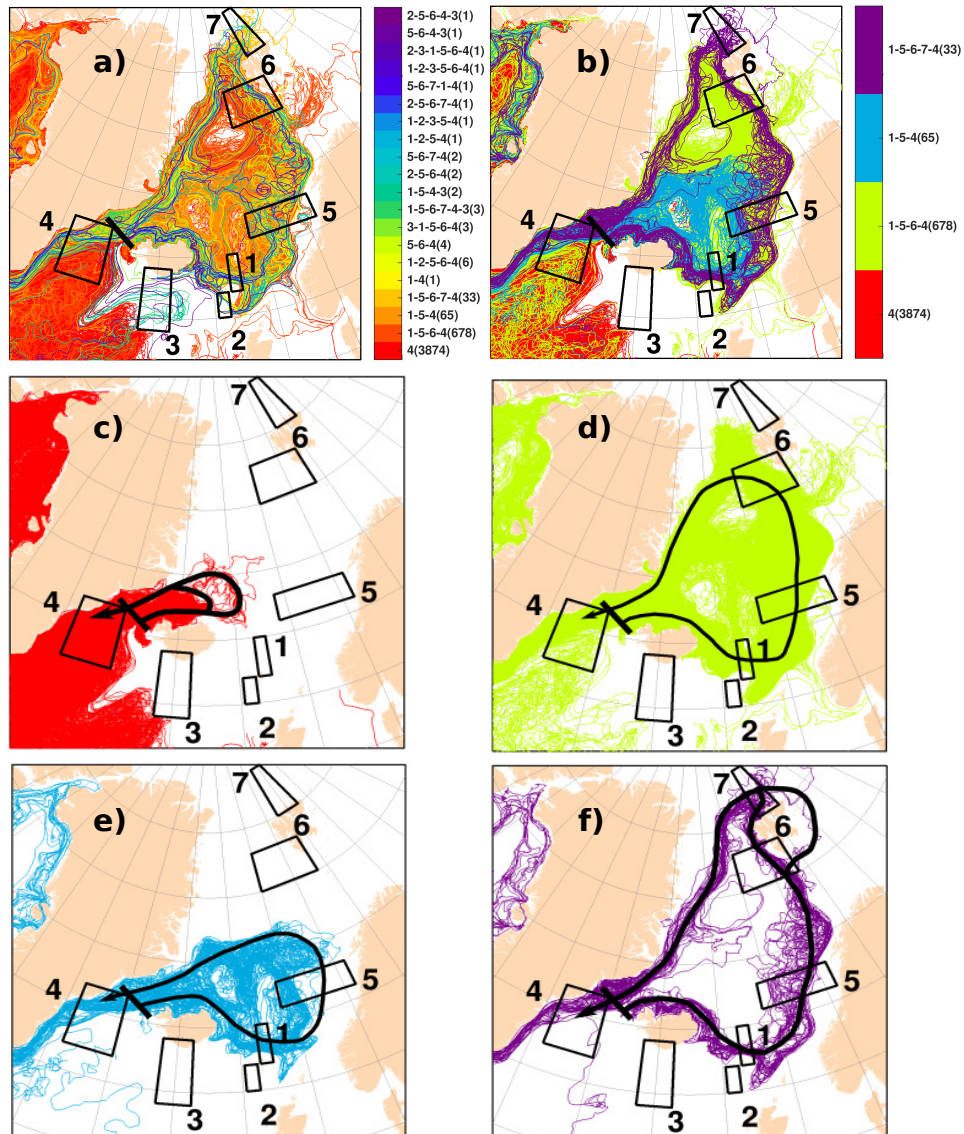


Figure 4.4: For the experiment ANHA4: a) Trajectories of all the particles released on January 1st, 2005 and integrated up to December 31st 2014, entering and leaving the Nordic Seas through Denmark Strait. b) shows the main four routes found for the particles that enter and later leave through Denmark Strait (not necessarily within the DSOW): c) Route 1, d) Route 2, e) Route 3 and f) Route 4. The numbers such as 4 or 1-5-6, represent the number of the boxes the float travels through while the number within brackets tells us how many particles follow the route.

The majority of the particles follow four major routes (Figure 4.4.b). Figures A.1-A.5 show the trajectories of the floats released in other years and months. Although there is some variability the overwhelming feature is that the same four major routes are dominant.

We now focus on those four routes which are separately represented in Figures 4.4.c, 4.4.d, 4.4.e and 4.4.f. Few particles enter the interior of the Greenland, Iceland and Norwegian basins. Most particles remain within the boundary currents. From the 4722 particles entering and leaving the Nordic Seas through Denmark Strait, 3874 (82%) pass only through box 4 before they leave (Figure 4.4.c). Thus these floats only recirculate north of Iceland before leaving the Nordic Seas. There is little exchange into the interior of the Iceland Sea. There is a higher incidence of particles that follow this route if they are released in Denmark Strait in October (Figure A.5). This is a function of the predominant wind pattern over the region at this time of the year (not shown) which is favourable for a strong recirculation of the AW as it enters through Denmark Strait, enhancing exchange out of the Nordic Seas.

A second major route (678 particles, 14.4% of total), 1-5-6-4 (Figures 4.4.b and 4.4.d), represents floats that travel around the entire Nordic Seas within the rim current system circulating around one or more of the Norwegian, Iceland or Greenland gyres. There is still only limited exchange into the interior of the gyres. Two minor routes are shown in Figures 4.4.e and 4.4.f. 65 floats (1.4% of total) enter through Denmark Strait before circulating around the southern Nordic Seas, feeding into the Iceland Sea gyre and returning via the Jan Mayen Current. 33 floats (0.7% of total) follow the rim current without entering any of the three gyres within the Nordic Seas.

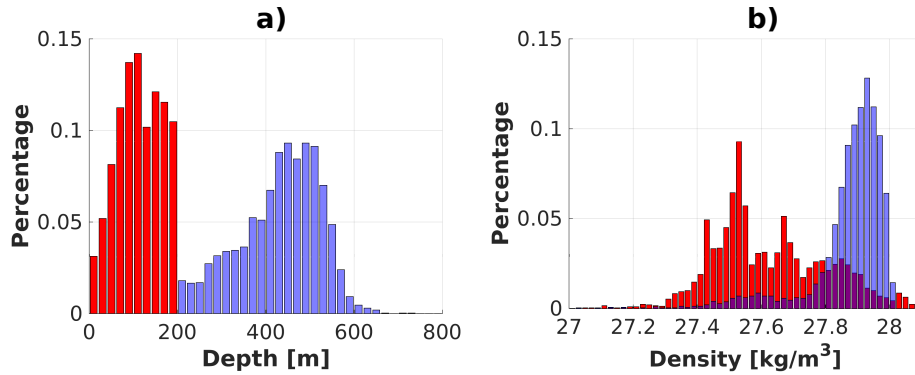


Figure 4.5: a) Depth distributions, in terms of relative percentages, for floats that enter through Denmark Strait (red) and then leave through Denmark Strait (blue) at depths greater than 200 m (as for Figure 4.2.a but for the ANHA4 experiment). Purple shading is used to indicate the percentage for whichever of the inflow/outflow has a smaller percentage in a given bin. b) As for a, but for density.

Figures 4.5.a and 4.5.b (just like in Figure 4.2.a and 4.2.b) illustrate the transformation the

AW undergoes. Figure 4.5 (a and b) clearly shows again how the AW that leaves the Nordic Seas below 200 m is transformed to densities that may be high enough to contribute to the DSOW, and the depth at where they are exported is above the depth of the Denmark Strait sill. Following the MEIW criteria (like in the experiment KAB001), approximately 70% of the water imported by the NIIC gets transformed in the Nordic Seas into MEIW and exported through the Denmark Strait within 10 years. The mean density increase experienced is 0.3 kg/m^3 , from 27.64 ± 0.14 to $27.93 \pm 0.04 \text{ kg/m}^3$. The associated depth increased (measured at the sill) is approximately 314 m, from $86 \pm 1.3 \text{ m}$ to $400 \pm 25 \text{ m}$.

Where within the basin is this transformation occurring? We separate from all the particles following the main four routes those that get transformed to a density high enough to contribute eventually to the DSOW once they leave through Denmark Strait. In order to do so, we first identify the characteristics of the DSOW in the ANHA4 experiment. A TS diagram (Figure B.1) of the water masses in Denmark Strait showed the modelled DSOW as a water mass with density equal to or higher than 27.93 kg/m^3 , colder than 1.5°C and a salinity between 34.9 and 34.95.

Figure 4.6.a shows the density of the selected floats. The floats are found to follow the rim of the deepest basins within the Nordic Seas. There are two regions where the densities reach values between $28.02 - 28.08 \text{ kg/m}^3$: north of Iceland and west and south of Svalbard. The particles transformed north of Iceland appear to be densified as they travel around the rim of the Iceland Sea and while travelling southward within the East Greenland Current. The second region shows floats that are transformed as they travel within the NwAC and the West Spitsbergen Current (WSC).

The depth of the selected floats (Figure 4.6.b) confirms that the transformation is occurring on the continental slope. The deepest floats are found above 900 m, mainly those travelling within the WSC. A few floats following the EGC along the rim of the Iceland Sea and over the Jan Mayen Fracture Zone reach $\sim 800 \text{ m}$ depth. There are two regions where the floats are found at depths shallower than 100 m: north-west of Vestfirðir (north-west of Iceland), mostly in the vicinities of the Ísafjarðjúp Fjord, Iceland, and around Spitsbergen, south and north of Prins Karls Forland, and north of Widgefjorden Fjord, in northern Spitsbergen. The transformation occurring north-west of Vestfirðir is most likely captured in Figure 4.5.b which

shows that there is a small percent of AW that gets transformed to densities higher than 28 kg/m^3 before entering the Nordic Seas. The majority of the floats travelling within the rim current system reach between 300 - 700 m depth.

The floats flowing along the Icelandic shelfbreak show a salinity decrease from 34.95 and 34.92 (Figure 4.6.c). This slight freshening is most likely due to some entrainment from the EGC. The floats that separate from the Icelandic shelfbreak (from north-east of Iceland to the Faroe Islands) show a salinity increase from 34.92 to 34.95. This could occur due to entrainment from the branch of the North Atlantic Currents (NAC) which enters the Nordic Seas across the Iceland-Scotland Ridge. The salinity of most of the floats flowing within the NwAC and the WSC is between 34.945 to 34.95. As we are only showing those floats whose density is equal or denser than 27.93 kg/m^3 , the gap without floats between the Faroe Islands and the NwAC suggests that the already transformed AW is transformed back to lighter densities driven by an increase in the salinity and temperature (Figure 4.6.c) due to entrainment.

As the floats recirculate southward in Fram Strait and enter the EGC, their salinity decreases and is found to be between 34.9 and 34.915 (Figure 4.6.c). Nevertheless there are a few floats within the EGC whose salinity reaches 34.95. Along the EGC, from Scoresby Sund, south-east Greenland, to Denmark Strait, the salinity of the floats decreases down to 34.9. For all the floats flowing within the rim current, it is in this region of the Iceland Plateau where the floats show the lowest salinity. The evolution of the salinity fields point out that oceanographic features like the NwAC and the EGC play a role in the transformation of the AW entering through Denmark Strait.

The shallower floats found north-west of Vestfirðir and south and north of Prins Karls Forland have salinities of 34.95, while those located north of the Widgefjorden Fjord are a bit fresher with a salinity of 34.9. Floats located over the Jan Mayen Fracture Zone have salinities mostly between 34.9 and 34.915. Nevertheless, some of the floats show a salinity of 34.95.

The temperature of the selected floats as they transit around the Nordic Seas is shown in Figure 4.6.d. Over the Iceland Plateau the temperature of the floats goes from 0 to 1.5°C . The floats closer to the Icelandic shelfbreak have a temperature between $1.5 - 2^\circ\text{C}$. The floats located along the eastern part of the Icelandic shelfbreak to the Faroe Islands have a temper-

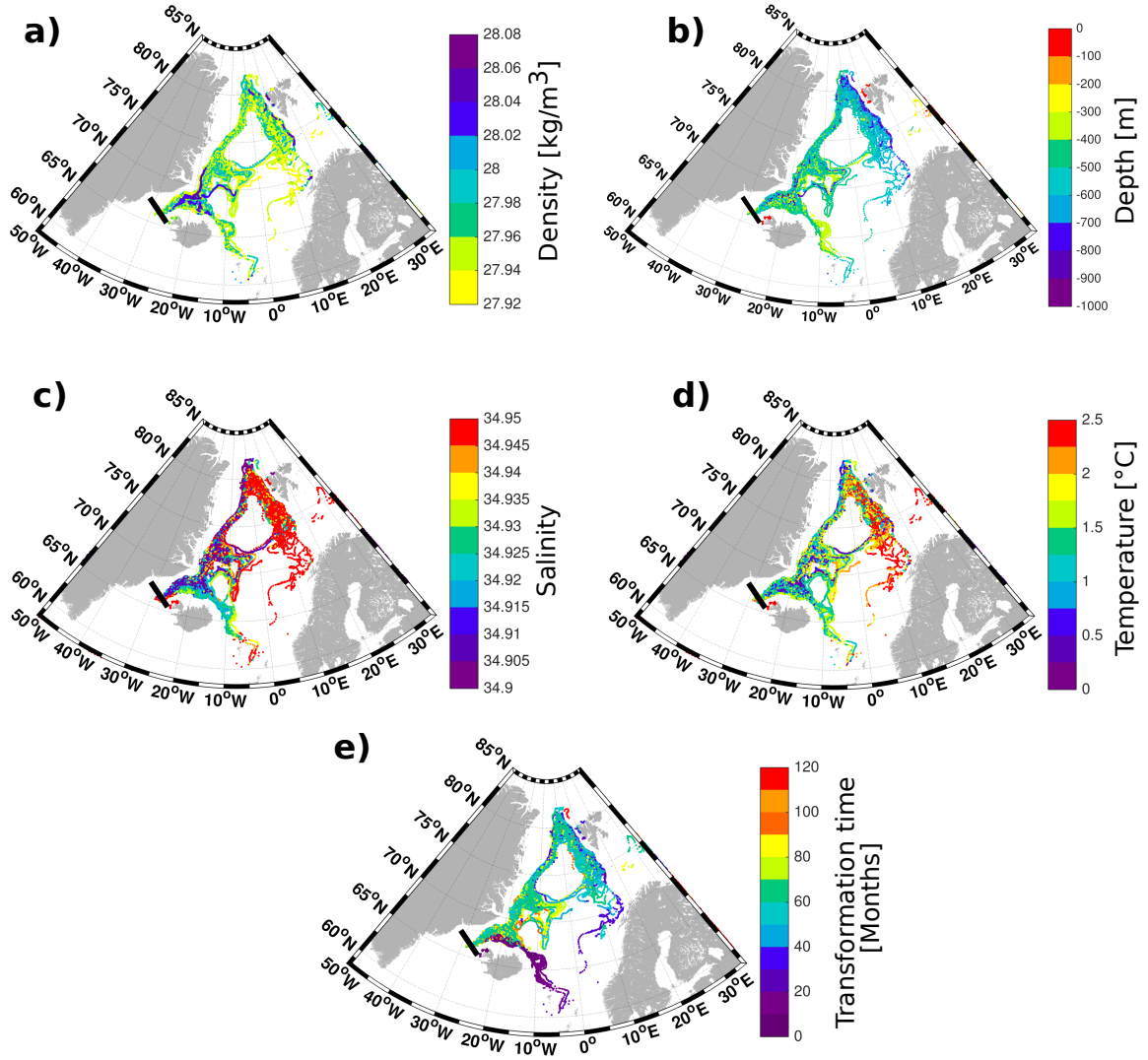


Figure 4.6: Properties of the floats that enter the Nordic Seas within the NIIC and are transformed to DSOW with densities higher than 27.93 kg/m^3 (ANHA4): (a) density, (b) depth, (c) salinity, (d) temperature and (e) transformation time.

ature between $1 - 2^\circ\text{C}$, getting warmer (2.5°C) the closer they get to the Faroe Islands. In general, floats travelling within the NwAC and the WSC have a temperature between $2 - 2.5^\circ\text{C}$. Nevertheless a few particles along the WSC have a lower temperature between $0.25 - 1.5^\circ\text{C}$. The floats flowing within the EGC have a temperature between $0.25 - 2^\circ\text{C}$. The floats found north-west of Vestfirðir have a temperature between $2.25 - 2.5^\circ\text{C}$. The floats north of Prins Karls Forland, as well as those located north of the Widgefjorden Fjord have a temperature between $0.25 - 0.75^\circ\text{C}$.

It takes up to 110 months for the selected floats to enter the Nordic Seas, get transformed to

higher densities and leave later through Denmark Strait, potentially as DSOW (Figure 4.6.e). Within 20 months the floats flowing along the Icelandic shelfbreak travel from Denmark Strait all the way to the Faroe Islands. Those floats following the NwAC and the WSC take between 60 to 70 months to get transformed to overflow-like water. A few floats, mostly those travelling closer to Norway and Spitsbergen shelfbreak, get transformed within 20 to 40 months. That is also the case for the floats found north of Prins Karls Forland, as well as those located north of the Widgefjorden Fjord in Iceland.

Along the EGC the floats show a transformation time around 60 to 80 months. A small number of floats show a travel time up to 100 months, mostly those located over and around Jan Mayen Fracture Zone. The older floats are found around the Iceland Sea, taking up to 110 months.

4.4 NIIC waters transformation north of Iceland

In this section we consider only those floats transformed to densities equal or higher than 27.93 kg/m^3 along the Iceland shelfbreak within 20 months. The main purpose here is to link the transformation of the AW north of Iceland with the NIJ which feeds the DSOW.

We noticed that, in spite of their set-up differences, the analysis from KAB001 and ANHA4 have similar outcomes with the majority of the particles travelling around the shelf system of the Nordic Seas rather than going into the deeper part of the basin (Figures 4.2.c and 4.2.d for KAB001 and Figure 4.4 for ANHA4). It was also shown that both experiments have a similar percentage of particles leaving through Denmark Strait at depth greater than 200 m with overflow-like densities (Figures 4.2.a and 4.2.b for KAB001 and Figures 4.5.a and 4.5.b for ANHA4). At the same time both experiments show that part of the particles are getting transformed in a loop north of Iceland where they reach densities higher than 27.9 kg/m^3 . Thus, we will focus only on the results from the ANHA4 experiment in order to explore the transformation occurring north of Iceland of the waters carried by the NIIC. Even when the experiment KAB001 provides a longer time series, considering that the travel time of the particles taking this route is 1 year from the moment they enter to their export (already transformed) through Denmark Strait, the integration time on the ANHA4 experiment is

enough to explore the process.

Figure 4.7 shows the property evolution of the selected floats along the Icelandic shelfbreak, which are found to follow the 1000-1500 m isobaths. Figure 4.7.a shows the density of those floats which can be as high as 28.04 kg/m^3 . North and north-east of Iceland the floats are found to be not deeper than 600 m, while north-west of Iceland and closer to Denmark Strait the floats are found between 200 - 700 m depth (Figure 4.7.b). The floats located north-west of Vestfirðir (mostly in the interior of the Ísafjarðjúp Fjord, Iceland) are as dense as 27.98 kg/m^3 and not deeper than 100 m (Figure 4.7.b).

As the floats enter the Nordic Seas their salinity decreases during their travel along the Icelandic shelfbreak (Figure 4.7.c). North-west of Iceland and closer to Denmark Strait, the floats located closest to the Icelandic shelfbreak have a salinity around 34.95, while those farther from the shelfbreak have a salinity that goes from 34.9 to 34.92. That difference represents the in-flowing (saltier) and the out-flowing (fresher and transformed) floats. North of Iceland and along the shelfbreak the salinity decreases gradually to 34.91. As the floats continue their travel along the north-eastern Icelandic shelfbreak their salinity increases again up to 34.94.

The along-shelfbreak transformation can also be observed in the evolution of the temperature of the floats (Figure 4.7.d). As the floats enter their temperature decreases from 2.5°C to 0.5°C north of Iceland, where the coldest temperatures are found. North-east of Iceland and along the shelfbreak the temperature increases again up to 2°C . All the transformation mentioned above occurs within 12 months from the moment the floats enter through Denmark Strait (Figure 4.7.e).

Our results point out that, as the water gets transformed to higher densities along the shelfbreak, it eventually cascades into deeper layers of the Iceland Sea driven by the density increase. The transformed waters that contribute to the DSOW find their way towards the strait thanks to the predominant flow pattern along the north Icelandic shelfbreak (Figure 4.8). The seasonal climatology of the current velocity (Figures 4.8.a to 4.8.d) shows that, 100 to 200 km from the Icelandic coast the predominant current direction is towards the west. This will imply that, once that the transformed waters reach a depth greater than 500 m they will be trapped within the westward flow and hence exported out of the Nordic Seas as part

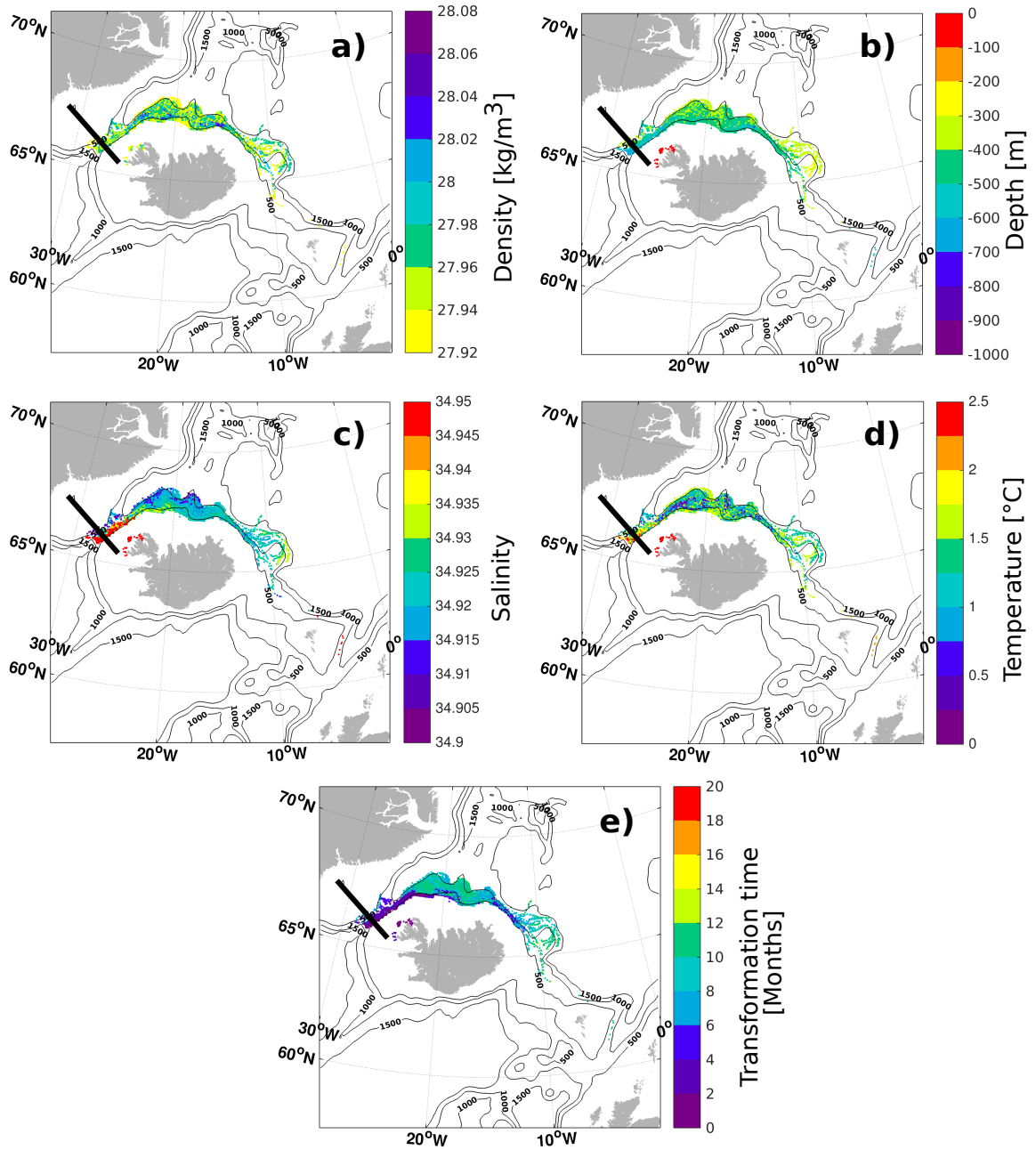


Figure 4.7: Properties of the floats that enter the Nordic Seas within the NIIC and are transformed to densities higher than 27.93 kg/m^3 in less than 1 year (ANHA4): (a) density, (b) depth, (c) salinity, (d) temperature and (e) transformation time.

of the DSOW.

Figure 4.9 shows the monthly climatology of total heat loss for the months October through March, when the heat loss is the highest in the ANHA4 experiment. For each month, the largest heat loss occurs on the shelf surrounding the Nordic Seas (except the Greenland side

most likely due to ice cover conditions), while less heat loss occurs in the interior of the Iceland, Norwegian and Greenland gyres. Also interesting is the strong heat loss that takes place in Denmark Strait. This heat loss is largest near the coast of Iceland, which coincides with the pathway of the NIIC as it enters the Nordic Seas. Along the west coast of Svalbard and coinciding with the pathway of the WSC, the heat loss is also strong mostly during January to March.

Either in Denmark Strait or along the west coast of Svalbard, the heat loss can be as high as 400 W/m^2 in March. This would induce a decrease in the temperature of the AW as it transits, for example, along the Icelandic shelfbreak. This water mass with an already high salt content, would then gain in density as its temperature decreases induced by the strong heat loss.

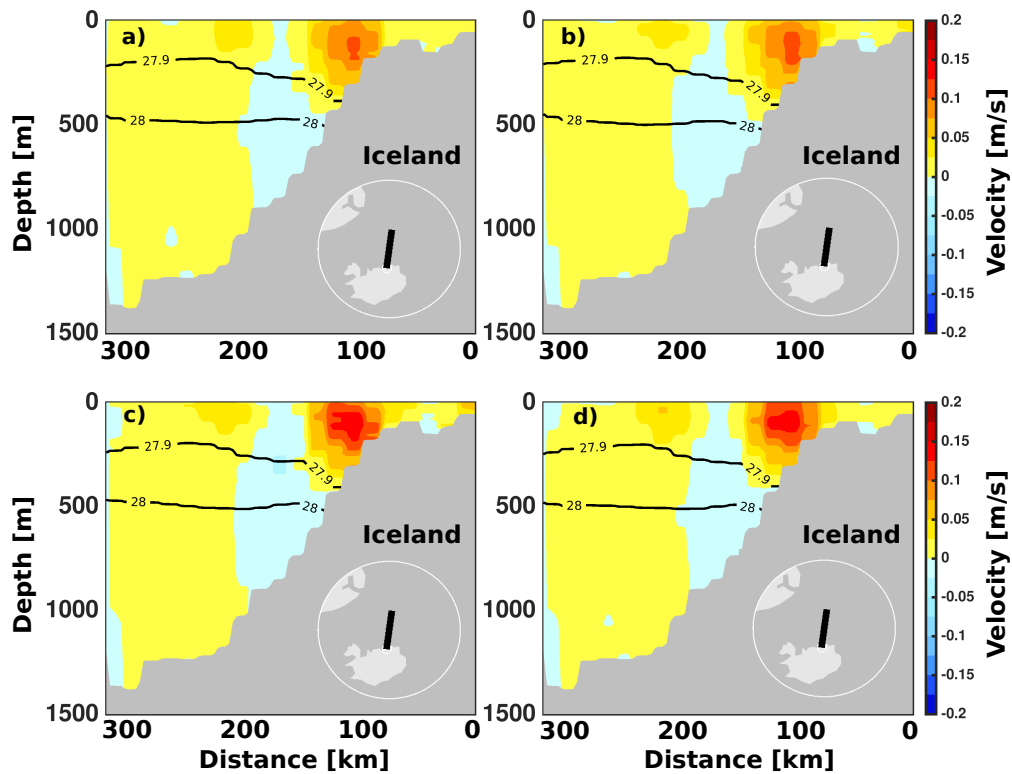


Figure 4.8: Seasonal flow velocity normal to a cross section of the north Icelandic shelfbreak: a) Winter (January to March), b) Spring (April to June), c) Summer (July to September) and d) Fall (October to December). Location of the section is indicated by the map on the lower right corner of each panel. The length of the section is indicated in km.

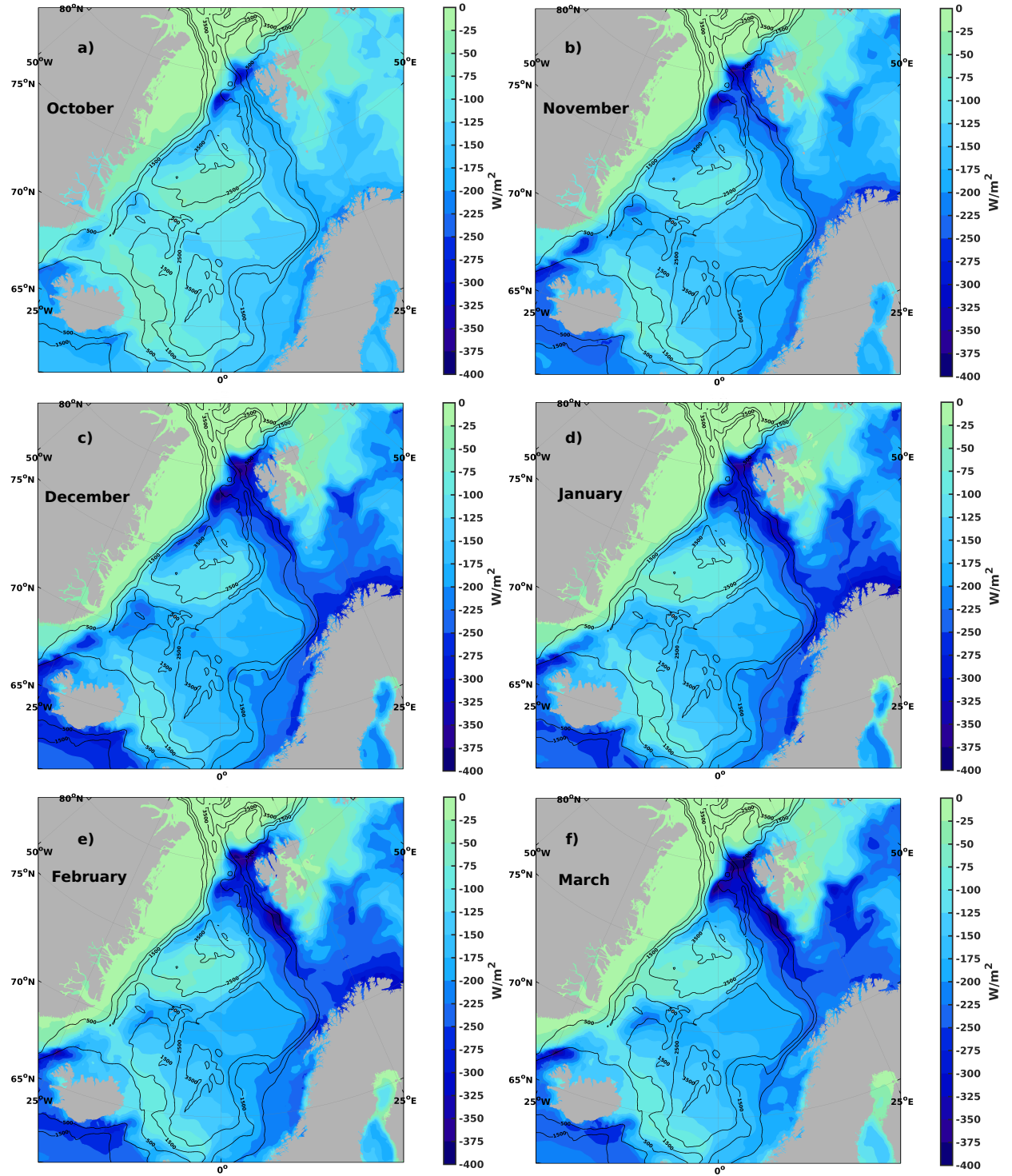


Figure 4.9: Monthly climatology (2005-2014) of total heat loss diagnosed from the experiment ANHA4, for the months: a) October, b) November, c) December, d) January, e) February, and f) March

4.5 Discussion and Conclusions

We have explored the transformation of the NIIC as it enters the Nordic Seas through Denmark Strait as well as the role played by this transformation in supplying the NIJ. We consider this question using two different configurations of an eddy-permitting ocean general circulation model and the off-line Lagrangian tracking tool, Ariane. This tool has been used in other studies examining both the upper and lower limbs of the MOC [e.g. Desbruyères et al. (2013); Lique et al. (2010); Gary et al. (2011, 2012); Lozier et al. (2013)], and is ideal for examining the pathways and properties transformation of a given water mass [e.g. Guillard et al. (prep)]. We thus insert a large numbers of particles at Denmark Strait to track the transformation pathways of the NIIC into the Nordic Seas.

The two configurations used have different setups whose main features appear in Table 4.1. This was done in order to show that our results are robust and independent of the setup of a given model configuration. Both experiments, KAB001 and ANHA4, show that the majority of the particles travel around the shelf system of the Nordic Seas rather than going into the deeper part of the basin (Figures 4.2.c and 4.2.d for KAB001 and Figure 4.4 for ANHA4). Both experiments also have a similar percentage of particles leaving through Denmark Strait at depth greater than 200 m with overflow-like densities (Figures 4.2.a and 4.2.b for KAB001 and Figures 4.5.a and 4.5.b for ANHA4). For the case of the experiment KAB001 we do not explore in details the transformation of the NIIC waters found to occur north of Iceland. We focus on ANHA4 here because of the higher vertical resolution and more recent atmospheric forcing. However as in the case of ANHA4, the experiment KAB001 shows that part of the particles are getting transformed north of Iceland to densities higher than 27.9 kg/m^3 .

The experiment KAB001 shows that, based on the time-line for the particles to leave the Nordic Seas, the residence time for AW carried into the basin within the NIIC is 5 (72 % particles departed) to 10 years (92 % particles departed). However, since the majority of the particles that leave do so untransformed through the Barents Sea Opening and Fram Strait, the residence time for AW in the combined Arctic Mediterranean may be much larger (Rudels et al., 2015). However, we did not consider the role of those particles that entered the Arctic Ocean.

In the case of the ANHA4 experiment, 47% of the total particles (around 10000 each time) released in January 2005, were found to leave the Nordic Seas through Denmark Strait within 10 years. 34% of these particles transformed to densities higher than 27.93 kg/m^3 and fed the DSO within 6 years. This transformation was found to occur in a rim current overturning loop around the Nordic Seas. A faster transformation occurred along the north Icelandic shelfbreak. We found that 30% of the particles inflowing within the NIIC transformed to densities higher than 27.93 kg/m^3 north of Iceland in less than a year. This transformation leads to a contribution to the NIJ which is consistent with the new circulation scheme proposed by Våge et al. (2011).

Despite the statement by Våge et al. (2011) that the transformation of the NIIC occurs inside the Iceland Sea gyre, we find in our analysis that much of the transformation is happening along the north Icelandic shelfbreak. As a matter of fact, both of the experiments used in this study showed that most of the particles inflowing within the NIIC stay on the shelf system rather than entering the Iceland, Norwegian and Greenland gyres. We found this outcome to be in agreement with Jeansson et al. (2008) who, by using water mass analysis from tracer observations, found that the contribution from the Greenland Sea to the DSOW is only 10%, while the remaining 90% was found to have its source in the eastern Nordic Seas and the Arctic Ocean. Our results also agree with Behrens et al. (2017). By using Eulerian and Lagrangian diagnostics they analyse the upstream sources of the DSOW in a global simulation at $1/20^\circ$ resolution, from 1948 to 2009. They found that the sources of the NIJ are mainly originated from the transformation of the NIIC north of Iceland. This transformation, they argue, occurs mainly along the northern Icelandic shelfbreak, contrary to recent findings from Våge et al. (2013) and Våge et al. (2015).

None of the particles transformed to densities higher than 27.93 kg/m^3 within one year were found to pass through the interior of the Iceland Sea gyre (ANHA4 experiment; Figure 4.7). Similarly the particles transformed to the same densities within 6 years along the shelf system of the Nordic Sea, did not enter the Greenland, Norwegian or the Iceland gyres (Figure 4.6). The transformation in less than one year that was found to occur on the Icelandic shelfbreak suggests that the in-phase interannual variability in salinity of the inflowing NIIC with that of the outflowing NIJ (Pickart et al., 2017) might actually be given by the NIIC salinity signal

dictating that of the NIJ.

The transformation of the AW circulating around the Nordic Seas was found to be driven by heat loss. Strong heat loss occurs at Denmark Strait, along the Icelandic shelfbreak, which coincides with the pathway followed by the NIIC. During this transit the density of the Atlantic inflow increases on an average of 0.3 kg/m^3 , from 27.64 ± 0.14 to $27.93 \pm 0.04 \text{ kg/m}^3$, leading to an increase in depth by around 314 m, from 86 ± 1.3 m to 400 ± 25 m. A strong heat loss also occurs for those particles transiting within the NwAC and the WSC, leading to the further transformation of the AW.

This result confirms the hypothesis by Mauritzen (1996) and agrees with the results of Isachsen et al. (2007). By using air-sea fluxes from reanalysis products and climatological hydrographic data, Isachsen et al. (2007) found that a strong light-to-dense transformation takes place east of the Mohn-Knipovich Ridge system, which coincides with the region where we found (Figures 4.9.a - 4.9.f) a strong heat loss happening during the winter months together with light-to-dense water transformation (Figures 4.6.a - 4.6.e). By using air-sea fluxes from reanalysis products and hydrographic data from Argo floats Latarius and Quadfasel (2016) investigated the water mass transformation exclusively in the deepest basins of the Nordic Seas. They found that, in fact, the Greenland Sea does not impact the density of the overflow water, given that much of the density transformation was found to occur, agreeing with Isachsen et al. (2007), in the eastern basins of the Nordic Seas.

We do not expand here on to what causes the heat loss pattern in the Nordic Seas as it is not under the scope of our study. However, given its role on driving the AW transformation it is a topic that needs further study. An increase in the air temperature over the Nordic Seas will imply, eventually, a reduction in the oceanic heat loss and hence a decrease in the light-to-dense transformation of the AW occurring north of Iceland and in the eastern shelf system of the Nordic Seas. This will be reflected in the overflow strength and the Atlantic MOC.

One limitation of the simulations used in this study is that the underlying model used is only eddy-permitting, with resolution insufficient to resolve all the eddies (Hallberg, 2013). One of the main mechanisms by which AW and therefore particles, is exchanged out of the boundary currents is thus missing. However similar analysis carried out using $1/12^\circ$ resolution

(not shown) confirmed that the transformation does occur along the shelf system in the Nordic Seas, and not within the Iceland, Norwegian and Greenland gyres. Given that the particles leaving the Nordic Seas through Denmark Strait reach densities of $\geq 27.92 \text{ kg/m}^3$ confirms that even the most dense parts of the overflows can come from boundary current transformations, rather than deep convection in the interior of the Nordic Seas. That said, we can not rule out other sources, including interior deep waters, contributing to the overflow.

In a model inter-comparison study using passive tracers to track pathways of melt waters from the Greenland Ice Sheet, Dukhovskoy et al. (2016) showed that the take-up of the tracer in the interior of the Nordic Seas was about double, over 10 years, using a $1/12^\circ$ degree model as compared to a $1/4^\circ$ simulation. However, the same study showed that some of the Greenland melt passive tracer reached the interior of the Greenland Sea in the $1/4^\circ$ model, mainly via the East Greenland Current. Therefore, although it would be useful to perform a study similar to ours at higher resolution, we believe that our narrative of the majority of inflow transformation occurring in the Nordic Seas boundary currents (as opposed to gyres interior) is not unrealistic. Thus, provided that AW is still transformed by winter cooling in the boundary currents, even a significant influx of fresh water to the interior of the Nordic Seas (leading to a prolonged cessation of convection) may not have a significant impact on the local overflow strength and global MOC.

4.6 Acknowledgements

We gratefully acknowledge the financial and logistic support of grants from the Natural Sciences and Engineering Research Council (NSERC) of Canada. These includes a Discovery Grant (rgpin227438-09) awarded to P.G. Myers, Climate Change and Atmospheric Research Grant (VITALS - RGPCC 433898), and an International Create (ArcTrain - 432295). We are grateful to the NEMO development team and the Drakkar project for providing the model and continuous guidance, and to Westgrid and Compute Canada for computational resources. We would also like to thank G. Smith for the CGRF forcing fields, made available by Environment and Climate Change Canada. Output from the KAB001 run of ORCA025 was provided by C. Boening's group at GEOMAR, Kiel, Germany. To gain access to the dataset used in this

study please contact Paul G. Myers.

Bibliography

- Aagaard, K., J. H. Swift, and E. C. Carmack (1985), Thermohaline circulation in the Arctic Mediterranean Seas, *Journal of Geophysical Research: Oceans*, *90*(C3), 4833–4846, doi:10.1029/JC090iC03p04833.
- Bamber, J., M. den Broeke, J. Ettema, J. Lenaerts, and E. Rignot (2012), Recent large increases in freshwater fluxes from Greenland into the North Atlantic, *Geophysical Research Letters*, *39*(19), doi:10.1029/2012GL052552.
- Behrens, E., A. Biastoch, and C. W. Böning (2013), Spurious AMOC trends in global ocean sea-ice models related to subarctic freshwater forcing, *Ocean Modelling*, *69*, 39 – 49, doi:https://doi.org/10.1016/j.ocemod.2013.05.004.
- Behrens, E., K. Våge, B. Harden, A. Biastoch, and C. W. Böning (2017), Composition and variability of the Denmark Strait Overflow Water in a high-resolution numerical model hindcast simulation, *Journal of Geophysical Research: Oceans*, *122*(4), doi:10.1002/2016JC012158.
- Bernard, B., G. Madec, T. Penduff, J.-M. Molines, A.-M. Treguier, J. L. Sommer, A. Beckmann, A. Biastoch, C. Böning, J. Dengg, C. Derval, E. Durand, S. Gulev, E. Remy, C. Talandier, S. Theetten, M. Maltrud, J. McClean, and B. D. Cuevas (2006), Impact of partial steps and momentum advection schemes in a global ocean circulation model at eddy-permitting resolution, *Ocean Dynamics*, *56*(5-6), 543–567, doi:10.1007/s10236-006-0082-1.
- Biastoch, A., C. W. Böning, J. Getzlaff, J.-M. Molines, and G. Madec (2008), Causes of Interannual–Decadal Variability in the Meridional Overturning Circulation of the Mid-latitude North Atlantic Ocean, *Journal of Climate*, *21*(24), 6599–6615, doi:10.1175/2008JCLI2404.1.
- Blanke, B., and S. Raynaud (1997), Kinematics of the Pacific Equatorial Undercurrent: An Eulerian and Lagrangian approach from GCM results, *Journal of Physical Oceanography*, *27*(6), 1038–1053, doi:10.1175/1520-0485(1997)027<1038:KOTPEU>2.0.CO;2.
- Blanke, B., M. Arhan, G. Madec, and S. Roche (1999), Warm water paths in the Equatorial

- Atlantic as diagnosed with a General Circulation Model, *Journal of Physical Oceanography*, *29*(11), 2753–2768, doi:10.1175/1520-0485(1999)029<2753:WWPITE>2.0.CO;2.
- Dai, A., T. Qian, K. E. Trenberth, and J. D. Milliman (2009), Changes in continental freshwater discharge from 1948 to 2004, *Journal of Climate*, *22*(10), 2773–2792, doi:10.1175/2008JCLI2592.1.
- Desbruyères, D., V. Thierry, and H. Mercier (2013), Simulated decadal variability of the meridional overturning circulation across the A25-Ovide section, *Journal of Geophysical Research: Oceans*, *118*(1), 462–475, doi:10.1029/2012JC008342.
- Dickson, R. R., and J. Brown (1994), The production of north atlantic deep water: Sources, rates, and pathways, *Journal of Geophysical Research: Oceans*, *99*(C6), 12,319–12,341, doi:10.1029/94JC00530.
- DRAKKAR Group (2007), Eddy-permitting ocean circulation hindcasts of past decades, *CLIVAR Exchanges*, *12*(3), 8 – 10.
- Drinkwater, K., E. Colbourne, H. Loeng, S. Sundby, and T. Kristiansen (2013), Comparison of the atmospheric forcing and oceanographic responses between the Labrador Sea and the Norwegian and Barents seas, *Progress in Oceanography*, *114*, 11 – 25, doi:https://doi.org/10.1016/j.pocean.2013.03.007.
- Dukhovskoy, D. S., P. G. Myers, G. Platov, M.-L. Timmermans, B. Curry, A. Proshutinsky, J. L. Bamber, E. Chassignet, X. Hu, C. M. Lee, and R. Somavilla (2016), Greenland freshwater pathways in the sub-Arctic Seas from model experiments with passive tracers, *Journal of Geophysical Research: Oceans*, *121*(1), 877–907, doi:10.1002/2015JC011290.
- Eldevik, T., J. E. Ø. Nilsen, D. Iovino, K. A. Olsson, A. B. Sandø, and H. Drange (2009), Observed sources and variability of Nordic seas overflow, *Nature Geoscience*, *2*(6), 406–410, doi:10.1038/ngeo518.
- Ferry, N., L. Parent, S. Masina, A. Storto, H. Zuo, and M. Balmaseda (2016), *Product user manual for Global Ocean Reanalysis Products GLOBAL-REANALYSIS-PHYS-001-*

009, *GLOBAL-REANALYSIS-PHYS-001-011 and GLOBAL-REANALYSIS-PHYS-001-017*, EU Copernicus Marine Service.

- Fichefet, T., and M. Maqueda (1997), Sensitivity of a global sea ice model to the treatment of ice thermodynamics and dynamics, *Journal of Geophysical Research: Oceans (1978–2012)*, *102*(C6), 12,609–12,646, doi:10.1029/97JC00480.
- Fischer, J., J. Karstensen, R. Zantopp, M. Visbeck, A. Biastoch, E. Behrens, C. Böning, D. Quadfasel, K. Jochumsen, H. Valdimarsson, S. Jónsson, S. Bacon, N. Holliday, S. Dye, M. Rhein, and C. Mertens (2015), Intra-seasonal variability of the DWBC in the western subpolar North Atlantic, *Progress in Oceanography*, *132*, 233 – 249, doi:10.1016/j.pocean.2014.04.002.
- Gary, S. F., M. S. Lozier, C. W. Böning, and A. Biastoch (2011), Deciphering the pathways for the deep limb of the meridional overturning circulation, *Deep Sea Research Part II: Topical Studies in Oceanography*, *58*(17), 1781 – 1797, doi:10.1016/j.dsr2.2010.10.059.
- Gary, S. F., M. S. Lozier, A. Biastoch, and C. W. Böning (2012), Reconciling tracer and float observations of the export pathways of Labrador Sea Water, *Geophysical Research Letters*, *39*(24), doi:10.1029/2012GL053978.
- Gerdes, R., W. Hurlin, and S. M. Griffies (2006), Sensitivity of a global ocean model to increased run-off from Greenland, *Ocean Modelling*, *12*(3), 416 – 435, doi:10.1016/j.ocemod.2005.08.003.
- Gillard, L. C., X. Hu, P. G. Myers, and J. L. Bamber (2016), Meltwater pathways from marine terminating glaciers of the Greenland ice sheet, *Geophysical Research Letters*, *43*(20), 10,873–10,882, doi:10.1002/2016GL070969, 2016GL070969.
- Griffies, S. M., A. Biastoch, C. Böning, F. Bryan, G. Danabasoglu, E. P. Chassignet, M. H. England, R. Gerdes, H. Haak, R. W. Hallberg, et al. (2009), Coordinated ocean-ice reference experiments (COREs), *Ocean Modelling*, *26*(1), 1–46, doi:10.1016/j.ocemod.2008.08.007.
- Hallberg, R. (2013), Using a resolution function to regulate parameterizations of oceanic mesoscale eddy effects, *Ocean Modelling*, *72*, 92 – 103, doi:10.1016/j.ocemod.2013.08.007.

- Hansen, B., and S. Østerhus (2000), North Atlantic–Nordic Seas exchanges, *Progress in Oceanography*, 45(2), 109–208, doi:10.1016/S0079-6611(99)00052-X.
- Hansen, B., and S. Østerhus (2007), Faroe Bank Channel Overflow 1995–2005, *Progress in Oceanography*, 75(4), 817–856, doi:10.1016/j.pocean.2007.09.004.
- Hansen, B., W. R. Turrell, and S. Østerhus (2001), Decreasing overflow from the Nordic seas into the Atlantic Ocean through the Faroe Bank channel since 1950, *Nature*, 411(6840), 927–930, doi:10.1038/35082034.
- Harden, B., R. Pickart, H. Valdimarsson, K. Våge, L. de Steur, C. Richards, F. Bahr, D. Torres, E. Børve, S. Jónsson, A. Macrander, S. Østerhus, L. Håvik, and T. Hattermann (2016), Upstream sources of the Denmark Strait Overflow: Observations from a high-resolution mooring array, *Deep Sea Research Part I: Oceanographic Research Papers*, 112, 94 – 112, doi:10.1016/j.dsr.2016.02.007.
- Holdsworth, A. M., and P. G. Myers (2015), The influence of high-frequency atmospheric forcing on the circulation and deep convection of the Labrador Sea, *Journal of Climate*, 28(12), 4980–4996, doi:10.1175/JCLI-D-14-00564.1.
- Hu, A., G. A. Meehl, W. Han, and J. Yin (2011), Effect of the potential melting of the Greenland Ice Sheet on the Meridional Overturning Circulation and global climate in the future, *Deep Sea Research Part II: Topical Studies in Oceanography*, 58(17), 1914 – 1926, doi:10.1016/j.dsr2.2010.10.069.
- Hu, X., and P. G. Myers (2013), A Lagrangian view of Pacific water inflow pathways in the Arctic Ocean during model spin-up, *Ocean Modelling*, 71, 66–80, doi:10.1016/j.ocemod.2013.06.0077.
- Isachsen, P. E., C. Mauritzen, and H. Svendsen (2007), Dense water formation in the Nordic Seas diagnosed from sea surface buoyancy fluxes, *Deep Sea Research Part I: Oceanographic Research Papers*, 54(1), 22–41, doi:10.1016/j.dsr.2006.09.008.
- Jeansson, E., S. Jutterström, B. Rudels, L. G. Anderson, K. A. Olsson, E. P. Jones, W. M. Smethie, and J. H. Swift (2008), Sources to the east greenland current and its contribution

- to the denmark strait overflow, *Progress in Oceanography*, 78(1), 12 – 28, doi:10.1016/j.pocean.2007.08.031.
- Jochumsen, K., D. Quadfasel, H. Valdimarsson, and S. Jónsson (2012), Variability of the Denmark Strait overflow: Moored time series from 1996–2011, *Journal of Geophysical Research: Oceans*, 117(C12), doi:10.1029/2012JC008244.
- Jochumsen, K., M. Moritz, N. Nunes, D. Quadfasel, K. M. H. Larsen, B. Hansen, H. Valdimarsson, and S. Jonsson (2017), Revised transport estimates of the Denmark Strait overflow, *Journal of Geophysical Research: Oceans*, 122(4), 3434–3450, doi:10.1002/2017JC012803.
- Large, W. G., and S. G. Yeager (2009), The global climatology of an interannually varying air–sea flux data set, *Climate Dynamics*, 33(2), 341–364, doi:10.1007/s00382-008-0441-3.
- Latarius, K., and D. Quadfasel (2016), Water mass transformation in the deep basins of the nordic seas: Analyses of heat and freshwater budgets, *Deep Sea Research Part I: Oceanographic Research Papers*, 114, 23 – 42, doi:10.1016/j.dsr.2016.04.012.
- Lique, C., A. M. Treguier, B. Blanke, and N. Grima (2010), On the origins of water masses exported along both sides of Greenland: A Lagrangian model analysis, *Journal of Geophysical Research: Oceans*, 115(C5), doi:10.1029/2009JC005316.
- Lozier, M. S., S. F. Gary, and A. S. Bower (2013), Simulated pathways of the overflow waters in the North Atlantic: Subpolar to subtropical export, *Deep Sea Research Part II: Topical Studies in Oceanography*, 85, 147 – 153, doi:http://dx.doi.org/10.1016/j.dsr2.2012.07.037.
- Macrandar, A., U. Send, H. Valdimarsson, S. Jónsson, and K. R. H. (2005), Interannual changes in the overflow from the Nordic Seas into the Atlantic Ocean through Denmark Strait, *Geophysical Research Letters*, 32(6), doi:10.1029/2004GL021463.
- Madec, G. and the NEMO team (2008), *NEMO ocean engine*, Note du Pôle de modélisation, Institut Pierre-Simon Laplace (IPSL), France, No 27, ISSN No 1288-1619.
- Mauritzen, C. (1996), Production of dense overflow waters feeding the North Atlantic across the Greenland-Scotland Ridge. Part 1: Evidence for a revised circulation scheme, *Deep*

- Sea Research Part I: Oceanographic Research Papers*, 43(6), 769 – 806, doi:10.1016/0967-0637(96)00037-4.
- Mertens, C., M. Rhein, M. Walter, C. W. Böning, E. Behrens, D. Kieke, R. Steinfeldt, and U. Stöber (2014), Circulation and transports in the newfoundland basin, western subpolar north atlantic, *Journal of Geophysical Research: Oceans*, 119(11), 7772–7793, doi:10.1002/2014JC010019.
- More, C. (2010), Circulation patterns and outflow characteristics across the Greenland-Scotland Ridge of North Atlantic Current water in the Nordic Sea, Master’s thesis, University of Alberta, Edmonton, Alberta, Canada.
- Müller, V., D. Kieke, P. G. Myers, C. Pennelly, and C. Mertens (2017), Temperature flux carried by individual eddies across 47°N in the Atlantic Ocean, *Journal of Geophysical Research: Oceans*, 122(3), 2441–2464, doi:10.1002/2016JC012175.
- Orvik, K. A., and P. Niiler (2002), Major pathways of atlantic water in the northern north atlantic and nordic seas toward arctic, *Geophysical Research Letters*, 29(19), 2–1–2–4, doi:10.1029/2002GL015002.
- Pickart, R. S., M. A. Spall, D. J. Torres, K. Våge, H. Valdimarsson, C. Nobre, G. W. K. Moore, S. Jonsson, and D. Mastropole (2017), The North Icelandic Jet and its relationship to the North Icelandic Irminger Current, *Journal of Marine Research*, 75(5), 605–639, doi:10.1357/002224017822109505.
- Rhein, M. (1991), Ventilation rates of the Greenland and Norwegian Seas derived from distributions of the chlorofluoromethanes F11 and F12, *Deep Sea Research Part A. Oceanographic Research Papers*, 38(4), 485 – 503, doi:10.1016/0198-0149(91)90048-K.
- Rudels, B., M. Korhonen, U. Schauer, S. Pisarev, B. Rabe, and A. Wisotzki (2015), Circulation and transformation of Atlantic water in the Eurasian Basin and the contribution of the Fram Strait inflow branch to the Arctic Ocean heat budget, *Progress in Oceanography*, 132, 128 – 152, doi:10.1016/j.pocean.2014.04.003.

- Schlosser, P., G. Bönisch, M. Rhein, and R. Bayer (1991), Reduction of deepwater formation in the greenland sea during the 1980s: Evidence from tracer data, *Science*, *251*(4997), 1054–1056, doi:10.1126/science.251.4997.1054.
- Send, U., M. Lankhorst, and T. Kanzow (2011), Observation of decadal change in the Atlantic meridional overturning circulation using 10 years of continuous transport data, *Geophysical Research Letters*, *38*(24), doi:10.1029/2011GL049801.
- Smith, G. C., F. Roy, P. Mann, F. Dupont, B. Brasnett, J.-F. Lemieux, S. Laroche, and S. Bélair (2014), A new atmospheric dataset for forcing ice–ocean models: Evaluation of reforecasts using the Canadian global deterministic prediction system, *Quarterly Journal of the Royal Meteorological Society*, *140*(680), 881–894, doi:10.1002/qj.2194.
- Somavilla, R., U. Schauer, and G. Budéus (2013), Increasing amount of Arctic Ocean deep waters in the Greenland Sea, *Geophysical Research Letters*, *40*(16), 4361–4366, doi:10.1002/grl.50775.
- Stouffer, R. J., J. Yin, J. M. Gregory, K. W. Dixon, M. J. Spelman, W. Hurlin, A. J. Weaver, M. Eby, G. M. Flato, H. Hasumi, A. Hu, J. H. Jungclaus, I. V. Kamenkovich, A. Levermann, M. Montoya, S. Murakami, S. Nawrath, A. Oka, W. R. Peltier, D. Y. Robitaille, A. Sokolov, G. Vettoretti, and S. L. Weber (2006), Investigating the causes of the response of the thermohaline circulation to past and future climate changes, *Journal of Climate*, *19*(8), 1365–1387, doi:10.1175/JCLI3689.1.
- Swingedouw, D., P. Braconnot, P. Delecluse, E. Guilyardi, and O. Marti (2007), The impact of global freshwater forcing on the thermohaline circulation: adjustment of North Atlantic convection sites in a CGCM, *Climate Dynamics*, *28*(2-3), 291–305, doi:10.1007/s00382-006-0171-3.
- Våge, K., R. S. Pickart, M. A. Spall, H. Valdimarsson, S. Jonsson, D. J. Torres, S. Østerhus, and T. Eldevik (2011), Significant role of the North Icelandic Jet in the formation of Denmark Strait overflow water, *Nature Geoscience*, *4*, 723 – 727, doi:10.1038/ngeo1234.
- Våge, K., R. S. Pickart, M. A. Spall, G. Moore, H. Valdimarsson, D. J. Torres, S. Y. Erofeeva,

- and J. E. Ø. Nilsen (2013), Revised circulation scheme north of the Denmark Strait, *Deep Sea Research Part I: Oceanographic Research Papers*, 79, 20 – 39, doi:10.1016/j.dsr.2013.05.007.
- Våge, K., G. Moore, S. Jónsson, and H. Valdimarsson (2015), Water mass transformation in the Iceland Sea, *Deep Sea Research Part I: Oceanographic Research Papers*, 101, 98 – 109, doi:10.1016/j.dsr.2015.04.001.
- Weijer, W., M. E. Maltrud, M. W. Hecht, H. A. Dijkstra, and M. A. Kliphuis (2012), Response of the Atlantic Ocean circulation to Greenland Ice Sheet melting in a strongly-eddy ocean model, *Geophysical Research Letters*, 39(9), doi:10.1029/2012GL051611, 109606.
- Yang, J., and L. J. Pratt (2013), On the Effective Capacity of the Dense-Water Reservoir for the Nordic Seas Overflow: Some Effects of Topography and Wind Stress, *Journal of Physical Oceanography*, 43(2), 418–431, doi:10.1175/JPO-D-12-087.1.
- Yashayaev, I., and D. Seidov (2015), The role of the Atlantic Water in multidecadal ocean variability in the Nordic and Barents Seas, *Progress in Oceanography*, 132, 68–127, doi: 10.1016/j.pocean.2014.11.009.

Chapter 5

The North Icelandic Jet is fed by transformation of Atlantic Waters on the Icelandic shelf

Planned to submit October 2019 to Nature Geoscience. **Garcia-Quintana, Y.**, Hu X., & Myers P.G.

ABSTRACT

Exchange flows between the sub-polar North Atlantic and the Arctic Ocean via the Nordic Seas are key components of the global climate system. The northward heat transport by the Atlantic Water affects Arctic sea ice and land ice cover, ecosystems, European weather and global climate, while the southward deep overflows feed the abyssal limb of the Atlantic Meridional Overturning Circulation (AMOC), influencing global climate. Here we explore a potential source for the North Icelandic Jet, the densest component of the AMOC. To do so, we use an eddy-permitting, $1/12^\circ$ regional configuration of the Nucleus for European Modelling of the Ocean (NEMO). We examine the transformation of the North Icelandic Irminger Current (NIIC) in a region of the northwest Icelandic shelf and the large-scale circulation response, over the period 2002 to 2018. We propose an overturning loop where the upper limb is the transformation of the NIIC on the Icelandic shelf, and the NIJ being the lower limb. Strong winter heat lost on the northwest Icelandic shelf increases the density of the NIIC waters,

allowing them to sink to the shelf bottom. A dense (denser than 27.8 kg/m^3) plume is generated as a result and travels anticyclonically on the Icelandic shelf from the formation region, cascading down slope north of Iceland forced by bathymetric irregularities. As a response to the dense plume a depression in the sea surface high propagates also anticyclonically from the formation region which in turns generates an offshore cyclonic flow that carries the dense waters back towards Denmark Strait, as they cascade. The mean transport of dense waters (denser than 27.8 kg/m^3) crossing the 500 m isobath towards deeper layers, north of Iceland, was found to be in the range 0.25 - 1.25 Sv (seasonally changing), which is sufficient to feed the observed transport of the NIJ. The dense water formation process has its maximum generally from December to March. The dense water formation timing points out for it to be the source of the strong regime of the NIJ. The identified loop can be dynamically explained by previous modelling work exploring the large-scale circulation response to dense water formation near an island. Observational data from 1929 to present confirms the presence of waters denser than 28 kg/m^3 in the study region.

5.1 Introduction

The Nordic Seas comprise the Iceland, Greenland and Norwegian Seas. The basin (Figure 4.1) plays an important role in the dynamics of the climate of the North Atlantic realm (Drinkwater et al., 2013). Compared to its latitude it has the strongest positive sea surface and air temperature anomalies in the world, and is a region particularly important for water mass modification and formation (Mauritzen, 1996; Eldevik et al., 2009; Våge et al., 2011) and air-sea interaction (Eldevik et al., 2009). It is the major transport route for freshwater, ice and heat between the North Atlantic and the Arctic Oceans (Hawker, 2005). The inflow of warm, salty Atlantic waters and the outflow of ice and cold, fresh Arctic waters, form two major components of the Nordic Seas circulation, and influence the long-term variability of the overflows into the North Atlantic. Dense water formed in the Nordic Seas overflows the ridges and sinks in the North Atlantic (Dickson et al., 2008). The overflow through Denmark Strait provides the densest component of the North Atlantic Deep Water, a principal component of the AMOC (e.g., Jochumsen et al., 2017).

The Denmark Strait Overflow Water (DSOW) is the largest dense water plume from the Nordic Seas to feed the lower limb of the Atlantic Meridional Overturning Circulation. The strength of the DSOW has been observed at the sill for over a decade with its transport estimated to be around 3 to 3.5 Sv (Våge et al., 2013; Jochumsen et al., 2015; Harden et al., 2016; Jochumsen et al., 2017). Its upstream sources, however, are still a topic of study (Våge et al., 2011, 2013, 2015; Pickart et al., 2017; Huang et al., 2019). Its primary source was commonly thought to be the East Greenland Current (EGC). However, Jonsson and Valdimarsson (2004) presented the first evidence of a previously unknown current that flows along the continental slope of Iceland towards the Denmark Strait: the North Icelandic Jet (NIJ) (Figure 5.1). They used vessel mounted ADCP (acoustic doppler currentmeter profiler) and CTD (conductivity, temperature and density) measurements taken along three sections located north and north-west of Iceland, in November 2001 and 2002 (see their manuscript for more details). They found the current to be narrow, of about 15-20 km wide, and extending from 500-700 m depth up to about 100 m depth, without reaching the surface. Their observations from 2002 estimated the NIJ transport to be 2.7 Sv ($1 \text{ Sv} = 10^6 \text{ m}^3/\text{s}$). Hence, they argued, the transport of the NIJ is sufficient to account for a major part of the transport of the DSOW as measured at the sill, assuming some entrainment of ambient water along the route. In fact Mastropole et al. (2017) found that the deepest part of the DSOW in the Denmark Strait to be linked with the NIJ waters. Jonsson and Valdimarsson (2004) also claimed the NIJ can be traced from the sill back into the Iceland Sea. This represented a new scenario for the formation of DSOW and it raised questions about this crucial component of the Earth's climate system.

Later on, Våge et al. (2011) showed that, indeed, the NIJ supplied approximately half of the total overflow transport. They used two high-resolution hydrographic (CTD) and velocity (mounted as well as upward and downward-facing lowered ADCP systems) surveys, which were carried out in October 2008 and in August 2009. During the two surveys they found the NIJ to be the primary source of the densest component of the DSOW. Their manuscript also includes simulations with an ocean general circulation model that suggests that the import of warm, salty water from the North Icelandic Irminger Current (NIIC) and water-mass transformation in the interior of the Iceland Sea, are critical to the formation of the NIJ.

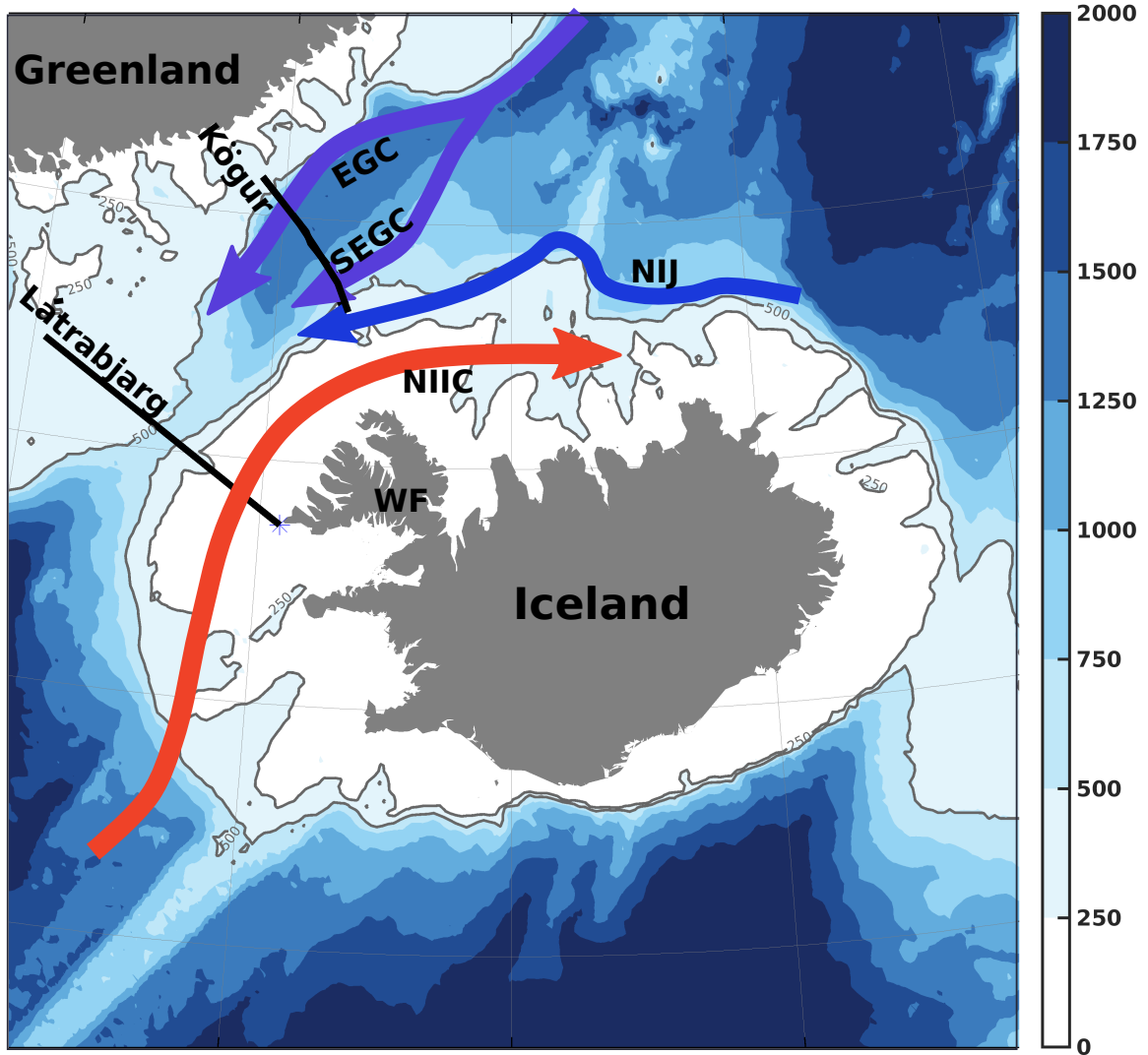


Figure 5.1: Schematic, following Våge et al. (2013), showing the main currents northwest of Iceland: shelfbreak East Greenland Current (EGC), separated East Greenland Current (SEGC), North Icelandic Irminger Current (NIIC) and the North Icelandic Jet (NIJ). The sections Kögur and Látrabjarg used in the sub-section Model Evaluation are represented by black lines. The region called Westfjords (WF) located on the northwest coast of Iceland is also indicated. The color scale indicates the ocean depth in meters.

The origin of the NIJ has been topic of various studies, and still nowadays questions about its origin, dynamics, variability and pathways, remain. Following its discovery by Jonsson and Valdimarsson (2004), it was suggested that the NIJ was not an independent current, but rather a branch of the EGC that bifurcates upstream of the strait (Köhl et al., 2007). In a numerical model study Köhl (2010), on the other hand, proposed that the source of the NIJ was linked to the magnitude of the cyclonic wind stress curl in the region. They claimed that when the

curl is strong the NIJ has its origin in the EGC. On the contrary, when the curl was weak the source of the NIJ was in the northern Iceland Sea, fed by an "offshoot of the weakening cyclonic circulation in the Iceland Sea. Using idealized configurations of a similar model, Käse et al. (2009) found that at times the NIJ originates from a southward dense current flowing along the Jan Mayen Ridge.

Våge et al. (2011) traced the NIJ upstream as far as the north east corner of Iceland, where they found the current to weakened substantially. By using an idealized numerical model they argued that the NIJ is an independent current from the EGC and that it originates "along the north slope of Iceland as a deep limb of a local overturning cell whose upper branch is the NIIC". According to their manuscript waters from the NIIC are exchanged laterally (via eddies) with dense water transformed (densified by winter convection) in the interior of the Iceland Sea. They claimed that the dense water subsequently sinks near the boundary to form the NIJ. These findings were later supported by Våge et al. (2013) by using historical and recently collected in situ data, together with an idealized numerical model and atmospheric reanalysis fields. They defined the strength of the NIJ to be around 1.4 Sv. Meanwhile Harden et al. (2016) estimated the NIJ transport to be around 1 Sv, which represents, they argued, 28% of the total transport carried by the DSOW.

Våge et al. (2015) used an updated version of the historical hydrographic data set employed by Våge et al. (2013) to explore the wintertime water mass transformation occurring in the Iceland Sea. Among their findings, they point out that only a minor fraction (2%) of late-winter profiles (since 1980) from the north-central Iceland Sea, recorded a mixed layer dense enough to provide the waters that could feed the NIJ. They mention the possibility of a weakening of the convection in the Iceland Sea. In fact, Moore et al. (2015) found that wintertime retreat of sea ice in the region, together with different rates of warming for the atmosphere and the sea surface of the Greenland and Iceland Seas, has resulted in approximately a 20% reduction of the winter air-sea heat fluxes since 1979. They argued that, if these conditions were to continued, the convection in both basins would be depth-limited in the future.

To examine the relationship between the NIJ and the NIIC, Pickart et al. (2017) used shipboard hydrographic and velocity sections. They found that the interannual variability in salinity of the NIIC is in phase with that of the NIJ. They argued that the NIIC signal does

not dictate that of the NIJ. They propose instead that the salinity of the NIJ is in phase with the changes in evaporation minus precipitation over a region in the northwest of the Iceland Sea. This points out to the overturning process proposed by Våge et al. (2013) is rather fast. Considering that the dense waters within the Iceland Sea are mostly isolated within closed geostrophic contours (Yang and Pratt, 2013), Pickart et al. (2017)'s argument makes the Våge et al. (2013) hypothesis of the Iceland Sea to be the source of the NIJ, something to be questioned.

Using a numerical model with an horizontal resolution of $1/20^\circ$ (VIKING20) and an off-line lagrangian tool, Behrens et al. (2017) investigated the upstream sources of the DSOW. They back-tracked the sources for the NIJ to find it originated mainly from the NIIC and water mass transformation north of Iceland. Contrary to what Våge et al. (2011) proposed with the overturning occuring in the central Iceland Sea, Behrens et al. (2017) found it to occur mainly along the northern Icelandic shelfbreak.

The disagreement among some of these findings makes us question if, as hypothesized by Våge et al. (2011), the NIJ is fed by water densification occurring in the interior of the Iceland Sea during wintertime convection. At the same time it has not yet been clearly established the dynamics of the eddies that have been claimed to export the dense water out of the Iceland Sea interior. Is this eddy activity strong enough to account for the almost 2 Sv that the NIJ provides to the DSOW? An understanding of the circulation and exchanges occurring in the Nordic Seas are vital for any consideration of the implications of high latitude climate change to variability in the Atlantic Meridional Overturning Circulation (AMOC) and consequences for regional (European) climate.

In the present study we aim to shed some light on the drivers of the NIJ. Our hypothesis is that the transformation of the NIIC that occurs west/northwest of Iceland (around the West fjords) provides the majority of the dense water transported by the NIJ, without ignoring ambient water entrainment. In order to test our hypothesis we use (a high resolution) model output from 2002 to 2018. As we know already that strong transformations occurs during the winter months (Chapter 4), we will focus our study mainly on the months from December to March.

The current Chapter is organized as it follows: Section 2 provides details on the numerical

model used and model evaluation; Section 3 describes the main findings; while Section 4 brings up some Discussion and the main Conclusions.

5.2 Methods and Data

This section describes the details of the model and the configuration used. An evaluation of the model is provided as well.

5.2.1 Ocean-Sea Ice Model

The model used is the Nucleus for European Modelling of the Ocean (NEMO) numerical framework version 3.4 (Madec, 2008). The model is coupled with the Louvain-la-Neuve sea ice model LIM2 (Fichefet and Maqueda, 1997). The configuration used is called *Arctic and Northern Hemisphere Atlantic* (ANHA) with a $1/12^\circ$ resolution (ANHA12) (Figure 5.2). The horizontal resolution spans 1.9 km in Dease Strait (northern Canada) to 9.3 km at the equator, with a resolution 4-5 km in the Nordic Seas.

The configuration covers the whole Arctic Ocean, North Atlantic and a part of the South Atlantic with two open boundaries, one close to Bering Strait and the other one at 20°S . The mesh grid is extracted from the $1/12^\circ$ global tripolar grid, ORCA012.

The configuration has 50 vertical levels, with the layer thickness smoothly increasing from 1.05 m at the surface, to 453.13 m in the last level. High resolution is applied to the upper ocean (i.e., 22 levels for the top 100 m). Partial step is also enabled to better resolve the sea floor (Bernard et al., 2006).

Initial temperature, salinity, horizontal velocities (zonal and meridional) and sea surface height fields are obtained from *Global Ocean Reanalysis and Simulations* (GLORYS) from MERCATOR (Masina et al., 2017). Lateral open boundary conditions (salinity, temperature and horizontal velocities) are also from GLORYS (2002-2008 from GLORYS1 and 2009-2018 from GLORYS2v3). This approach helps to reduce the model spin-up time allowing for the simulations to just have a short adjustment period. No temperature or salinity restoring is applied leaving the model to evolve freely without constraining the drift.

The vertical mixing represented in the ocean module is parametrised by a Turbulent Kine-

matic Energy closure scheme. The vertical eddy viscosity and diffusivity are set to 1×10^{-4} m^2/s and 1×10^{-5} m^2/s , respectively.

The atmospheric forcing data used in ANHA12 comes from the *Canadian Meteorological Centre's Global Deterministic Prediction System (CGRF)* (Smith et al., 2014). CGRF provides 10 m surface wind, 2 m air temperature and specific humidity, downward long-wave and short-wave radiation fluxes and total precipitation. This dataset has a time resolution of one hour and a spatial resolution of 0.45° in longitude and 0.3° in latitude. The Coordinated Ocean-ice Reference Experiments (CORE) bulk formulae were applied to compute fluxes of heat, water and momentum (Large and Yeager, 2009).

Monthly interannual river discharge from 1° by 1° Global River Flow and Continental Discharge Dataset (Dai and Trenberth, 2002; Dai et al., 2009) is carefully remapped (volume conserved) onto the model grid. The original dataset goes up to 2007, after that the runoff from 2007 is repeated. The river discharge from the adjacent areas of the Labrador Sea was found to be $117.9 \text{ km}^3/\text{year}$ in this dataset. Freshwater fluxes from Greenland (liquid component only) are based on Bamber et al. (2012). The liquid freshwater fluxes from Greenland goes up to 2010, and afterwards the runoff from 2010 is repeated.

The simulation has an integration time from January 1st, 2002 to December 31st, 2018.

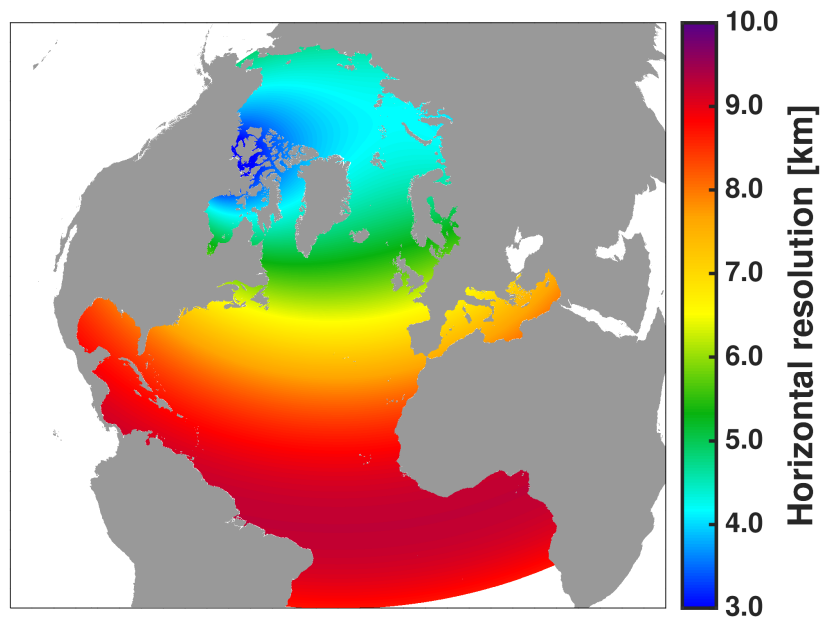


Figure 5.2: ANHA12 horizontal resolution (in km) over its entire domain.

5.2.2 Model Evaluation

Mean physical properties have been evaluated across two sections: Kogur and Latrabjarg (locations shown in Figure 5.1). When extracting the model data, the same latitude and longitude from the observational hydrographic sections were used. First, we use hydrographic data along the Latrabjarg line across Denmark Strait between 2004-2012, which is freely available at <http://kogur.whoi.edu/>. The data available for this section covers mainly the months of February, May, August and November. We decided to present the data corresponding to the months of February and November only as our main focus is on the winter months.

February and November mean density, temperature and salinity, averaged from 2004 to 2012 along the Latrabjarg section, for model and observations, are shown in Figures 5.3 and 5.4, respectively. It can be noticed that in general the model represents nicely the overflow waters as they approach the sill on Denmark Strait. In the case of the density field the model properly represents the upper limit of the overflow transport (Figures 5.3.a and 5.4.a) indicated by the $\sigma_0 = 27.8 \text{ kg/m}^3$ isopycnal (e.g., Pickart et al., 2017; Våge et al., 2013).

The Atlantic inflow signature of the NIIC is clearly visible at the Icelandic shelfbreak which results in temperature signals higher than 5° C (Figures 5.3.e and 5.4.e) and salinity higher than 35 (Figures 5.3.c and 5.4.c). The fresh signal of the EGC is clearly visible as well in the western flank of the Latranjarg section.

The salinity field in the model is higher than in the observations. This becomes more evident in the strong signature of the NIIC represented in the model (Figures 5.3.c and 5.4.c), compared observations (Figures 5.3.d and 5.4.d). This difference, however, does not appear to have a strong impact in the overall representation of the overflow structure.

In the case of the Kogur section, we use time series (available from September 1st, 2011 to July 30th, 2012) of gridded vertical sections of hydrographic variables from the Kogur mooring array (Huang et al., 2019). The dataset can be freely accessed at <http://kogur.whoi.edu/>. In order to be seasonally consistent with the evaluation along the Latrabjarg section, we analyse here the months of December, January and February. Different from the analysis at the Latrabjarg section, we decided to use the month of December instead of November, first because the variables representation for both months are very similar (not shown), and

secondly to keep a time continuity.

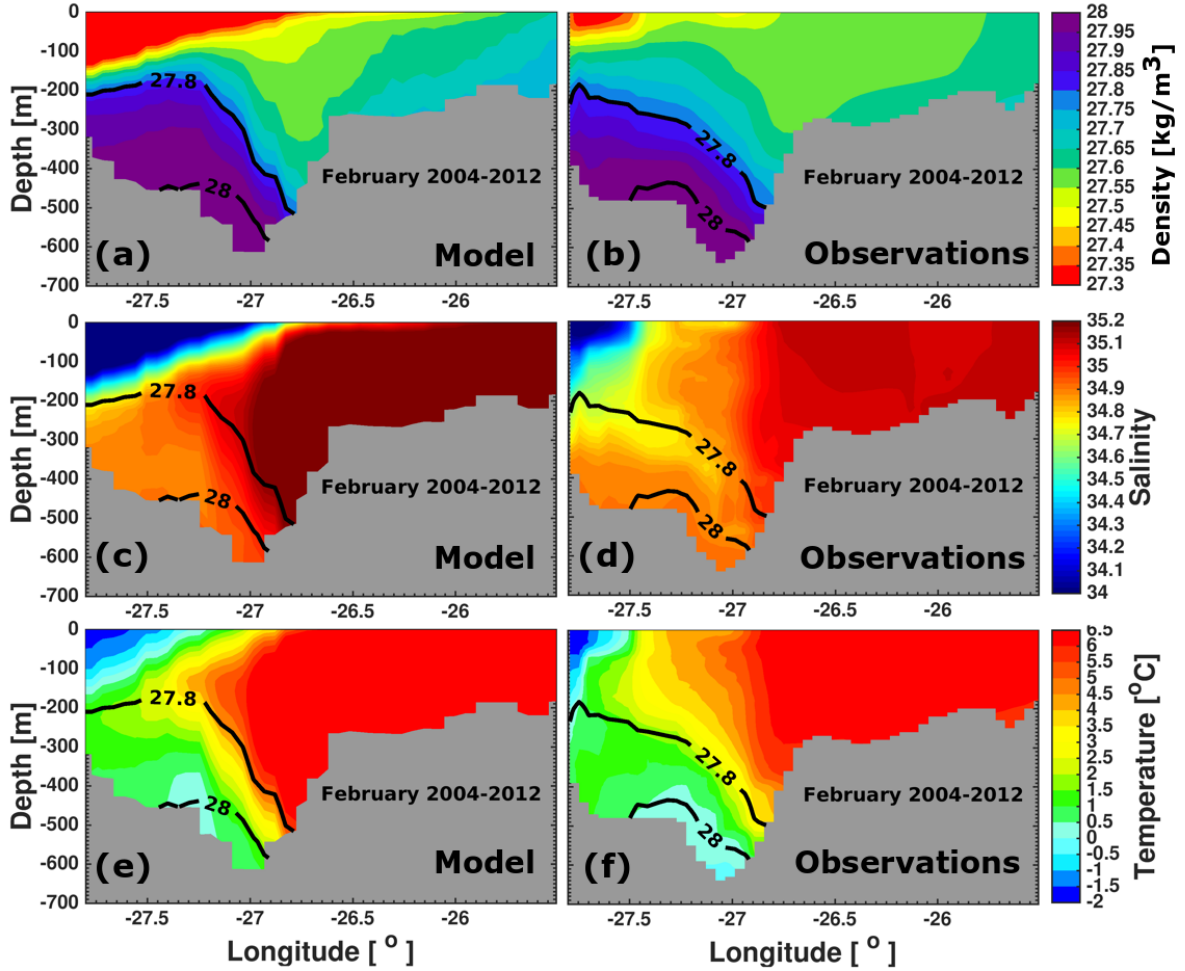


Figure 5.3: Mean February density (a,b), salinity (c,d) and temperature (e,f), averaged over the period 2004 to 2012 along the Latrabjarg section (shown in Figure 5.1). Panels on the left show model data while those on the right represent data from observations.

Mean density, salinity and temperature fields along the Kogur section (shown in Figure 5.1), for model and observations are represented in Figure 5.5. The data used correspond to a continuous occupation of the Kogur section from September 2011 to July 2012. Here we show the monthly means for December 2011 and January and February 2012. This specific period was selected as our focus is on the winter months (same criteria was applied to the Latrabjarg section). In the case of the density field, all three months show a similar behaviour (Figures 5.5.a-c). We can see the larger difference between the model and the observations from the surface to 300 m depth, where the model appears to be less dense than the observations by around $0.1 \text{ kg}/\text{m}^3$. From 300 m depth to the bottom both model and observations show an

almost identical pattern.

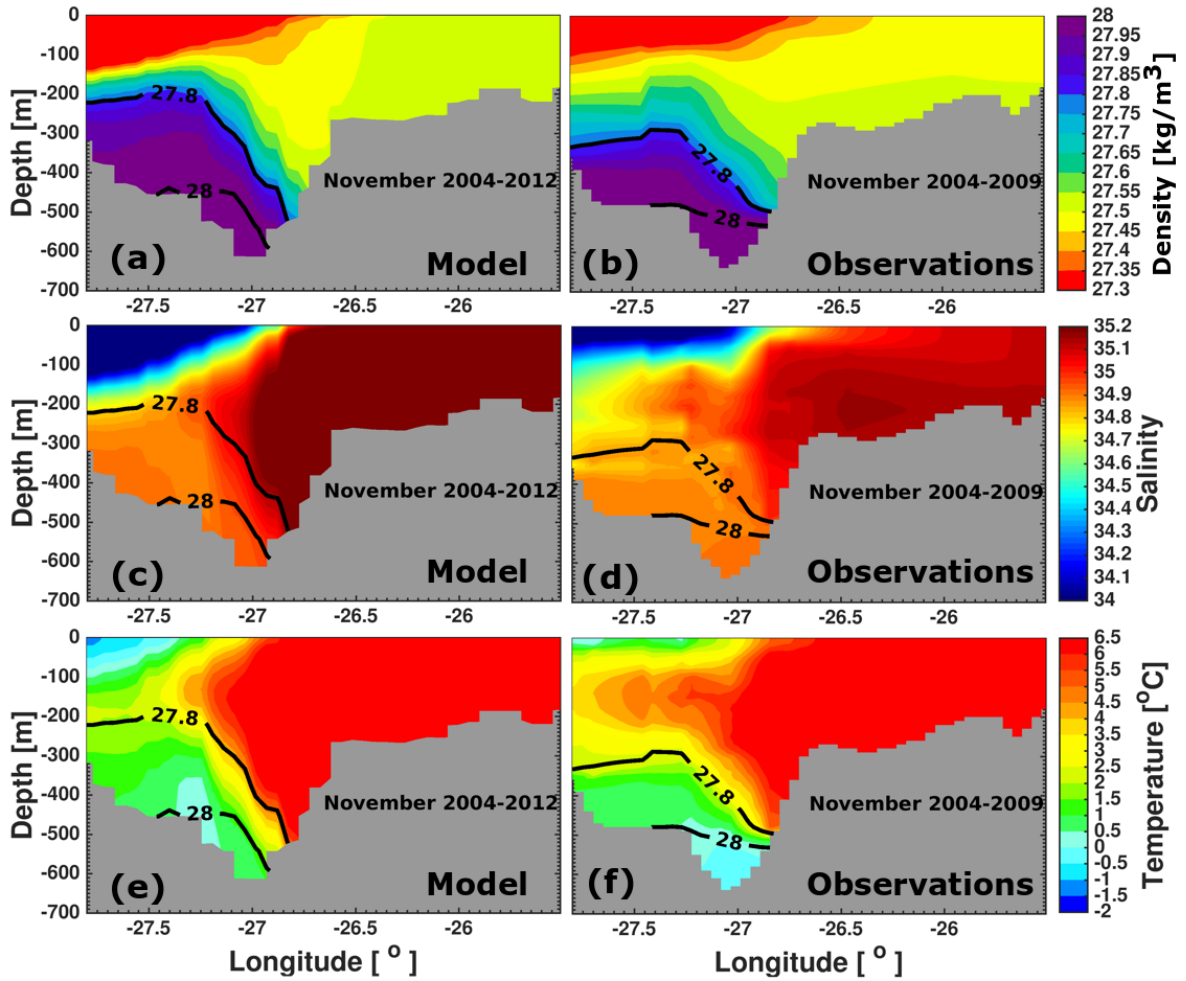


Figure 5.4: Mean November density (a,b), salinity (c,d) and temperature (e,f), averaged over the period 2004 to 2012 along the Latrabjarg section (shown in Figure 5.1). Panels on the left show model data while those on the right represent data from observations.

Similar to the density field, for the salinity field the largest difference between the model and the observations is found in the layer between the surface to 300 m depth (Figures 5.5.d-f), with the observations being saltier (by around 1.6) than the model. Below 300 m they both are similar. In the case of the temperature field (Figures 5.5.g-i), the observations appear to be warmer from the surface to 200 m by around 0.8° C (in December) to 1.5° C (in January, and by 1.1° C in February). Below 200 m depth the model stays warmer (by 0.8°) in all three months. In spite of these differences the model does a nice job in representing all the three fields through the water column.

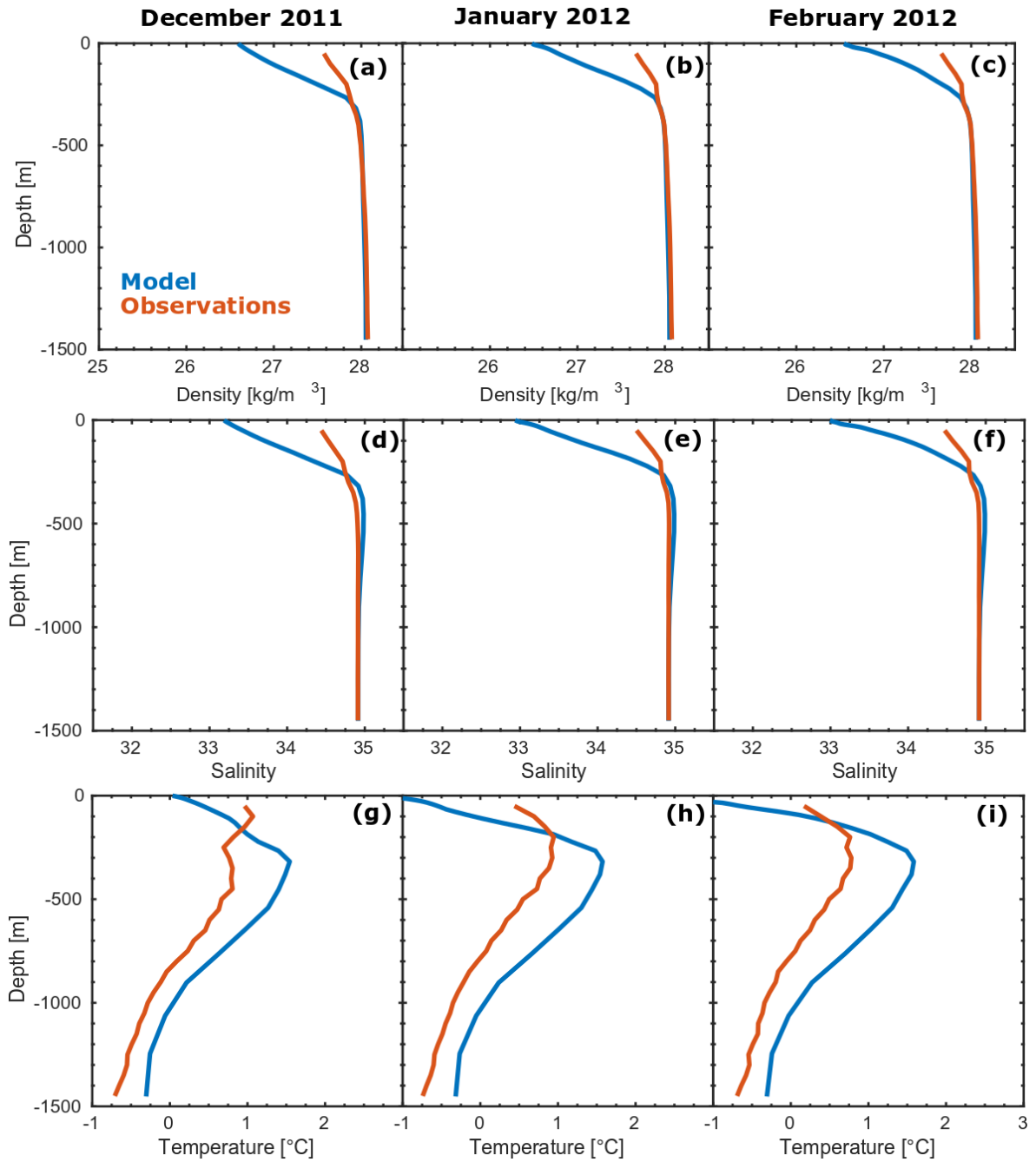


Figure 5.5: Mean vertical profiles (model and observations) of density (a-b), salinity (d-f) and temperature (g-i) along the Kogur section (shown in Figure 5.1, for the month of December 2011 (left panels), January 2012 (center panels) and February 2012 (right panels)). The model data is shown in blue while observation data is represented in orange. In the case of the observations, the measurements of the different variables start at 50 m depth.

5.3 Results

5.3.1 December 2007 to March 2008: a Case of Study

Previously (Chapter 4) it was shown that the transformation of the NIIC which occurs west/northwest of the Icelandic shelf, appears to be strongly linked to the winter heat loss over the region. In order to investigate this link, monthly mean heat loss for the months from December (2007) to March (2008) are shown in Figure 5.6. Rather than making the analysis over a monthly climatology (averaging over a number of years), we decided to select a case of study: December 2007 to March 2008. This way we can have a better representation of features/patterns occurring due to inter-annual variability (e.g., one winter being stronger than the previous one), which could be otherwise smoothed out when monthly-averaging over the years.

5.3.2 On the Relationship between Winter Heat Loss and NIIC Transformation

For all the four months represented in Figure 5.6, it becomes evident that the stronger heat loss occurs on the Icelandic shelf, west/northwest of Iceland. It is also strong at the ice edge on Denmark Strait. The largest heat loss occurs during the months of January and February. It starts to decrease during the month of March. In every case, even during March, the heat loss over the Icelandic shelf was found to be as high as 400 W/m^2 .

Next, we analyse how the water column responds to this strong heat loss. We selected a specific area on the shelf (from the coast to 250 m depth) west/northwest of Iceland, where the model heat loss is observed to be the strongest. The region selected appears represented (in deep blue) in the map attached to the upper left corner of Figure 5.7. Temperature and salinity (TS) diagrams (Figure 5.7) show the transformation the waters within the region go through. We present here as examples model output for March 1st and March 6th. Density contours are included starting at the isopycnal $\sigma_0 = 27.8 \text{ kg/m}^3$, which marks the upper limit of the overflow waters. Note that when using the term transformation, we refer to the dense water formation process occurring as the surface waters gain density and sink.

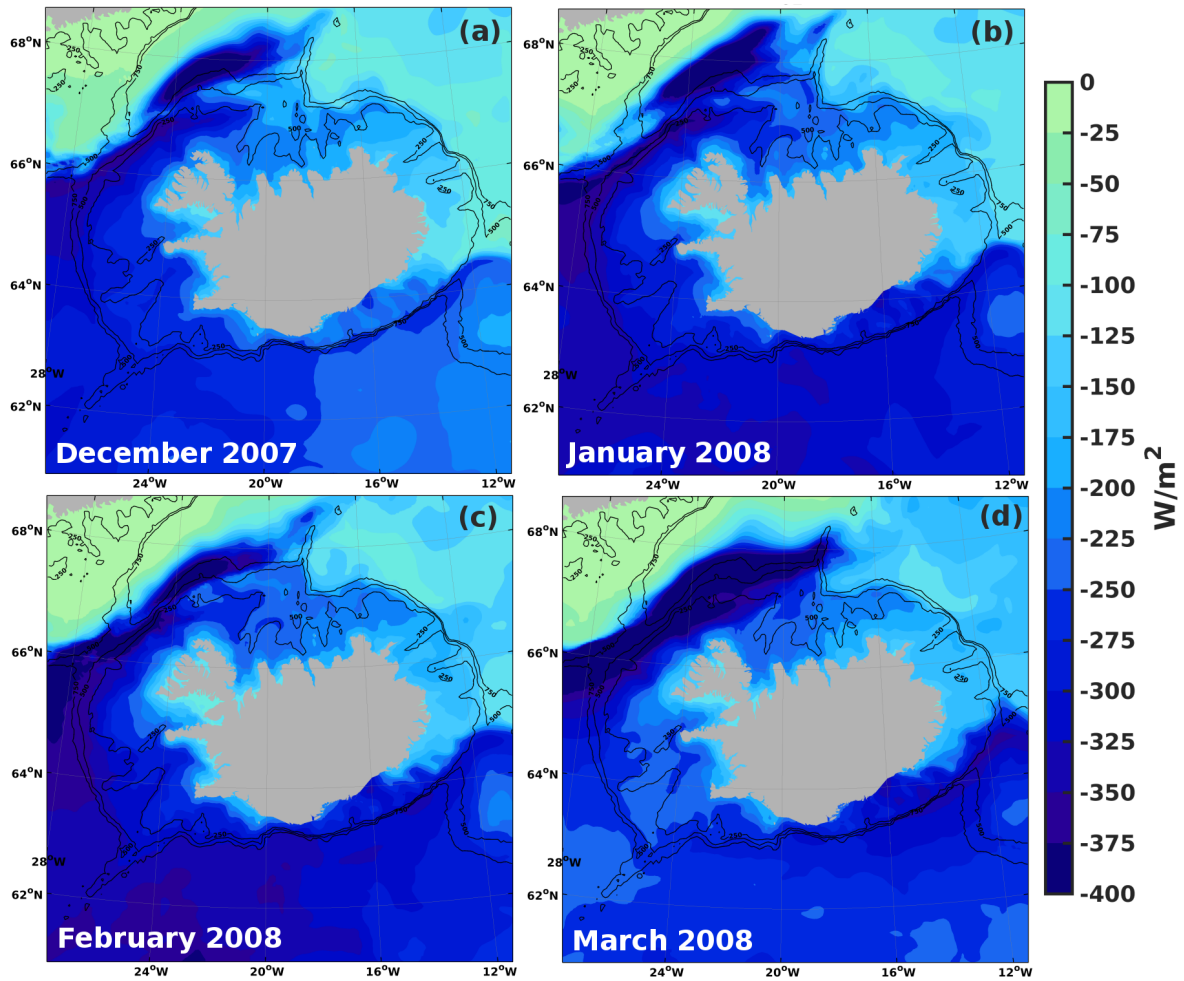


Figure 5.6: Model monthly heat loss around Iceland for the months of December 2007 (a) and from January to March of 2008 (b to d).

It can be noticed that through the month surface waters are transformed to greater densities. In fact, the density can get as high as $28.1 \text{ kg}/\text{m}^3$ (Figure 5.7.a-b). This transformation, however, does not occur only during the month of March, 2008. TS diagrams from previous months (not shown) indicate that this transformation starts as soon as December of the previous year for almost every year in the simulation.

Is the winter heat loss over the study region strong enough to cause the waters within the inflowing NIIC to transform to such high densities? Figure 5.8 shows a comparison between the maximum density, the heat loss and the resistance energy over the study region.

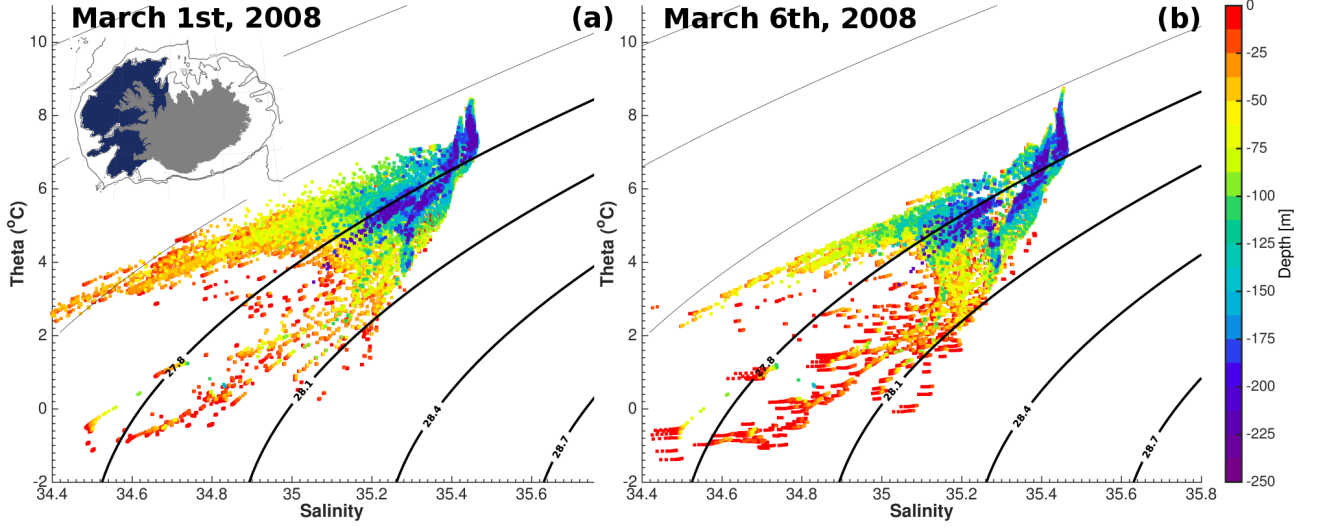


Figure 5.7: TS diagrams over the study region (represented in deep blue in the map attached to the upper left corner of panel a) for every model output during the month of March 2008. The specific date of each diagram appears labeled in the upper-most left corner of every panel.

The resistant energy (RE in Eq. 5.1) is defined as the amount of energy needed to be removed from the region, such that the density will become homogenized down to a certain depth (Holdsworth and Myers, 2015). The mathematical expression to compute the resistance energy is expressed as:

$$RE(h) = \frac{g}{A} \int \int \left[h\rho_{pot}(h) - \int_0^h \rho_{pot}(z)dz \right] dA \quad (5.1)$$

where g is the gravitational constant, A is the surface are of each grid cell, $\rho_{pot}(z)$ and $\rho_{pot}(h)$ are the potential density at each grid cell and the potential density of the grid cell at the reference depth h , respectively. In our case of study $h = 250$ m.

For the density the maximum value for every 5-days model output over the study region is shown (Figure 5.8.a-b). In the case of the resistance energy and heat loss (as well as for temperature and salinity, later on shown) the every 5 days over-the-study-region average is shown. When comparing the maximum density and the heat loss, it is noticed that the density reaches its highest value around the same time as the heat loss (Figure 5.8.a). The resistance energy, on the other hand, decreases by the time the density is the highest (Figure 5.8.b). When we compare it (resistance energy) with the heat loss (Figure 5.8.c) we notice that during the periods when the density reaches its highest values, the heat loss is (every

year) stronger than the resistance energy. This means that, the amount of energy removed from the ocean due to heat loss is indeed enough to increase the density (overflow-like) of the surface waters, making them sink while homogenizing the entire water column down to the bottom.

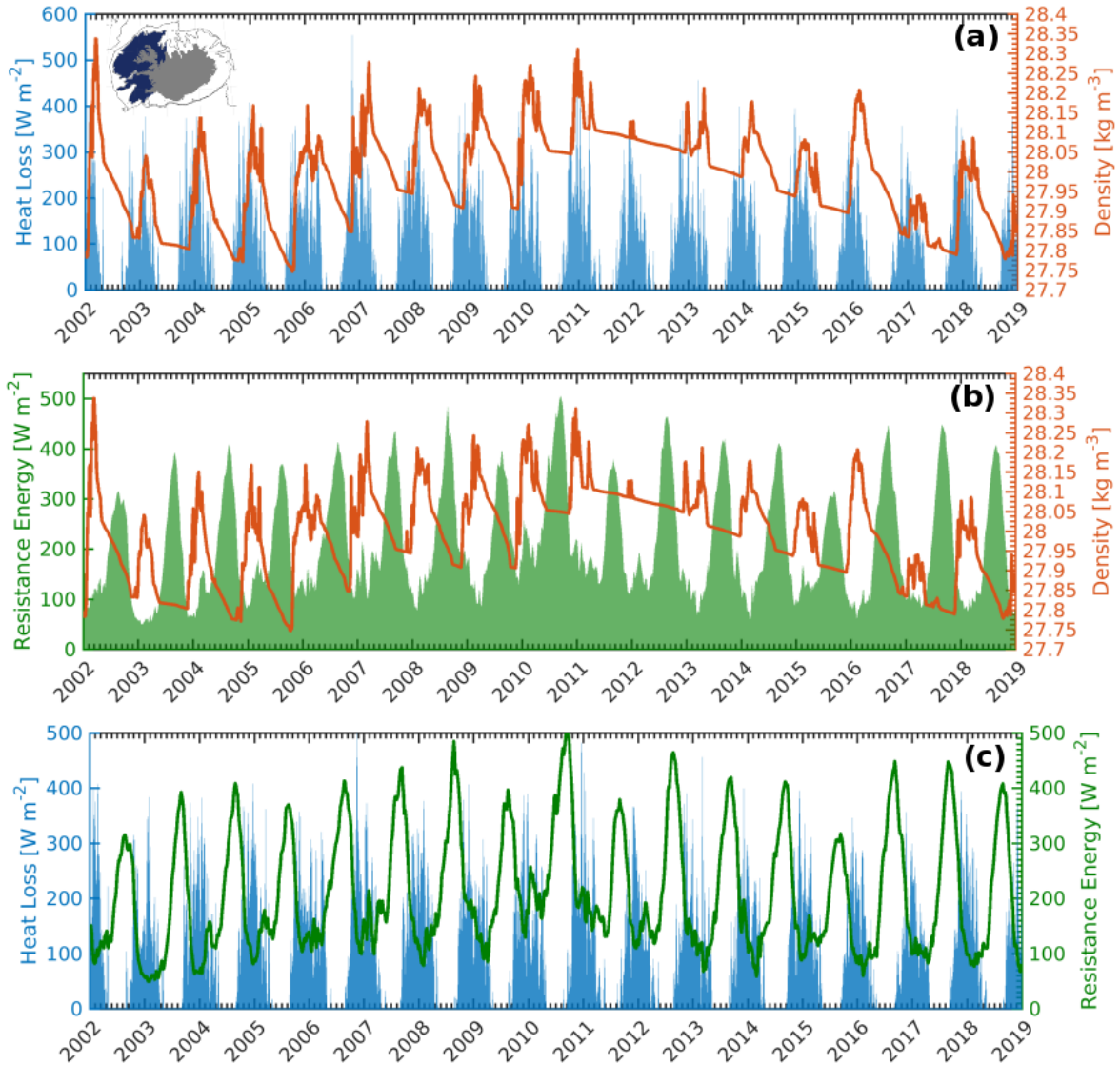


Figure 5.8: Model time series over the study region (shown in deep blue in the map attached to the upper left corner in panel a) of maximum density (a-b), resistance energy (b-c) and heat loss (a and c), from 2002 to 2018.

The trend of the maximum density over the entire period of study appears to be in phase with the salinity (Figure 5.9.a). This would indicate that the inter-annual variability of the density reached by the waters transformed is in phase with the salinity of the inflowing NIIC.

In the case of the temperature, (Figure 5.9.b) the maximum density reaches its highest value at the same time the temperature does so. This takes us back to the link between the maximum density and the ocean heat loss: the surface waters get denser at the same time the water column loses temperature due to an increase in the oceanic heat loss. Figure 5.10 shows the position of the maximum density represented in Figures 5.8 and 5.9. This confirms that the densest transformation occurs in the northwestern corner of the Icelandic shelf, and for waters found mainly between the surface and 175 m depth.

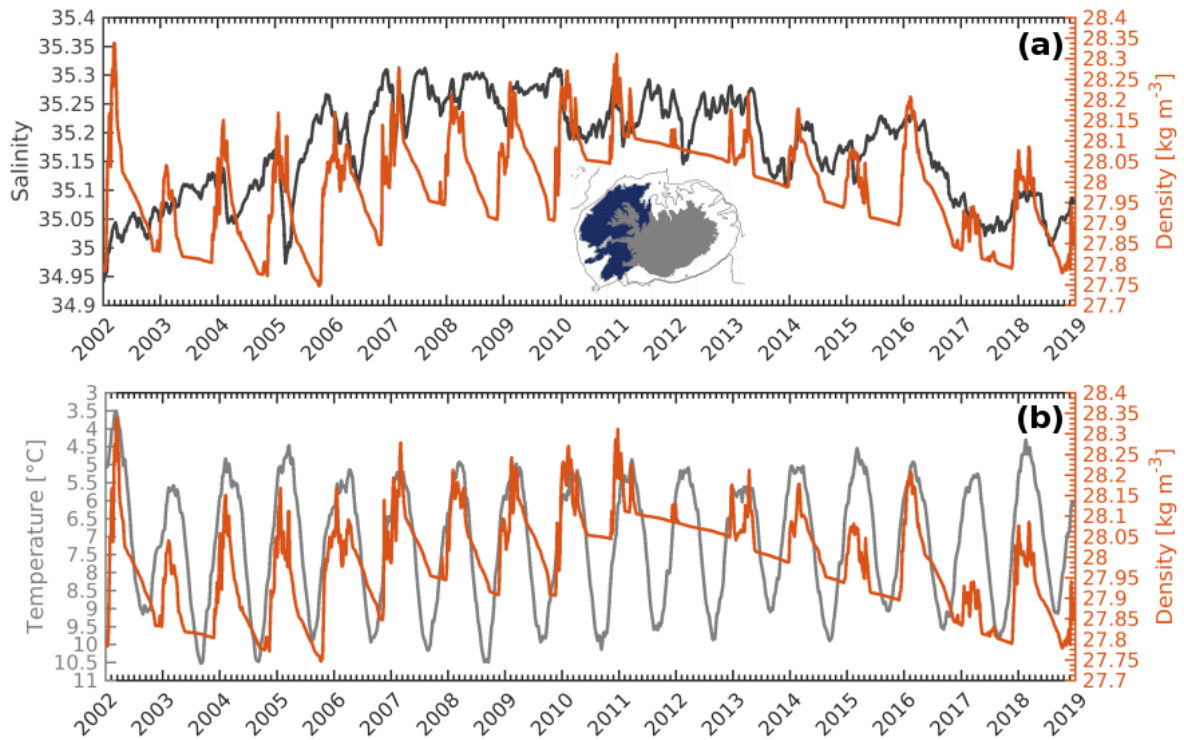


Figure 5.9: Model time series over the study region (shown in deep blue in the map attached to the upper left corner in panel a) of maximum density (a-b), salinity (a) and temperature (b), from 2002 to 2018. Note that for temperature (left y-axis in a) the scale have been inverted.

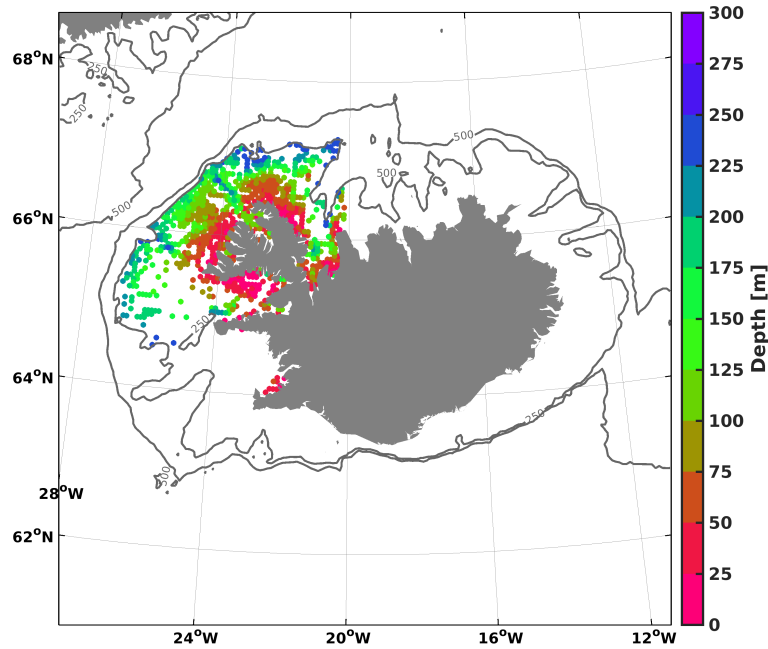


Figure 5.10: Model position of the maximum density (represented in Figures 5.8 and 5.9) for every model output over the study region (shown in deep blue in the map attached to the upper left corner in Figure 5.8.a). This means one unique value for each model output. No density threshold was considered.

5.3.3 Dense Plume Evolution

Once the transformation occurs a dense plume (denser than 27.95 kg/m^3) travels eastward along the Icelandic shelf, cascading down the shelf at different points. Figure 5.11 shows the evolution of the plume generated from January 2008. By the beginning of the month the at-the-surface transformed waters have already reached the bottom (Figure 5.11.a). By the end of the month the dense signature occupies a bigger area and it has started to travel eastward along the shelf (Figure 5.11.b). In the February 24th output it can be seen that the plume appears to start cascading down the shelf, north of Iceland (Figure 5.11.c). By the end of March the plume appears connected already with the dense waters below 500 m depth in a more continuous flow (Figure 5.11.d), north of Iceland. While all this happens, the initial dense signal located in the northwestern corner of the Icelandic shelf continues to gain in area. By March 31st the region with bottom densities higher than 27.95 kg/m^3 has expanded south of the northwestern corner of Iceland, along the shelf.

By examining every TS diagrams for every model output, for the period 2002-2018 and over

the study region, we determined that the transformation occurs mainly during the months from December (previous year) to May. Except for 2017, every year the maximum density of the transformed waters reached the density of 28 kg/m^3 . Considering the location of the region where this densification occurs and the evolution of the transformed waters, it could be expected that the generated dense plume would contribute to (or be a source of) the NIJ and hence, the DSOW.

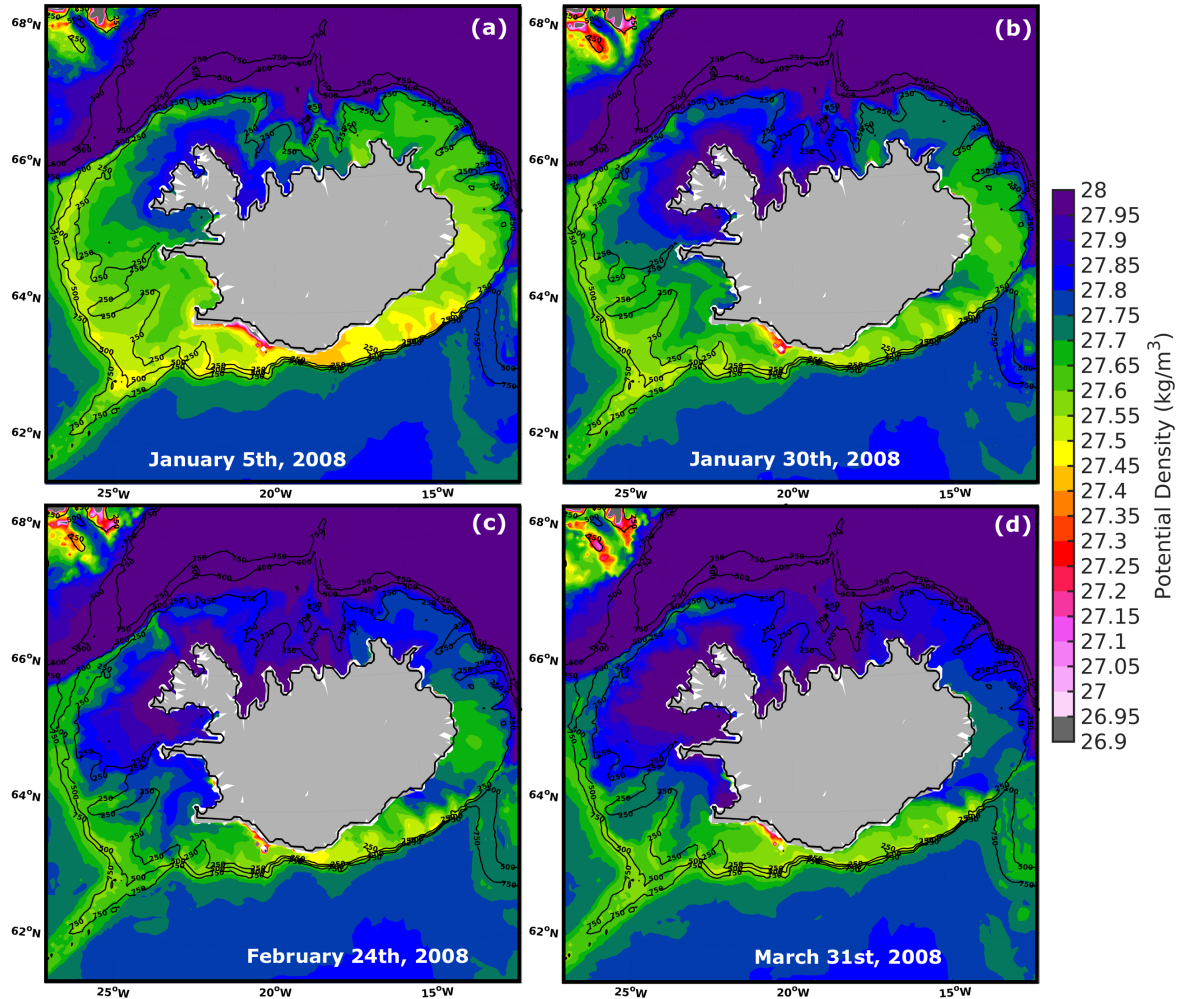


Figure 5.11: Model bottom density for different model outputs from January 2008 to the end of March 2008. The exact date of each output is labeled on the bottom of each panel (slightly towards the right).

5.3.4 Dense Water Transport

In order to investigate this possibility, we compute the transport of waters denser than 27.8 kg/m^3 across 7 sections around Iceland (Figures 5.12 and 5.14). The sections are based on the

hydrographic sections regularly monitored by the Marine and Freshwater Research Institute of Iceland. Some of the sections, however, are slightly modified in order to better capture the transport of the transformed waters: Faxaflói section (re-located slightly northward); Látrabjarg, Húnaflói, Siglunes, and Krossanes sections (angle with respect to the coast changed); Kögur and Langanes NE sections (unchanged); and Langanes E (re-located slightly southward).

We first computed the transport of waters denser than 27.8 kg/m^3 across the different sections from the coast to 250 m depth (Figure 5.12). Positive values indicate eastward/clockwise transport, while negative values indicate westward/counter-clockwise transport. The mean (2002-2018) transport of dense water across the Faxaflói section is 0.01 Sv, with values that go from 0.1 Sv (2004) to almost 0.4 Sv in 2016 (Figure 5.12.a). The mean transport of dense water across the Látrabjarg section increases to 0.025 Sv, varying from 0.1 to 0.4 Sv (Figure 5.12.a-b). Along the Kögur section the mean transport of dense water is 0.043 Sv, ranging from 0.1 to 0.6 Sv (2016) (Figure 5.12.b). Across the Húnaflói section the mean transport of dense water is 0.081 Sv reaching up to 1 Sv in 2016 (Figure 5.12.c-d). The mean transport of dense water across the Siglunes section (Figure 5.12.d-e), on the other hand, decreases with respect to that in Húnaflói by 0.051 Sv. The mean transport of dense water across Langanes NE (Figure 5.12.e-f) increases again up to 0.041 Sv, only to decrease to 0.026 Sv across the Langanes E section (Figure 5.12.f-g). The mean transport of dense water across the Krossanes section decreases with respect to the one from the Langanes E section by 0.001 Sv only (Figure 5.12.g).

As a general observation, note that the transport for all the sections is mainly positive, meaning that the transport of waters denser than 27.8 kg/m^3 along the Icelandic shelf (from the coast to the 250 m isobath) is eastward/clockwise. The magnitude of the mean transport of dense water across each section indicates that it increases as the dense plume flows eastward along the shelf, decreasing at the Siglunes, Langanes E and Krossanes sections. Also note that for every section the every-5-days transport increases at the beginning of the year, except for 2003 when very little transport is registered. The timing of the maximum transport agrees well with the transformation process analysed and the subsequent dense plume generated. In fact, the region where the dense plume is found to cascade (Figures 5.11.c-d) coincides with the region located between the Húnaflói and Siglunes sections. Hence, the decrease in the

mean (and the every-5-days) transport across the Siglunes section means that a considerable portion of the dense waters cascade down across the 250 m isobath shortly after crossing the Húnaflói section. The location for the cascading in this case seems to be related with the narrowing of the shelf between the coast and the 250 m isobath.

We also computed the transport of waters denser than 27.8 kg/m^3 across the 250, 500 and 750 m isobaths, from the Faxaflói to the Krossanes sections (Figure 5.13). Positive values means the transport is towards deeper layers after crossing the given isobath. The mean (2002-2018) transport across the 250 m isobath is 0.1 Sv, oscillating from around 0.1 Sv to 1 Sv in 2016. Across the 500 m isobath the mean transport of dense water is 0.2 Sv, reaching 1 Sv in 2008, 2013, 2014, 2016 (1.3 Sv this year) and 2018. The mean transport of dense water across the 750 m isobath is 0.6 Sv, varying between 0.5 to 1.9 Sv (2008 and 2016). We do not assume, however, that all the transport of waters denser than 27.8 kg/m^3 registered crossing the 750 m isobath is coming from the Icelandic shelf. But we can assume that the dense water crossing the 250 m and latter the 500 m isobaths, contribute to the transport across the 750 m isobath. In fact, the 250 m and 500 m isobath transports are correlated at 60%, while the 500 m and 750 m isobath transports are correlated at 84%. This means that their variability are closely linked, and by examining Figure 5.13, their magnitude as well.

Next we explore the transport of waters denser than 27.8 kg/m^3 across the 7 sections previously established, but this time from 250 to 750 m depth (Figure 5.14). Different from the coast-to-250 m isobath transport, in this case (and as expected) the transport is mostly westward/counter-clockwise (negative values). This is the case for all the sections except for the Langanes E and Krossanes sections which means that the transport through those sections is mainly is eastward/clockwise (Figure 5.14.f-g). Following the pattern of the shallower analysis, the mean transport of dense water across the Krossanes section increases with respect with the previous one (Langanes E), from 0.13 to 0.2 Sv. While the transport across Krossanes is mainly clockwise, the section Langanes E appears to have episodes of counter-clockwise transport, even when its mean is positive. The mean transport of dense water across the section Langanes NE is 0.13 Sv (negative) and generally counter-clockwise (Figure 5.14.e). It increases across the Siglunes section, where the mean is 0.7 Sv (negative) while seasonally it can be around 1 Sv (Figure 5.14.d-e). Across the Húnaflói section the mean transport of dense

water is 0.8 Sv (negative), exceeding 1 Sv in some years (Figure 5.14.c-d). The mean transport of dense water across the Kögur section is 1.1 Sv (negative), being 1.5 Sv in years like 2011 (by the end) and 2014. The mean transport of dense water across the Látrabjarg and Faxaflói sections decreases considerable (close to zero) with respect to the previous section, suggesting that the great majority of the dense water is exported through Denmark Strait after crossing the Kögur section.

We notice that the transport increases westward this time, reaching a maximum at the Kögur section. The mean transport of dense water from the Siglunes to the Húnaflói sections increases by 0.5 Sv. This is consistent with the cascading point and with the decrease found in the mean transport of dense water for the shallower analysis. In fact, the decrease in the mean dense water transport found in the Siglunes and Langanes E sections coincide with an increase in the mean dense water transport across the same sections down slope.

The decreased in the mean transport (from the coast to the 250 m isobath) found at the Siglunes, Langanes E and Krossanes sections, altogether, is equivalent to 0.067 Sv. This represents the 67% of the mean dense water transport that crosses the 250 m isobath. On the other hand the mean dense water transport (from the 250 to the 750 m isobaths) increased cyclonically from one section to the next one, from the LanganesE to the Kögur sections. Overall, this mean transport increase can be estimated to be round 1.23 Sv. This is roughly two times higher than the mean transport of dense waters crossing the 750 m isobaths (0.6 Sv). This means that some of the waters travelling cyclonically along the shelfbreak between 250 to 750 m depth, might not necessarily cross the 750 m isobath towards deeper layers. We might be capturing as well part of the transport corresponding to the SEGC which joins the NIJ along the northwest Icelandic shelfbreak (Figure 5.1). This would also explain the mean transport of dense water from the 250 to the 750 m isobaths, which is two times larger than the mean transport of dense water across the 750 m isobath. These comparisons, however, must be interpreted carefully as we are referring to mean transport which can considerably change seasonally.

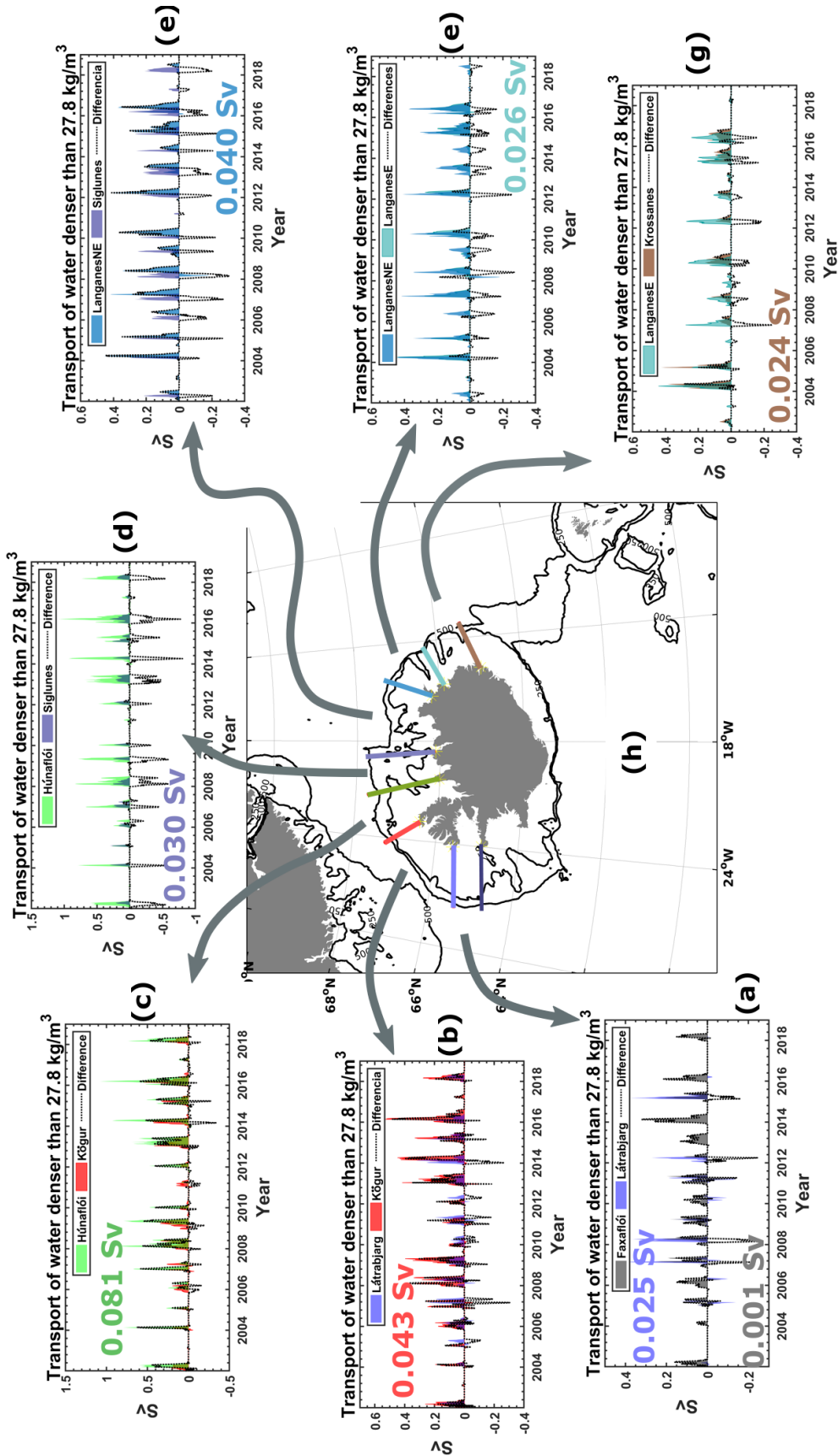


Figure 5.12: Model time series (from 2002 to 2018) of transport for waters denser than 27.8 kg/m^3 , across 7 different sections located from west to east around the Icelandic shelf, from the coast to 250 m depth. The name of each section appears on the legend of each panel. The mean transport of dense water across each section appears color-coded following the color of the given section. Transport differences between sections are represented by dotted black lines. The transport across sections are plotted in pairs in order to better visualize when the transport builds up or decreases compared to a previous section.

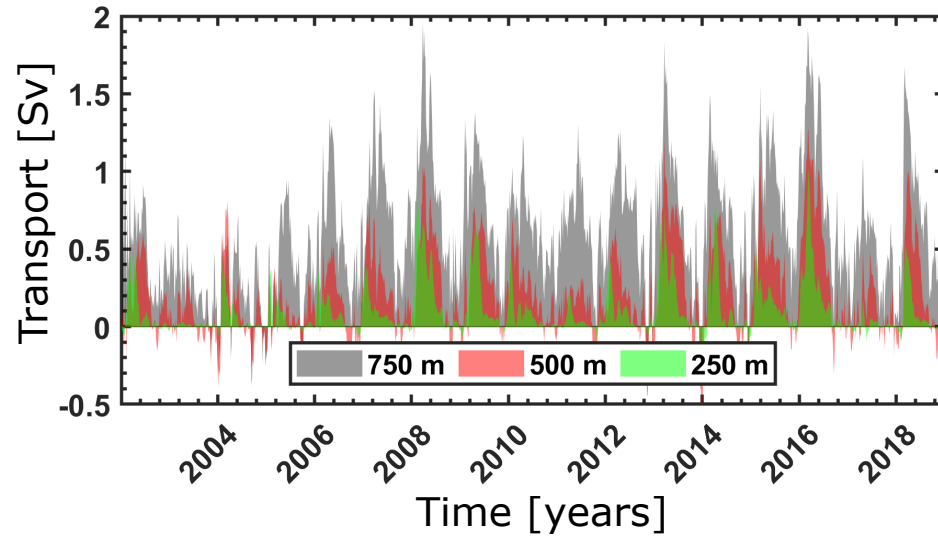


Figure 5.13: Model time series (from 2002 to 2018) of transport for waters denser than 27.8 kg/m^3 across the 250, 500 and 750 m isobaths around Icelandic shelf, from the Faxaflói (west of Iceland) to the Krossanes (east of Iceland) sections

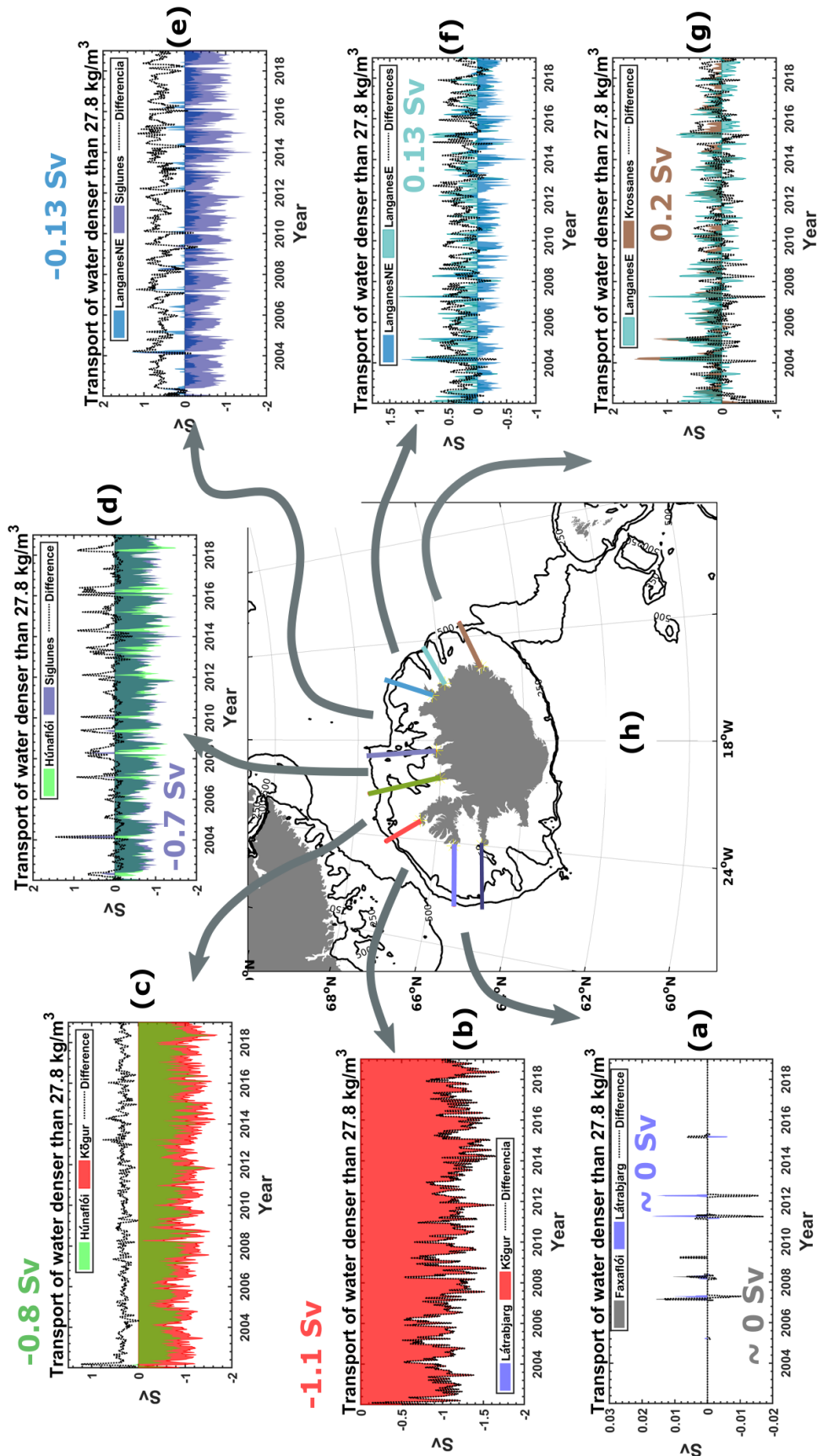


Figure 5.14: Model time series (from 2002 to 2018) of transport for waters denser than 27.8 kg/m^3 , across 7 different sections located from west to east around the Icelandic shelfbreak, from 250 to 750 m depth. The name of each section appears on the legend of each panel. The mean transport of dense water across each section appears color-coded following the color of the given section. Transport differences between sections are represented by dotted black lines. The transport across sections are plotted in pairs in order to better visualize when the transport builds up or decreases compared to a previous section.

5.4 Discussion and Conclusions

By using a $1/12^\circ$ horizontal resolution model output, from 2002 to 2018, we have investigated the transformation of the inflowing NIIC on the west/northwest portion of the Icelandic shelfbreak and the contribution of the transformed waters to the NIJ.

Our results point out that the winter heat loss (December to March) over the study region (upper left corner of Figure 5.7.a) is strong enough to make the surface waters to gain in density and sink, homogenizing the water column down to the bottom (250 m depth) (Figure 5.8). The maximum density of the waters transformed was found to be higher than 28 kg/m^3 throughout most of the study period (Figure 5.7), reaching a maximum of 28.3 kg/m^3 towards the end of 2010. We found the maximum density to be closely linked to the salinity (Figure 5.9.a). Considering that warm, saline Atlantic Water (from the NIIC) is found over the Icelandic shelf and slope (Våge et al., 2013), we can assume that the salinity of the waters carried by the NIIC into the Nordic Seas, define the maximum density of the transformed waters. This is actually in line with Pickart et al. (2017) who found the interannual variability in salinity of the NIIC to be in phase with that of the NIJ.

As a response of the dense water formation episodes, a dense plume travels anticyclonically on the Icelandic shelf (Figure 5.11), cascading occasionally down slope at different locations (north of Iceland). One of those locations can be seen in Figure 5.11.b, which coincides with a narrowing, with respect to the coast, of the 250 m isobath. In fact, the locations where the dense plume cascades down slope, they all coincide with regions where the 250 m isobaths narrows (with respect to the coast) (Figure 5.1). At the same time we see the presence of canyons or troughs which might play a role on steering the dense waters down slope and offshore. This points out that these irregularities in the bathymetry may force the dense waters to cascade.

A physical explanation for the dense plume evolution and the large-scale circulation response to it, is provided by Spall et al. (2017). By using a primitive equation model and rotating-tank experiments, they investigated the circulation response to a localized dense water formation region over a sloping bottom. Their work was motivated by "topography around islands or shallow shoals in which convection resulting from brine rejection or surface heat loss

reaches the bottom". They found that a depression in sea surface height (SSH) propagates from the formation region anticyclonically, around the island. As a response a cyclonic current is generated around the topography, travelling in the opposite way of the dense water plume at a speed in the range 2-15 cm/s.

Exploring the SSH magnitude and variability (from 2002 to 2018) over the formation region we noticed that, indeed, maximum low SSH occur when the maximum density is at its highest (Figure 5.15). SSH from every 5 days model output for January 5th and Marc 11th 2008 show the response to the dense plume travelling anticyclonically around the Icelandic shelf (Figure 5.16). Figure 5.16.a, which is when the signal of the dense plume appears northwest on the Icelandic shelf (Figure 5.11.a), shows the SSH around the shelf to be relatively high compare to its surroundings and the flow to be mainly anticyclonic. Once the dense plume travels from its source, a depression in the SSH has expanded anticyclonically from the formation region and the flow changes to cyclonic (Figure 5.16.b). Some recirculation occurs in the vicinities of the Húnaflói and Siglunes sections most likely induced by the rough bathymetry along that part of the shelf.

Also consistent with Spall et al. (2017), the along-section velocity at the Húnaflói section (downstream of the cascading point) shows the offshore flow, all the way from the surface to the bottom and around 90 km from the coast, to be cyclonic (Figure 5.17). Note that we have captured here some of the bathymetry induced recirculation observed in Figure 5.16. The velocity of the flow varies from 2.5 to 20 cm/s, reaching its maximum by the end of March. This flow was found to be present during the entire simulation (2002-2018), with its magnitude and position changing slightly from section to section and seasonally, being at its maximum from December to April. Its signal was found to be stronger along the sections Húnaflói and Kögur. This is understandable considering they are the most downstream from the cascading points.

As none of the sections used in the present study is located on the south portion of the Icelandic shelf, we cannot confirm (nor deny) that the current is indeed the cyclonic circum-island flow discussed in Spall et al. (2017). Our findings, however, point out that indeed the mechanism of Spall et al. (2017) might actually be at work around the Icelandic shelf.

With respect to the location of the cascading point, Spall et al. (2017) (who refer to it as

separation or detachment point) established for it to be 80° clockwise from the dense water formation region. However in their model as well as for the tank experiment the bottom topography increases smoothly from shallow to deep waters, and in a circular fashion. This is nothing like the bathymetry around the Icelandic shelf. Which is why we state that, rather than depending on the position of the source, the separation/cascading point is linked to the bottom bathymetry in this case.

We examined the transport of waters denser than 27.8 kg/m^3 across 7 sections located around the Icelandic shelf, from the coast to 250 m and from 250 to 750 m depth (Figures 5.12 and 5.14). At the same time the transport across the 250, 500 and 750 m isobath, also for waters denser than 27.8 kg/m^3 (Figure 5.13), was determined. The transport analysis indicates that from the coast to 250 m depth the flow is anticyclonic along all the sections. From 250 to 750 m depth the flow changes to cyclonic in almost all the sections, remaining (mainly) anticyclonic along the Langanes E and Krossanes sections (Figure 5.14.f-g). We noticed that as the dense plume travels clockwise on the Icelandic shelf (coast to 250 m) its transport decreases in two locations (between the section Húnaflói and Siglunes, and between the sections Langanes E and Langanes NE) (Figure 5.12). We assume that this points out the regions where the dense water cascade down slope. From the Langanes NE section the transport from 250 to 750 m depth increases towards the west, only to decrease again after the Kögur section, where the mean is 1.1 Sv, reaching 1.5 Sv episodically (Figure 5.14). The overall transport of dense water from the Icelandic shelf that crosses the 250, 500 and 750 m isobath (Figure 5.13), when at its maximum, is sufficient to supply the dense waters carried by the NIJ (e.g., Jonsson and Valdimarsson, 2004; Våge et al., 2013, 2015).

Although the magnitude of the analysed model transport matches that for the NIJ, considering that the dense plume is generated during the months between December to March, we cannot assume their dense waters are the sole source of the NIJ, but one of them. Recently, by using mooring data from September 2011 to July 2013, on the Iceland slope (part of the Kögur section), Huang et al. (2019) determined three different scenarios of the NIJ. Their manuscript focused on an NIJ dominant scenario where the current was found to be strong, advecting anomalously dense water in its core and at its climatological mean position. During the first year (2011-2012) of observations this regime was present from September to

February, and from January to July the second year (2012-2013). In order to establish a link between the timing of the dominant regime and the atmospheric forcing upstream of Denmark Strait, they looked into lagged correlations between the dominant NIJ regime with monthly heat fluxes and wind speed. They showed that for turbulent heat fluxes two regions came out to be statistically significant +2-month time lag correlated: one region located on the north slope of Iceland around the 1000 m isobath (south side of the Spar Fracture zone), while their other region is basically our study area, on the west/northwest corner of the Icelandic shelf (see Figures 12.c, 13.a and 13.b of Huang et al., 2019). They found the same pattern to be present for the latent and heat fluxes separately. However they focused on the first region mentioned.

Their findings point out that larger heat fluxes over the identified region(s) leads to the NIJ dominant regime. We then can assume that the dominant regime of the NIJ established by Huang et al. (2019) is merely a response to the dense plume generated from the NIIC transformation during strong winter heat loss episodes. Considering the timing of the dense plume in our case of study (Figure 5.11): by February 24th, 2008, the dense plume has started to cascade, from the cascading point and at a speed of 15 cm/s, it would take the dense waters around 20 days to reach the Kögur section. This is less than three months from the moment the first signal of dense bottom water appears around the source region (Figure 5.11.a) and almost 2 month after the heat loss is at its maximum (Figure 5.6.b). This is consistent with Huang et al. (2019) findings.

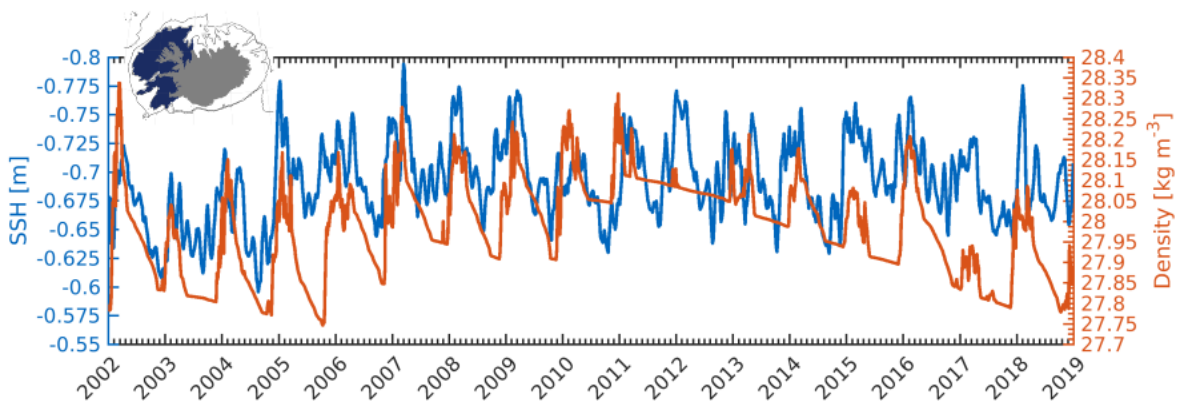


Figure 5.15: Model time series of mean SSH and maximum density, from 2002 to 2018 over the study region (area represented in deep blue in the map attached to the upper left corner of the figure). Note that the scale for the left y-axis have been inverted.

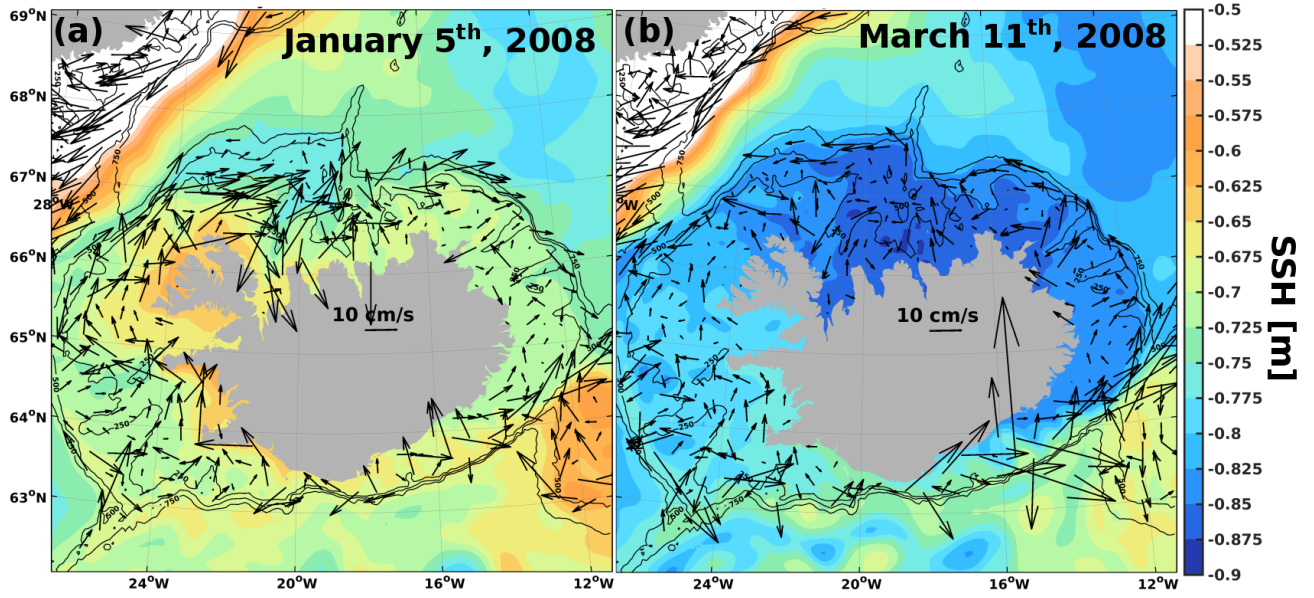


Figure 5.16: Model sea surface height (SSH) and ocean current speed at 5 m depth, for a) January 5th and b) and March 11th, 2008. The date of each output is labeled in the upper left corner of every panel.

We understand that, as the model is somewhat salty compared to the observations (Figures 5.3.c and 5.4.c) the formation of the dense plume might be interpreted as an artificial signal of the model induced by its salinity drift. First, we are able to see the formation of the dense plume right from the beginning of the simulation, and secondly, there is actual observational evidence of dense water on the Icelandic shelf. Figure 5.18 shows the analysis of all the temperature and salinity profiles from 1929 to present, between -28° to -17° W and 64° to 67° N (Figure 5.18.a), available in the International Council for the Exploration of the Sea (ICES) database. We filtered the data and selected only those profiles located in waters shallower than 250 m depth and where the density was equal or higher than 27.8 kg/m^3 . Contrary to what has generally been thought, there is in fact water denser than 27.8 kg/m^3 on the Icelandic shelf (Figure 5.18.b). When we looked into the month when all the profiles were taken (before applying density and depth criteria) we found that the vast majority were registered during the months from April to October (Figure 5.18.c). This omits the time of the year when the dense waters form west/northwest of Iceland. The profiles shallower than 250 m and where water denser than 27.8 kg/m^3 was present, were indeed registered mostly from April to October (Figure 5.18.d). A TS diagram of the filtered data (Figure 5.19) shows

that the density of the water can be as high as 28 kg/m^3 , which is consistent with our findings (Figure 5.7). Considering that these densities are present in the months from April to October, we can assume that during the months from November to March when the heat loss is stronger, the density of the waters would be larger.

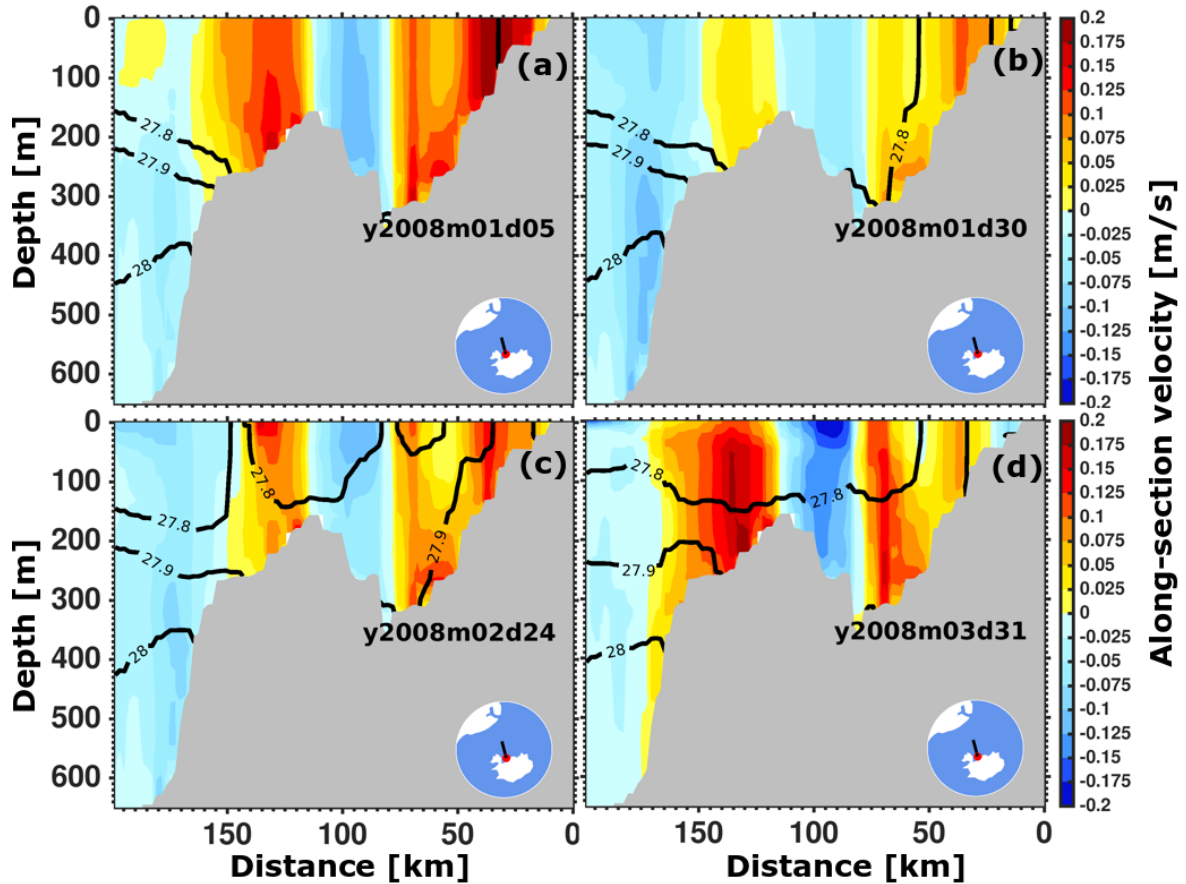


Figure 5.17: Model along-section velocity at the Húnaflói section for different model outputs from January 2008 to the end of March 2008 (consistent with Figure 5.11). The date of the model output is labeled on each panel. The position of the section is represented on the map attached to the lower-right corner of each panel. Positive values means the flow is towards the right of the section (clockwise/anticyclonic) while negative values represent the flow traveling towards the left of the section (counterclockwise/cyclonically).

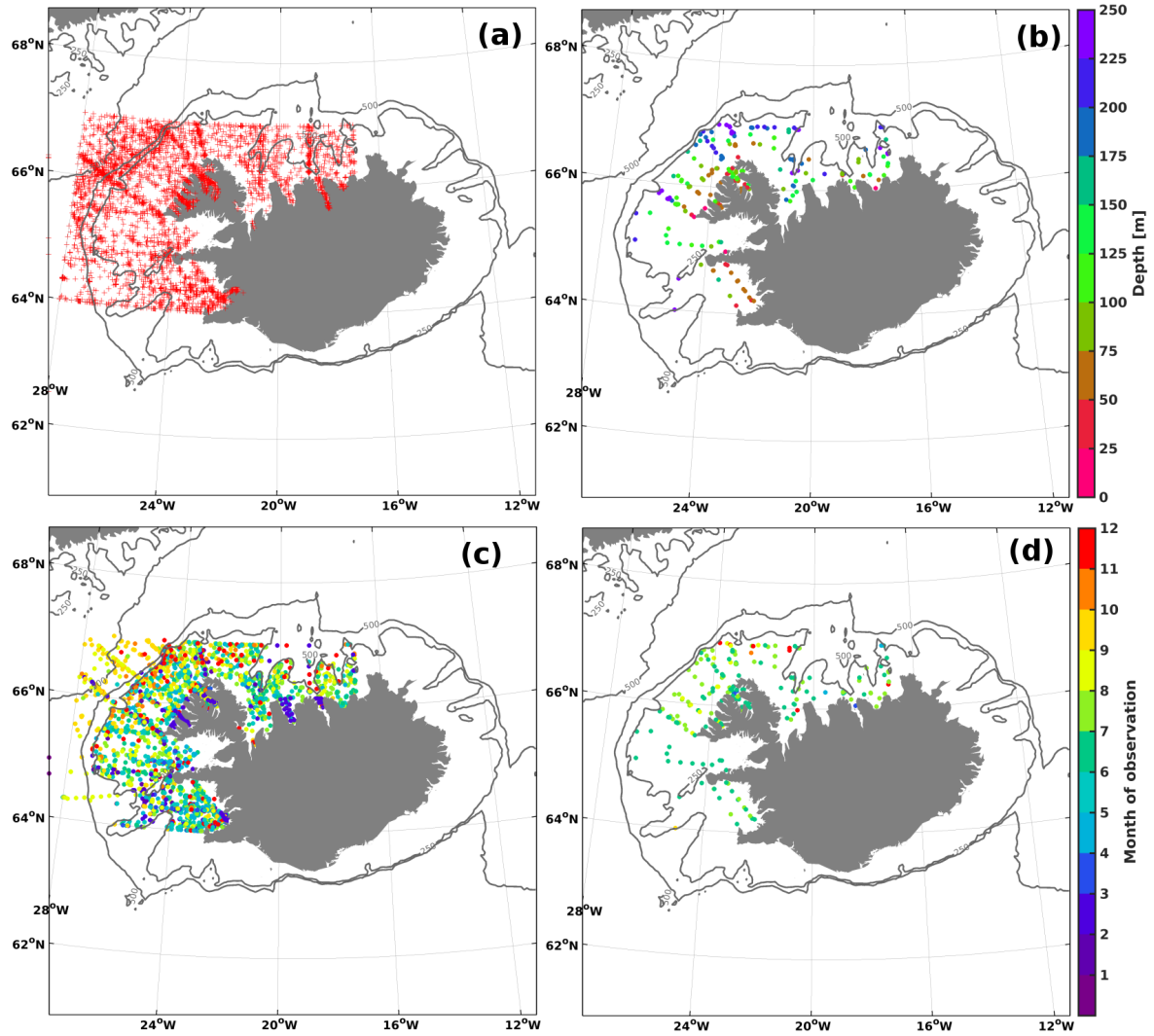


Figure 5.18: Temperature and salinity profiles, from 1929 to present, between -28° to -17° W and 64° to 67° N, available at the International Council for the Exploration of the Sea (ICES) database. (a) Location of all the profiles. (b) Position of the profiles shallower than 250 m on the Icelandic shelf, and with density higher than 27.8 kg/m^3 . (c) Month of the year when all the temperature and salinity profiles (represented in a) were taken. (d) Like in (c) but only for the profiles shallower than 250 m (on the Icelandic shelf) where water denser than 27.8 kg/m^3 was registered.

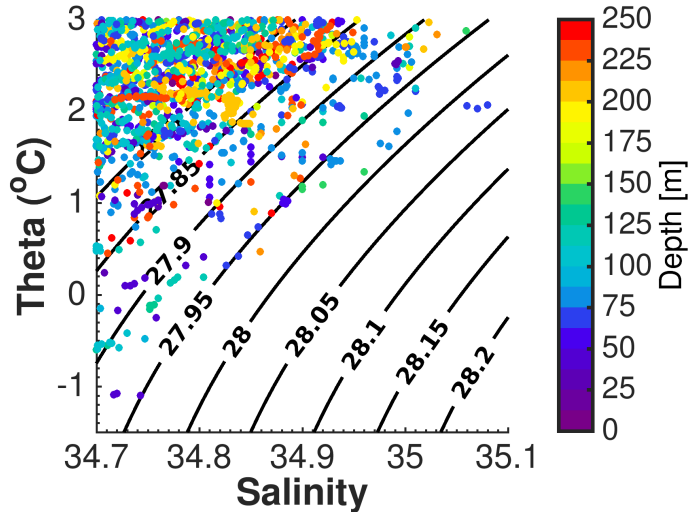


Figure 5.19: Temperature and salinity diagram of the profiles represented in Figures 5.18.b and 5.18.d (profiles on the Icelandic shelf, in waters shallower than 250 m and points denser than 27.8 kg/m^3).

As a conclusion of the present study we propose the following circulation scheme (Figure 5.20): as the NIIC travels around the Westfjords, strong winter heat loss make the surface waters to gain in density and sink down to the bottom. This dense water formation process generates a dense plume that travels anticyclonically on the shelf, cascading down slope at different locations north of Iceland, forced by the narrowing of the shelf from shore to 250 m isobath. The cascaded dense waters travel then cyclonically along the Icelandic shelfbreak within the (cyclonic) flow resultant from the SSH depression which travels clockwise from the source region. The overall result is an enhanced equatorward flow on the continental slope which is consistent with the strong NIJ regime proposed by Huang et al. (2019).

Due to the horizontal resolution of our model, which is not eddy resolving, we cannot discard the Våge et al. (2011) hypothesis for the formation of the NIJ. Moreover, given the timing of dense water formation we can not assume for it to be the sole source of the NIJ. We can assume, however, that it is the source of the enhanced NIJ regime, defined as type3 by Huang et al. (2019). In fact the dense water transport crossing the different isobaths towards deeper layers (Figure 5.13) is enough to feed the observed transport of the NIJ (Våge et al., 2013; Harden et al., 2016).

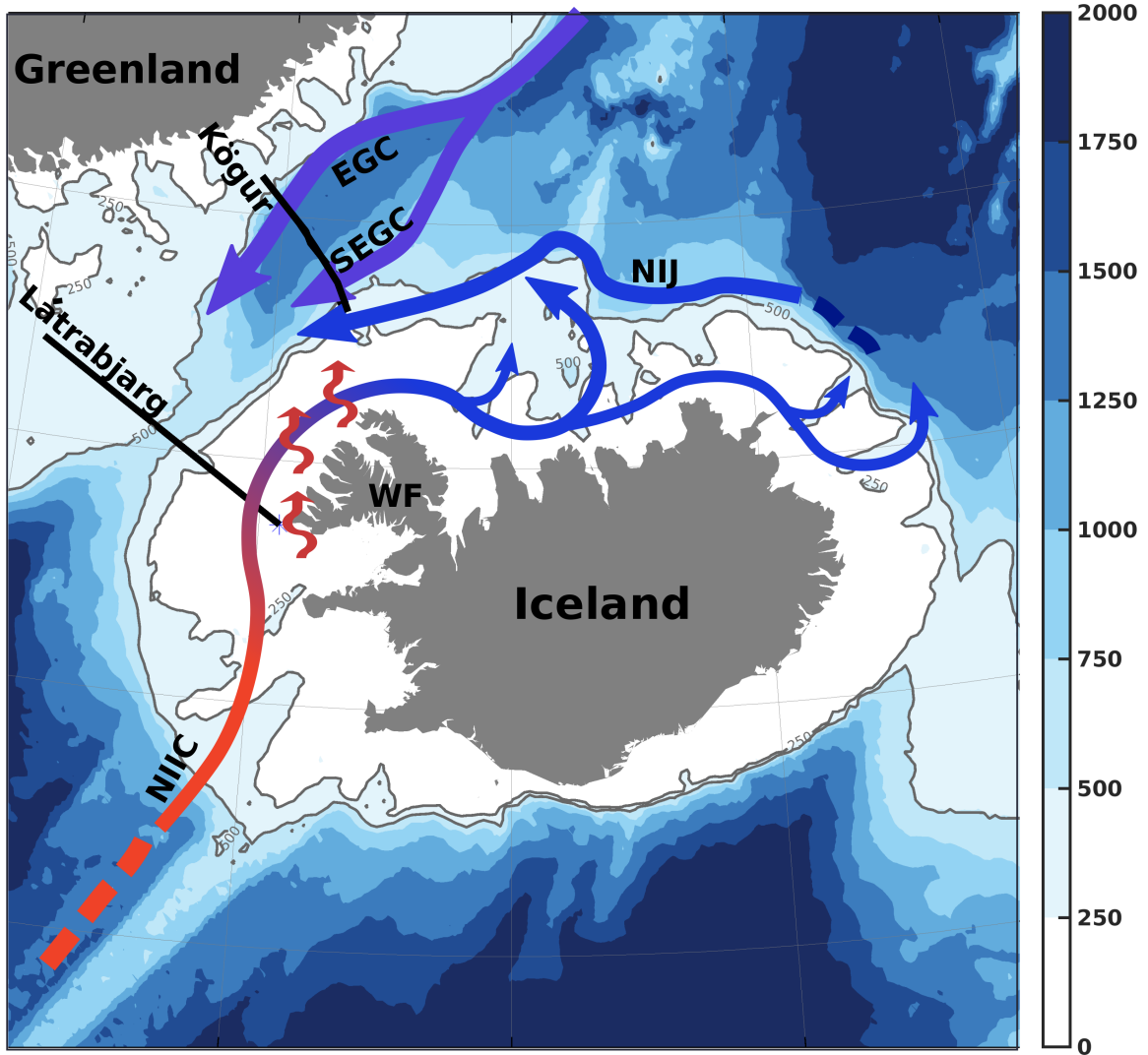


Figure 5.20: Schematic circulation in the area northwest/north of Iceland discussed in the text. Here we proposed the following: the NIJ represents the lower limb of a local overturning loop where the heat loss induced transformation (represented by red wiggly arrows in the northwest corner of Iceland) of the inflowing NIIC generates a dense plume which travels anticyclonically around and on the Icelandic shelf. The dense plume then cascades down the Icelandic shelf at different locations. The cascaded dense waters feed the cyclonic circulation which results from the SSH depression (Figure 5.16) as stated by Spall et al. (2017), and which carries the dense waters towards Denmark Strait, enhancing equatorward flow on the continental slope there, and hence, a stronger NIJ (Huang et al., 2019). The color scale indicates the ocean depth in meters.

These findings are of a great significance considering that the NIJ is basically the densest component of the AMOC lower limb. Assuming the inflow of the NIIC to remain unchanged, a decrease in the heat loss over the southern portion of the Nordic Seas poses the bigger threat for the replenishment of the lower limb of the AMOC. Mostly by considering the projected

poleward shift of the storm tracks under global warming conditions (Yin, 2005; Tamarin and Kaspi, 2017). A freshening of the NIIC waters would also affect the density of the waters formed on the Icelandic shelf, hence the AMOC.

On another note, we did not explore the existence of the cyclonic circum-island flow which according to Spall et al. (2017) is induced by the SSH depression. We understand that this subject requires further investigation. We did find that a cyclonic current with a speed range from 2 - 20 cm/s, of around 150 km wide from the 300 m isobath (position changes slightly for each section) is at work across all the studied sections (Figures 5.14 and 5.17). This cyclonic flow carries the dense water formed towards the Denmark Strait.

Bibliography

- Bamber, J., den Broeke, M., Ettema, J., Lenaerts, J., and Rignot, E. (2012). Recent large increases in freshwater fluxes from Greenland into the North Atlantic. *Geophysical Research Letters*, 39(19).
- Behrens, E., Våge, K., Harden, B., Biastoch, A., and Böning, C. W. (2017). Composition and variability of the Denmark Strait Overflow Water in a high-resolution numerical model hindcast simulation. *Journal of Geophysical Research: Oceans*, 122(4).
- Bernard, B., Madec, G., Penduff, T., Molines, J.-M., Treguier, A.-M., Sommer, J. L., Beckmann, A., Biastoch, A., Böning, C., Dengg, J., Derval, C., Durand, E., Gulev, S., Remy, E., Talandier, C., Theetten, S., Maltrud, M., McClean, J., and Cuevas, B. D. (2006). Impact of partial steps and momentum advection schemes in a global ocean circulation model at eddy-permitting resolution. *Ocean Dynamics*, 56(5-6):543–567.
- Dai, A., Qian, T., Trenberth, K. E., and Milliman, J. D. (2009). Changes in continental freshwater discharge from 1948 to 2004. *Journal of Climate*, 22(10):2773–2792.
- Dai, A. and Trenberth, K. E. (2002). Estimates of Freshwater Discharge from Continents: Latitudinal and Seasonal Variations. *Journal of Hydrometeorology*, 3(6):660–687.
- Dickson, B., Meincke, J., and Rhines, P. (2008). *Arctic–Subarctic Ocean Fluxes: Defining the Role of the Northern Seas in Climate*. Springer.
- Drinkwater, K., Colbourne, E., Loeng, H., Sundby, S., and Kristiansen, T. (2013). Comparison of the atmospheric forcing and oceanographic responses between the Labrador Sea and the Norwegian and Barents seas. *Progress in Oceanography*, 114:11 – 25.
- Eldevik, T., Nilsen, J. E. Ø., Iovino, D., Olsson, K. A., Sandø, A. B., and Drange, H. (2009). Observed sources and variability of Nordic seas overflow. *Nature Geoscience*, 2(6):406–410.
- Fichefet, T. and Maqueda, M. (1997). Sensitivity of a global sea ice model to the treatment of ice thermodynamics and dynamics. *Journal of Geophysical Research: Oceans (1978–2012)*, 102(C6):12609–12646.

- Harden, B., Pickart, R., Valdimarsson, H., Våge, K., de Steur, L., Richards, C., Bahr, F., Torres, D., Børve, E., Jónsson, S., Macrander, A., Østerhus, S., Håvik, L., and Hattermann, T. (2016). Upstream sources of the Denmark Strait Overflow: Observations from a high-resolution mooring array. *Deep Sea Research Part I: Oceanographic Research Papers*, 112:94 – 112.
- Hawker, E. J. (2005). *The Nordic Seas circulation and exchanges*. PhD thesis, University of Southampton.
- Holdsworth, A. M. and Myers, P. G. (2015). The influence of high-frequency atmospheric forcing on the circulation and deep convection of the Labrador Sea. *Journal of Climate*, 28(12):4980–4996.
- Huang, J., Pickart, R. S., Valdimarsson, H., Lin, P., Spall, M. A., and Xu, F. (2019). Structure and variability of the north icelandic jet from two years of mooring data. *Journal of Geophysical Research: Oceans*.
- Jochumsen, K., Köllner, M., Quadfasel, D., Dye, S., Rudels, B., and Valdimarsson, H. (2015). On the origin and propagation of Denmark Strait overflow water anomalies in the Irminger Basin. *Journal of Geophysical Research: Oceans*, 120(3):1841–1855.
- Jochumsen, K., Moritz, M., Nunes, N., Quadfasel, D., Larsen, K. M. H., Hansen, B., Valdimarsson, H., and Jonsson, S. (2017). Revised transport estimates of the Denmark Strait overflow. *Journal of Geophysical Research: Oceans*, 122(4):3434–3450.
- Jonsson, S. and Valdimarsson, H. (2004). A new path for the denmark strait overflow water from the iceland sea to denmark strait. *Geophysical Research Letters*, 31.
- Käse, R. H., Serra, N., Köhl, A., and Stammer, D. (2009). Mechanisms for the variability of dense water pathways in the nordic seas. *Journal of Geophysical Research: Oceans*, 114(C1).
- Köhl, A. (2010). Variable source regions of denmark strait and faroe bank channel overflow waters. *Tellus A*, 62(4):551–568.
- Köhl, A., Käse, R. H., Stammer, D., and Serra, N. (2007). Causes of changes in the denmark strait overflow. *Journal of Physical Oceanography*, 37(6):1678–1696.

- Large, W. G. and Yeager, S. G. (2009). The global climatology of an interannually varying air–sea flux data set. *Climate Dynamics*, 33(2):341–364.
- Madec, G. and the NEMO team (2008). *NEMO ocean engine*. Note du Pôle de modélisation, Institut Pierre-Simon Laplace (IPSL), France, No 27, ISSN No 1288-1619.
- Masina, S., Storto, A., Ferry, N., Valdivieso, M., Haines, K., Balmaseda, M., Zuo, H., Drevillon, M., and Parent, L. (2017). An ensemble of eddy-permitting global ocean reanalyses from the MyOcean project. *Climate Dynamics*, 49(3):813–841.
- Mastropole, D., Pickart, R. S., Valdimarsson, H., Våge, K., Jochumsen, K., and Girton, J. (2017). On the hydrography of denmark strait. *Journal of Geophysical Research: Oceans*, 122(1):306–321.
- Mauritzen, C. (1996). Production of dense overflow waters feeding the North Atlantic across the Greenland-Scotland Ridge. Part 1: Evidence for a revised circulation scheme. *Deep Sea Research Part I: Oceanographic Research Papers*, 43(6):769 – 806.
- Moore, G. W. K., Våge, K., Pickart, R. S., and Renfrew, I. A. (2015). Decreasing intensity of open-ocean convection in the greenland and iceland seas. *Nature Climate Change*, 5.
- Pickart, R. S., Spall, M. A., Torres, D. J., Våge, K., Valdimarsson, H., Nobre, C., Moore, G. W. K., Jonsson, S., and Mastropole, D. (2017). The North Icelandic Jet and its relationship to the North Icelandic Irminger Current. *Journal of Marine Research*, 75(5):605–639.
- Smith, G. C., Roy, F., Mann, P., Dupont, F., Brasnett, B., Lemieux, J.-F., Laroche, S., and Bélair, S. (2014). A new atmospheric dataset for forcing ice–ocean models: Evaluation of reforecasts using the Canadian global deterministic prediction system. *Quarterly Journal of the Royal Meteorological Society*, 140(680):881–894.
- Spall, M. A., Pedlosky, J., and Cenedese, C. (2017). Circulation induced by isolated dense water formation over closed topographic contours. *Journal of Physical Oceanography*, 47(9):2251–2265.
- Tamarin, T. and Kaspi, Y. (2017). The poleward shift of storm tracks under global warming: A lagrangian perspective. *Geophysical Research Letters*, 44(20):10,666–10,674.

- Våge, K., Moore, G., Jónsson, S., and Valdimarsson, H. (2015). Water mass transformation in the Iceland Sea. *Deep Sea Research Part I: Oceanographic Research Papers*, 101:98 – 109.
- Våge, K., Pickart, R. S., Spall, M. A., Moore, G., Valdimarsson, H., Torres, D. J., Erofeeva, S. Y., and Nilsen, J. E. Ø. (2013). Revised circulation scheme north of the Denmark Strait. *Deep Sea Research Part I: Oceanographic Research Papers*, 79:20 – 39.
- Våge, K., Pickart, R. S., Spall, M. A., Valdimarsson, H., Jonsson, S., Torres, D. J., Østerhus, S., and Eldevik, T. (2011). Significant role of the North Icelandic Jet in the formation of Denmark Strait overflow water. *Nature Geoscience*, 4:723 – 727.
- Yang, J. and Pratt, L. J. (2013). On the Effective Capacity of the Dense-Water Reservoir for the Nordic Seas Overflow: Some Effects of Topography and Wind Stress. *Journal of Physical Oceanography*, 43(2):418–431.
- Yin, J. H. (2005). A consistent poleward shift of the storm tracks in simulations of 21st century climate. *Geophysical Research Letters*, 32(18).

Chapter 6

Conclusions

Recent studies based on observations (Cheng et al., 2019) have shown a rapid increase in the ocean's heat content since 1990. This has contributed to an increase in precipitation intensity (Trenberth et al., 2003), rising sea levels and the declining of the ice sheets (glaciers, Greenland Ice Sheet (GrIS, etc.) (Rhein et al., 2013). An enhancement in the hydrological cycle and the continuous declining of the ice sheets are expected to increase the freshwater input into the Arctic and Sub-Arctic basins (Wentz et al., 2007). The input of cold and fresh waters can limit vertical mixing processes in the upper ocean, which drive meridional ocean heat transport cells such as the Atlantic Meridional Ocean Circulation (AMOC).

The AMOC, which is known to strongly moderate the climate in densely populated mid-latitude regions such as western Europe, feeds from basins where deep water formation occurs (Kuhlbrodt et al., 2007), where vertical mixing is a key component and at risk due to global warming. To understand the implications of the global warming related changes on these basins and the waters formed within, it is imperative to have a better understanding of the processes involved in deep water formation.

In this thesis I addressed processes involved in the formation of two of the main components that feed the AMOC as part of the North Atlantic Deep Water (NADW): Labrador Sea Water (LSW) and Denmark Strait Overflow Water (DSOW). My main goals were:

- I. To study the hydrodynamic response of water formation in the Labrador Sea due to an increase in the precipitation and Greenland melt increase, a decrease in the number of

storms crossing the basing, and changes in model resolution.

- II. To investigate the transformation of the Atlantic Water as it enters the Nordic Seas and its role on driving the densest component of the DSOW;
- III. To explore the possible existence of a not-yet-accounted-for source for DSOW which results from the densification of the North Icelandic Irminger Current (NIIC) on the Icelandic shelf.

The following sections expand my main findings in more details.

6.1 Principal findings

6.1.1 Labrador Sea Water formation sensitivity

I found that with $1/4^\circ$ resolution the LSW formation rate was 19% larger compared with its counterpart at $1/12^\circ$ resolution. Due to an increase in the eddy activity allowed by the use of $1/12^\circ$ horizontal resolution, freshwater advection increases. This in turn was found to impact the depth and area of the maximum mixed layer. My results point out that $1/4^\circ$ horizontal resolution models might overestimate LSW formation. This is of a great significance considering that the typical horizontal resolution of the numerical models used in the assessment reports of the Intergovernmental Panel on Climate Change (IPCC) is roughly 1° to 2° for the atmospheric component and around 1° for the ocean (Flato et al., 2013), with some now reaching the $1/4^\circ$.

My results show that, an increase in either precipitation or Greenland melt in the Labrador Sea, is not likely to decrease the overall LSW formation rate or the maximum convection depth. In fact, there has been a progressive deepening in the observed convection in the Labrador Sea since 2012, and $LSW_{2012-2016}$ is one of the deepest ever observed back to 1983 (Yashayaev and Loder, 2017). However the formation of denser LSW would decrease which, by affecting the large scale density gradients, may have longer-term dynamic implications. An increase in freshwater fluxes from GrIS or due to an increase in the precipitation over the mid-latitudes, would most likely impact the AMOC due to a decrease in the replenishment of denser LSW, rather than due to a decrease in the depth of the convection. These implications however,

cannot be further seen in my analysis as they are not likely to emerge within the years that my study covers (Böning et al., 2016).

I found that by filtering out the storms the heat loss over the Labrador Sea decreased by 44%. This reduction was enough to shut down the deep convection in the basin, with the March mixed layer depth going not deeper than 400 m. It took less than a year of filtered atmospheric forcing for the *Filtered* simulation to show a considerably decrease in the LSW formation rate. It is important to note here that high frequency atmospheric phenomena are projected to decrease based on relatively coarse resolution coupled models. How this result would change if high resolution projections were available, is still uncertain.

Overall, my findings point out that a decrease in the storms crossing the Labrador Sea with a consequent reduction in the winter heat loss, might be a bigger threat to deep convection and LSW formation (and hence the AMOC) in the future than the expected increases in the freshwater input.

6.1.2 Atlantic Water transformation in the Nordic Seas as a source to the overflow waters

I have explored the transformation of the North Icelandic Irminger Current (NIIC) as it enters the Nordic Seas through Denmark Strait as well as the role played by this transformation in driving the North Icelandic Jet (NIJ). I consider this question using two different configurations of an eddy-permitting ocean general circulation model and the off-line Lagrangian tracking tool, Ariane.

Transformation to greater densities is found to occur in the boundary currents of the Nordic Seas. These waters leaving at depth through Denmark Strait are found to do so within six years. A faster transformation occurs in a loop along the north Icelandic shelfbreak with export occurring in the NIJ within one year. Despite the transformation to denser water occurring in the boundary currents, the maximum densities reached by the particles are consistent with the maximum densities observed in the DSOW (e.g., Jochumsen et al., 2012; Våge et al., 2013; Jochumsen et al., 2015, 2017).

Different from Våge et al. (2013) who found that the transformation of the NIIC occurs inside the Iceland Sea gyre, I find in our analysis that much of the transformation is happening

along the north Icelandic shelfbreak. My findings are, however, consistent with Behrens et al. (2017) who by using a model with a $1/20^\circ$ horizontal resolution, found the sources of the NIJ mainly originated from the transformation of the NIIC north of Iceland.

My results indicate that even the most dense parts of the Denmark Strait Overflow Water could come from boundary current transformations, rather than deep convection in the interior of the Nordic Seas. Thus, provided that Atlantic Water is still transformed by winter cooling in the boundary currents, even a significant influx of fresh water to the interior of the Nordic Seas (leading to a prolonged cessation of convection) may not have a significant impact on the local overflows strength nor the AMOC.

6.1.3 A new source for the North Icelandic Jet

I examine the transformation of the NIIC in a region of the northwest Icelandic shelf and the large-scale circulation response, over the period 2002 to 2018. I propose an overturning loop whose upper limb is the transformation of the NIIC on the Icelandic shelf, with the NIJ the lower limb. Strong winter heat lost in a region of the northwest Icelandic shelf allows the NIIC waters to gain in density and sink to the bottom. A dense (denser than 27.8 kg/m^3) plume is generated as a result and travels anticyclonically on the Icelandic shelf from the formation region, cascading down the slope north of Iceland forced by bathymetry irregularities. As a response to the dense plume a depression in the sea surface height also propagates anticyclonically from the formation region which in turns generates an offshore cyclonic flow that carries the dense waters back towards Denmark Strait as they cascade. The transport of dense waters (denser than 27.8 kg/m^3) crossing the 500 m isobath towards deeper waters, north of Iceland, was found to be in the range 0.25 - 1.25 Sv, which is sufficient to feed the observed transport of the NIJ. The dense water formation process has its maximum generally from December to March, which allows for it to be the source of the strong regime of the NIJ. The identified loop is dynamically consistent with Spall et al. (2017) who explored the large-scale circulation response to dense water formation near an island.

Due to the horizontal resolution of my model, which is not eddy resolving, I cannot discard the Våge et al. (2011) hypothesis for the formation of the NIJ. Moreover, given the timing of the dense water formation I can not assume for it to be the sole source of the NIJ. I can

assume, however, that it is the source of the enhanced NIJ regime.

My findings are also consistent with the observational study of Huang et al. (2019) who found that larger heat fluxes over the west/northwest Icelandic shelf leads to an enhanced NIJ transport with a two month lag. Observational data registered from 1929 to present confirms the presence of waters denser than 28 kg/m^3 in the study region, on the northwest Icelandic shelf.

These findings are of a great significance considering that the NIJ is basically the densest component of the lower limb of the AMOC. Assuming the inflow of the NIIC to remain unchanged, a decrease in the heat loss due to, for example, a decrease in the storms crossing over the southern portion of the Nordic Seas, poses the bigger threat for the replenishment of the lower limb of the AMOC, rather than a halt in the convection in the Greenland and Iceland Seas. Mostly considering the projected poleward shift of the storm tracks under global warming conditions (Yin, 2005; Tamarin and Kaspi, 2017).

6.1.4 Thesis Summary

By using a set of model simulations conducted with a coupled ocean and sea ice regional configuration based on the Nucleus for European Modelling of the Ocean (NEMO) numerical framework 3.4, together with observational data, I have explored different processes closely linked with the formation of NADW. The main contributions of this thesis are:

- Increased Greenland melt and precipitation impact denser LSW replenishment; the overall LSW formation rate and maximum MLD was not found to significantly decrease.
- Potential decreases in Labrador Sea winter heat loss due to global warming may be a bigger threat to LSW formation than freshwater increase.
- Strong light-to-dense Atlantic Water transformation driven by heat loss occurs in the boundary currents of the Nordic Seas, with densities reaching that of DSOW.
- Water entering the Nordic Seas within the NIIC is transformed into overflow waters in the shelf system of the Nordic Seas within 6 years

- Along the north Icelandic shelfbreak the transformation is faster with export of the transformed waters occurring in the NIJ within 1 year
- A new overturning loop is proposed in this thesis with the NIIC being the upper limb and the NIJ the lower limb. I found that the transformation that the NIIC waters undergo, contrary to what have been thought, occurs on and along the west/northwest portion of the Icelandic shelf.

Bibliography

- Behrens, E., Våge, K., Harden, B., Biastoch, A., and Böning, C. W. (2017). Composition and variability of the Denmark Strait Overflow Water in a high-resolution numerical model hindcast simulation. *Journal of Geophysical Research: Oceans*, 122(4).
- Böning, C. W., Behrens, E., Biastoch, A., Getzlaff, K., and Bamber, J. L. (2016). Emerging impact of greenland meltwater on deepwater formation in the north atlantic ocean. *Nature Geoscience*, 9:523–527.
- Cheng, L., Abraham, J., Hausfather, Z., and Trenberth, K. E. (2019). How fast are the oceans warming? *Science*, 363(6423):128–129.
- Flato, G., Marotzke, J., Abiodun, B., Braconnot, P., Chou, S., Collins, W., Cox, P., Driouech, F., Emori, S., Eyring, V., Forest, C., Gleckler, P., Guilyardi, E., Jakob, C., Kattsov, V., Reason, C., and Rummukainen, M. (2013). *Evaluation of Climate Models. In: Climate Change 2013: The Physical Science Basis. Contribution of Working Group I to the Fifth Assessment Report of the Intergovernmental Panel on Climate Change [Solomon, S. and Qin, D. and Manning, M. and Chen, Z. and Marquis, M. and Averyt, -K.B. and Tignor, M. and Miller, H.L. (eds.)]*. Cambridge University Press, Cambridge, United Kingdom and New York, NY, USA.
- Huang, J., Pickart, R. S., Valdimarsson, H., Lin, P., Spall, M. A., and Xu, F. (2019). Structure and variability of the north icelandic jet from two years of mooring data. *Journal of Geophysical Research: Oceans*.
- Jochumsen, K., Köllner, M., Quadfasel, D., Dye, S., Rudels, B., and Valdimarsson, H. (2015). On the origin and propagation of Denmark Strait overflow water anomalies in the Irminger Basin. *Journal of Geophysical Research: Oceans*, 120(3):1841–1855.
- Jochumsen, K., Moritz, M., Nunes, N., Quadfasel, D., Larsen, K. M. H., Hansen, B., Valdimarsson, H., and Jonsson, S. (2017). Revised transport estimates of the Denmark Strait overflow. *Journal of Geophysical Research: Oceans*, 122(4):3434–3450.

- Jochumsen, K., Quadfasel, D., Valdimarsson, H., and Jónsson, S. (2012). Variability of the Denmark Strait overflow: Moored time series from 1996–2011. *Journal of Geophysical Research: Oceans*, 117(C12).
- Kuhlbrodt, T., Griesel, A., Montoya, M., Levermann, A., Hofmann, M., and Rahmstorf, S. (2007). On the driving processes of the Atlantic meridional overturning circulation. *Reviews of Geophysics*, 45(2).
- Rhein, M., Rintoul, S., Aoki, S., Campos, E., Chambers, D., Feely, R., Gulev, S., Johnson, G., Josey, S., Kostianoy, A., Mauritzen, C., Roemmich, D., Talley, L., and Wang, F. (2013). Observations: Ocean. In: *Climate Change 2013: The Physical Science Basis. Contribution of Working Group I to the Fifth Assessment Report of the Intergovernmental Panel on Climate Change* [Stocker, T.F., D. Qin, G.-K. Plattner, M. Tignor, S.K. Allen, J. Boschung, A. Nauels, Y. Xia, V. Bex and P.M. Midgley (eds.)].
- Spall, M. A., Pedlosky, J., and Cenedese, C. (2017). Circulation induced by isolated dense water formation over closed topographic contours. *Journal of Physical Oceanography*, 47(9):2251–2265.
- Tamarin, T. and Kaspi, Y. (2017). The poleward shift of storm tracks under global warming: A lagrangian perspective. *Geophysical Research Letters*, 44(20):10,666–10,674.
- Trenberth, K. E., Dai, A., Rasmussen, R. M., and Parsons, D. B. (2003). The changing character of precipitation. *Bulletin of the American Meteorological Society*, 84(9):1205–1218.
- Våge, K., Pickart, R. S., Spall, M. A., Moore, G., Valdimarsson, H., Torres, D. J., Erofeeva, S. Y., and Nilsen, J. E. Ø. (2013). Revised circulation scheme north of the Denmark Strait. *Deep Sea Research Part I: Oceanographic Research Papers*, 79:20 – 39.
- Wentz, F. J., Ricciardulli, L., Hilburn, K., and Mears, C. (2007). How much more rain will global warming bring? *Science*, 317(5835):233–235.
- Yashayaev, I. and Loder, J. W. (2017). Further intensification of deep convection in the labrador sea in 2016. *Geophysical Research Letters*, 44(3):1429–1438. 2016GL071668.

Yin, J. H. (2005). A consistent poleward shift of the storm tracks in simulations of 21st century climate. *Geophysical Research Letters*, 32(18).

Bibliography

- Aagaard, K., Swift, J. H., and Carmack, E. C. (1985). Thermohaline circulation in the Arctic Mediterranean Seas. *Journal of Geophysical Research: Oceans*, 90(C3):4833–4846.
- Anderson, L. G., Drange, H., Chierici, M., Fransson, A., Johannessen, T., Skjelvan, I., and Rey, F. (2000). Annual carbon fluxes in the upper Greenland Sea based on measurements and a box-model approach. *Tellus B*, 52(3):1013–1024.
- Asselin, R. (1972). Frequency filter for time integrations. *Monthly Weather Review*, 100(6):487–490.
- Azetsu-Scott, K., Clarke, A., Falkner, K., Hamilton, J., Jones, E. P., Lee, C., Petrie, B., Prinsenber, S., Starr, M., and Yeats, P. (2010). Calcium carbonate saturation states in the waters of the Canadian Arctic Archipelago and the Labrador Sea. *Journal of Geophysical Research: Oceans*, 115(C11).
- Azetsu-Scott, K., Jones, E. P., Yashayaev, I., and Gershey, R. M. (2003). Time series study of CFC concentrations in the Labrador Sea during deep and shallow convection regimes (1991–2000). *Journal of Geophysical Research: Oceans*, 108(C11).
- Bamber, J., den Broeke, M., Ettema, J., Lenaerts, J., and Rignot, E. (2012). Recent large increases in freshwater fluxes from Greenland into the North Atlantic. *Geophysical Research Letters*, 39(19).

- Barnier, B., LeSommer, J., Molines, J. M., Penduff, T., Theetten, S., Treguier, A. M., Madec, G., Biastoch, A., Böning, C., Dengg, J., Gulev, S., Bourdallé, B. R., Chanut, J., Garric, G., Coward, A., de Cuevas, B., New, A., Haines, K., Smith, G. C., Drijfhout, S., Hazeleger, W., Severijns, C., and Myers, P. (2007). Eddy-permitting ocean circulation hindcasts of the past decades. *CLIVAR-Exchanges*, 12(3):8–10.
- Behrens, E., Biastoch, A., and Böning, C. W. (2013). Spurious AMOC trends in global ocean sea-ice models related to subarctic freshwater forcing. *Ocean Modelling*, 69:39 – 49.
- Behrens, E., Våge, K., Harden, B., Biastoch, A., and Böning, C. W. (2017). Composition and variability of the Denmark Strait Overflow Water in a high-resolution numerical model hindcast simulation. *Journal of Geophysical Research: Oceans*, 122(4).
- Bernard, B., Madec, G., Penduff, T., Molines, J.-M., Treguier, A.-M., Sommer, J. L., Beckmann, A., Biastoch, A., Böning, C., Dengg, J., Derval, C., Durand, E., Gulev, S., Remy, E., Talandier, C., Theetten, S., Maltrud, M., McClean, J., and Cuevas, B. D. (2006). Impact of partial steps and momentum advection schemes in a global ocean circulation model at eddy-permitting resolution. *Ocean Dynamics*, 56(5-6):543–567.
- Biastoch, A., Böning, C. W., Getzlaff, J., Molines, J.-M., and Madec, G. (2008). Causes of Interannual–Decadal Variability in the Meridional Overturning Circulation of the Midlatitude North Atlantic Ocean. *Journal of Climate*, 21(24):6599–6615.
- Blanke, B., Arhan, M., Madec, G., and Roche, S. (1999). Warm water paths in the Equatorial Atlantic as diagnosed with a General Circulation Model. *Journal of Physical Oceanography*, 29(11):2753–2768.
- Blanke, B. and Raynaud, S. (1997). Kinematics of the Pacific Equatorial Undercurrent: An Eulerian and Lagrangian approach from GCM results. *Journal of Physical Oceanography*, 27(6):1038–1053.
- Blayo, E. and Debreu, L. (1999). Adaptive mesh refinement for finite-difference ocean models: first experiments. *Journal of Physical Oceanography*, 29(6):1239–1250.

- Blindheim, J. and Østerhus, S. (2005). The Nordic Seas, main oceanographic features. *The Nordic seas: An integrated perspective*, pages 11–37.
- Boning, C., Bryan, F., Holland, W., and Doscher, R. (1997). Deep-water formation and meridional overturning in a high-resolution model of the North Atlantic. *Oceanographic Literature Review*, 3(44):175.
- Böning, C. W., Scheinert, M., Dengg, J., Biastoch, A., and Funk, A. (2006). Decadal variability of subpolar gyre transport and its reverberation in the North Atlantic overturning. *Geophysical Research Letters*, 33(21):n/a–n/a. L21S01.
- Brakstad, A., Våge, K., Håvik, L., and Moore, G. W. K. (2019). Water mass transformation in the greenland sea during the period 1986–2016. *Journal of Physical Oceanography*, 49(1):121–140.
- Brunnabend, S.-E., Schröter, J., Rietbroek, R., and Kusche, J. (2015). Regional sea level change in response to ice mass loss in Greenland, the West Antarctic and Alaska. *Journal of Geophysical Research: Oceans*.
- Chanut, J., Barnier, B., Large, W., Debreu, L., Penduff, T., Molines, J.-M., and Mathiot, P. (2008). Mesoscale Eddies in the Labrador Sea and Their Contribution to Convection and Restratification. *Journal of Physical Oceanography*, 38(8):1617–1643.
- Cheng, L., Abraham, J., Hausfather, Z., and Trenberth, K. E. (2019). How fast are the oceans warming? *Science*, 363(6423):128–129.
- Ciais, P., Sabine, C., Bala, G., Bopp, L., Brovkin, V., Canadell, J., Chhabra, A., DeFries, R., Galloway, J., Heimann, M., Jones, C., Quéré, C. L., Myneni, R., Piao, S., and Thornton, P. (2013). Carbon and Other Biogeochemical Cycles. In: *Climate Change 2013: The Physical Science Basis. Contribution of Working Group I to the Fifth Assessment Report of the Intergovernmental Panel on Climate Change* [Stocker, T.F., D. Qin, G.-K. Plattner, M. Tignor, S.K. Allen, J. Boschung, A. Nauels, Y. Xia, V. Bex and P.M. Midgley (eds.)], publisher = Cambridge University Press, Cambridge, United Kingdom and New York, NY, USA.

- Condrón, A. and Renfrew, I. A. (2013). The impact of polar mesoscale storms on northeast Atlantic Ocean circulation. *Nature Geoscience*, 6(1):34–37.
- Courtois, P., G.-Q. Y., Hu, X., and Myers, P. (submitted). Subduction Rate of Labrador Sea Water (in prep).
- C.S., S. D. M. G. R. D. M. B. J. W. B. M. M. (2017). Atlantic meridional overturning circulation observed by the rapid-mocha-wbts (rapid-meridional overturning circulation and heatflux array-western boundary time series) array at 26n from 2004 to 2017. *British Oceanographic Data Centre - Natural Environment Research Council, UK*.
- Da Costa, M. V., Mercier, H., and Treguier, A. M. (2005). Effects of the mixed layer time variability on kinematic subduction rate diagnostics. *Journal of physical oceanography*, 35(4):427–443.
- Dai, A., Qian, T., Trenberth, K. E., and Milliman, J. D. (2009). Changes in continental freshwater discharge from 1948 to 2004. *Journal of Climate*, 22(10):2773–2792.
- Dai, A. and Trenberth, K. E. (2002). Estimates of Freshwater Discharge from Continents: Latitudinal and Seasonal Variations. *Journal of Hydrometeorology*, 3(6):660–687.
- de Jong, M. F., Bower, A. S., and Furey, H. H. (2014). Two years of observations of warm-core anticyclones in the labrador sea and their seasonal cycle in heat and salt stratification. *Journal of Physical Oceanography*, 44(2):427–444.
- Debreu, L., Vouland, C., and Blayo, E. (2008). AGRIF: Adaptive grid refinement in Fortran. *Computers & Geosciences*, 34(1):8–13.
- Desbruyères, D., Thierry, V., and Mercier, H. (2013). Simulated decadal variability of the meridional overturning circulation across the A25-Ovide section. *Journal of Geophysical Research: Oceans*, 118(1):462–475.
- Dickson, B., Meincke, J., and Rhines, P. (2008). *Arctic–Subarctic Ocean Fluxes: Defining the Role of the Northern Seas in Climate*. Springer.

- Dickson, R., Lazier, J., Meincke, J., and Rhines, P. (1996). Long-term coordinated changes in the convective activity of the North Atlantic. In *Decadal Climate Variability*, pages 211–261. Springer.
- Dickson, R., Rudels, B., Dye, S., Karcher, M., Meincke, J., and Yashayaev, I. (2007). Current estimates of freshwater flux through arctic and subarctic seas. *Progress in Oceanography*, 73:210–230.
- Dickson, R. R. and Brown, J. (1994a). The production of north atlantic deep water: Sources, rates, and pathways. *Journal of Geophysical Research: Oceans*, 99(C6):12319–12341.
- Dickson, R. R. and Brown, J. (1994b). The production of north atlantic deep water: Sources, rates, and pathways. *Journal of Geophysical Research: Oceans*, 99(C6):12319–12341.
- Dickson, R. R., Meincke, J., Malmberg, S.-A., and Lee, A. J. (1988). The “great salinity anomaly” in the northern North Atlantic 1968–1982. *Progress in Oceanography*, 20(2):103–151.
- DRAKKAR Group (2007). Eddy-permitting ocean circulation hindcasts of past decades. *CLIVAR Exchanges*, 12(3):8 – 10.
- Drange, H., Dokken, T., Furevik, T., Gerdes, R., Berger, W., Nesje, A., Arild Orvik, K., Skagseth, Ø., Skjelvan, I., and Østerhus, S. (2005). *The Nordic Seas: an overview*. Wiley Online Library.
- Drinkwater, K., Colbourne, E., Loeng, H., Sundby, S., and Kristiansen, T. (2013). Comparison of the atmospheric forcing and oceanographic responses between the Labrador Sea and the Norwegian and Barents seas. *Progress in Oceanography*, 114:11 – 25.
- Dukhovskoy, D. S., Myers, P. G., Platov, G., Timmermans, M.-L., Curry, B., Proshutinsky, A., Bamber, J. L., Chassignet, E., Hu, X., Lee, C. M., and Somavilla, R. (2016). Greenland freshwater pathways in the sub-Arctic Seas from model experiments with passive tracers. *Journal of Geophysical Research: Oceans*, 121(1):877–907.
- Eby, M. and Holloway, G. (1994). Grid transformation for incorporating the arctic in a global ocean model. *Climate Dynamics*, 10(4):241–247.

- Eldevik, T., Nilsen, J. E. Ø., Iovino, D., Olsson, K. A., Sandø, A. B., and Drange, H. (2009). Observed sources and variability of Nordic seas overflow. *Nature Geoscience*, 2(6):406–410.
- Ferry, N., Parent, L., Masina, S., Storto, A., Zuo, H., and Balmaseda, M. (2016). *Product user manual for Global Ocean Reanalysis Products GLOBAL-REANALYSIS-PHYS-001-009, GLOBAL-REANALYSIS-PHYS-001-011 and GLOBAL-REANALYSIS-PHYS-001-017*. EU Copernicus Marine Service.
- Feucher, C., Garcia-Quintana, Y., Yashayaev, I., Hu, X., and Myers, P. (2019). Labrador sea water formation rate and its impact on the meridional overturning circulation. *Geophysical Research Oceans*.
- Fichefet, T. and Maqueda, M. (1997). Sensitivity of a global sea ice model to the treatment of ice thermodynamics and dynamics. *Journal of Geophysical Research: Oceans (1978–2012)*, 102(C6):12609–12646.
- Fischer, J., Karstensen, J., Zantopp, R., Visbeck, M., Biastoch, A., Behrens, E., Böning, C., Quadfasel, D., Jochumsen, K., Valdimarsson, H., Jónsson, S., Bacon, S., Holliday, N., Dye, S., Rhein, M., and Mertens, C. (2015). Intra-seasonal variability of the DWBC in the western subpolar North Atlantic. *Progress in Oceanography*, 132:233 – 249.
- Flato, G., Marotzke, J., Abiodun, B., Braconnot, P., Chou, S., Collins, W., Cox, P., Driouech, F., Emori, S., Eyring, V., Forest, C., Gleckler, P., Guilyardi, E., Jakob, C., Kattsov, V., Reason, C., and Rummukainen, M. (2013). *Evaluation of Climate Models. In: Climate Change 2013: The Physical Science Basis. Contribution of Working Group I to the Fifth Assessment Report of the Intergovernmental Panel on Climate Change [Solomon, S. and Qin, D. and Manning, M. and Chen, Z. and Marquis, M. and Averyt, -K.B. and Tignor, M. and Miller, H.L. (eds.)]*. Cambridge University Press, Cambridge, United Kingdom and New York, NY, USA.
- Forsberg, R., Sørensen, L., and Simonsen, S. (2017). Greenland and Antarctica ice sheet mass changes and effects on global sea level. *Surveys in Geophysics*, 38(1):89–104.
- García-Ibáñez, M. I., Pardo, P. C., Carracedo, L. I., Mercier, H., Lherminier, P., Ríos, A. F.,

- and Pérez, F. F. (2015). Structure, transports and transformations of the water masses in the Atlantic Subpolar Gyre. *Progress in Oceanography*, 135:18–36.
- Gary, S. F., Lozier, M. S., Biastoch, A., and Böning, C. W. (2012). Reconciling tracer and float observations of the export pathways of Labrador Sea Water. *Geophysical Research Letters*, 39(24).
- Gary, S. F., Lozier, M. S., Böning, C. W., and Biastoch, A. (2011). Deciphering the pathways for the deep limb of the meridional overturning circulation. *Deep Sea Research Part II: Topical Studies in Oceanography*, 58(17):1781 – 1797.
- Gelderloos, R., Katsman, C. A., and Drijfhout, S. S. (2011). Assessing the roles of three eddy types in restratifying the labrador sea after deep convection. *Journal of Physical Oceanography*, 41(11):2102–2119.
- Gelderloos, R., Straneo, F., and Katsman, C. A. (2012). Mechanisms behind the Temporary Shutdown of Deep Convection in the Labrador Sea: Lessons from the Great Salinity Anomaly Years 1968–71. *Journal of Climate*, 25(19):6743–6755.
- Gelderoos, R., Straneo, F., and Katsman, C. (2012). Mechanisms behind the temporary shutdown of deep convection in the Labrador Sea: Lessons from the Great Salinity Anomaly Years 1968-71. *Journal of Climate*, 25:6743–6755.
- Gerdes, R., Hurka, J., Karcher, M., Kauker, F., and Köberle, C. (2005). Simulated History of Convection in the Greenland and Labrador Seas, 1948—2001. *The Nordic Seas: An Integrated Perspective*, pages 221–238.
- Gerdes, R., Hurlin, W., and Griffies, S. M. (2006). Sensitivity of a global ocean model to increased run-off from Greenland. *Ocean Modelling*, 12(3):416 – 435.
- Getzlaff, J., Böning, C. W., Eden, C., and Biastoch, A. (2005). Signal propagation related to the North Atlantic overturning. *Geophysical Research Letters*, 32(9):n/a–n/a. L09602.
- Griffies, S. M., Biastoch, A., Böning, C., Bryan, F., Danabasoglu, G., Chassignet, E. P., England, M. H., Gerdes, R., Haak, H., Hallberg, R. W., et al. (2009). Coordinated ocean-ice reference experiments (COREs). *Ocean Modelling*, 26(1):1–46.

- Guillard, L. C., Hu, X., Myers, P. G., and Bamber, J. L. (inprep). Meltwater Pathways from Marine Terminating Glaciers of the Greenland Ice Sheet.
- Haine, T., Böning, C., Brandt, P., Fischer, J., Funk, A., Kieke, D., Kvaleberg, E., Rhein, M., and Visbeck, M. (2008). North Atlantic deep water formation in the Labrador Sea, recirculation through the subpolar gyre, and discharge to the subtropics. In *Arctic-Subarctic Ocean Fluxes*, pages 653–701. Springer.
- Hallberg, R. (2013). Using a resolution function to regulate parameterizations of oceanic mesoscale eddy effects. *Ocean Modelling*, 72:92 – 103.
- Hansen, B. and Østerhus, S. (2000). North Atlantic–Nordic Seas exchanges. *Progress in Oceanography*, 45(2):109–208.
- Hansen, B. and Østerhus, S. (2007). Faroe bank channel overflow 1995–2005. *Progress in Oceanography*, 75(4):817–856.
- Hansen, B., Turrell, W. R., and Østerhus, S. (2001). Decreasing overflow from the Nordic seas into the Atlantic Ocean through the Faroe Bank channel since 1950. *Nature*, 411(6840):927–930.
- Harden, B., Pickart, R., Valdimarsson, H., Våge, K., de Steur, L., Richards, C., Bahr, F., Torres, D., Børve, E., Jónsson, S., Macrander, A., Østerhus, S., Håvik, L., and Hattermann, T. (2016). Upstream sources of the Denmark Strait Overflow: Observations from a high-resolution mooring array. *Deep Sea Research Part I: Oceanographic Research Papers*, 112:94 – 112.
- Hawker, E. J. (2005). *The Nordic Seas circulation and exchanges*. PhD thesis, University of Southampton.
- Holdsworth, A. M. and Myers, P. G. (2015). The Influence of high-frequency atmospheric forcing on the circulation and deep convection of the Labrador Sea. *Journal of Climate*, 28(12):4980–4996.
- Hollingworth, C. (2005). The Norwegian Sea Ecosystem. *Fish and Fisheries*, 6(1):90–91.

- Holte, J. and Straneo, F. (2017). Seasonal overturning of the labrador sea as observed by argo floats. *Journal of Physical Oceanography*, 47(10):2531–2543.
- Holte, J., Talley, L. D., Gilson, J., and Roemmich, D. (2017). An argo mixed layer climatology and database. *Geophysical Research Letters*, 44(11):5618–5626. 2017GL073426.
- Hopkins, T. S. (1991). The GIN Sea—A synthesis of its physical oceanography and literature review 1972–1985. *Earth-Science Reviews*, 30(3):175–318.
- Houssais, M.-N. and Herbaut, C. (2011). Atmospheric forcing on the Canadian Arctic Archipelago freshwater outflow and implications for the Labrador Sea variability. *Journal of Geophysical Research: Oceans*, 116(C8).
- Hu, A., Meehl, G. A., Han, W., and Yin, J. (2011). Effect of the potential melting of the Greenland Ice Sheet on the Meridional Overturning Circulation and global climate in the future. *Deep Sea Research Part II: Topical Studies in Oceanography*, 58(17):1914 – 1926.
- Hu, X. and Myers, P. G. (2013). A Lagrangian view of Pacific water inflow pathways in the Arctic Ocean during model spin-up. *Ocean Modelling*, 71:66–80.
- Huang, J., Pickart, R. S., Valdimarsson, H., Lin, P., Spall, M. A., and Xu, F. (2019). Structure and variability of the north icelandic jet from two years of mooring data. *Journal of Geophysical Research: Oceans*.
- Huang, R. X. (2010). *Part II: Wind-driven and thermohaline circulation, in Ocean Circulation: Wind-Driven and Thermohaline Processes*, pages 261–791. Cambridge University Press.
- Hunke, E. and Dukowicz, J. (1997). An elastic-viscous-plastic model for sea ice dynamics. *Journal of Physical Oceanography*, 27(9):1849–1867.
- Hunke, E. C. (2001). Viscous–plastic sea ice dynamics with the evp model: Linearization issues. *Journal of Computational Physics*, 170(1):18 – 38.
- Huntington, T. G. (2006). Evidence for intensification of the global water cycle: Review and synthesis. *Journal of Hydrology*, 319(1):83–95.

- Hurrell, J. W. and van Loon, H. (1997). Decadal variations in climate associated with the north atlantic oscillation. *Climatic Change*, 36(3):301–326.
- Isachsen, P. E., Mauritzen, C., and Svendsen, H. (2007). Dense water formation in the Nordic Seas diagnosed from sea surface buoyancy fluxes. *Deep Sea Research Part I: Oceanographic Research Papers*, 54(1):22–41.
- Jeansson, E., Jutterström, S., Rudels, B., Anderson, L. G., Olsson, K. A., Jones, E. P., Smethie, W. M., and Swift, J. H. (2008). Sources to the east greenland current and its contribution to the denmark strait overflow. *Progress in Oceanography*, 78(1):12 – 28.
- Jochumsen, K., Köllner, M., Quadfasel, D., Dye, S., Rudels, B., and Valdimarsson, H. (2015). On the origin and propagation of Denmark Strait overflow water anomalies in the Irminger Basin. *Journal of Geophysical Research: Oceans*, 120(3):1841–1855.
- Jochumsen, K., Moritz, M., Nunes, N., Quadfasel, D., Larsen, K. M. H., Hansen, B., Valdimarsson, H., and Jonsson, S. (2017). Revised transport estimates of the Denmark Strait overflow. *Journal of Geophysical Research: Oceans*, 122(4):3434–3450.
- Jochumsen, K., Quadfasel, D., Valdimarsson, H., and Jónsson, S. (2012). Variability of the Denmark Strait overflow: Moored time series from 1996–2011. *Journal of Geophysical Research: Oceans*, 117(C12).
- Jones, H. and Marshall, J. (1993). Convection with rotation in a neutral ocean: A study of open-ocean deep convection. *Journal of Physical Oceanography*, 23(6):1009–1039.
- Jones, H. and Marshall, J. (1997). Restratification after Deep Convection. *Journal of Physical Oceanography*, 27(10):2276–2286.
- Jonsson, S. and Valdimarsson, H. (2004). A new path for the denmark strait overflow water from the iceland sea to denmark strait. *Geophysical Research Letters*, 31.
- Josey, S. A. and Marsh, R. (2005). Surface freshwater flux variability and recent freshening of the North Atlantic in the eastern subpolar gyre. *Journal of Geophysical Research: Oceans*, 110(C5):2276–2287.

- Jung, T., Serrar, S., and Wang, Q. (2014). The oceanic response to mesoscale atmospheric forcing. *Geophysical Research Letters*, 41(4):1255–1260.
- Käse, R. H., Girton, J., and Sanford, T. (2003). Structure and variability of the Denmark Strait Overflow: Model and observations. *Journal of Geophysical Research: Oceans*, 108(C6).
- Käse, R. H., Serra, N., Köhl, A., and Stammer, D. (2009). Mechanisms for the variability of dense water pathways in the nordic seas. *Journal of Geophysical Research: Oceans*, 114(C1).
- Kawasaki, T. and Hasumi, H. (2014). Effect of freshwater from the west greenland current on the winter deep convection in the labrador sea. *Ocean Modelling*, 75:51 – 64.
- Khatiwala, S., Schlosser, P., and Visbeck, M. (2002). Rates and Mechanisms of Water Mass Transformation in the Labrador Sea as Inferred from Tracer Observations*. *Journal of Physical Oceanography*, 32(2):666–686.
- Khatiwala, S. and Visbeck, M. (2000). An estimate of the eddy-induced circulation in the Labrador Sea. *Geophysical Research Letters*, 27(15):2277–2280.
- Kieke, D., Rhein, M., Stramma, L., Smethie, W. M., Bullister, J. L., and LeBel, D. A. (2007). Changes in the pool of labrador sea water in the subpolar north atlantic. *Geophysical Research Letters*, 34(6):n/a–n/a. L06605.
- Kieke, D., Rhein, M., Stramma, L., Smethie, W. M., LeBel, D. A., and Zenk, W. (2006). Changes in the CFC inventories and formation rates of Upper Labrador Sea Water, 1997-2001. *Journal of Physical Oceanography*, 36(1):64–86.
- Kieke, D. and Yashayaev, I. (2015). Studies of Labrador Sea Water formation and variability in the subpolar North Atlantic in the light of international partnership and collaboration. *Progress in Oceanography*, 132:220–232.
- Köhl, A. (2010). Variable source regions of denmark strait and faroe bank channel overflow waters. *Tellus A*, 62(4):551–568.
- Köhl, A., Käse, R. H., Stammer, D., and Serra, N. (2007). Causes of changes in the denmark strait overflow. *Journal of Physical Oceanography*, 37(6):1678–1696.

- Kolstad, E. W. and Bracegirdle, T. J. (2008). Marine cold-air outbreaks in the future: an assessment of IPCC AR4 model results for the Northern Hemisphere. *Climate Dynamics*, 30(7-8):871–885.
- Körtzinger, A., Schimanski, J., Send, U., and Wallace, D. (2004). The ocean takes a deep breath. *Science*, 306(5700):1337–1337.
- Kuhlbrodt, T., Griesel, A., Montoya, M., Levermann, A., Hofmann, M., and Rahmstorf, S. (2007). On the driving processes of the Atlantic meridional overturning circulation. *Reviews of Geophysics*, 45(2).
- Large, W. G. and Yeager, S. G. (2004). Diurnal to Decadal Global Forcing for Ocean and Sea-Ice Models: The Data Sets and Flux Climatologies. *NCAR Technical Note*.
- Large, W. G. and Yeager, S. G. (2009). The global climatology of an interannually varying air-sea flux data set. *Climate Dynamics*, 33(2):341–364.
- Latarius, K. and Quadfasel, D. (2016). Water mass transformation in the deep basins of the nordic seas: Analyses of heat and freshwater budgets. *Deep Sea Research Part I: Oceanographic Research Papers*, 114:23 – 42.
- Laurent, D., Eric, B., and Bernard, B. (2005). A general adaptive multi-resolution approach to ocean modelling: Experiments in a primitive equation model of the North Atlantic. In *Adaptive Mesh Refinement-Theory and Applications*, pages 303–313. Springer.
- LeBel, D. A., Smethie, W. M., Rhein, M., Kieke, D., Fine, R. A., Bullister, J. L., Min, D.-H., Roether, W., Weiss, R. F., Andrié, C., Smythe-Wright, D., and Jones, E. P. (2008). The formation rate of North Atlantic Deep Water and Eighteen Degree Water calculated from CFC-11 inventories observed during WOCE. *Deep Sea Research Part I: Oceanographic Research Papers*, 55(8):891 – 910.
- Lilly, J. M., Rhines, P. B., Schott, F., Lavender, K., Lazier, J., Send, U., and D’Asaro, E. (2003). Observations of the Labrador Sea eddy field. *Progress in Oceanography*, 59(1):75–176.

- Lique, C., Treguier, A. M., Blanke, B., and Grima, N. (2010). On the origins of water masses exported along both sides of Greenland: A Lagrangian model analysis. *Journal of Geophysical Research: Oceans*, 115(C5).
- Liu, C. and Wang, Z. (2014). On the response of the global subduction rate to global warming in coupled climate models. *Advances in Atmospheric Sciences*, 31(1):211–218.
- Lozier, M. S., Gary, S. F., and Bower, A. S. (2013). Simulated pathways of the overflow waters in the North Atlantic: Subpolar to subtropical export. *Deep Sea Research Part II: Topical Studies in Oceanography*, 85:147 – 153.
- Lozier, M. S., Li, F., Bacon, S., Bahr, F., Bower, A. S., Cunningham, S. A., de Jong, M. F., de Steur, L., deYoung, B., Fischer, J., Gary, S. F., Greenan, B. J. W., Holliday, N. P., Houk, A., Houpert, L., Inall, M. E., Johns, W. E., Johnson, H. L., Johnson, C., Karstensen, J., Koman, G., Le Bras, I. A., Lin, X., Mackay, N., Marshall, D. P., Mercier, H., Oltmanns, M., Pickart, R. S., Ramsey, A. L., Rayner, D., Straneo, F., Thierry, V., Torres, D. J., Williams, R. G., Wilson, C., Yang, J., Yashayaev, I., and Zhao, J. (2019). A sea change in our view of overturning in the subpolar north atlantic. *Science*, 363(6426):516–521.
- Macrander, A. (2004). *Variability and processes of the Denmark Strait overflow*. PhD thesis, Uni Kiel.
- Macrander, A., Send, U., Valdimarsson, H., Jónsson, S., and H., K. R. (2005). Interannual changes in the overflow from the Nordic Seas into the Atlantic Ocean through Denmark Strait. *Geophysical Research Letters*, 32(6).
- Madec, G. (2008). NEMO ocean engine. *Note du Pole de modelisation*, 27:1288–1619.
- Marsh, R. (2000). Recent variability of the North Atlantic thermohaline circulation inferred from surface heat and freshwater fluxes. *Journal of climate*, 13(18):3239–3260.
- Marsh, R., Josey, S., De Nurser, A., Cuevas, B., and Coward, A. (2005). Water mass transformation in the North Atlantic over 1985-2002 simulated in an eddy-permitting model. *Ocean Science*, 1(2):127–144.

- Marshall, J. and Schott, F. (1999). Open-ocean convection: Observations, theory, and models. *Reviews of Geophysics*, 37(1):1–64.
- Marzocchi, A., Hirschi, J. J.-M., Holliday, N. P., Cunningham, S. A., Blaker, A. T., and Coward, A. C. (2015). The North Atlantic subpolar circulation in an eddy-resolving global ocean model. *Journal of Marine Systems*, 142:126 –143.
- Masina, S., Storto, A., Ferry, N., Valdivieso, M., Haines, K., Balmaseda, M., Zuo, H., Drevillon, M., and Parent, L. (2017). An ensemble of eddy-permitting global ocean reanalyses from the MyOcean project. *Climate Dynamics*, 49(3):813–841.
- Mauritzen, C. (1996). Production of dense overflow waters feeding the North Atlantic across the Greenland-Scotland Ridge. Part 1: Evidence for a revised circulation scheme. *Deep Sea Research Part I: Oceanographic Research Papers*, 43(6):769 – 806.
- Mauritzen, C. and Häkkinen, S. (1999). On the relationship between dense water formation and the “Meridional Overturning Cell” in the North Atlantic Ocean. *Deep Sea Research Part I: Oceanographic Research Papers*, 46(5):877–894.
- McCarthy, G., Smeed, D., Johns, W., Frajka-Williams, E., Moat, B., Rayner, D., Baringer, M., Meinen, C., Collins, J., and Bryden, H. (2015). Measuring the Atlantic Meridional Overturning Circulation at 26° N. *Progress in Oceanography*, 130:91–111.
- McCartney, M. S. and Talley, L. D. (1982). The subpolar mode water of the North Atlantic Ocean. *Journal of Physical Oceanography*, 12(11):1169–1188.
- Mertens, C., Rhein, M., Walter, M., Böning, C. W., Behrens, E., Kieke, D., Steinfeldt, R., and Stöber, U. (2014). Circulation and transports in the newfoundland basin, western subpolar north atlantic. *Journal of Geophysical Research: Oceans*, 119(11):7772–7793.
- Mesinger, F. and Arakawa, A. (1976). Numerical methods used in atmospheric models. *GARP Publication Series*, 1(17).
- Moore, G. W. K., Våge, K., Pickart, R. S., and Renfrew, I. A. (2015). Decreasing intensity of open-ocean convection in the greenland and iceland seas. *Nature Climate Change*, 5.

- Müller, V., Kieke, D., Myers, P. G., Pennelly, C., and Mertens, C. (2017). Temperature flux carried by individual eddies across 47°N in the Atlantic Ocean. *Journal of Geophysical Research: Oceans*, 122(3):2441–2464.
- Murray, R. J. (1996). Explicit generation of orthogonal grids for ocean models. *Journal of Computational Physics*, 126(2):251–273.
- Myers, P. G. (2005). Impact of freshwater from the Canadian Arctic archipelago on Labrador Sea water formation. *Geophysical Research Letters*, 32(6).
- Myers, P. G. and Donnelly, C. (2008). Water mass transformation and formation in the Labrador Sea. *Journal of Climate*, 21(7):1622–1638.
- Myers, P. G., Kulan, N., and Ribergaard, M. H. (2007). Irminger water variability in the west greenland current. *Geophysical Research Letters*, 34(17).
- Nash, S. and Hartnett, M. (2014). Development of a nested coastal circulation model: Boundary error reduction. *Environmental Modelling & Software*, 53(Supplement C):65 – 80.
- Orvik, K. A. and Nilner, P. (2002). Major pathways of atlantic water in the northern north atlantic and nordic seas toward arctic. *Geophysical Research Letters*, 29(19):2–1–2–4.
- Pickart, R. S. and Spall, M. A. (2007). Impact of Labrador Sea convection on the North Atlantic meridional overturning circulation. *Journal of Physical Oceanography*, 37(9):2207–2227.
- Pickart, R. S., Spall, M. A., Torres, D. J., Våge, K., Valdimarsson, H., Nobre, C., Moore, G. W. K., Jonsson, S., and Mastropole, D. (2017). The North Icelandic Jet and its relationship to the North Icelandic Irminger Current. *Journal of Marine Research*, 75(5):605–639.
- Qiu, B. and Huang, R. X. (1995). Ventilation of the North Atlantic and North Pacific: Subduction Versus Obduction. *Journal of Physical Oceanography*, 25(10):2374–2390.
- Rao, S. T. and Zurbenko, I. G. (1994). Detecting and tracking changes in ozone air quality. *Air & waste*, 44(9):1089–1092.

- Rattan, S., Myers, P. G., Tréguier, A.-M., Theetten, S., Biastoch, A., and Böning, C. (2010). Towards an understanding of Labrador Sea salinity drift in eddy-permitting simulations. *Ocean Modelling*, 35(1):77–88.
- Reynolds, O. (1895). IV. On the dynamical theory of incompressible viscous fluids and the determination of the criterion. *Philosophical Transactions of the Royal Society of London A: Mathematical, Physical and Engineering Sciences*, 186:123–164.
- Rhein, M. (1991). Ventilation rates of the Greenland and Norwegian Seas derived from distributions of the chlorofluoromethanes F11 and F12. *Deep Sea Research Part A. Oceanographic Research Papers*, 38(4):485 – 503.
- Rhein, M., Fischer, J., Smethie, W. M., Smythe-Wright, D., Weiss, R. F., Mertens, C., Min, D.-H., Fleischmann, U., and Putzka, A. (2002). Labrador Sea Water: Pathways, CFC Inventory, and Formation Rates. *Journal of Physical Oceanography*, 32(2):648–665.
- Rhein, M., Kieke, D., Hüttl-Kabus, S., Roessler, A., Mertens, C., Meissner, R., Klein, B., Böning, C. W., and Yashayaev, I. (2011). Deep water formation, the subpolar gyre, and the meridional overturning circulation in the subpolar north atlantic. *Deep Sea Research Part II: Topical Studies in Oceanography*, 58(17–18):1819–1832.
- Rhein, M., Kieke, D., and Steinfeldt, R. (2015). Advection of North Atlantic Deep Water from the Labrador Sea to the southern hemisphere. *Journal of Geophysical Research: Oceans*, 120(4):2471–2487.
- Rhein, M., Rintoul, S., Aoki, S., Campos, E., Chambers, D., Feely, R., Gulev, S., Johnson, G., Josey, S., Kostianoy, A., Mauritzen, C., Roemmich, D., Talley, L., and Wang, F. (2013). Observations: Ocean. In: *Climate Change 2013: The Physical Science Basis. Contribution of Working Group I to the Fifth Assessment Report of the Intergovernmental Panel on Climate Change* [Stocker, T.F., D. Qin, G.-K. Plattner, M. Tignor, S.K. Allen, J. Boschung, A. Nauels, Y. Xia, V. Bex and P.M. Midgley (eds.)].
- Rhines, P. B. and Häkkinen, S. (2003). Is the oceanic heat transport in the North Atlantic irrelevant to the climate in Europe. *ASOF Newsletter*, 2:13–17.

- Robert, A. J. (1966). The integration of a low order spectral form of the primitive meteorological equations. *Journal of the Meteorological Society of Japan. Ser. II*, 44(5):237–245.
- Roberts, J. L., Heil, P., Murray, R. J., Holloway, D. S., and Bindoff, N. L. (2006). Pole relocation for an orthogonal grid: An analytic method. *Ocean Modelling*, 12(1):16 – 31.
- Rudels, B., Korhonen, M., Schauer, U., Pisarev, S., Rabe, B., and Wisotzki, A. (2015). Circulation and transformation of Atlantic water in the Eurasian Basin and the contribution of the Fram Strait inflow branch to the Arctic Ocean heat budget. *Progress in Oceanography*, 132:128 – 152.
- Rykova, T., Straneo, F., and Bower, A. S. (2015). Seasonal and interannual variability of the West Greenland Current System in the Labrador Sea in 1993–2008. *Journal of Geophysical Research: Oceans*, 120(2):1318–1332.
- Sabine, C. L., Feely, R. A., Gruber, N., Key, R. M., Lee, K., Bullister, J. L., Wanninkhof, R., Wong, C., Wallace, D. W., Tilbrook, B., et al. (2004). The oceanic sink for anthropogenic CO₂. *science*, 305(5682):367–371.
- Schlosser, P., Bönisch, G., Rhein, M., and Bayer, R. (1991). Reduction of deepwater formation in the greenland sea during the 1980s: Evidence from tracer data. *Science*, 251(4997):1054–1056.
- Schulze, L. M., Pickart, R. S., and Moore, G. W. K. (2016). Atmospheric forcing during active convection in the Labrador Sea and its impact on mixed-layer depth. *Journal of Geophysical Research: Oceans*, 121(9):6978–6992.
- Seager, R., Battisti, D. S., Yin, J., Gordon, N., Naik, N., Clement, A. C., and Cane, M. A. (2002). Is the Gulf Stream responsible for Europe’s mild winters? *Quarterly Journal of the Royal Meteorological Society*, 128(586):2563–2586.
- Semtner, A. J. (1976). A model for the thermodynamic growth of sea ice in numerical investigations of climate. *Journal of Physical Oceanography*, 6(3):379–389.
- Send, U., Lankhorst, M., and Kanzow, T. (2011). Observation of decadal change in the Atlantic

- meridional overturning circulation using 10 years of continuous transport data. *Geophysical Research Letters*, 38(24).
- Smeed, D., McCarthy, G., Cunningham, S., Frajka-Williams, E., Rayner, D., Johns, W., Meinen, C., Baringer, M., Moat, B., Duchez, A., et al. (2014). Observed decline of the Atlantic meridional overturning circulation 2004–2012. *Ocean Science*, 10(1):29–38.
- Smeed, D. A., Josey, S. A., Beaulieu, C., Johns, W. E., Moat, B. I., Frajka-Williams, E., Rayner, D., Meinen, C. S., Baringer, M. O., Bryden, H. L., and McCarthy, G. D. (2018). The north atlantic ocean is in a state of reduced overturning. *Geophysical Research Letters*, 45(3):1527–1533.
- Smith, G. C., Roy, F., Mann, P., Dupont, F., Brasnett, B., Lemieux, J.-F., Laroche, S., and Bélair, S. (2014). A new atmospheric dataset for forcing ice–ocean models: Evaluation of reforecasts using the Canadian global deterministic prediction system. *Quarterly Journal of the Royal Meteorological Society*, 140(680):881–894.
- Somavilla, R., Schauer, U., and Budéus, G. (2013). Increasing amount of Arctic Ocean deep waters in the Greenland Sea. *Geophysical Research Letters*, 40(16):4361–4366.
- Spall, M. A., Pedlosky, J., and Cenedese, C. (2017). Circulation induced by isolated dense water formation over closed topographic contours. *Journal of Physical Oceanography*, 47(9):2251–2265.
- Speer, K. and Tziperman, E. (1992). Rates of water mass formation in the North Atlantic Ocean. *Journal of Physical Oceanography*, 22(1):93–104.
- Srokosz, M., Baringer, M., Bryden, H., Cunningham, S., Delworth, T., Lozier, S., Marotzke, J., and Sutton, R. (2012). Past, present, and future changes in the Atlantic meridional overturning circulation. *Bulletin of the American Meteorological Society*, 93(11):1663–1676.
- Steinfeldt, R., Rhein, M., Bullister, J. L., and Tanhua, T. (2009). Inventory changes in anthropogenic carbon from 1997–2003 in the Atlantic Ocean between 20 S and 65 N. *Global Biogeochemical Cycles*, 23(3).

- Stendardo, I. and Gruber, N. (2012). Oxygen trends over five decades in the North Atlantic. *Journal of Geophysical Research: Oceans*, 117(C11).
- Stouffer, R. J., Yin, J., Gregory, J. M., Dixon, K. W., Spelman, M. J., Hurlin, W., Weaver, A. J., Eby, M., Flato, G. M., Hasumi, H., Hu, A., Jungclaus, J. H., Kamenkovich, I. V., Levermann, A., Montoya, M., Murakami, S., Nawrath, S., Oka, A., Peltier, W. R., Robitaille, D. Y., Sokolov, A., Vettoretti, G., and Weber, S. L. (2006). Investigating the causes of the response of the thermohaline circulation to past and future climate changes. *Journal of Climate*, 19(8):1365–1387.
- Stramma, L., Kieke, D., Rhein, M., Schott, F., Yashayaev, I., and Koltermann, K. P. (2004). Deep water changes at the western boundary of the subpolar North Atlantic during 1996 to 2001. *Deep Sea Research Part I: Oceanographic Research Papers*, 51(8):1033–1056.
- Straneo, F. (2006). Heat and freshwater transport through the central Labrador Sea*. *Journal of Physical Oceanography*, 36(4):606–628.
- Swingedouw, D., Braconnot, P., Delecluse, P., Guilyardi, E., and Marti, O. (2007). The impact of global freshwater forcing on the thermohaline circulation: adjustment of North Atlantic convection sites in a CGCM. *Climate Dynamics*, 28(2-3):291–305.
- Takahashi, T., Sutherland, S. C., Sweeney, C., Poisson, A., Metzl, N., Tilbrook, B., Bates, N., Wanninkhof, R., Feely, R. A., Sabine, C., et al. (2002). Global sea–air CO₂ flux based on climatological surface ocean pCO₂, and seasonal biological and temperature effects. *Deep Sea Research Part II: Topical Studies in Oceanography*, 49(9):1601–1622.
- The Lab Sea Group (1998). The Labrador Sea Deep Convection Experiment. *Bulletin of the American Meteorological Society*, 79(10):2033–2058.
- Trenberth, K. E., Dai, A., Rasmussen, R. M., and Parsons, D. B. (2003). The changing character of precipitation. *Bulletin of the American Meteorological Society*, 84(9):1205–1218.
- Trossman, D. S., Thompson, L. A., Kelly, K. A., and Kwon, Y.-O. (2009). Estimates of North Atlantic Ventilation and Mode Water Formation for Winters 2002–06. *Journal of Physical Oceanography*, 39(10):2600–2617.

- van Angelen, J. H., M. Lenaerts, J. T., van den Broeke, M. R., Fettweis, X., and van Meijgaard, E. (2013). Rapid loss of firn pore space accelerates 21st century Greenland mass loss. *Geophysical Research Letters*, 40(10):2109–2113.
- van den Broeke, M., Bamber, J., Ettema, J., Rignot, E., Schrama, E., van de Berg, W. J., van Meijgaard, E., Velicogna, I., and Wouters, B. (2009). Partitioning recent Greenland mass loss. *science*, 326(5955):984–986.
- Velicogna, I., Sutterley, T. C., and van den Broeke, M. R. (2014). Regional acceleration in ice mass loss from Greenland and Antarctica using GRACE time-variable gravity data. *Geophysical Research Letters*, 41(22):8130–8137.
- Våge, K., Moore, G., Jónsson, S., and Valdimarsson, H. (2015). Water mass transformation in the Iceland Sea. *Deep Sea Research Part I: Oceanographic Research Papers*, 101:98 – 109.
- Våge, K., Papritz, L., Håvik, L., Spall, M. A., and Moore, G. W. K. (2018). Ocean convection linked to the recent ice edge retreat along east greenland. *Nature Communications*, 9.
- Våge, K., Pickart, R. S., Spall, M. A., Moore, G., Valdimarsson, H., Torres, D. J., Erofeeva, S. Y., and Nilsen, J. E. Ø. (2013). Revised circulation scheme north of the Denmark Strait. *Deep Sea Research Part I: Oceanographic Research Papers*, 79:20 – 39.
- Våge, K., Pickart, R. S., Spall, M. A., Valdimarsson, H., Jonsson, S., Torres, D. J., Østerhus, S., and Eldevik, T. (2011). Significant role of the North Icelandic Jet in the formation of Denmark Strait overflow water. *Nature Geoscience*, 4:723 – 727.
- Våge, K., Pickart, R. S., Thierry, V., Reverdin, G., Lee, C. M., Petrie, B., Agnew, T. A., Wong, A., and Ribergaard, M. H. (2008a). Surprising return of deep convection to the subpolar north atlantic ocean in winter 2007-2008. *Nature Geoscience*, 2:67–72.
- Våge, K., Pickart, R. S., Thierry, V., Reverdin, G., Lee, C. M., Petrie, B., Agnew, T. A., Wong, A., and Ribergaard, M. H. (2008b). Surprising return of deep convection to the subpolar north atlantic ocean in winter 2007-2008. *Nature Geoscience*, 2:67–72.
- Wang, G., Wang, D., Trenberth, K. E., Erfanian, A., Yu, M., Bosilovich, M. G., and Parr,

- D. T. (2017). The peak structure and future changes of the relationships between extreme precipitation and temperature. *Nature Clim. Change*, 7:268–274.
- Weijer, W., Maltrud, M. E., Hecht, M. W., Dijkstra, H. A., and Kliphuis, M. A. (2012). Response of the Atlantic Ocean circulation to Greenland Ice Sheet melting in a strongly-eddy ocean model. *Geophysical Research Letters*, 39(9). L09606.
- Wentz, F. J., Ricciardulli, L., Hilburn, K., and Mears, C. (2007). How much more rain will global warming bring? *Science*, 317(5835):233–235.
- Yang, J. and Pratt, L. J. (2013). On the Effective Capacity of the Dense-Water Reservoir for the Nordic Seas Overflow: Some Effects of Topography and Wind Stress. *Journal of Physical Oceanography*, 43(2):418–431.
- Yang, Q., Timothy, H. D., Paul, G. M., Bonin, J., Chambers, D., van den M., R. B., Mads, H. R., and Mortensen, J. (2016). Recent increases in Arctic freshwater flux affects Labrador Sea convection and Atlantic overturning circulation. *Nature Communications*, 7.
- Yashayaev, I. (2007). Hydrographic changes in the Labrador Sea, 1960–2005. *Progress in Oceanography*, 73(3):242–276.
- Yashayaev, I., Bersch, M., van Aken, H., and Clarke, A. (2004). A new study of the production, spreading and fate of the Labrador Sea Water in the subpolar North Atlantic. *ASOF Newsletter*, (2):20–23.
- Yashayaev, I., Bersch, M., and van Aken, H. M. (2007). Spreading of the Labrador Sea Water to the Irminger and Iceland basins. *Geophysical Research Letters*, 34(10).
- Yashayaev, I. and Clarke, A. (2006). Recent warming of the Labrador Sea. *AZMP Bulletin PMZA*, 5:12–20.
- Yashayaev, I. and Dickson, B. (2008). *Transformation and Fate of Overflows in the Northern North Atlantic*. Springer.
- Yashayaev, I., Holliday, N. P., Bersch, M., and Aken, H. M. (2008). *The History of the Labrador Sea Water: Production, Spreading, Transformation and Loss*. Springer.

- Yashayaev, I. and Loder, J. W. (2009). Enhanced production of Labrador Sea water in 2008. *Geophysical Research Letters*, 36(1).
- Yashayaev, I. and Loder, J. W. (2016). Recurrent replenishment of labrador sea water and associated decadal-scale variability. *Journal of Geophysical Research: Oceans*, 121(11):8095–8114.
- Yashayaev, I. and Loder, J. W. (2017). Further intensification of deep convection in the labrador sea in 2016. *Geophysical Research Letters*, 44(3):1429–1438. 2016GL071668.
- Yashayaev, I. and Seidov, D. (2015). The role of the Atlantic Water in multidecadal ocean variability in the Nordic and Barents Seas. *Progress in Oceanography*, 132:68–127.
- Zahn, M. and von Storch, H. (2010a). Decreased frequency of North Atlantic polar lows associated with future climate warming. *Nature*, 467(7313):309–312.
- Zahn, M. and von Storch, H. (2010b). Decreased frequency of North Atlantic polar lows associated with future climate warming. *Nature*, 467(7313):309–312.
- Zurbenko, I., Porter, P., Gui, R., Rao, S., Ku, J., and Eskridge, R. (1996). Detecting discontinuities in time series of upper-air data: development and demonstration of an adaptive filter technique. *Journal of climate*, 9(12):3548–3560.

Appendix A

Trajectories of all the particles
entering and leaving the Nordic Seas
through Denmark Strait for different
releases.

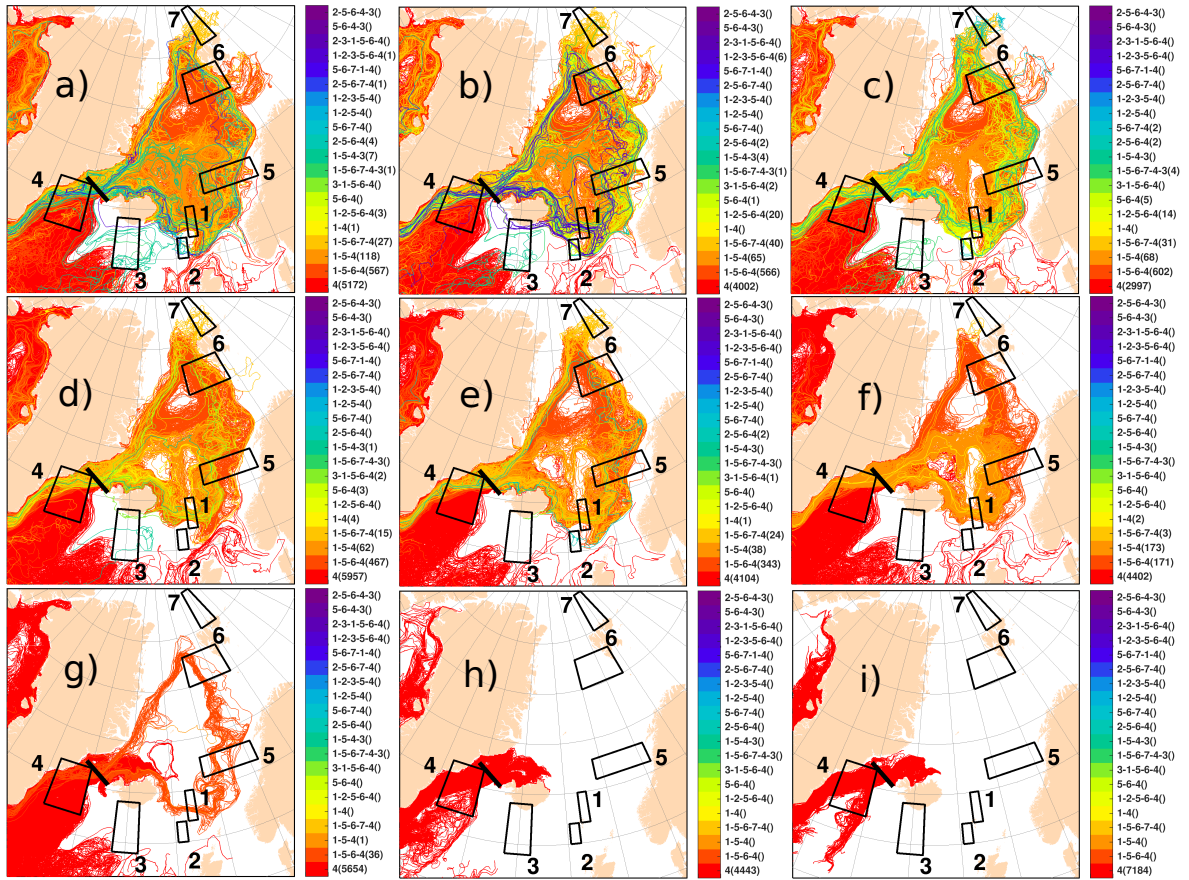


Figure A.1: Trajectories of all the particles entering and leaving the Nordic Seas through Denmark Strait. The figure illustrates those floats released at the Denmark Strait each January from 2005 to 2014. Trajectory integration times are: (a) January 1st, 2006 to December 31st, 2014, (b) January 1st, 2007 to December 31st, 2014, (c) January 1st, 2008 to December 31st, 2014, (d) January 1st, 2009 to December 31st, 2014, (e) January 1st, 2010 to December 31st, 2014, (f) January 1st, 2011 to December 31st, 2014, (g) January 1st, 2012 to December 31st, 2014, (h) January 1st, 2013 to December 31st, 2014 and (i) January 1st, 2014 to December 31st, 2014.

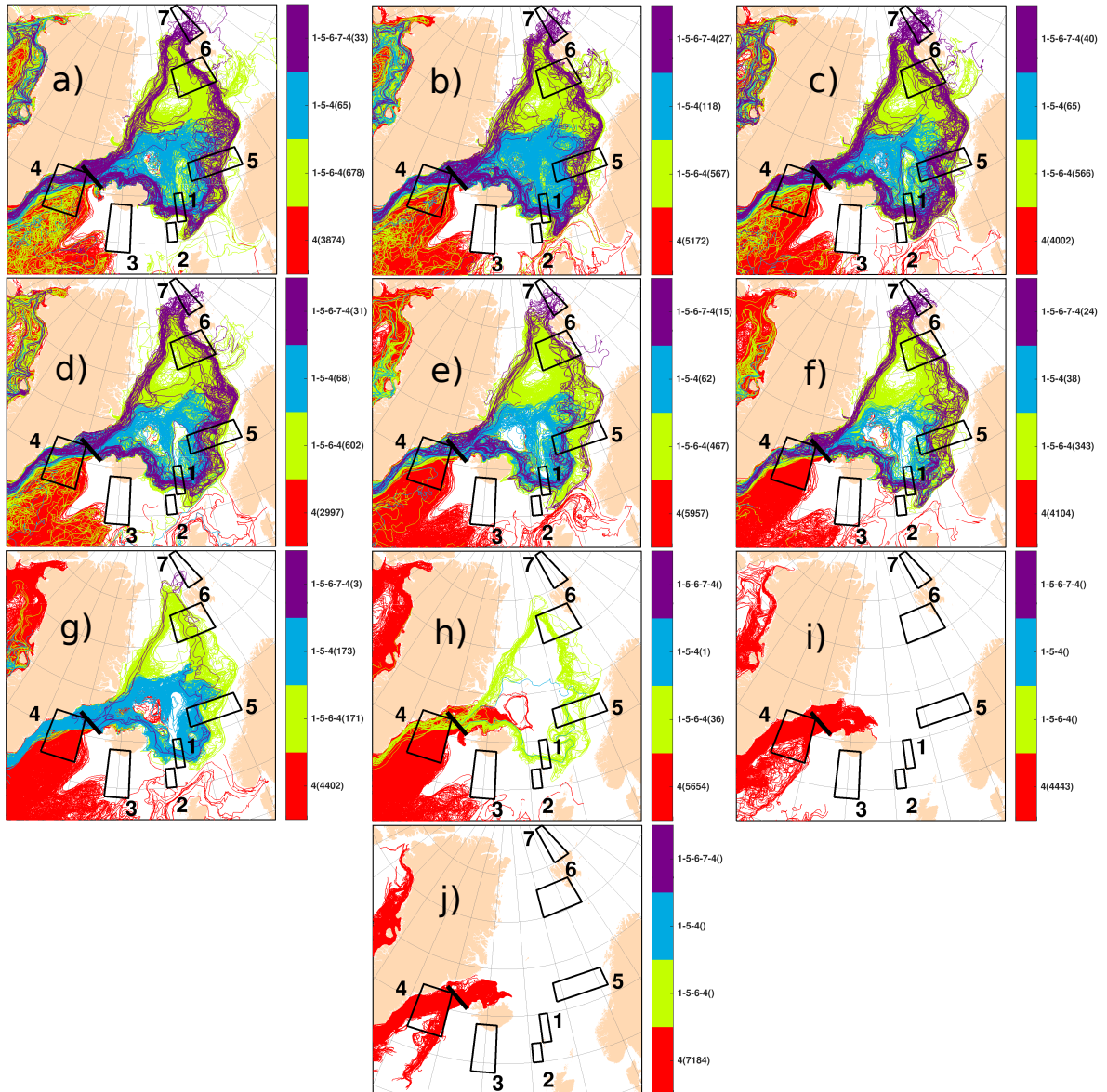


Figure A.2: Four main pathways follow by the particles entering and leaving the Nordic Seas through Denmark Strait. The figure illustrates those floats released at the Denmark Strait each January from 2005 to 2014. Trajectory integration times are: (a) January 1st, 2005 to December 31st, 2014, (b) January 1st, 2006 to December 31st, 2014, (c) January 1st, 2007 to December 31st, 2014, (d) January 1st, 2008 to December 31st, 2014, (e) January 1st, 2009 to December 31st, 2014, (f) January 1st, 2010 to December 31st, 2014, (g) January 1st, 2011 to December 31st, 2014, (h) January 1st, 2012 to December 31st, 2014, (i) January 1st, 2013 to December 31st, 2014 and (j) January 1st, 2014 to December 31st, 2014

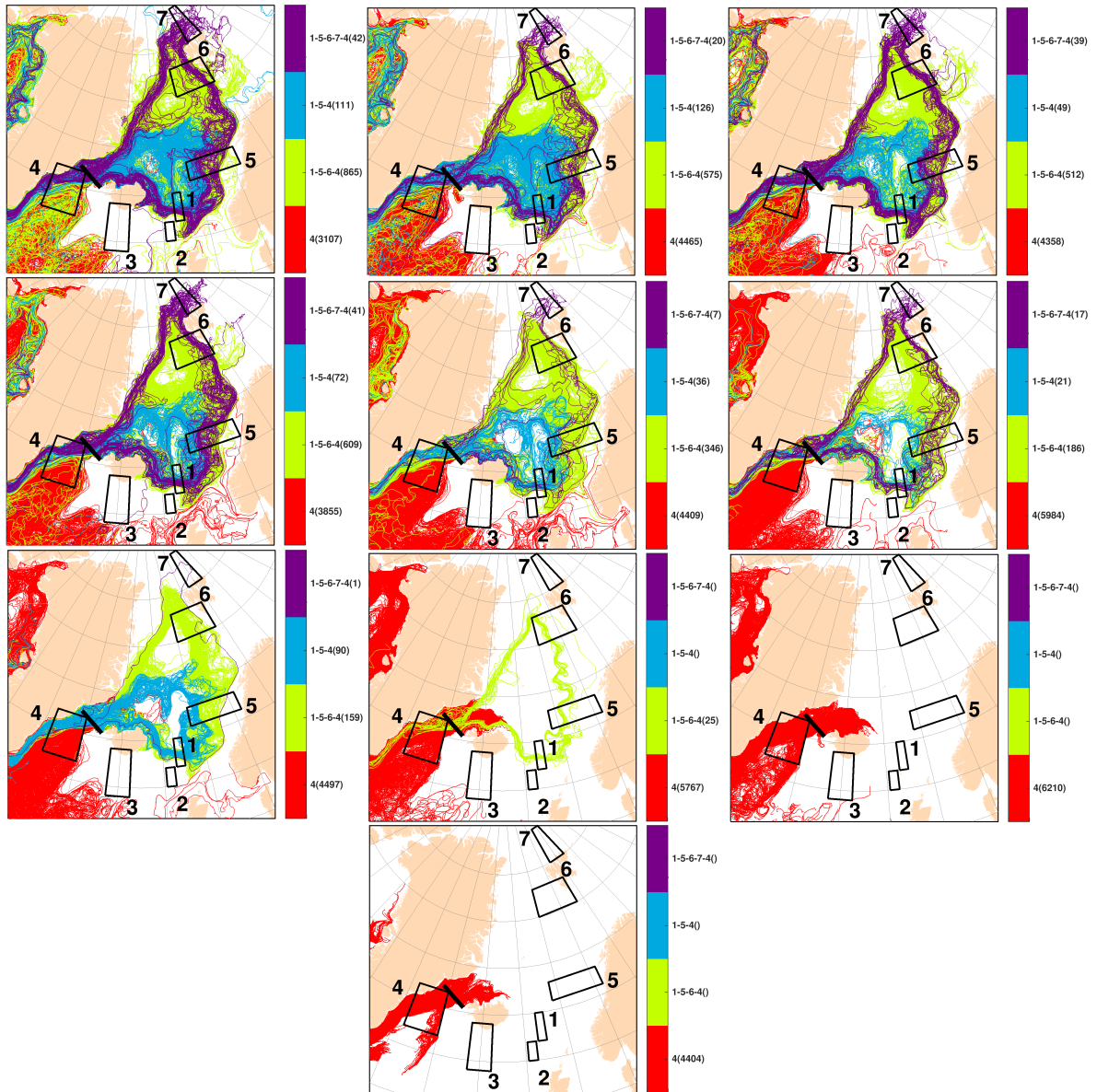


Figure A.3: Four main pathways follow by the particles entering and leaving the Nordic Seas through Denmark Strait. The figure illustrates those floats released at the Denmark Strait each April from 2005 to 2014. Trajectories integration times are: (a) April 1st, 2005 to December 31st, 2014, (b) April 1st, 2006 to December 31st, 2014, (c) April 1st, 2007 to December 31st, 2014, (d) April 1st, 2008 to December 31st, 2014, (e) April 1st, 2009 to December 31st, 2014, (f) April 1st, 2010 to December 31st, 2014, (g) April 1st, 2011 to December 31st, 2014, (h) April 1st, 2012 to December 31st, 2014, (i) April 1st, 2013 to December 31st, 2014 and (j) April 1st, 2014 to December 31st, 2014

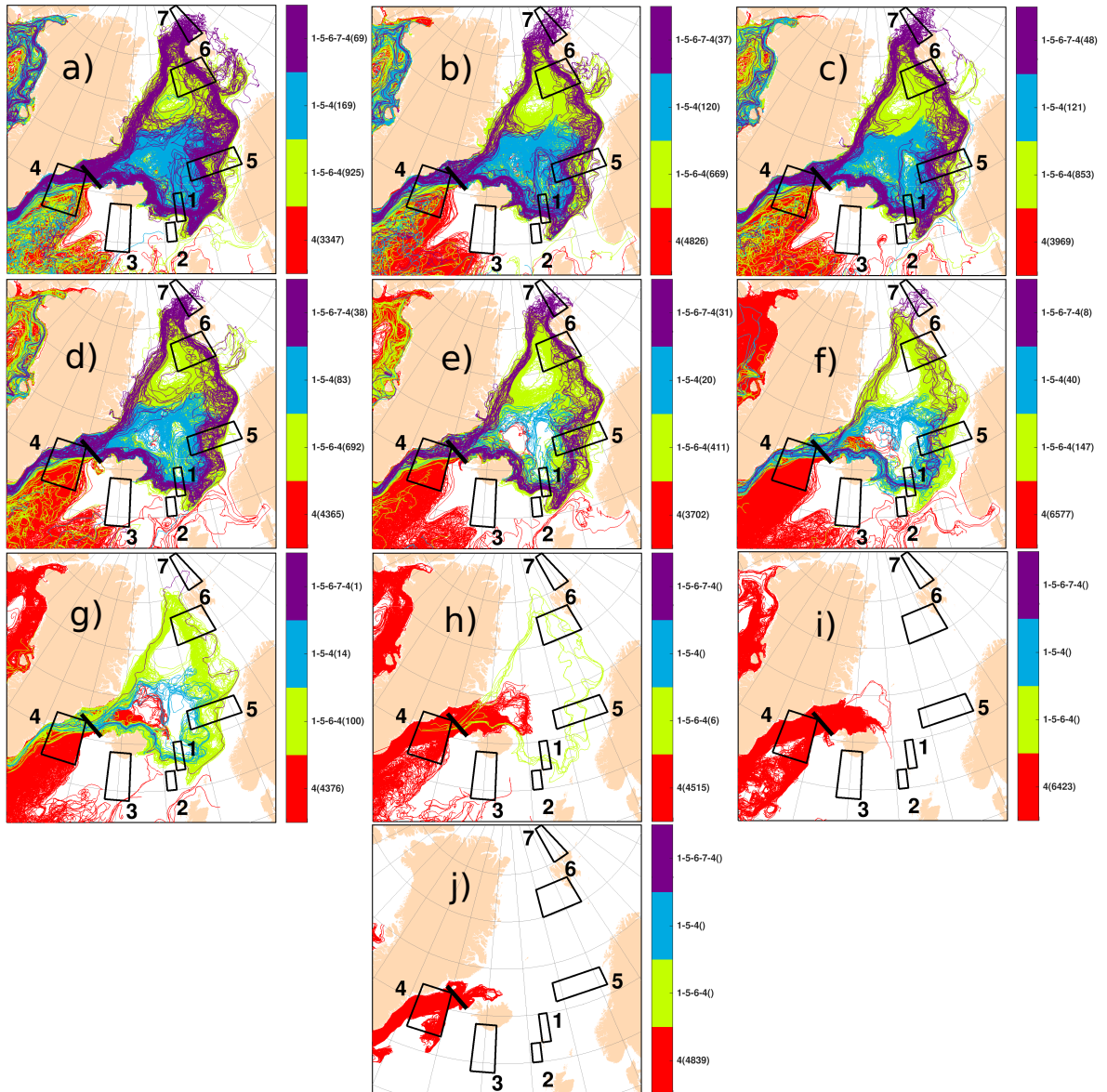


Figure A.4: Four main pathways follow by the particles entering and leaving the Nordic Seas through Denmark Strait. The figure illustrates those floats released at the Denmark Strait each July from 2005 to 2014. Trajectories integration times are: (a) July 1st, 2005 to December 31st, 2014, (b) July 1st, 2006 to December 31st, 2014, (c) July 1st, 2007 to December 31st, 2014, (d) July 1st, 2008 to December 31st, 2014, (e) July 1st, 2009 to December 31st, 2014, (f) July 1st, 2010 to December 31st, 2014, (g) July 1st, 2011 to December 31st, 2014, (h) July 1st, 2012 to December 31st, 2014, (i) July 1st, 2013 to December 31st, 2014 and (j) July 1st, 2014 to December 31st, 2014

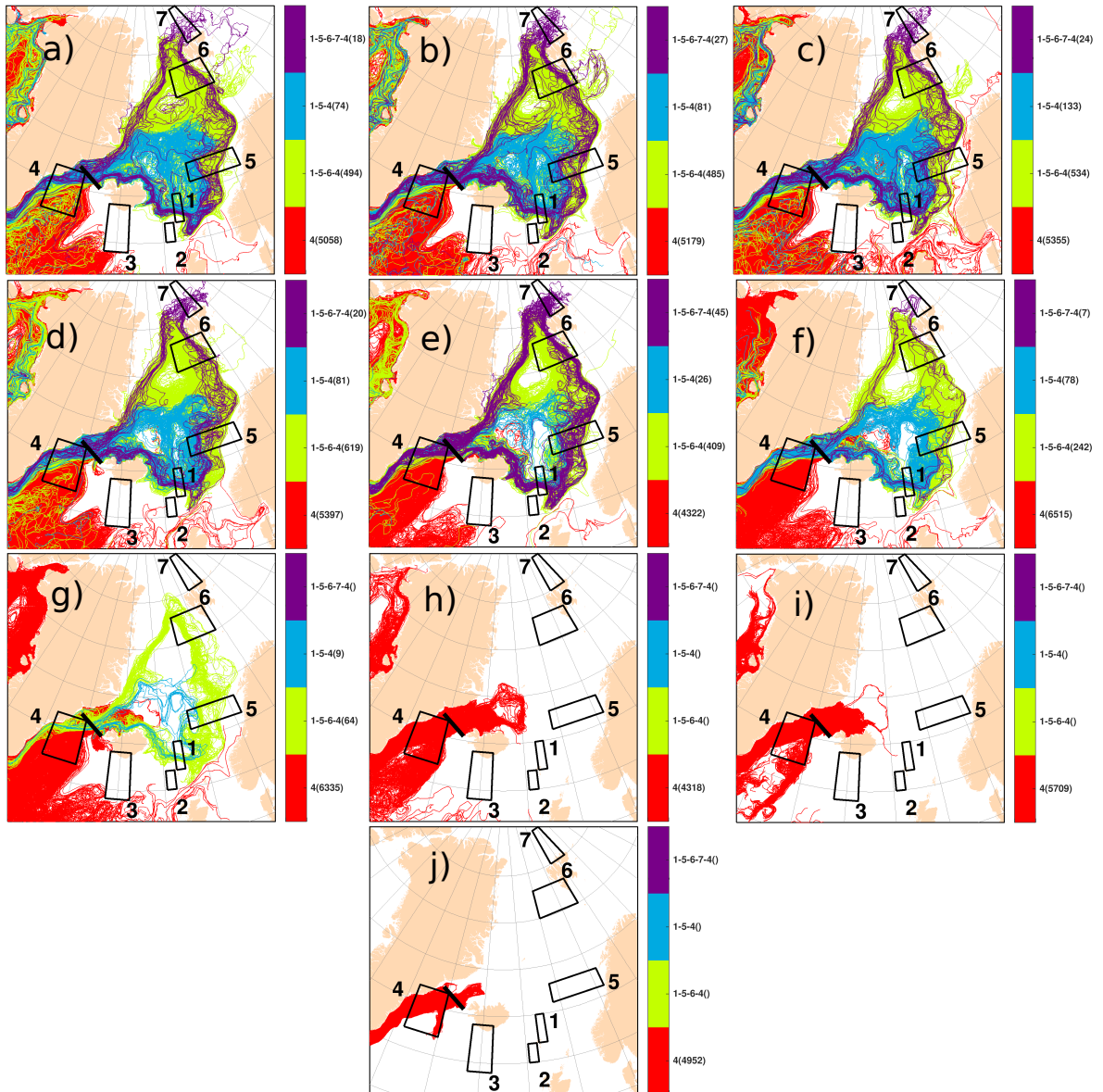


Figure A.5: Four main pathways follow by the particles entering and leaving the Nordic Seas through Denmark Strait. The figure illustrates those floats released at the Denmark Strait each October from 2005 to 2014. Trajectories integration times are: (a) October 1st, 2005 to December 31st, 2014, (b) October 1st, 2006 to December 31st, 2014, (c) October 1st, 2007 to December 31st, 2014, (d) October 1st, 2008 to December 31st, 2014, (e) October 1st, 2009 to December 31st, 2014, (f) October 1st, 2010 to December 31st, 2014, (g) October 1st, 2011 to December 31st, 2014, (h) October 1st, 2012 to December 31st, 2014, (i) October 1st, 2013 to December 31st, 2014 and (j) October 1st, 2014 to December 31st, 2014

Appendix B

Model temperature and salinity
diagram in Denmark Strait.

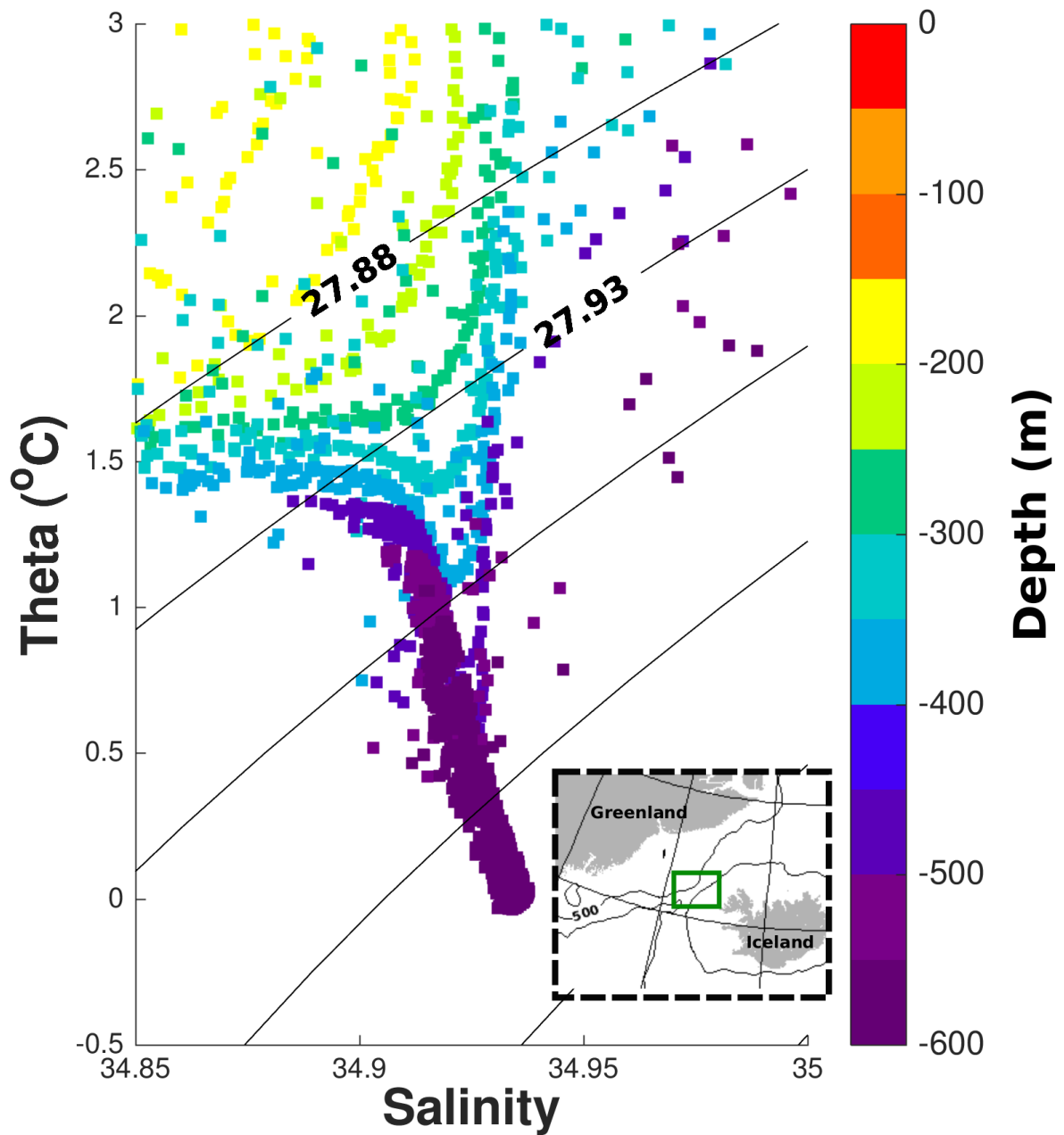


Figure B.1: TS diagram of the water masses in Denmark Strait, particularly in the region within the green box showed in the lower-right-corner map, for the simulation ANHA4. Black contour lines in the TS diagram show the density anomaly expressed in kg/m^3 .

II Weak ocean stratification beneath the surface (Figure 1.2.c). This can be induced for example due to convection in the previous year .

III Weakly stratified underlying waters must be brought up so they can be exposed to the strong surface atmosphere forcing. The presence of a cyclonic boundary currents in the Labrador Sea enables a doming of the isopycnals up to the surface (Figure 1.2.b).

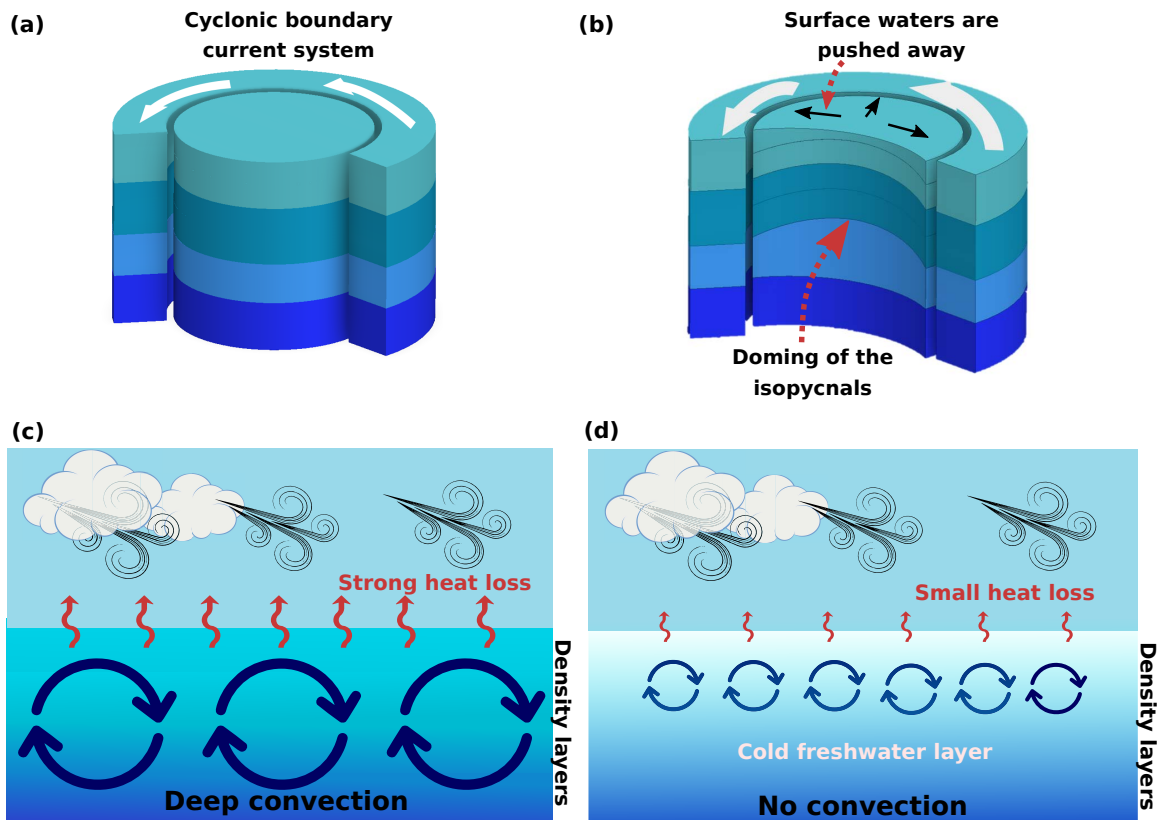


Figure 1.2: Schematic showing the different stages of convection in the Labrador Sea: pre-conditioning (a and b) and convection (c) or its absence (d) given the existence of a cold and fresh layer of water at the surface of the ocean. Cyclonic boundary circulation in the Labrador Seas is indicated with white arrows (a and b), while the black arrows in (b) indicate the surface waters being pushed away due to the cyclonic circulation. The strength of the convection is represented by circular dark blue arrows while the magnitude of the ocean heat loss is represented by the wavy red arrows (c and d).

The last two conditions (II and III) are satisfied in the Labrador Sea and they are commonly referred to as "preconditioning" (The Lab Sea Group, 1998). Figure 1.2 illustrates these different processes leading to deep convection. There are, however, processes that could potentially affect the depth of the convection in the Labrador Sea. Some of them are, for example, a

of where and how the DSOW is formed, is still missing.

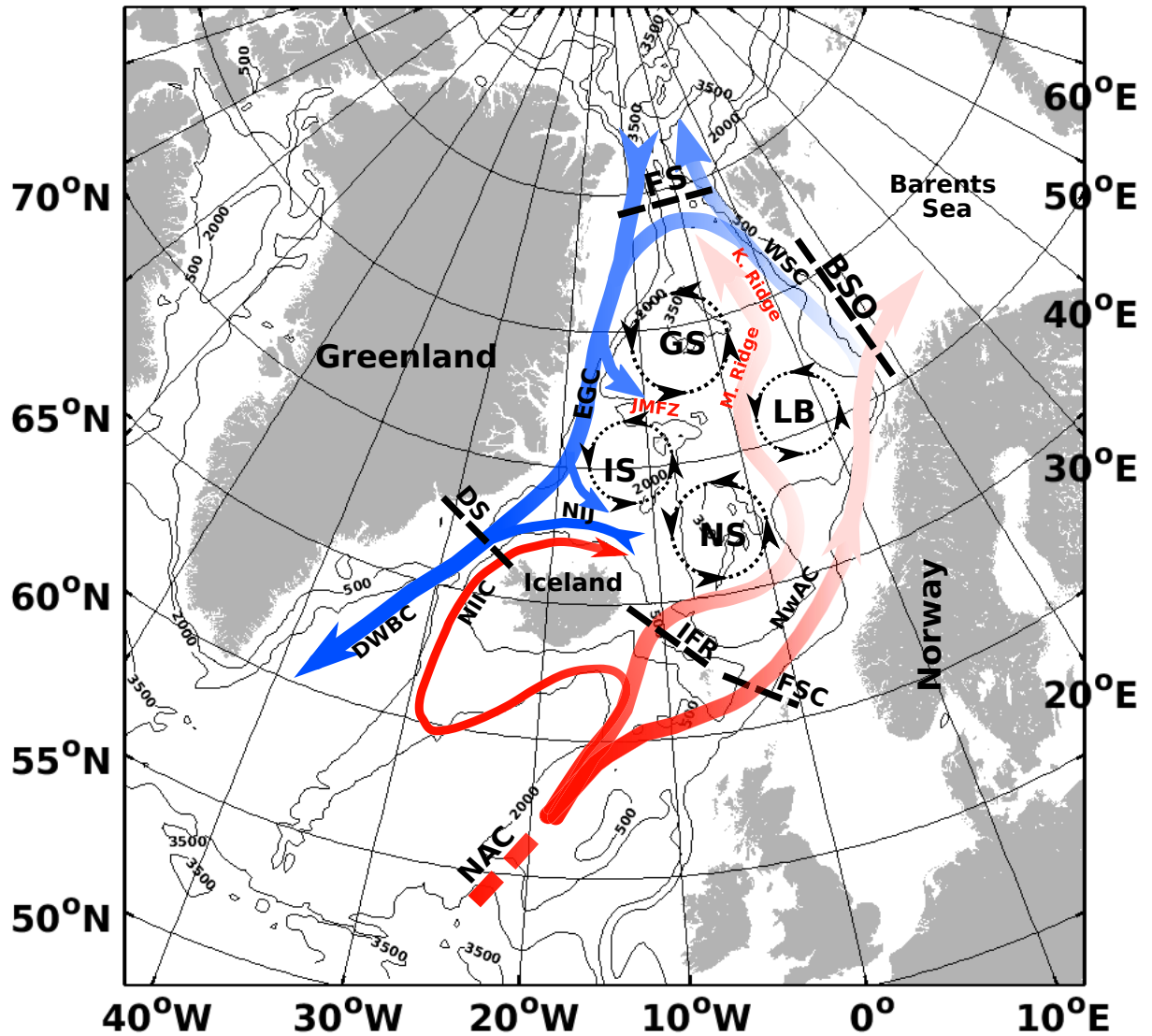


Figure 4.1: Schematic of the Nordic Seas, showing the main basins, inflows, outflows and geographical features, following Orvik and Niiler (2002) and Våge et al. (2013). For the currents, red colors represent light surface waters which are transformed into cold, dense overflow waters represented in blue colors. Main current acronyms: NAC - North Atlantic Current; NIIC - North Icelandic Irminger Current; NwAC - Norwegian Atlantic Current; WSC - West Spitsbergen Current; EGC - East Greenland Current; DWBC - Deep Western Boundary Current; NIJ - North Icelandic Jet. Black dashed lines represent the main straits that separate the Nordic Seas from the Atlantic and Arctic Oceans: Denmark Strait (DS), Iceland Faroe Ridge (IFR), Faroe Shetland Channel (FSC), Barents Sea Opening (BSO) and Fram Strait (FS). Main basins: Norwegian Sea (NS), Iceland Sea (IS), Lofoten Basin (LB) and the Greenland Sea (GS). For each of the basins its circulation is illustrated by black dashed circles with the arrow heads pointing the direction of the circulation. In red appear the Knipovich Ridge (K. Ridge), Mohn Ridge and the Jan Mayen Fracture Zone (JMFZ). Black contour lines represent the isobaths, spaced every 1500 m.

secondly to keep a time continuity.

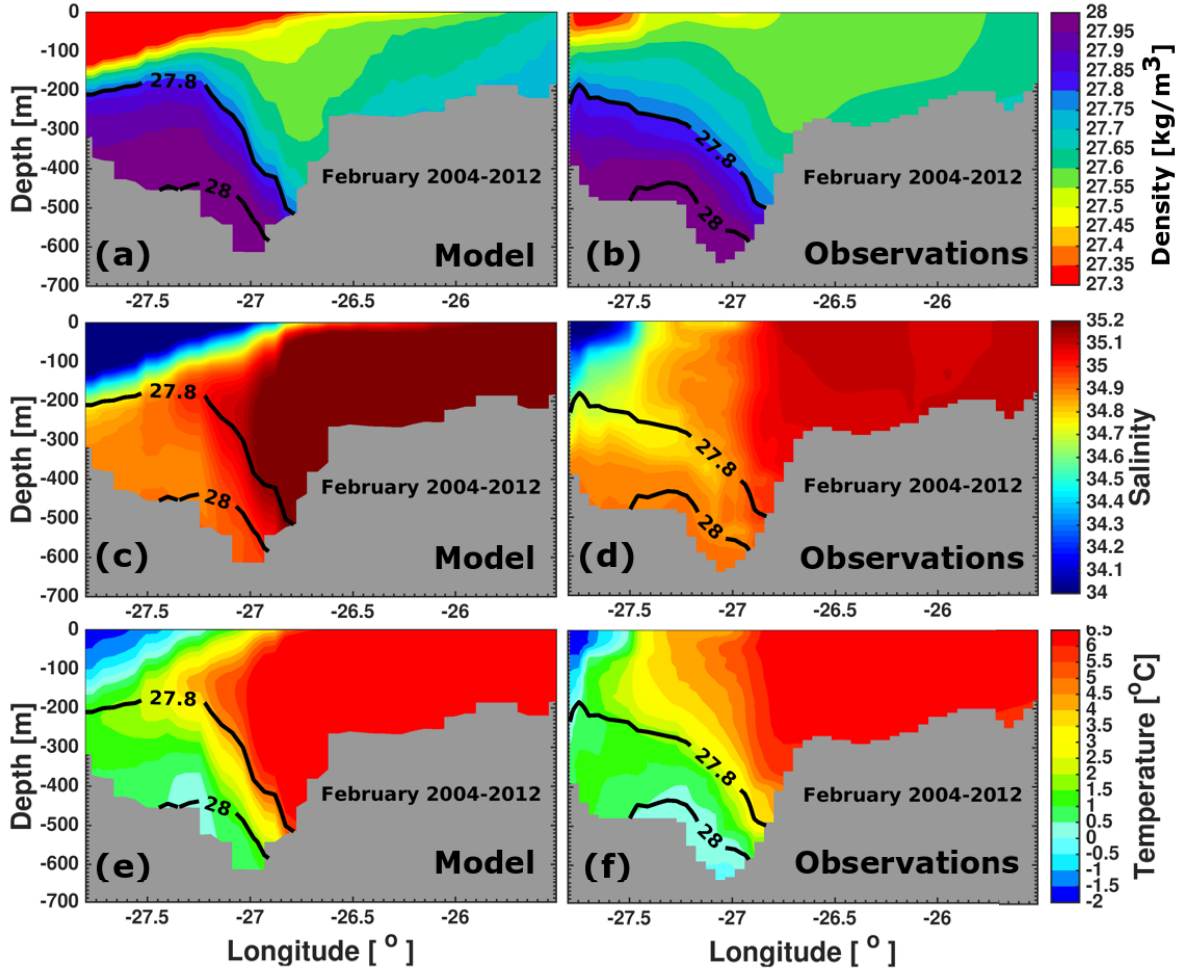


Figure 5.3: Mean February density (a,b), salinity (c,d) and temperature (e,f), averaged over the period 2004 to 2012 along the Latrabjarg section (shown in Figure 5.1). Panels on the left show model data while those on the right represent data from observations.

Mean density, salinity and temperature fields along the Kogur section (shown in Figure 5.1), for model and observations are represented in Figure 5.5. The data used correspond to a continuous occupation of the Kogur section from September 2011 to July 2012. Here we show the monthly means for December 2011 and January and February 2012. This specific period was selected as our focus is on the winter months (same criteria was applied to the Latrabjarg section). In the case of the density field, all three months show a similar behaviour (Figures 5.5.a-c). We can see the larger difference between the model and the observations from the surface to 300 m depth, where the model appears to be less dense than the observations by around 0.1 kg/m^3 . From 300 m depth to the bottom both model and observations show an

almost identical pattern.

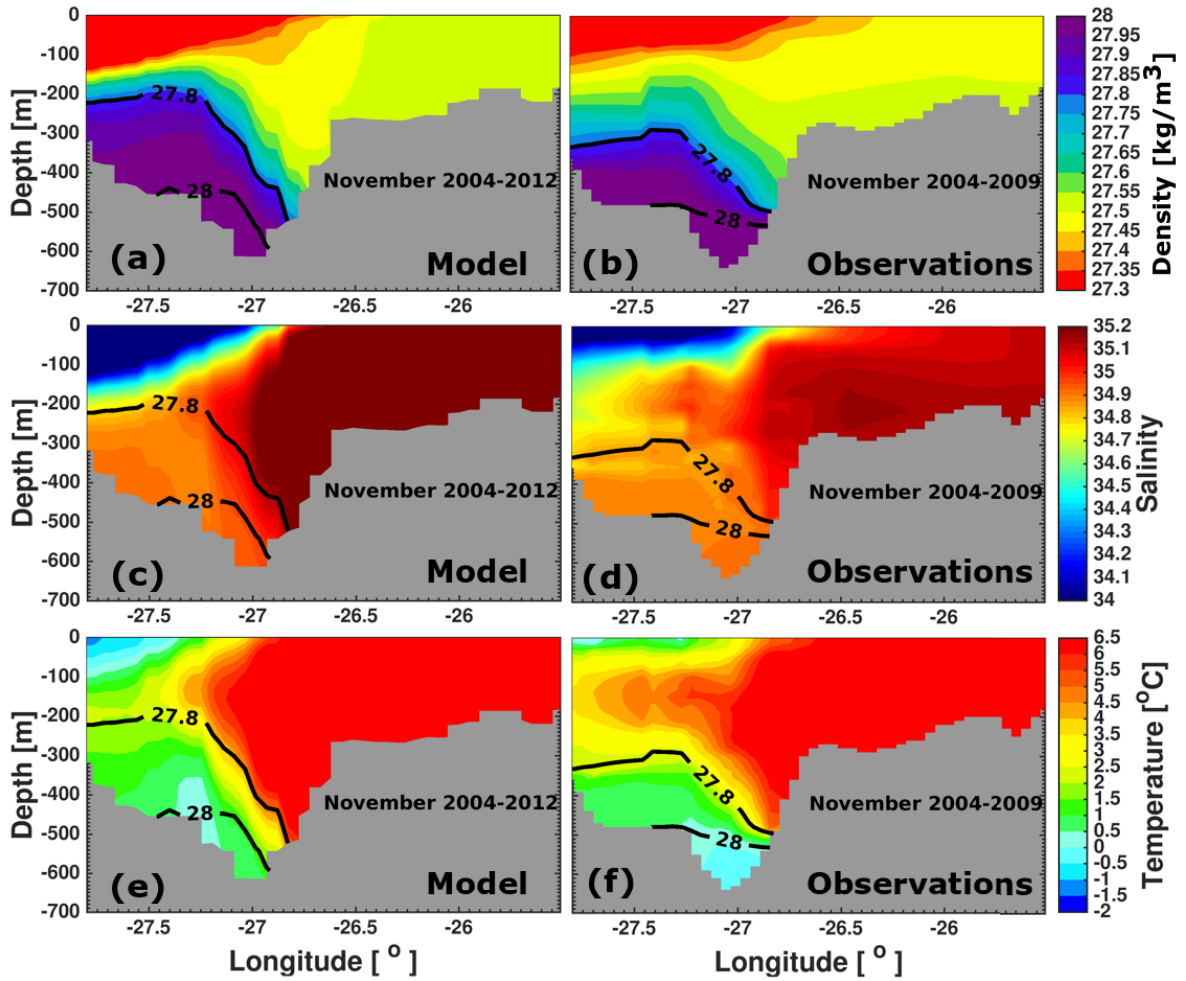


Figure 5.4: Mean November density (a,b), salinity (c,d) and temperature (e,f), averaged over the period 2004 to 2012 along the Latrabjarg section (shown in Figure 5.1). Panels on the left show model data while those on the right represent data from observations.

Similar to the density field, for the salinity field the largest difference between the model and the observations is found in the layer between the surface to 300 m depth (Figures 5.5.d-f), with the observations being saltier (by around 1.6) than the model. Below 300 m they both are similar. In the case of the temperature field (Figures 5.5.g-i), the observations appear to be warmer from the surface to 200 m by around 0.8° C (in December) to 1.5° C (in January, and by 1.1° C in February). Below 200 m depth the model stays warmer (by 0.8°) in all three months. In spite of these differences the model does a nice job in representing all the three fields through the water column.

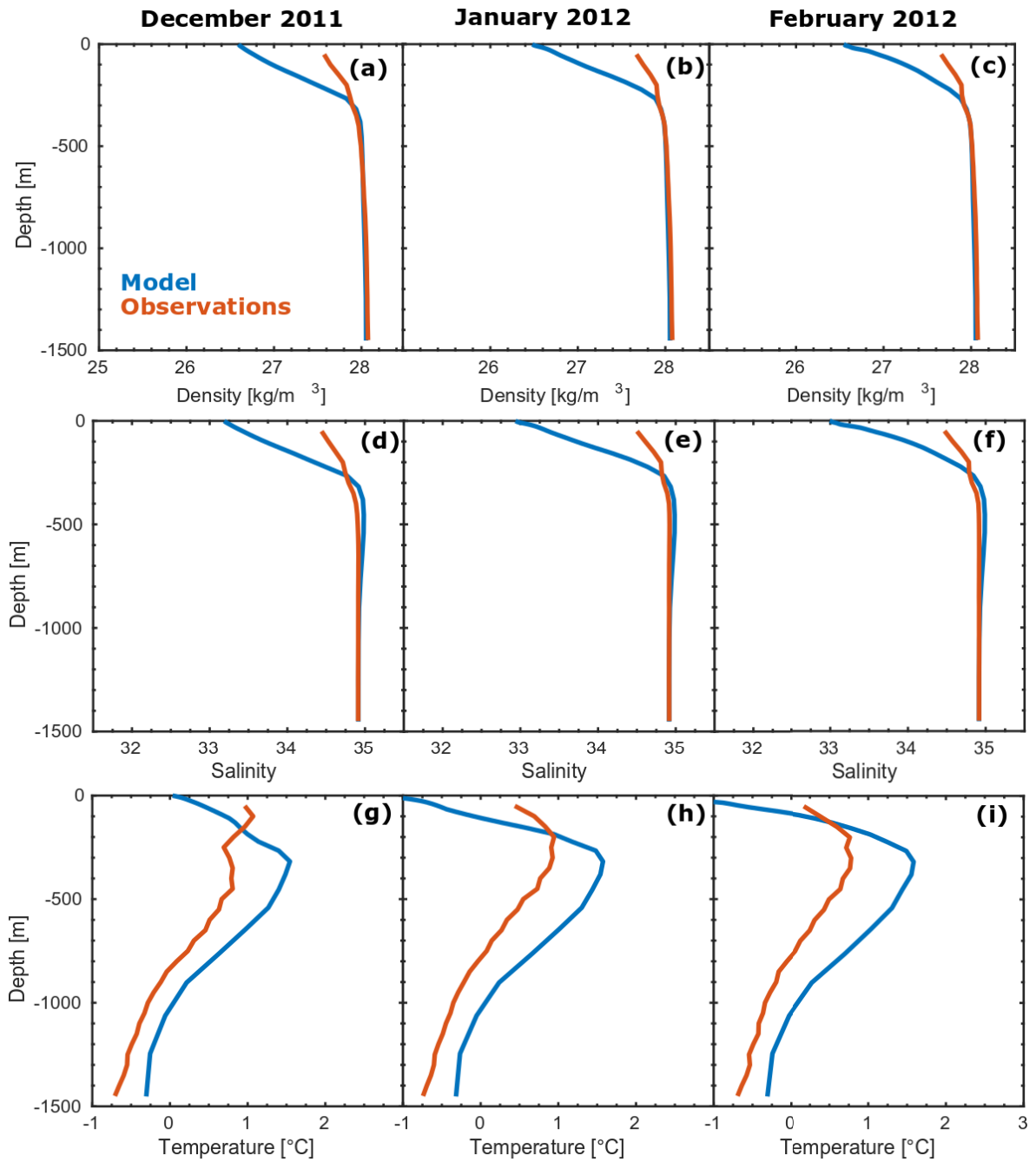


Figure 5.5: Mean vertical profiles (model and observations) of density (a-b), salinity (d-f) and temperature (g-i) along the Kogur section (shown in Figure 5.1, for the month of December 2011 (left panels), January 2012 (center panels) and February 2012 (right panels)). The model data is shown in blue while observation data is represented in orange. In the case of the observations, the measurements of the different variables start at 50 m depth.

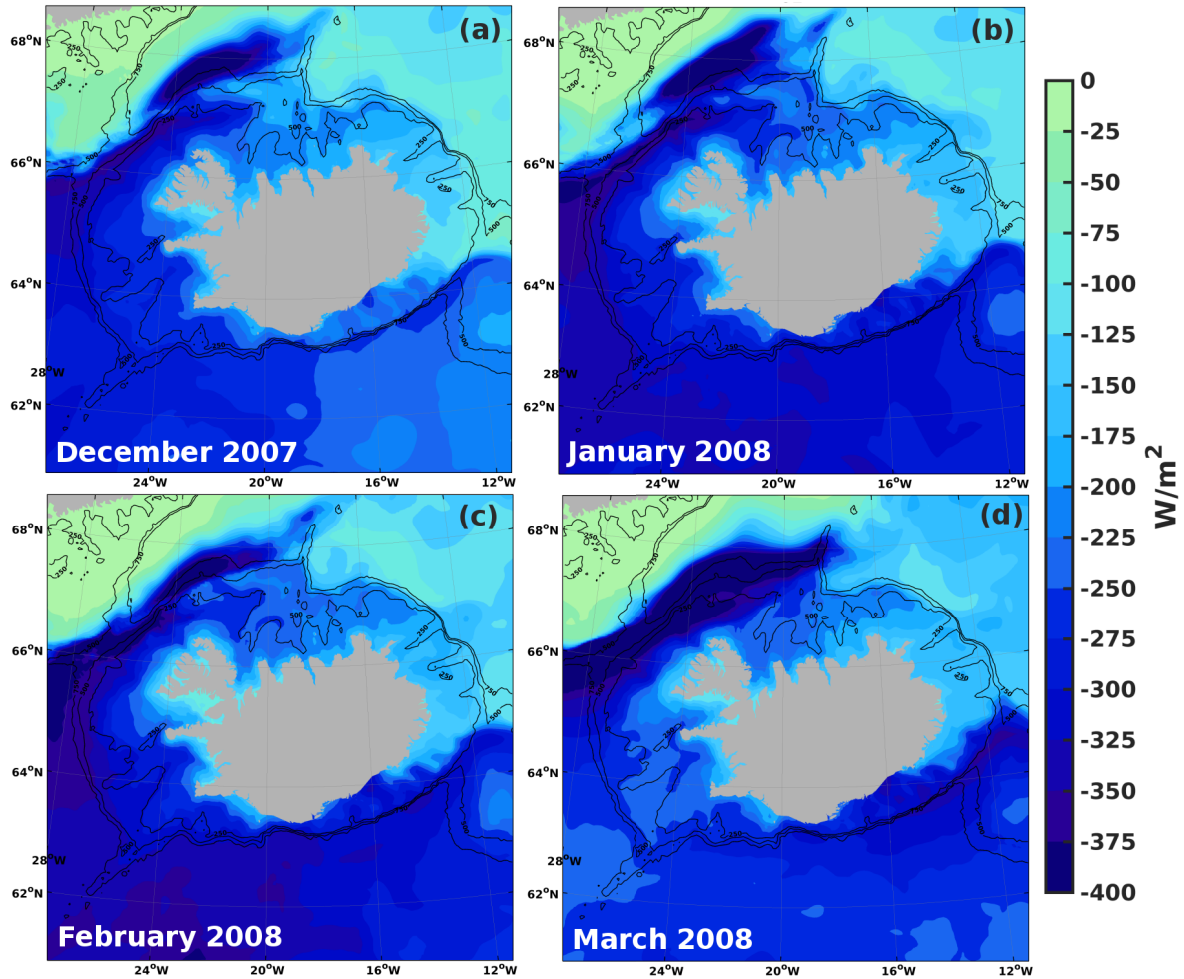


Figure 5.6: Model monthly heat loss around Iceland for the months of December 2007 (a) and from January to March of 2008 (b to d).

It can be noticed that through the month surface waters are transformed to greater densities. In fact, the density can get as high as $28.1 \text{ kg}/\text{m}^3$ (Figure 5.7.a-b). This transformation, however, does not occur only during the month of March, 2008. TS diagrams from previous months (not shown) indicate that this transformation starts as soon as December of the previous year for almost every year in the simulation.

Is the winter heat loss over the study region strong enough to cause the waters within the inflowing NIIC to transform to such high densities? Figure 5.8 shows a comparison between the maximum density, the heat loss and the resistance energy over the study region.

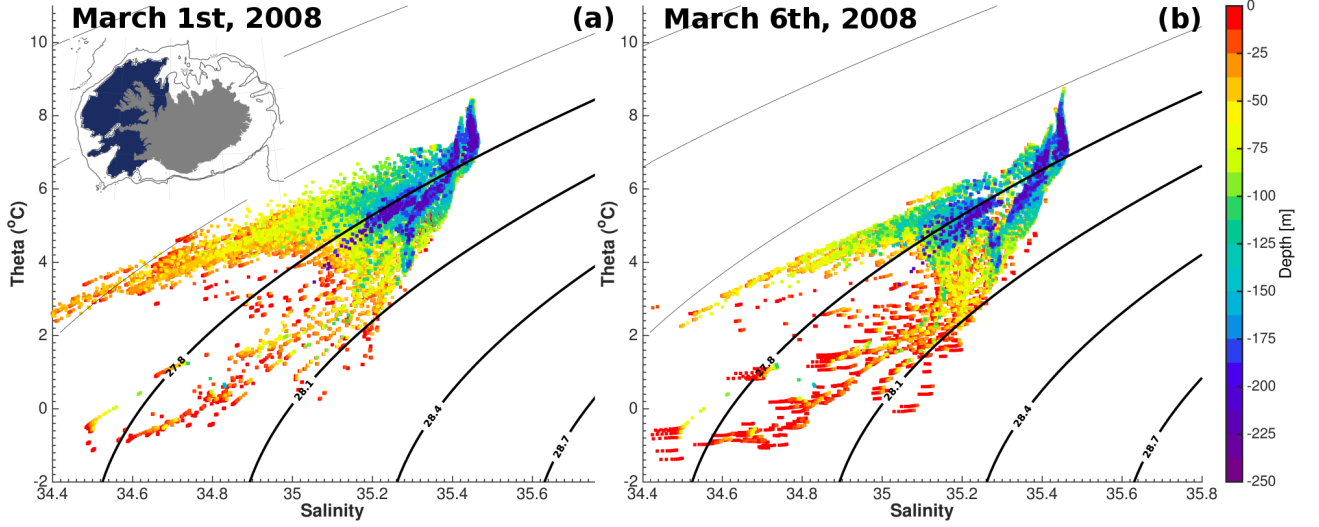


Figure 5.7: TS diagrams over the study region (represented in deep blue in the map attached to the upper left corner of panel a) for every model output during the month of March 2008. The specific date of each diagram appears labeled in the upper-most left corner of every panel.

The resistant energy (RE in Eq. 5.1) is defined as the amount of energy needed to be removed from the region, such that the density will become homogenized down to a certain depth (Holdsworth and Myers, 2015). The mathematical expression to compute the resistance energy is expressed as:

$$RE(h) = \frac{g}{A} \int \int \left[h\rho_{pot}(h) - \int_0^h \rho_{pot}(z)dz \right] dA \quad (5.1)$$

where g is the gravitational constant, A is the surface are of each grid cell, $\rho_{pot}(z)$ and $\rho_{pot}(h)$ are the potential density at each grid cell and the potential density of the grid cell at the reference depth h , respectively. In our case of study $h = 250$ m.

For the density the maximum value for every 5-days model output over the study region is shown (Figure 5.8.a-b). In the case of the resistance energy and heat loss (as well as for temperature and salinity, later on shown) the every 5 days over-the-study-region average is shown. When comparing the maximum density and the heat loss, it is noticed that the density reaches its highest value around the same time as the heat loss (Figure 5.8.a). The resistance energy, on the other hand, decreases by the time the density is the highest (Figure 5.8.b). When we compare it (resistance energy) with the heat loss (Figure 5.8.c) we notice that during the periods when the density reaches its highest values, the heat loss is (every

year) stronger than the resistance energy. This means that, the amount of energy removed from the ocean due to heat loss is indeed enough to increase the density (overflow-like) of the surface waters, making them sink while homogenizing the entire water column down to the bottom.

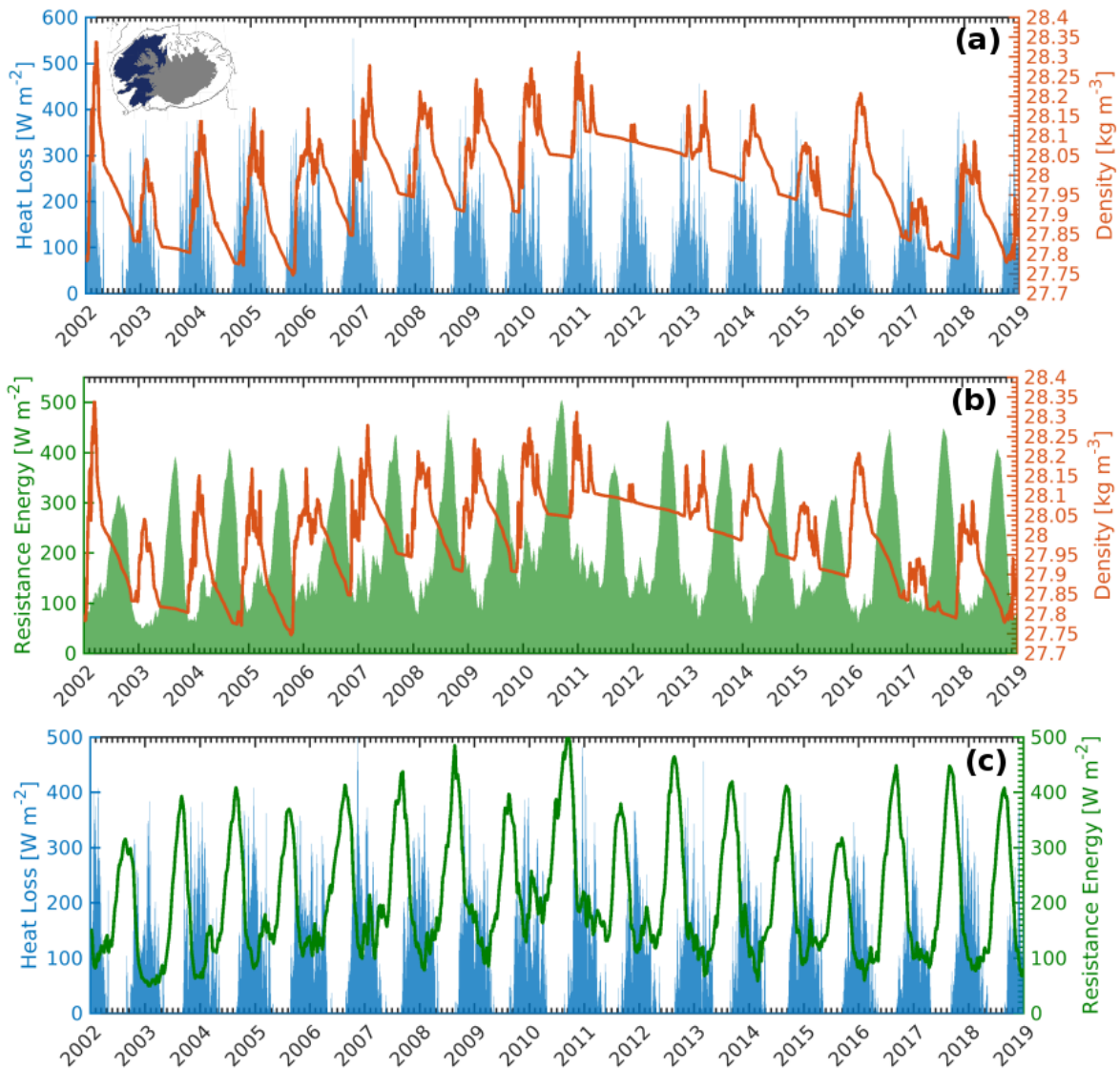


Figure 5.8: Model time series over the study region (shown in deep blue in the map attached to the upper left corner in panel a) of maximum density (a-b), resistance energy (b-c) and heat loss (a and c), from 2002 to 2018.

The trend of the maximum density over the entire period of study appears to be in phase with the salinity (Figure 5.9.a). This would indicate that the inter-annual variability of the density reached by the waters transformed is in phase with the salinity of the inflowing NIIC.

In the case of the temperature, (Figure 5.9.b) the maximum density reaches its highest value at the same time the temperature does so. This takes us back to the link between the maximum density and the ocean heat loss: the surface waters get denser at the same time the water column loses temperature due to an increase in the oceanic heat loss. Figure 5.10 shows the position of the maximum density represented in Figures 5.8 and 5.9. This confirms that the densest transformation occurs in the northwestern corner of the Icelandic shelf, and for waters found mainly between the surface and 175 m depth.

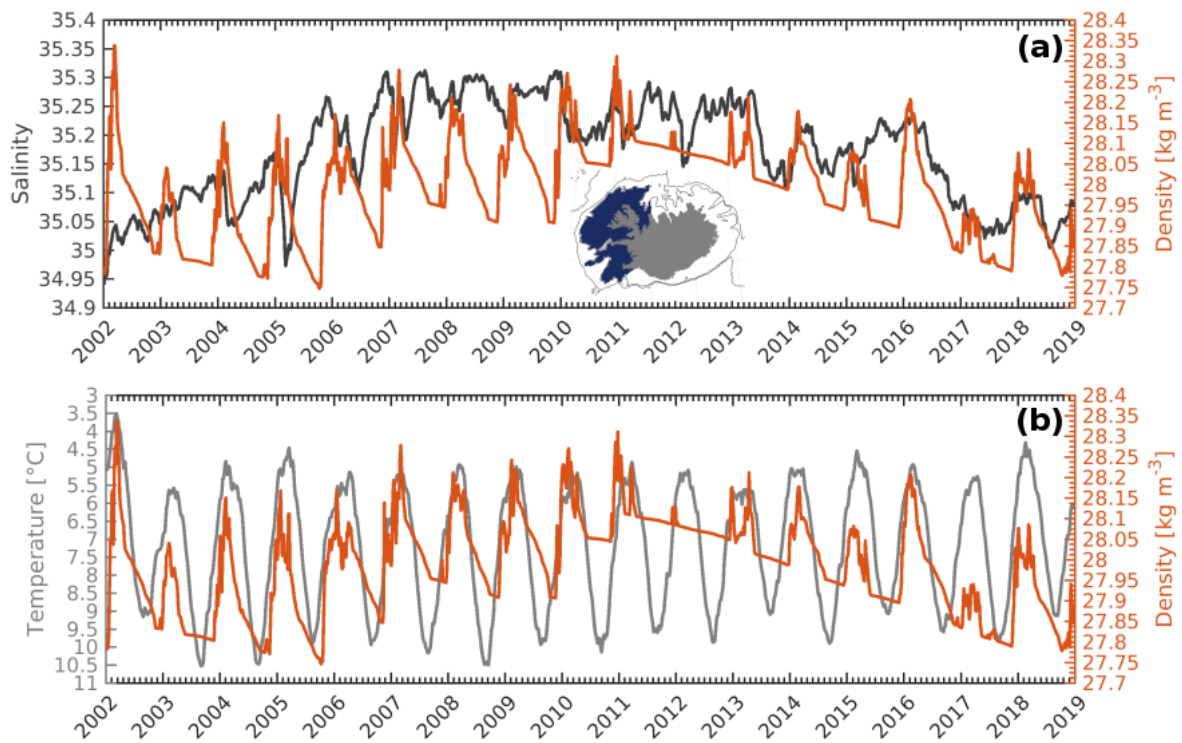


Figure 5.9: Model time series over the study region (shown in deep blue in the map attached to the upper left corner in panel a) of maximum density (a-b), salinity (a) and temperature (b), from 2002 to 2018. Note that for temperature (left y-axis in a) the scale have been inverted.

the study region, we determined that the transformation occurs mainly during the months from December (previous year) to May. Except for 2017, every year the maximum density of the transformed waters reached the density of 28 kg/m^3 . Considering the location of the region where this densification occurs and the evolution of the transformed waters, it could be expected that the generated dense plume would contribute to (or be a source of) the NIJ and hence, the DSOW.

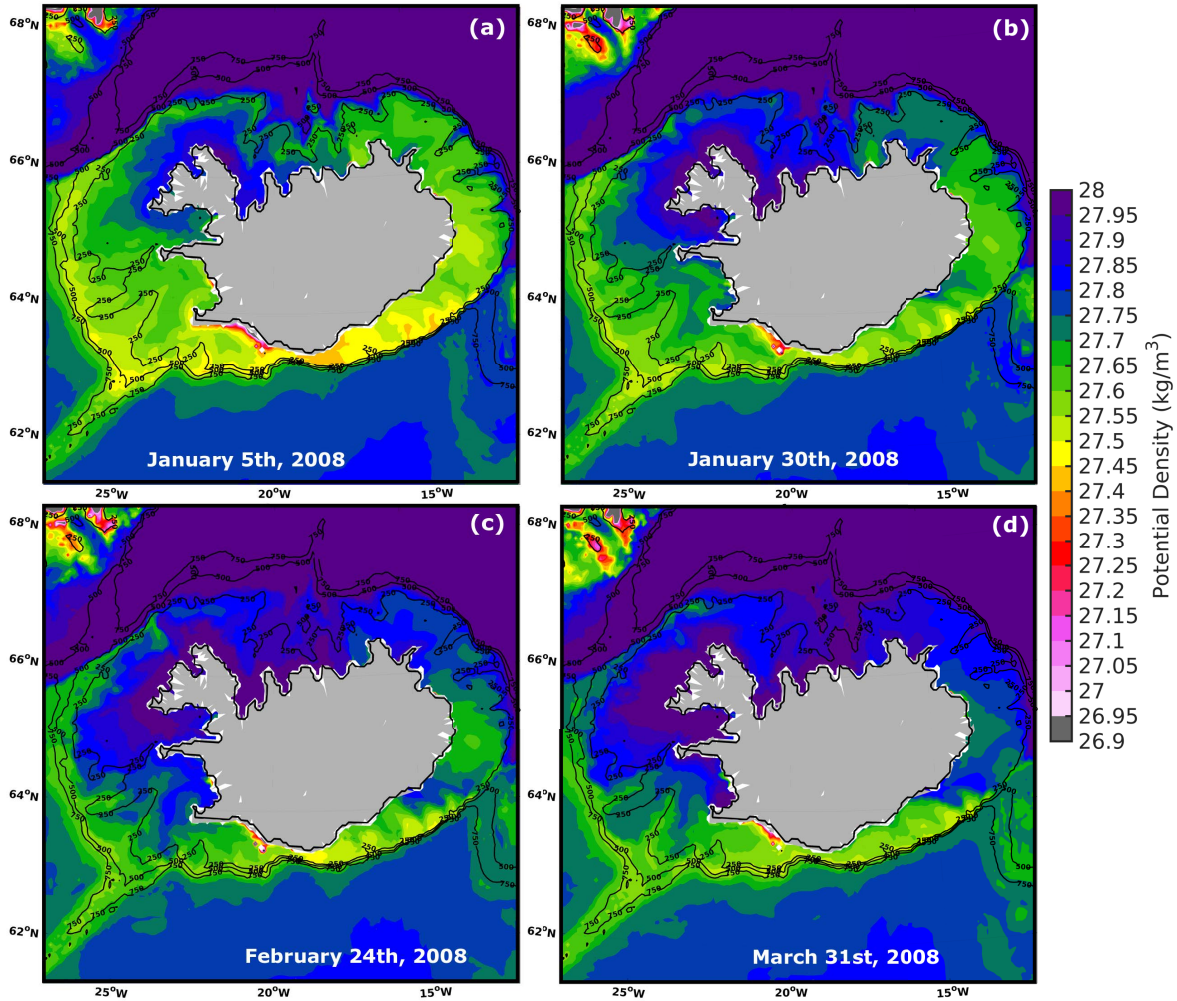


Figure 5.11: Model bottom density for different model outputs from January 2008 to the end of March 2008. The exact date of each output is labeled on the bottom of each panel (slightly towards the right).

5.3.4 Dense Water Transport

In order to investigate this possibility, we compute the transport of waters denser than 27.8 kg/m^3 across 7 sections around Iceland (Figures 5.12 and 5.14). The sections are based on the

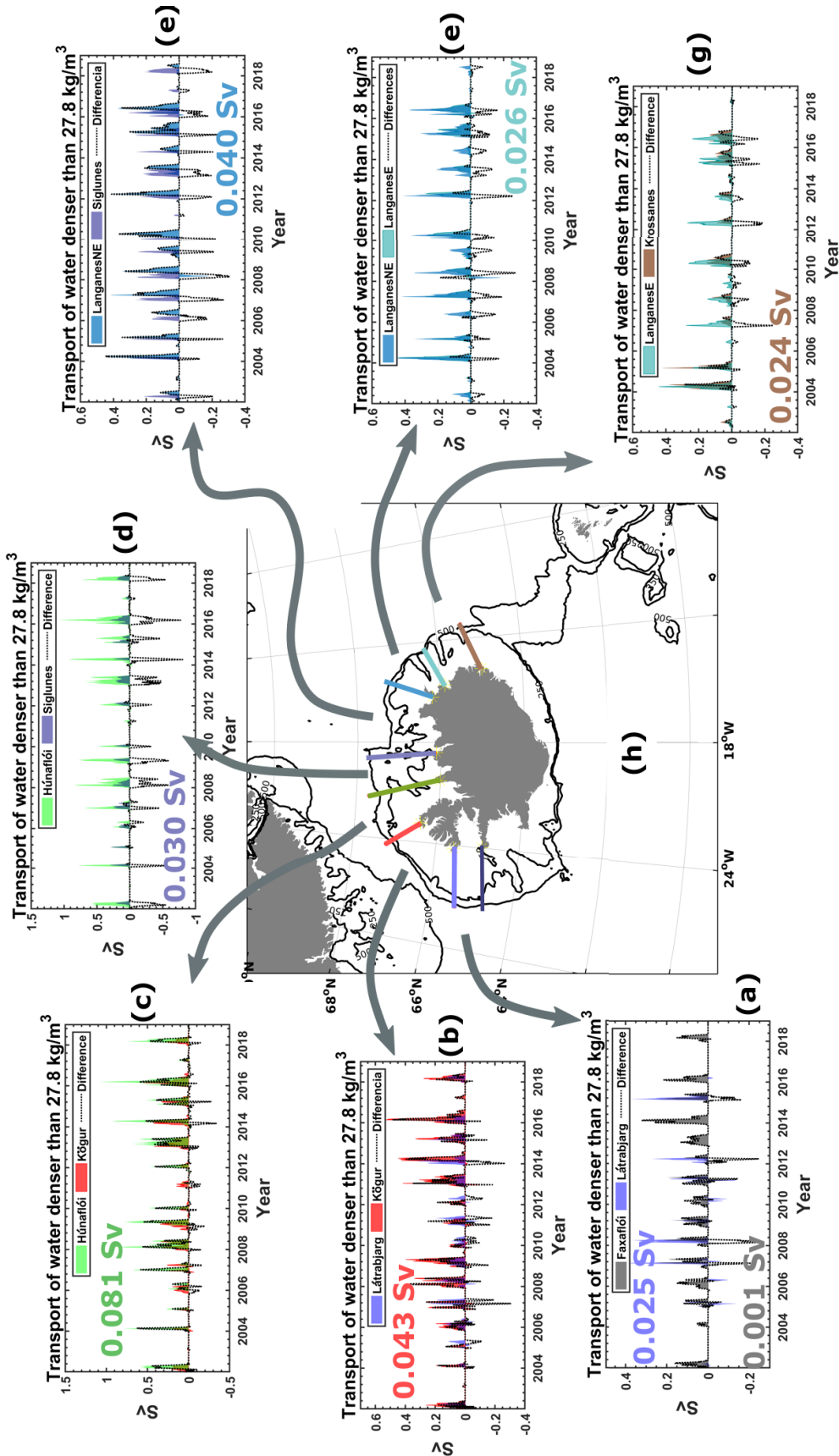


Figure 5.12: Model time series (from 2002 to 2018) of transport for waters denser than 27.8 kg/m^3 , across 7 different sections located from west to east around the Icelandic shelf, from the coast to 250 m depth. The name of each section appears on the legend of each panel. The mean transport of dense water across each section appears color-coded following the color of the given section. Transport differences between sections are represented by dotted black lines. The transport across sections are plotted in pairs in order to better visualize when the transport builds up or decreases compared to a previous section.

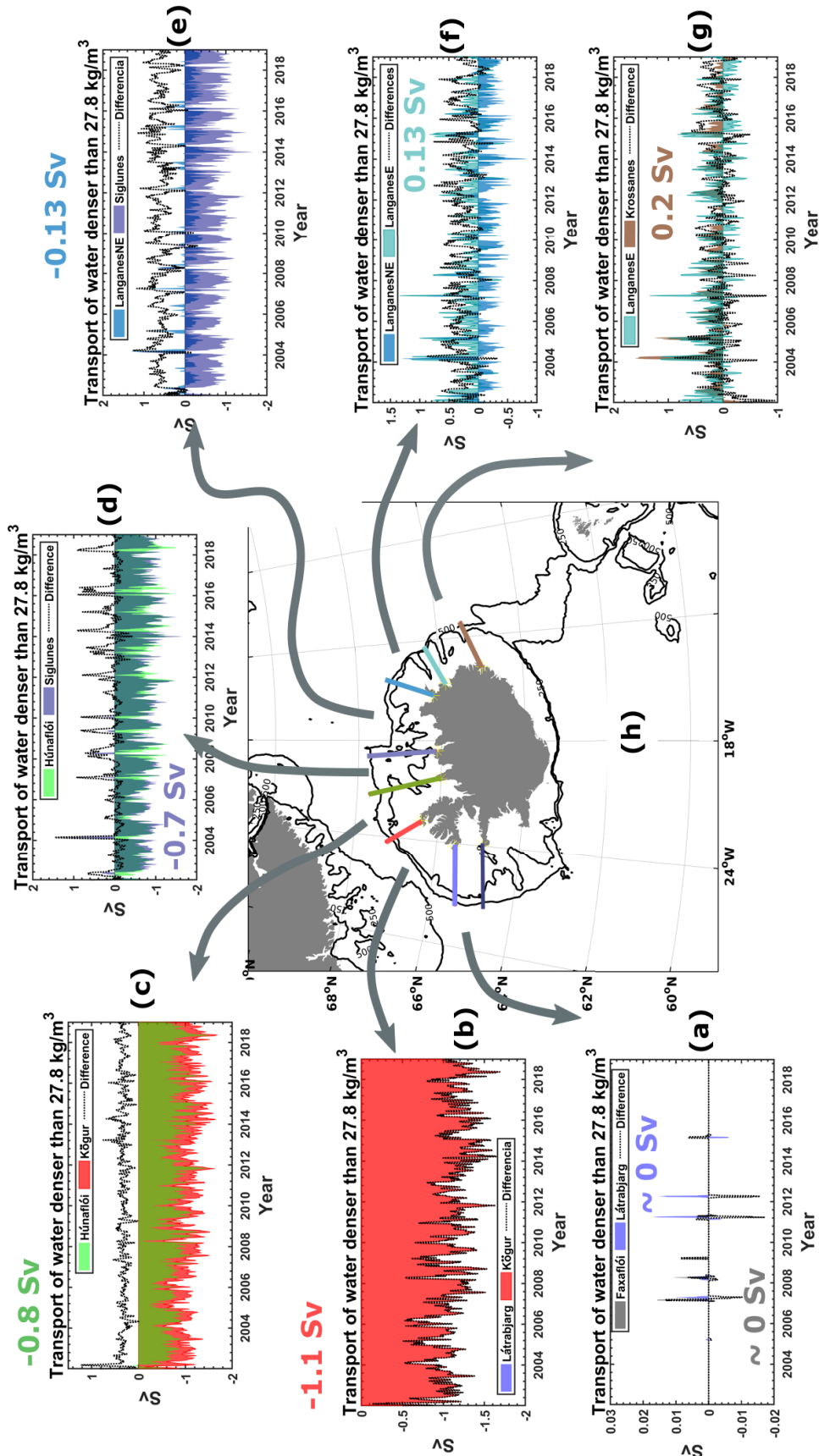


Figure 5.14: Model time series (from 2002 to 2018) of transport of waters denser than 27.8 kg/m^3 , across 7 different sections located from west to east around the Icelandic shelfbreak, from 250 to 750 m depth. The name of each section appears on the legend of each panel. The mean transport of dense water across each section appears color-coded following the color of the given section. Transport differences between sections are represented by dotted black lines. The transport across sections are plotted in pairs in order to better visualize when the transport builds up or decreases compared to a previous section.

February, and from January to July the second year (2012-2013). In order to establish a link between the timing of the dominant regime and the atmospheric forcing upstream of Denmark Strait, they looked into lagged correlations between the dominant NIJ regime with monthly heat fluxes and wind speed. They showed that for turbulent heat fluxes two regions came out to be statistically significant +2-month time lag correlated: one region located on the north slope of Iceland around the 1000 m isobath (south side of the Spar Fracture zone), while their other region is basically our study area, on the west/northwest corner of the Icelandic shelf (see Figures 12.c, 13.a and 13.b of Huang et al., 2019). They found the same pattern to be present for the latent and heat fluxes separately. However they focused on the first region mentioned.

Their findings point out that larger heat fluxes over the identified region(s) leads to the NIJ dominant regime. We then can assume that the dominant regime of the NIJ established by Huang et al. (2019) is merely a response to the dense plume generated from the NIIC transformation during strong winter heat loss episodes. Considering the timing of the dense plume in our case of study (Figure 5.11): by February 24th, 2008, the dense plume has started to cascade, from the cascading point and at a speed of 15 cm/s, it would take the dense waters around 20 days to reach the Kögur section. This is less than three months from the moment the first signal of dense bottom water appears around the source region (Figure 5.11.a) and almost 2 month after the heat loss is at its maximum (Figure 5.6.b). This is consistent with Huang et al. (2019) findings.

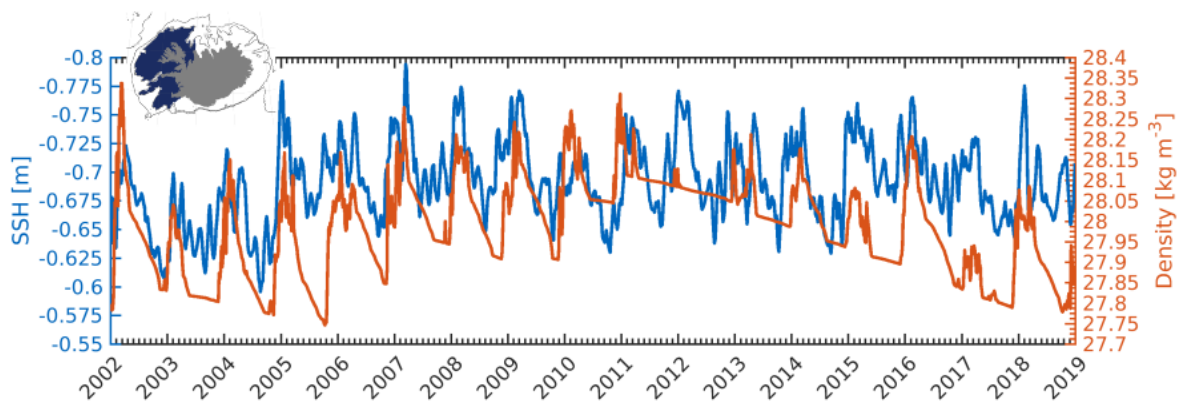


Figure 5.15: Model time series of mean SSH and maximum density, from 2002 to 2018 over the study region (area represented in deep blue in the map attached to the upper left corner of the figure). Note that the scale for the left y-axis have been inverted.

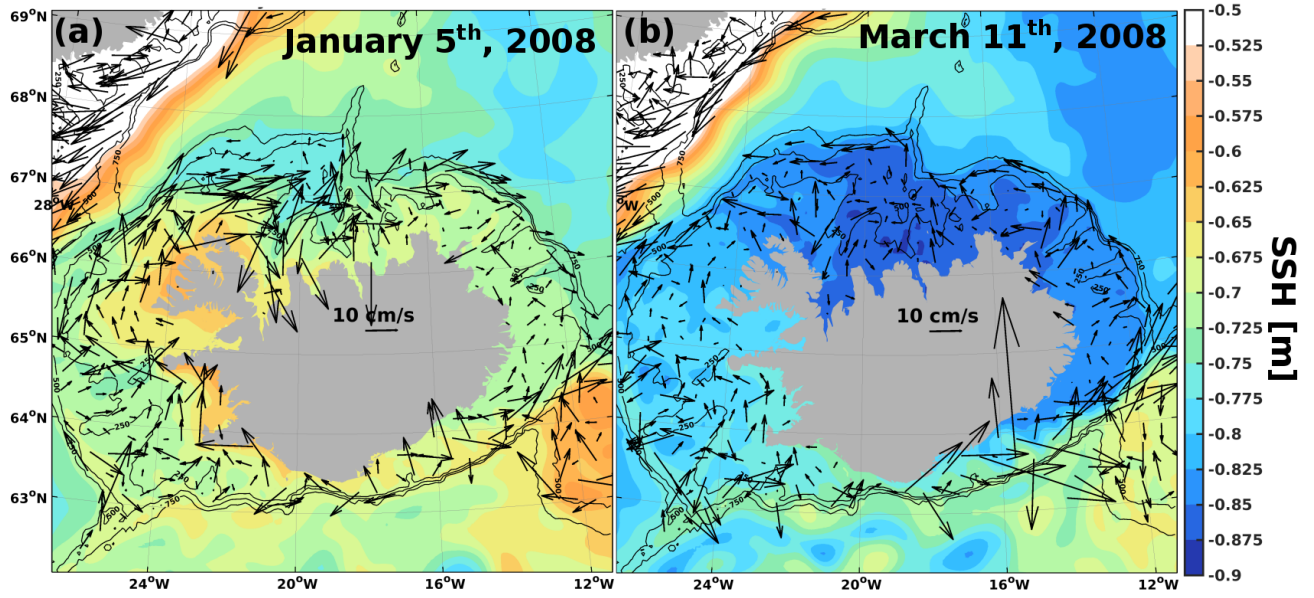


Figure 5.16: Model sea surface height (SSH) and ocean current speed at 5 m depth, for a) January 5th and b) and March 11th, 2008. The date of each output is labeled in the upper left corner of every panel.

We understand that, as the model is somewhat salty compared to the observations (Figures 5.3.c and 5.4.c) the formation of the dense plume might be interpreted as an artificial signal of the model induced by its salinity drift. First, we are able to see the formation of the dense plume right from the beginning of the simulation, and secondly, there is actual observational evidence of dense water on the Icelandic shelf. Figure 5.18 shows the analysis of all the temperature and salinity profiles from 1929 to present, between -28° to -17° W and 64° to 67° N (Figure 5.18.a), available in the International Council for the Exploration of the Sea (ICES) database. We filtered the data and selected only those profiles located in waters shallower than 250 m depth and where the density was equal or higher than 27.8 kg/m^3 . Contrary to what has generally been thought, there is in fact water denser than 27.8 kg/m^3 on the Icelandic shelf (Figure 5.18.b). When we looked into the month when all the profiles were taken (before applying density and depth criteria) we found that the vast majority were registered during the months from April to October (Figure 5.18.c). This omits the time of the year when the dense waters form west/northwest of Iceland. The profiles shallower than 250 m and where water denser than 27.8 kg/m^3 was present, were indeed registered mostly from April to October (Figure 5.18.d). A TS diagram of the filtered data (Figure 5.19) shows

that the density of the water can be as high as 28 kg/m^3 , which is consistent with our findings (Figure 5.7). Considering that these densities are present in the months from April to October, we can assume that during the months from November to March when the heat loss is stronger, the density of the waters would be larger.

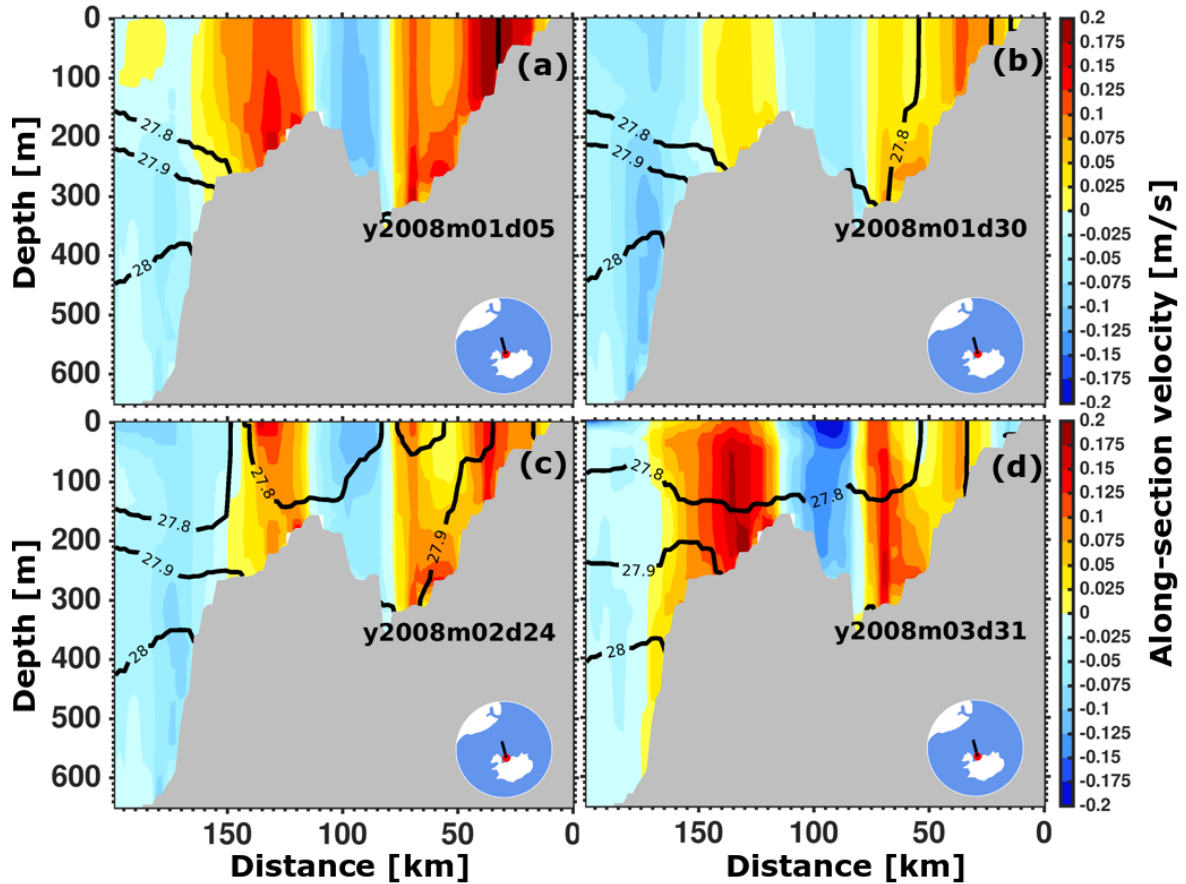


Figure 5.17: Model along-section velocity at the Húnaflói section for different model outputs from January 2008 to the end of March 2008 (consistent with Figure 5.11). The date of the model output is labeled on each panel. The position of the section is represented on the map attached to the lower-right corner of each panel. Positive values means the flow is towards the right of the section (clockwise/anticyclonic) while negative values represent the flow traveling towards the left of the section (counterclockwise/cyclonically).

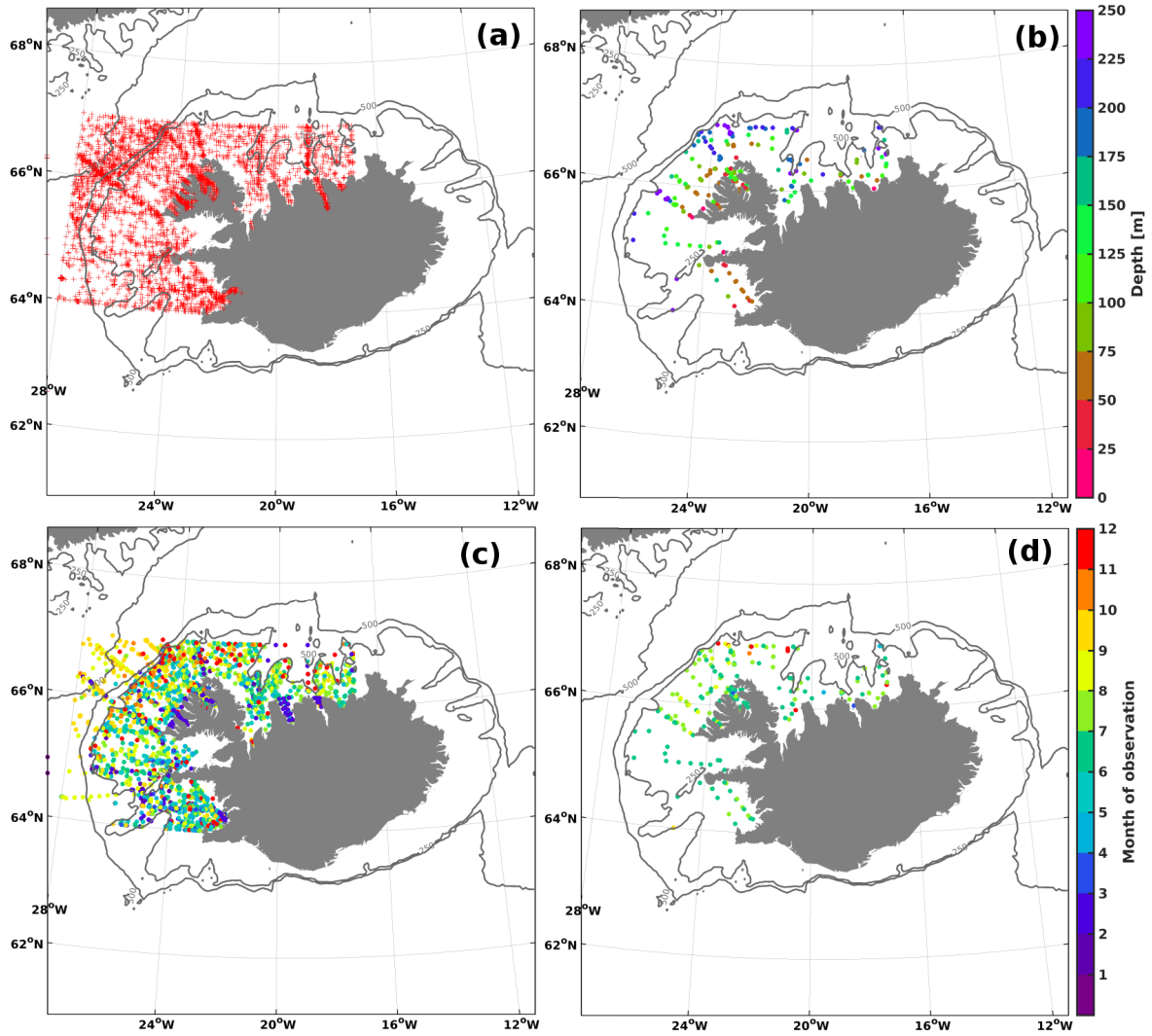


Figure 5.18: Temperature and salinity profiles, from 1929 to present, between -28° to -17° W and 64° to 67° N, available at the International Council for the Exploration of the Sea (ICES) database. (a) Location of all the profiles. (b) Position of the profiles shallower than 250 m on the Icelandic shelf, and with density higher than 27.8 kg/m^3 . (c) Month of the year when all the temperature and salinity profiles (represented in a) were taken. (d) Like in (c) but only for the profiles shallower than 250 m (on the Icelandic shelf) where water denser than 27.8 kg/m^3 was registered.

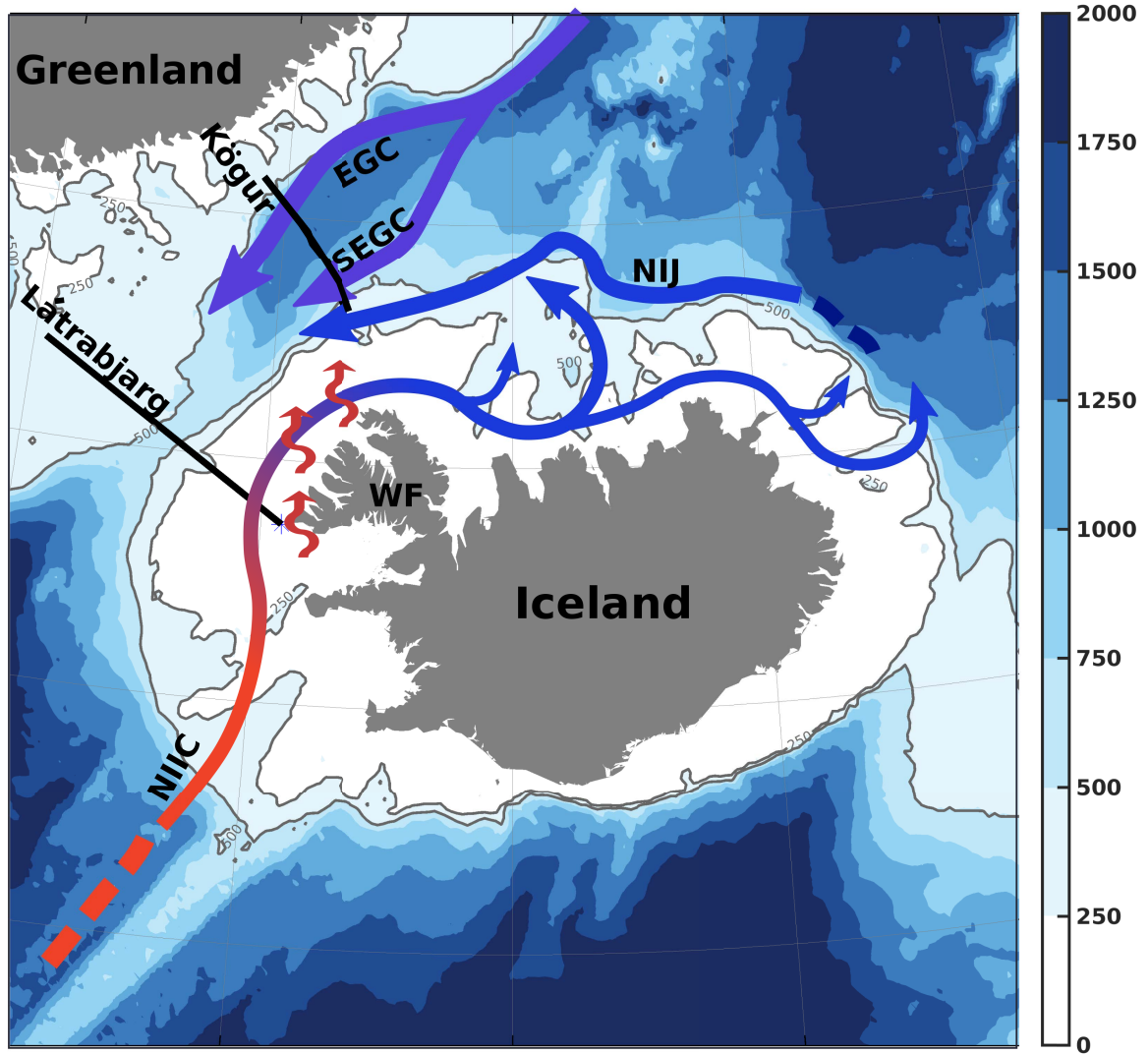


Figure 5.20: Schematic circulation in the area northwest/north of Iceland discussed in the text. Here we proposed the following: the NIJ represents the lower limb of a local overturning loop where the heat loss induced transformation (represented by red wiggly arrows in the northwest corner of Iceland) of the inflowing NIIC generates a dense plume which travels anticyclonically around and on the Icelandic shelf. The dense plume then cascades down the Icelandic shelf at different locations. The cascaded dense waters feed the cyclonic circulation which results from the SSH depression (Figure 5.16) as stated by Spall et al. (2017), and which carries the dense waters towards Denmark Strait, enhancing equatorward flow on the continental slope there, and hence, an stronger NIJ (Huang et al., 2019). The color scale indicates the ocean depth in meters.

These findings are of a great significance considering that the NIJ is basically the densest component of the AMOC lower limb. Assuming the inflow of the NIIC to remain unchanged, a decrease in the heat loss over the southern portion of the Nordic Seas poses the bigger threat for the replenishment of the lower limb of the AMOC. Mostly by considering the projected